

UNIVERSITY OF MONTENEGRO
FACULTY OF NATURAL SCIENCES AND MATHEMATICS
AND
UNIVERSITY OF ANTWERP
FACULTY OF SCIENCE
DEPARTMENT OF PHYSICS

Božidar Šoškic

MAGNETISM AND SUPERCONDUCTIVITY IN
TWO-DIMENSIONAL (2D) BORON CRYSTAL
STRUCTURES

Doctoral thesis

Podgorica, 2025.

UNIVERSITY OF MONTENEGRO
FACULTY OF NATURAL SCIENCES AND MATHEMATICS
AND
UNIVERSITY OF ANTWERP
FACULTY OF SCIENCE
DEPARTMENT OF PHYSICS

Božidar Šoškic

MAGNETISM AND SUPERCONDUCTIVITY IN
TWO-DIMENSIONAL (2D) BORON CRYSTAL
STRUCTURES

Doctoral thesis

Podgorica, 2025.

UNIVERZITET CRNE GORE
PRIRODNO-MATEMATIČKI FAKULTET

I

UNIVERZITET U ANTVERPENU
FAKULTET PRIRODNIH NAUKA
ODSJEK ZA FIZIKU

Božidar Šoškic

MAGNETIZAM I SUPERPROVODLJIVOST U
DVODIMENZIONALNIM (2D) KRISTALNIM
STRUKTURAMA BORA

Doktorska disertacija

Podgorica, 2025.

Acknowledgements

I am overwhelmingly thankful to my mentors, Prof. Dr. Predrag Miranović, Dr. Željko Šljivančanin, and Prof. Dr. Milorad Milošević, for their outstanding guidance, perceptive counsel, and steadfast support throughout the preparation of my doctoral thesis. Their profound expertise, invaluable critiques, and unwavering accessibility have been pivotal in directing my research. I would also like to sincerely acknowledge the members of my PhD jury for their invaluable and constructive feedback. I wish to convey my sincere gratitude to Prof. Dr. Borko Vujičić, whose confidence in my abilities and support during my bachelor's and master's studies have been crucial in "molding" my scientific career. I am especially thankful to him for introducing me to an outstanding research group at the Vinča Institute of Nuclear Sciences. My sincere gratitude also goes to my colleagues Dr. Srdjan Stavrić, Dr. Jonas Bekaert, M.Sc. Denis Šabani, Dr. Tribhuwan Pandey, M.Sc. Mikhail Petrov, and Dr. Cem Sevik, for their invaluable technical support, fruitful discussions, and assistance in writing this thesis.

I also owe a great debt of gratitude to my parents, Nikola and Stanojka, and my sister, Marina, for their unwavering encouragement and assistance throughout my personal and academic journey. A special thanks goes to my friends, Dušan Boljanić, Aleksa Popović, Marko Orozović, and others, for their understanding, patience, and support, which helped me to overcome the challenges I faced during my studies. Finally, I would like to thank my girlfriend, Marija Popović, whose unwavering love, patience, and steadfast support made the entire writing process significantly easier. Her constant encouragement and understanding have been invaluable throughout this "endeavor", and I am profoundly grateful for her presence by my side.

My research was supported by the Montenegrin Ministry of Science and Technological Development, the Special Research Fund of University of Antwerp (BOF-UA, Grant No. 542300011), and the Research Foundation – Flanders (FWO). Computational resources were provided by the Flemish Supercomputer

Center (VSC), funded by the FWO and the Flemish Government (department EWI), as well as by PRACE (Beskow supercomputer, KTH Royal Institute of Technology, Sweden) and CINECA (ISCRA initiative, University of Trieste). Financial support was also received from the Italian Ministry of Foreign Affairs and International Cooperation under the “Progetti di Grande Rilevanza” initiative. This research further benefited from EU COST Actions NANOCOHBRI (CA16218), SUPERQUMAP (CA21144), and Hi-SCALE (CA19108), along with the Erasmus KA107 Mobility Program between the University of Montenegro and the University of Belgrade.

Božidar Šoškić



This doctoral thesis was prepared and submitted

as part of a

**Partnership Agreement governing the joint supervision and awarding of a
doctoral diploma**

between

Universiteit Antwerpen (University of Antwerp) – Belgium

Faculty of Science, Department of Physics

and

Univerzitet Crne Gore (University of Montenegro) – Montenegro

Faculty of Natural Sciences and Mathematics, Department of Physics

The title of the doctoral thesis is given in:

English:

Magnetism and superconductivity in two-dimensional (2D) boron crystal structures

Montenegrin:

Magnetizam i superprovodljivost u dvodimenzionalnim (2D) kristalnim strukturama bora

Dutch:

Magnetisme en supergeleiding in twee-dimensionale (2D) boorkristalstructuren

Podgorica / Antwerpen, 2025.



1. *PERSONAL DATA AND INFORMATION ABOUT THE PHD STUDENT*

- **First name:** *Božidar*
- **Last name:** *Šoškić*
- **Place of birth:** *Einsiedeln, Switzerland*
- **Date of birth:** *26/02/1995*
- **Diploma – degree:** *M.Sc. Physics, issued by the University of Montenegro on 14/12/2018*

2. *PERSONAL DATA AND INFORMATION ABOUT THE SUPERVISORS*

(At the University of Montenegro)

- **SUPERVISOR I:** *Prof. Dr. Predrag Miranović, Faculty of Natural Sciences and Mathematics, University of Montenegro, Podgorica, Montenegro*
- **SUPERVISOR II:** *Dr. Željko Šljivančanin, Vinča Institute of Nuclear Sciences, University of Belgrade, Belgrade, Serbia*

(At the University of Antwerp)

- **SUPERVISOR I:** *Prof. Dr. Milorad Milošević, Department of Physics, Faculty of Science, University of Antwerp, Antwerp, Belgium*



3. *MEMBERS OF THE DOCTORAL JURY*

- *Prof. Dr. Predrag Miranović, University of Montenegro, Montenegro*
- *Dr. Željko Šljivančanin, Vinča Institute of Nuclear Sciences, University of Belgrade, Serbia*
- *Prof. Dr. Borko Vujičić, University of Montenegro, Montenegro*
- *Dr. Marin Petrović, Institute of Physics in Zagreb, Croatia*
- *Dr. Nenad Lazarević, Institute of Physics in Belgrade, Serbia*
- *Prof. Dr. Milorad Milošević, University of Antwerp, Belgium*
- *Prof. Dr. Francois Peeters, University of Antwerp, Belgium*

4. *THE DATE OF DEFENSE:*

- 16/07/2025



NAME OF DOCTORAL STUDIES:

- PHYSICS
-

TITLE OF DOCTORAL DISERTATION:

- MAGNETISM AND SUPERCONDUCTIVITY IN TWO-DIMENSIONAL (2D) BORON CRYSTAL STRUCTURES
-

KEYWORDS:

- BORON, BOROPHENE, DFT, SDFT, MAGNETISM, DFPT, SUPERCONDUCTIVITY, MIGDAL-ELIASHBERG THEORY
-

RESEARCH FIELD:

- CONDENSED MATTER PHYSICS
-

SUBFIELD:

- MAGNETISM AND SUPERCONDUCTIVITY IN LOW-DIMENSIONAL MATERIALS



NAZIV DOKTORSKIH STUDIJA:

-
- FIZIKA

NASLOV DOKTORSKE DISERTACIJE:

-
- MAGNETIZAM I SUPERPROVODLJIVOST U DVODIMENZIONALNIM (2D) KRISTALNIM STRUKTURAMA BORA

KLJUČNE RIJEČI:

-
- BOR, BOROFEN, DFT, SDFT, MAGNETIZAM, DFPT, SUPERPROVODLJIVOST, MIGDAL-ELIAŠBERG TEORIJA

NAUČNA OBLAST:

-
- FIZIKA KONDENZOVANOG STANJA MATERIJE

UŽA NAUČNA OBLAST:

-
- MAGNETIZAM I SUPERPROVODLJIVOST U NISKO DIMENZIONALNIM MATERIJALIMA



NAAM VAN DOCTORAATSOPLEIDING:

- DOCTORAAT IN DE WETENSCHAPPEN: FYSICA
-

TITLE:

- MAGNETISME EN SUPERGELEIDING IN TWEE-DIMENSIONALE (2D) BOORKRISTAL-STRUCTUREN
-

SLEUTELWOORDEN:

- BOOR, BOROFEEEN, DFT, SDFT, MAGNETISME, DFPT, SUPERGELEIDING, MIGDAL-ELIASHBERG THEORIE
-

ONDERZOEKSVELD:

- FYSICA VAN DE GECONDENSEERDE MATERIE
-

SUBVELD:

- MAGNETISME EN SUPERGELEIDING IN LAAG-DIMENSIONALE MATERIALEN

Abstract

Due to intrinsic electron deficiency, boron is renowned for its complex bonding nature and exhibits remarkable structural versatility, with 16 predicted bulk phases, though only a few have been experimentally confirmed. This adaptability, along with its intriguing physical and chemical properties, extends to the two-dimensional (2D) boron (B) sheet known as *borophene*, which exists in multiple polymorphic forms due to its flexible bonding arrangements. Theoretical studies have predicted exceptional physical properties for borophene, including high electrical conductivity, mechanical strength, metallicity, and potential for hosting superconductivity, positioning it as a more promising candidate than graphene and other emerging 2D elemental materials. However, its synthesis and large-scale production remain a significant challenge, primarily because it is relying on methods such as molecular beam epitaxy (MBE) or chemical vapor deposition (CVD), which require metallic substrates, high temperatures, and ultra-high vacuum (UHV) conditions. Alternative top-down strategies, like low-temperature liquid-phase exfoliation (LTLPE), have been explored but often suffer from residual contamination, insufficient domain sizes, and uncontrolled thickness, thereby limiting their scalability and practical implementation. Additionally, achieving true atomic resolution with scanning tunneling microscopy (STM) or other characterization techniques remains challenging for borophene, even with enhanced tip modifications. In this context, density functional theory (DFT) calculations are indispensable for gaining deeper insights into the true structures of the synthesized borophenes. However, one of the main challenges is its high chemical reactivity, which leads to rapid oxidation under ambient conditions, posing a fundamental obstacle to its integration into practical devices. To mitigate these challenges, passivation strategies, including surface hydrogenation of monolayer borophene, and functionalization of bilayer configurations, have been employed, rendering

borophene inert under ambient conditions while preserving its tunable mechanical, electronic and other physical properties.

This thesis investigates β_{12} borophene – by using spin-dependent density functional theory (SDFT) and other theoretical models – as a promising platform for stabilizing artificial Fe-based 2D magnets, leveraging its unique periodic lattice and high reactivity to prevent the clustering of adsorbed adatoms, in contrast to graphene. While these systems exhibit well-ordered 2D Fe magnetic structures, the Curie temperature remains below room temperature, suggesting that further optimization, such as substituting Fe with Co, could enhance it due to higher anisotropy. However, the material’s susceptibility to oxidation limits its practical applications. We propose therefore Mn-intercalated bilayer β_{12} borophene as a solution to this oxidation problem, as it is also the only dynamically stable structure among the considered intercalants that maintains some magnetic moment. We investigated the microscopic origin of magnetism in this system, revealing a dominant direct d_{yz} – d_{yz} interaction of Mn atoms and superexchange or super-superexchange interaction mediated by B- p_z orbitals, leading to stable long-range magnetic order, positioning therefore this material as a strong candidate for spintronic applications. In addition to magnetism, we investigated the potential of boron-based 2D materials for creation of superconducting nano-devices by employing density functional perturbation theory (DFPT) and by solving the anisotropic Migdal-Eliashberg equations. While previous studies suggested that the bare β_{12} borophene is an intrinsic superconductor, experimental confirmation has remained elusive. Our findings challenge these reports, showing that the bare β_{12} borophene is dynamically unstable in its freestanding form and can only be stabilized under biaxial tensile strain (substrate effect) but with absence of measurable superconductivity. This discrepancy with previous reports is explained by the reduced contribution of B- σ states to the total density of states (DOS) at the Fermi level (E_F) under influence of this strain effect. However, we demonstrate that hydrogenation actually stabilizes β_{12} borophene and enhances its superconducting properties. Strain engineering or hole doping further optimize these properties, achieving critical temperatures (T_c) up to 30 K, primarily due to the increased contributions of B- p_z and B- σ states to the DOS at the E_F . Our work opens a pathway for experimentally probing superconductivity in this system, knowing that the transfer of borophene from metallic to non-metallic substrates is nowadays possible. Additionally, we explore intercalated bilayer borophenes, including β_{12} , χ_3 , δ_4 , and kagome phases, identifying seventeen potential superconducting systems by using alkali, alkaline-earth, and transition metals as intercalants, which are exhibiting intriguing nesting effects, high Fermi

surface anisotropy, multi-gap behavior, and more. For their superconducting properties it is important to find a good balance between partial occupation of B- p_z and B- σ states. Among considered materials, Ca-intercalated kagome borophene emerges as the best candidate, with a T_c approaching 58 K. These findings underscore the dual potential of borophene-based materials for both magnetic and superconducting applications, providing valuable insights for further development of advanced 2D devices for spintronics and superconducting technologies.

Abstract – Dutch versie

Vanwege zijn intrinsieke elektronendeficiëntie staat boor bekend om zijn complexe bindingsstructuur en opmerkelijke structurele veelzijdigheid, met 16 voorspelde bulkfasen, waarvan er echter slechts enkele experimenteel zijn bevestigd. Deze aanpasbaarheid, samen met zijn intrigerende fysische en chemische eigenschappen, strekt zich uit tot de tweedimensionale (2D) boorstructuur, bekend als borofeen, dat in meerdere polymorfe vormen voorkomt vanwege zijn flexibele bindingsconfiguraties. Theoretische studies voorspellen uitzonderlijke fysische eigenschappen voor borofeen, waaronder een hoge elektrische geleidbaarheid, mechanische sterkte, metalliciteit en potentieel voor supergeleiding, waardoor het een veelbelovendere kandidaat is dan grafeen en andere opkomende 2D-elementaire materialen. Echter, de synthese en grootschalige productie blijven een aanzienlijke uitdaging, voornamelijk omdat het afhankelijk is van methoden zoals moleculaire bundelepitaxie (MBE) of chemische dampdepositie (CVD), die metalen substraten, hoge temperaturen en ultrahoog vacuüm (UHV) vereisen. Alternatieve top-down strategieën, zoals laagtemperatuur vloeistoffase-exfoliatie (LTLPE), zijn onderzocht, maar kampen vaak met restverontreiniging, onvoldoende domeingrootte en ongecontroleerde dikte, waardoor hun schaalbaarheid en praktische toepassing beperkt blijven. Bovendien blijft het verkrijgen van ware atomaire resolutie met rastertunnelmicroscopie (STM) of andere karakteriseringstechnieken een uitdaging voor borofeen, zelfs met verbeterde tipmodificaties. In deze context zijn berekeningen op basis van de dichtheidsfunctionaaltheorie (DFT) onmisbaar om diepere inzichten te verkrijgen in de ware structuren van gesynthetiseerde borofenen. Een van de belangrijkste uitdagingen is echter de hoge chemische reactiviteit, wat leidt tot snelle oxidatie onder omgevingsomstandigheden en een fundamentele belemmering vormt voor de integratie in praktische toepassingen. Om deze uitdagingen te overwinnen, zijn passivatiestrategieën, zoals oppervlaktehydrogenering van

monolaag borofeen en functionalisering van bilagenconfiguraties, toegepast om borofeen inert te maken onder omgevingsomstandigheden, terwijl de instelbare mechanische, elektronische en andere fysische eigenschappen behouden blijven.

Deze thesis onderzoekt β_{12} -borofeen – met behulp van spin-afhankelijk dichtheidsfunctionaaltheorie (SDFT) en andere theoretische modellen – als een veelbelovend platform voor het stabiliseren van kunstmatige Fe-gebaseerde 2D-magneten. Hierbij wordt gebruikgemaakt van de unieke periodieke roosterstructuur en hoge reactiviteit van borofeen om clustervorming van geadsorbeerde adatomen te voorkomen, in tegenstelling tot grafeen. Hoewel deze systemen goed geordende 2D-Fe-magnetische structuren vertonen, blijft de Curie-temperatuur onder kamertemperatuur, wat suggereert dat verdere optimalisatie, zoals substitutie van Fe door Co, dit zou kunnen verbeteren vanwege een hogere anisotropie. Echter, de gevoeligheid van het materiaal voor oxidatie beperkt de praktische toepassingen. Daarom stellen we Mn-geïntercaleerd bilagen- β_{12} -borofeen voor als oplossing voor dit oxidatieprobleem, aangezien het ook de enige dynamisch stabiele structuur is onder de beschouwde intercalanten die een magnetisch moment behoudt. We onderzochten de microscopische oorsprong van magnetisme in dit systeem en onthulden een dominante directe d_{yz} - d_{yz} -interactie tussen Mn-atomen, evenals superwisselwerking of super-superwisselwerking gemedieerd door B- p_z -orbitalen. Dit leidt tot stabiele langbereikmagnetische ordening, waardoor dit materiaal een sterke kandidaat wordt voor spintronische toepassingen. Naast magnetisme onderzochten we het potentieel van boorgebaseerde 2D-materialen voor de creatie van supergeleidende nanodevices door gebruik te maken van dichtheidsfunctionaalperturbatietheorie (DFPT) en het oplossen van de anisotrope Migdal-Eliashberg-vergelijkingen. Hoewel eerdere studies suggereerden dat het pure β_{12} -borofeen een intrinsieke supergeleider is, is experimentele bevestiging hiervan tot op heden uitgebleven. Onze bevindingen dagen deze rapporten uit en tonen aan dat onbehandeld β_{12} -borofeen dynamisch instabiel is in zijn vrijstaande vorm en alleen kan worden gestabiliseerd onder biaxiale trekspanning (substraat-effect), maar zonder meetbare supergeleiding. Deze discrepantie met eerdere studies wordt verklaard door de verminderde bijdrage van B- σ -toestanden aan de totale toestandsdichtheid (DOS) bij het Fermi-niveau (E_F) onder invloed van dit spanningseffect. Echter, we tonen aan dat hydrogenering β_{12} -borofeen stabiliseert en zijn supergeleidende eigenschappen verbetert. Spanning-engineering of gatendoping optimaliseren deze eigenschappen verder en bereiken kritische temperaturen (T_c) tot 30 K, voornamelijk door de verhoogde bijdragen van B- p_z - en B- σ -toestanden aan de DOS bij E_F . Ons werk opent een pad voor experimenteel onderzoek

naar supergeleiding in dit systeem, vooral gezien het feit dat de overdracht van borofeen van metalen naar niet-metalen substraten tegenwoordig mogelijk is. Daarnaast onderzochten we geïntercaleerde bilagen borofenen, waaronder β_{12} -, χ_3 -, δ_4 - en kagome-fasen, en identificeerden we zeventien potentiële supergeleidende systemen met behulp van alkalimetalen, aardalkalimetalen en overgangsmetalen als intercalanten. Deze vertonen intrigerende nestingeffecten, hoge Fermioppervlakanisotropie, multi-gap-gedrag en meer. Voor hun supergeleidende eigenschappen is het cruciaal om een goede balans te vinden tussen gedeeltelijke bezetting van B- p_z - en B- σ -toestanden. Onder de onderzochte materialen blijkt Ca-geïntercaleerd kagome-borofeen de beste kandidaat te zijn, met een T_c tot 58 K. Deze bevindingen benadrukken het dubbele potentieel van borofeen-gebaseerde materialen voor zowel magnetische als supergeleidende toepassingen en bieden waardevolle inzichten voor de ontwikkeling van geavanceerde 2D-apparaten voor spintronica en supergeleidende technologieën.

Otkrićem grafena 2004. godine – dvodimenzionalne (2D) ugljeničke strukture debljine jednog atoma – fizika materijala doživjela je značajan procvat, zahvaljujući njegovim izuzetnim fizičkim i hemijskim osobinama koje su dovele do revolucionarnih promjena u svijetu nauke, računarstva i kvantnih tehnologija. Ovo epohalno otkriće inspirisalo je naučnu zajednicu na intenzivnu potragu za sličnim 2D materijalima sastavljenim od jednog tipa atoma, među kojima se posebno izdvojio borofen – 2D alotrop bora sa jedinstvenim strukturnim i elektronskim osobinama. Zbog inherentnog nedostatka elektrona, atom bora gradi složene hemijske veze, koje omogućavaju postojanje više različitih trodimenzionalnih faza, od kojih je samo nekoliko njih eksperimentalno potvrđeno, kao i polimorfni varijanti borofena, čime se dodatno proširuje mogućnost njegove primjene u savremenim tehnologijama.

Iako teorijska istraživanja predviđaju izuzetne fizičke osobine borofena, koje umnogome nadmašuju one koje posjeduje grafen – uključujući visoku električnu provodljivost, mehaničku čvrstoću, izraženu elastičnost, metalni karakter i sposobnost da ispolji superprovodljive osobine – njegova sinteza, kao i proizvodnja u većim razmjerama, i dalje ostaje značajan izazov jer se uglavnom oslanja na određene tradicionalne „odozdo-nagore“ metode fabrikacije 2D materijala. Najčešće se primjenjuje epitaksija molekularnim snopom (MBE) ili hemijska depozicija pare (CVD), koje zahtijevaju metalne supstrate, visoke temperature i uslove ultravisokog vakuuma (UHV) za njegovu sintezu. Alternativne „odozgo-nadolje“ metode, poput eksfolijacije borofena u tečnoj fazi na niskim temperaturama (LTLPE), u velikoj mjeri su praćene prisutnošću različitih primjesa i nečistoća u njemu, ali i malim domenima i nekontrolisanom debljinom samog materijala, što značajno otežava njegovu praktičnu primjenu. Pored toga, postizanje odgovarajuće atomske rezolucije za njegovu karakterizaciju pomoću skenirajuće elektronske

mikroskopije (STM) ili drugih tehnika karakterizacije i dalje su praćena brojnim problemima, čak i sa poboljšanim vrhom mikroskopske sonde. U tom kontekstu, proračuni teorije funkcionala gustine (DFT) su neophodni za sticanje dubljih uvida u stvarne strukture sintetizovanih borofena. Međutim, kao glavni problem se ističe njegova izražena podložnost procesu oksidacije u vazduhu, što predstavlja i glavnu prepreku njegovoj integraciji u praktične uređaje. Da bi se prevazišli ovi izazovi, primjenjuju se strategije pasivizacije, koje uključuju površinsku hidrogenizaciju jednog sloja borofena, kao i funkcionalizaciju njegovih dvoslojnih konfiguracija, usljed čega borofen postaje inertniji na negativne uticaje okoline, uz istovremeno očuvanje njegovih prilagodljivih mehaničkih, elektronskih i drugih fizičkih osobina. U ovoj doktorskoj disertaciji, navedene strukture su istaknute kao izuzetno perspektivne za istraživanje magnetnih i superprovodljivih osobina, s velikim potencijalom za njihovu primjenu u spintronici i kreiranju superprovodljivih uređaja, čime se otvara prostor za dalja istraživanja i praktičnu implementaciju.

U početnoj fazi izrade ove disertacije postavili smo nekoliko osnovnih hipoteza koje smo željeli potvrditi:

- *Da li borofen, zbog svoje izražene reaktivnosti i pravilnog rasporeda heksagonalnih šupljina, adsorpcijom magnetnih atoma posjeduje potencijal da bude idealna podloga za formiranje i stabilizaciju vještačkih 2D magneta?*
- *Ukoliko je to slučaj, da li se interkalirani 2D vještački magnet može formirati i stabilizovati u dvosloju borofena, s obzirom na to da su ove strukture inertnije na oksidaciju, čime posjeduju veći potencijal za praktičnu primjenu u spintronici?*
- *Iako su prethodna istraživanja sugerisala da je „čisti“ β_{12} borofen „intrinzični“ superprovodnik, eksperimentalne potvrde i dalje nedostaju. To nas navodi na logično pitanje: da li su raniji teorijski modeli zaista tačni i može li hidrogenizacija iste strukture doprinijeti njenoj stabilizaciji i zaštiti od oksidacije?*
- *Da li se putem interkalacije dvosloja različitih borofenskih faza može pronaći idealni kandidat za superprovodljivost?*

Prije opisivanja primjenjivanih metoda za dobijanje odgovora na postavljene hipoteze, bitno je dati veoma kratak pregled glavnih problema u polju magnetizma i superprovodljivosti u ovim materijalima. Borofen je uglavnom nemagnetan, ali defekti poput šupljina ili dopiranje prelaznim metalima mogu indukovati spinski polarizovano ponašanje u ovim sistemima. Na

primjer, defekti u β_{12} borofenu indukuju feromagnetno ponašanje sa magnetnim momentima manjim od $0.5 \mu_B$ po atomu, dok dvoatomske šupljine kreiraju izraženije feromagnetne osobine materijala sa Kirijevom temperaturom od 100 K. Takođe, i u χ_3 borofenu, jednoatomske šupljine dovode do spinske polarizacije. Dopiranje $3d$ prelaznim metalima, poput Cr i Mn, indukuje magnetizam u β_{12} borofenu, dok u slučaju Mn-interkaliranom dvosloju β_{12} borofena, Mn posjeduje magnetni moment od $1 \mu_B$ a sistem dostiže Kirijevu temperaturu od 286.5 K. Iako su rezultati obećavajući, još uvijek nedostaje mikroskopski opis izmjenskih interakcija i detaljno ispitivanje dugodometnog magnetnog uređenja u borofenu. Sa druge strane, teorijska istraživanja predviđaju da faze kao što su β_{12} i χ_3 mogu postići superprovodljivu kritičnu temperaturu (T_c) od 16 K i 12 K, sa vrijednostima konstante elektron-fonon sprege od 0.8 i 0.6, respektivno. Međutim, u ovim fazama primijećene su fononske nestabilnosti, što sugerirše da su efekti uticaja podloge, kao što su istezanje ili dopiranje materijala, potrebni za njegovu stabilizaciju, ali su često praćeni negativnim posljedicama po njegove superprovodljive osobine. Uprkos tome što borofen posjeduje izraženu anizotropiju Fermijeve površi, što znači da je superprovodljivost u njemu anizotropna sa većim vrijednostima T_c , eksperimentalne potvrde prisutnosti superprovodljivih „tragova“ u njemu i dalje nedostaju. Raman spektroskopija je pokazala niže vrednosti T_c za prethodno pomenute faze (7.1 K i 9.8 K) u odnosu na teorijski očekivane vrijednosti, što ukazuje na hitnu potrebu za dodatnim istraživanjima.

Međutim, da bismo došli do konačnog odgovora na postavljene hipoteze, koristili smo softverske pakete koji se uglavnom baziraju na DFT metodi, ali i na drugim teorijskim modelima, kako bismo ispitali strukturne, elektronske, vibracione, magnetne i superprovodljive osobine razmatranih materijala. DFT je jedan od najvažnijih metoda kvantne mehanike za proučavanje elektronske strukture materijala. Njegova osnova leži u Hoenberg-Konovim teoremama, koje dokazuju da je osnovno stanje sistema jednoznačno određeno gustinom elektrona ($n(\mathbf{r})$). Time se problem višeelektronskog sistema svodi na jednostavniji problem koji se sada umjesto složene talasne funkcije opisuje uz pomoć gustine elektrona. Dodatno, Kon-Šamov formalizam uvodi „fiktivni“ sistem nezavisnih elektrona koji oponaša osobine realnog (interagujućeg) višeelektronskog sistema, omogućavajući praktične proračune uz upotrebu aproksimacija za izmjensko-korelacioni funkcional, poput aproksimacije lokalne gustine (LDA) i aproksimacije gradijentnog razvoja (GGA). Iako DFT daje odlične rezultate za širok spektar materijala, glavni problem i dalje ostaje precizno opisivanje izmjensko-korelacionih efekata. Proširenje DFT-a na spinski polarizovane sisteme (SDFT) uvodi dodatno i vektor magnetizacije ($\mathbf{m}(\mathbf{r})$) kao glavnu

promjenljivu pored $n(\mathbf{r})$, omogućavajući samim tim opis magnetnih materijala kroz efektivne spinski zavisne potencijale. Time se formalizam prilagođava kolinearnim, ali i nekolinearnim spinskim konfiguracijama, uz standardne aproksimacije za izmjensko-korelacioni potencijal poput aproksimacije lokalne gustine za spinske sisteme (LSDA) i GGA. Ovaj pristup je fundamentalno važan za razumijevanje magnetnih osobina i spinski zavisnih efekata, koji u svom formalizmu uključuje i spin-orbitne interakcije (SOC). Uz pomoću SDFT metodologije moguće je precizno izdvojiti vrijednosti izmjenskih interakcija analizom energetske razlika između različitih magnetnih konfiguracija. Dobijeni parametri se zatim fituju na klasični Hajzenbergov hamiltonijan, koji kvantitativno opisuje interakcije između lokalnih magnetnih momenata i time pruža uvid u mehanizme dugodometnog magnetnog uređenja sistema. Dodatno, u TB2J formalizmu se upotrebom Grinovih funkcija opisuju lokalne (male) rotacije spina kao perturbacije koje u konačnom, uz kombinaciju sa Vanijeovim transformacijama, daju orbitalni karakter izmjenske interakcije. Ovaj pristup omogućava dublje razumijevanje fundamentalnih magnetnih osobina materijala, čime SDFT postaje ključan alat u proučavanju i predviđanju magnetizma u složenim sistemima. Sa druge strane, perturbaciona teorija funkcionala gustine (DFPT) predstavlja formalno proširenje standardnog DFT-a koje omogućava efikasno računanje „odgovora“ sistema na male perturbacije, poput vibracija rešetke, tj. njegovih deformacija (malih oscilacija jona oko ravnotežnog položaja). Za razliku od standardnih pristupa koji zahtijevaju eksplicitno računanje stanja pobude, DFPT direktno izvodi linearne odgovore iz osnovnog stanja, što značajno smanjuje računsku operaciju. Ovaj metod je posebno koristan za određivanje fononskih spektara i elektron-fonon interakcija u materijalima, čime postavlja teorijski okvir za proučavanje širokog spektra kvantnih fenomena u čvrstim tijelima. Takođe, rezultati dobijeni ovim metodom se mogu dalje koristiti kao ulazni parametri za rješavanje anizotropnih Migdal-Eliašbergovih jednačina. Naime, Migdal-Eliašbergova teorija predstavlja ključni okvir za opisivanje interakcije između elektrona i fonona u superprovodnicima, naročito u okviru granica njihove jake interakcije. Ova teorija proširuje Bardin-Kuper-Šriferovu (BCS) teoriju superprovodljivosti, tako što pored efekta jakih elektron-fonon interakcija uzima u obzir i vrijeme koje je neophodno za njihovo odvijanje, a koje nije zapravo razmatrano u standardnim teorijskim okvirima. Dodatno, Migdal-Eliašbergova teorija omogućava precizno računanje superprovodljivih kritičnih temperatura (T_c), kao i drugih značajnih superprovodljivih osobina. Ovaj pristup je od posebne važnosti za razumijevanje mehanizama visokotemperaturne superprovodljivosti, kao i za modeliranje materijala sa kompleksnim elektronskim strukturama, u kojima klasične aproksimacije nijesu primjenljive. U kontekstu

primjene DFPT-a i Migdal-Eliašbergove teorije, Vanijeova transformacija igra ključnu ulogu u smanjivanju broja proračuna, posebno u složenim sistemima sa velikim brojem elektronskih stanja. Vanijeove funkcije omogućavaju transformaciju delokalizovanih elektronskih stanja u lokalizovane funkcije, čime se značajnije smanjuje broj potrebnih proračuna. Ova transformacija omogućava preciznije modeliranje lokalnih interakcija i lakšu implementaciju u numeričkim metodama, što je posebno korisno u proračunima za sisteme sa jakim korelacijama ili složenim elektronskim strukturama. Kada se koristi u kombinaciji sa DFPT-om, Vanijeova transformacija omogućava efikasno dobijanje fononskih spektara i elektron-fonon interakcija koje se zatim unose u Migdal-Eliašbergovu teoriju za predviđanje superprovodljivih osobina. Ovaj pristup značajno smanjuje računске troškove i omogućava detaljnije istraživanje kvantnih materijala sa složenim interakcijama.

Posebnu pažnju ćemo sada izdvojiti našim rezultatima, i to hronološkim redom. Prvo smo korišćenjem teorije funkcionala gustine za spinski polarizovane sisteme (SDFT) i drugih teorijskih modela istraživali da li β_{12} borofen može da posluži kao idealna platforma za stabilizaciju vještačkih 2D magneta sastavljenih od gvožđa. Strukturu smo dopirali jednim, pa sa više atoma gvožđa, a to je na kraju rezultiralo kreiranjem lanaca atoma gvožđa koji se efektivno mogu posmatrati kao 2D magnet. Ovakvo uređenje atoma se može pripisati jedinstvenoj periodičnoj kristalnoj rešetki borofena i visokoj reaktivnosti njegovih šupljina koji sprječavaju dalje grupisanje adsorbovanih atoma na njima, za razliku od grafena. Dodatno, ispitivali smo slučaj kada se atomi gvožđa nalaze između sloja borofena i supstrata srebra i dokazali da je energija veze za atome gvožđa u ovom slučaju značajno veća u odnosu na slučaj kada su atomi adsorbovani na borofenu. Međutim, o ovom položaju dolazi do veće delokalizacije Fe-3d elektrona što za posledicu ima da atomi gvožđa posjeduju manje magnetne momente. Međutim, energetska barijera od 1 eV da atom gvožđa prođe kroz šupljinu i da se nađe u „sendviču“ sugeriše da bi se u normalnim okolnostima ovi atomi ipak nalazili na sloju borofena. Dodavanjem više atoma formiraju se lanci dimera koji međusobno interaguju i uzimajući razliku u energijama za različite spinske konfiguracije mogli smo da izvučemo parametre izmjenske interakcije fitujući rezultate na Izingov model. U osnovnom magnetnom stanju sistem favorizuje jaku feromagnetnu interakciju unutar lanca i slabiju antiferomagnetnu interakciju između njih. Dobijeni rezultati su se dalje koristili kao input za Monte Karlo simulacije, koristeći anizotropni Hajzenbergov model za koji je neophodno bilo uključiti i spin-orbit interakcije kako bi smo dobili član za anizotropnu energiju. Za 2D feromagnetnu strukturu gvožđa formiranu iznad borofena dobili smo Kirijevu

temperaturu od 105 K, a u slučaju kada se ista struktura nalazi između supstrata i srebra, 30 K. Ovo sugerira da bi dalja optimizacija, kao što je zamjena gvožđa kobaltom, mogla da poveća Kirijevu temperaturu zbog njegove veće anizotropije. Međutim, podložnost materijala oksidaciji u velikoj mjeri ograničava njegovu praktičnu primjenu.

Da bi prevazišli problem sa oksidacijom, razmatrali smo dvosloj β_{12} borofena koji smo interkalirali različitim elementima iz grupe alkalnih, zemnoalkalnih i prelaznih metala. Pokazali smo da sa Mn dobijamo jedinu dinamički stabilnu strukturu i da je Mn jedini interkalant koji može da sačuva značajniju vrijednost magnetnog momenta (od $1 \mu_B$) u odnosu na ostale kandidate. Takođe, primijetili smo jaku hibridizaciju B- $2p$ i Mn- $3d$ stanja koja je rezultirala jakim naboranjem dvosloja borofena, kao i odsustvom procesa dimerizacije interkaliranih atoma. U želji da ispitamo mikroskopski izvor magnetizma u ovim sistemima koristili smo metod četiri spinska stanja (4SM) i TB2J metod. Uz pomoć 4SM metoda dobili smo feromagnetnu interakciju za prva tri najbliža susjeda kao i za šesti susjed, i antiferomagnetnu interakciju za četvrtog i petog najbližeg susjeda. Đalošinski-Morija interakcija nije prisutna u ovim sistemima usljed slabe SOC atoma bora kao i odsustvom narušenja inverzne simetrije. Jedina značajnija anizotropija dolazi od dva SIA člana, kao i prisutnom anizotropijom u simetričnom dijelu izmjenske interakcije. Međutim, upotrebom 4SM metoda bili smo uskraćeni za važniji uvid u mikroskopski izvor izmjenske interakcije u sistemu. Da bi prevazišli date prepreke koristili smo TB2J metod koji je otkrio dominantnu direktnu izmjensku interakciju između d_{yz} orbitala mangana u slučaju prvih najbližih susjeda, i superizmjensku ili super-superizmjensku interakciju posredovanu B- p_z orbitalama za preostalih pet najbližih susjeda. Znak izmjenske interakcije je isti ukoliko se uporede obje metode, sa malim izuzetkom u slučaju trećeg najbližeg susjeda. Dodatno, isključivanjem određenih „hopping“ parametara ustanovili smo i koji tačno tip superizmjenske interakcije, kao i u kolikoj mjeri, doprinosi ukupnoj izmjenskoj interakciji među najbližim susjedima. Na ovaj način smo uspjeli, da prvi put u polju borofena, opišemo mikroskopski izvor magnetizma.

Međutim, posebnu pažnju smo posvetili sistematičnom ispitivanju vibracionih i superprovodljivih osobina kako „čiste“ β_{12} faze, tako i hidrogenizovane. Primjenom DFPT metoda prvo smo dobili fononske disperzione relacije za sistem bez vodonika, a zatim sa vodonikom na „mostu“ (geometrijski položaj), na „vrhu“ jednog atoma bora, kao i kombinacijom ove dvije konfiguracije (dva atoma vodonika) – eksperimentalno potvrđene konfiguracije. U odnosu na prethodna teorijska istraživanja i dobijene rezultate, naša ispitivanja su pokazala da je čista

faza dinamički nestabilna i da se stabilnost iste postiže samo ukoliko se struktura istovremeno mehanički „isteže“ u oba pravca u ravni. Međutim, uprkos ostvarivanju dinamičke stabilnosti, superprovodljivost se narušava u ovakvim sistemima, najvećim dijelom zbog smanjenog doprinosa elektronske gustine vezujućih σ stanja atoma bora na Fermijevom nivou (E_F). S druge strane jedina hidrogenizovana stabilna konfiguracija je kada se atom vodonika nalazi na „mostu“ između dva atoma bora, sa superprovodljivom kritičnom temperaturom od 4 K. Iako se sistem dva atoma vodonika može stabilizovati dopiranjem elektronima, struktura ne ispoljava superprovodljive osobine i zbog toga nije bila interesantna za dalja ispitivanja. Rješavanjem anizotropnih Migdal-Eliášbergovih jednačina dobili smo jasan uvid u mikroskopski izvor superprovodljivih osobina, gdje pored σ stanja veliki doprinos daju i B- p_z stanja. Takođe, dobili smo da je ova struktura superprovodnik sa jednim procjepom i kritičnom temperaturom od 6 K. Pošto sistem ima izraženu strukturnu anizotropiju, primijenili smo različite kombinacije za vrijednosti (sabijanja)istezanja strukture. U jednom i/ili drugom pravcu smo koristili (sabijanje)istezanje od 1, 2, 3, 4, 5% što ukupno daje 121 kombinaciju. Dobili smo da je u jednom pravcu poželjno strukturu istežati u odnosu na drugi pravac, što se posebno odražava u vrijednostima konstante elektron-fonon sprege. Ona dostiže maksimum za istežanje samo u jednom pravcu, duž pravca „mosta“ gdje leži atom vodonika, sa kritičnom temperaturom od 17 K. Promjene u konstanti elektron-fonon sprege usljed primjene istežanja direktno su povezane sa promjenama u međuatomskim gustinama naelektrisanja. Pod „kompresivnim naponom“ (sabijanjem), smanjivanjem rastojanja između atoma dolazi do povećanja lokalne gustine naelektrisanja, dok ukupna gustina naelektrisanja unutar sistema ostaje konstantana. Nasuprot tome, pod istežanjem, rastojanja između atoma se uvećavaju, što rezultira smanjivanjem lokalne gustine naelektrisanja. Ove gustine naelektrisanja (oblaci) funkcionišu kao efikasne konstante opruge, gdje povećana elektronska gustina pod kompresijom odgovara čvršćim oprugama, a smanjena gustina pod uticajem istežanja slabijim oprugama. S obzirom na to da su fononske frekvencije ω kvalitativno povezane sa konstantama opruga preko relacije $\omega = \sqrt{k/m}$, ovo objašnjava zašto kompresivni napon dovodi do povećanja fononskih frekvencija, dok istežanje uzrokuje njihov pad, što može čak dovesti do „omekšavanja“ fonona. Kroz jednačinu za elektron-fonon spregu, $\lambda = 2 \int_0^\infty \alpha^2 F(\omega) \omega^{-1} d\omega$, postaje jasno zašto u ovom slučaju imamo poboljšane superprovodljive osobine materijala. Međutim, u našem sistemu situacija je još kompleksnija zbog izražene anizotropije strukture, koja se oslikava u različitim ponašanjima sistema kada se istežanje primijeni duž x ili y pravca. Naime, kada se napon istežanja primijeni duž y -pravca, poravnato sa B–H–B vezom, sve B–B i B–H veze

se istežu. S druge strane, kada se isti napon primijeni duž x -ose, iako se većina B–B i B–H veza produžava, B–B veza iznad kojih je atom vodnika pokazuje jedinstveno kompresovanje umjesto produžavanja, kako bi kompenzovala promjene u raspodjeli naelektrisanja. To rezultira različitim doprinosima ukupnoj elektronskoj gustini stanja na E_F u zavisnosti od toga u kom pravcu se primjenjuje napon. Iz navedene analize u slučaju istežanja samo duž y pravca od 5% dobija se najbolji superprovodljivi efekat, sa izraženom anizotropijom koja rezultira da prilikom rješavanja Migdal-Eliašbergovih jednačina dobijamo T_c od skoro 30 K. Doprinos je uglavnom od B- σ i B- p_z stanja. Takođe, ispitivali smo i efekat dopiranja šupljinama i elektronima, gdje smo dobili da dopiranje šupljinama dovodi do povećanja kritične temperature za razliku od dopiranja elektronima, koja uništava superprovodljive osobine sistema. Ovo je takođe povezano sa povećanim doprinosom B- σ i B- p_z stanja koje rezultira uvećanom vrijednošću elektron-fonon sprege i velikom kritičnom temperaturom. Međutim istovremeni efekat dopiranjem šupljinama kao i istežanja strukture ne rezultira u dodatno povećanje kritične temperature. Prema tome, naš rad ne samo što osporava prethodna istraživanja u ovom polju, već otvara i put za eksperimentalno ispitivanje superprovodljivosti u borofenskim sistema, posebno uzimajući u obzir činjenicu da je transfer borofena sa metalnih na nemetalne supstrate sada i eksperimentalno ostvariv.

Dodatno smo istraživali i interkalirane dvoslojne borofenske faze kao što su β_{12} , χ_3 , δ_4 i kagome faza, identifikujući sedamnaest potencijalnih superprovodljivih sistema korišćenjem alkalnih, zemnoalkalnih i prelaznih metala kao interkalanta. Poseban fokus je stavljen na povezanost između gustine elektronskih stanja na Fermijevom nivou ($\text{DOS}(E_F)$), karakteristika Fermijeve površine i rezultirajućih superprovodljivih kritičnih temperatura T_c . Interkalacija dvoslojnih borofenskih konfiguracija dovodi do značajnih promjena u elektronskoj strukturi, prvenstveno kroz hibridizaciju van-ravanskih (p_z) i ravanskih (σ) elektronskih stanja. Gustina stanja na Fermijevom nivou ($\text{DOS}(E_F)$) direktno utiče na jačinu elektron-fonon sprege, pri čemu se pokazalo da najveći doprinos dolazi od sistema kod kojih σ -stanja ostaju djelimično popunjena nakon interkalacije. U β_{12} fazi, interkalacija ne uspijeva da značajno poboljša elektron-fonon interakciju jer je većina σ -stanja potpuno popunjena, a elektronska gustina na Fermijevom nivou je niska, što rezultira veoma malim T_c vrednostima (~ 1 K). Kod χ_3 , δ_4 i kagome faze, hibridizacija p_z i σ elektronskih stanja omogućava povećanje $\text{DOS}(E_F)$ i jačanje elektron-fonon sprege, što neminovno daje i veće vrijednosti T_c . Najveći efekat postignut je u Ca-interkaliranom kagome borofenu, gdje izražena σ -stanja na Fermijevom nivou omogućavaju visok T_c od 27.1 K u izotropnoj aproksimaciji, dok anizotropni Migdal-Eliašbergovi

proračuni predviđaju porast T_c do čak 58 K. Interkalacija metala ne samo da mijenja elektronsku strukturu već i značajno utiče na dinamičku stabilnost i fononske modove. Fononski proračuni pokazuju da: (i) interkalacija povećava efektivne konstante opruge u kristalnoj rešetki, čime se sprečava neželjeno fononsko „omekšavanje“ i poboljšava stabilnost superprovodljivog stanja; (ii) u sistemima kao što su χ_3 i δ_4 faze, jačina elektron-fonon sprege posjeduje različito ponašanje u različitim djelovima Fermijeve površine, što dovodi do većih varijacija superprovodljivog procjepa, karakterističnog za superprovodnike sa više procjepa (u našem slučaju dva). Kako bi se preciznije opisala superprovodljivost u ovim sistemima, korišćeni su potpuno anizotropni Migdal-Eliašbergovi proračuni, koji omogućavaju detaljno praćenje raspodjele konstante elektron-fonon sprege na Fermijevoj površini. Rezultati pokazuju da Ca-interkalirani kagome borofen poseduje snažnu anizotropnu superprovodljivost, ali samo jedan procjep, sa velikom vrijednošću za T_c . Iako rezultati sugerišu visok potencijal ovih materijala za 2D superprovodljivost, dalja eksperimentalna istraživanja su neophodna kako bi se precizno odredili uticaji podloge, kao i anharmonijski efekti. Ovo istraživanje svakako postavlja osnovu za buduće studije interkaliranih borofenskih struktura, naglašavajući njihov potencijal kao perspektivnih 2D superprovodnika sa mogućim primjenama u kvantnim tehnologijama.

Prema tome, ova disertacija pruža sveobuhvatan uvid u magnetne i superprovodljive osobine borofenskih materijala, analizirajući jednoslojne i dvoslojne konfiguracije, kao i uicaj hidrogenacije i interkalacije, respektivno. Borofen se dakle može koristiti kao platforma za stabilizaciju 2D magnetskih nanostrukture. Pokazano je da Fe atomi na β_{12} borofenu/Ag(111) formiraju zanimljive stukture lanaca, sa feromagnetnim uređenjem unutar lanaca i slabijom antiferomagnetnom interakcijom između lanaca. Međutim, dobijene Kirijeve temperature su ispod sobne, što sugeriše potrebu za daljom optimizacijom, poput zamjene Fe atomima Co. Problem oksidacije ove strukture se može riješiti razmatranjem Mn-interkaliranog dvosloja borofena. Magnetna svojstva ove strukture analizirana su pomoću TB2J metoda i 4SM, pri čemu je dominantan mehanizam superizmjena posredovana p_z orbitalama bora. Ovi rezultati potvrđuju da elektronska struktura igra ključnu ulogu u određivanju magnetnog uređenja borofena. Dalje, detaljni DFPT i Migdal-Eliašbergovi proračuni pokazali su da „čisti“ β_{12} borofen nije intrinzični superprovodnik, što objašnjava nedostatak eksperimentalnih dokaza za superprovodljivost u borofenu. Ključni razlog je smanjen doprinos B- σ stanja gustini elektronskih stanja na Fermijevoj nivou pri istezanju strukture (što se može razmatrati kao efekat supstrata). Međutim, hidrogenizovani borofen (borofan) pokazuje povećanu stabilnost i postizanje T_c do 30 K, zah-

valjujući kombinovanom doprinosu $B-\sigma$ i $B-p_z$ stanja. Dodatno, identifikovano je sedamnaest potencijalnih superprovodljivih sistema u β_{12} , χ_3 , δ_4 i kagome fazama sa interkalantima iz grupe alkalnih, zemnoalkalnih i prelaznih metalima. Posebno se ističe Ca-interkalirani kagome borofen, koji dostiže T_c od 58 K, vođen jakom elektron-fonon spregom i povoljnom anizotropnom elektronskom strukturom. Ovi rezultati otvaraju nove pravce istraživanja borofena kao stabilne platforme za 2D magnetizam i superprovodljivost.

Abbreviations

1D	one-dimensional
2D	two-dimensional
3D	three-dimensional
4SM	four-state method
A	acoustic
AES	Auger electron spectroscopy
AFM	atomic force microscopy
ALD	atomic layer deposition
APW	augmented plane wave
ARPES	angle-resolved photoemission spectroscopy
ASR	acoustic sum rule
B-2D	borophene
BCS	Bardeen-Cooper-Schrieffer
BdG	Bogoliubov–de Gennes
BKT	Berezinskii-Kosterlitz-Thouless
BL	bilayer
BNR	borophene nanoribbon
BO	Born-Oppenheimer
BvK	Born-von Kármán
BZ	Brillouin zone
CDW	charge density waves
CN	coordination number
CVD	chemical vapor deposition
DBP	tetraphenyldibenzoperiflanthene
DFPT	density functional perturbation theory
DFT	density functional theory
DMF	dimethylformamide
DMI	Dzyaloshinskii-Moriya interaction
DMSO	dimethyl sulfoxide
DOS	density of states
<i>e-ph</i>	electron-phonon

EBL	electron beam lithography
EELS	electron energy loss spectroscopy
ELF	electron localization function
EMT	electron microscopy techniques
EPC	electron-phonon coupling
EPW	Electron-Phonon Wannier
FFT	fast Fourier transform
FET	field effect transistor
FHIB	focused helium ion beam
GGA	generalized gradient approximation
GKA	Goodenough–Kanamori–Anderson
<i>h</i>-BN	hexagonal boron nitride
HEED	high-energy electron diffraction
HEEM	high-energy electron microscopy
HH	hexagonal hollow(void)
HK	Hohenberg-Kohn
I	infrared
IBZ	irreducible Brillouin zone
ICD	induced charge density
IFC	interatomic force constant
IPA	isopropyl alcohol
JT	Jahn-Teller
KS	Kohn-Sham
L	ligand
<i>L</i>	longitudinal
LAPW	linearized augmented plane wave
LDA	local density approximation
LDOS	local density of states
LEED	low-energy electron diffraction
LEEM	low-energy electron microscopy
LPE	liquid-phase exfoliation
LSDA	local spin density approximation
MAD	McMillan-Allen-Dynes
MAE	magnetic anisotropy energy
MBE	molecular beam epitaxy
MC	Monte Carlo
ME	Migdal-Eliashberg
MECN	methylcyanide
MEE	mechanical exfoliation
MLWF	maximally localized Wannier function
MP	Methfessel-Paxton
MSC	Marsiglio–Schossmann–Carbotte
NCPP	norm-conserving pseudopotential
NIL	nanoimprint lithography
NIR	near-infrared regime
NN	nearest neighbor

NMP	N-methyl-2-pyrrolidone
NSL	nanosphere lithography
<i>O</i>	optical
O(P)L	optical(photo) lithography
PAW	projector-augmented wave
PBE	Perdew-Burke-Ernzerhof
PDMS	polydimethylsiloxane
PECVD	plasma enhanced chemical vapor deposition
PMMA	polymethyl methacrylate
PVD	physical vapor deposition
PW	plane waves
QE	Quantum ESPRESSO
QMC	Quantum Monte Carlo
R	Raman
RIE	reactive ion etching
RKKY	Ruderman-Kittel-Kasuya-Yosida
S	surface
SAED	selected area electron diffraction
SCDFT	density functional theory for superconductors
SCF	self-consistent field
SDFT	spin-dependent density functional theory
SEM	scanning electron microscopy
SIA	single ion anisotropy
SOC	spin-orbit coupling
SPL	scanning probe lithography
STEM	scanning transmission electron microscopy
<i>T</i>	transverse
TERS	tip-enhanced Raman spectroscopy
TEM	transmission electron microscopy
TM	transition metal
TOABr	tetra- <i>n</i> -octylammoniumbromide
UV	ultraviolet
UFM	ultrasonic force microscopy
UHV	ultra-high vacuum
USPP	ultrasoft pseudopotential
VASP	Vienna Ab initio Simulation Package
vdW	van der Waals
XPS	X-ray photoelectron spectroscopy
XRD	X-ray diffraction
WF	Wannier function

Table of Contents

Acknowledgements

Information about the doctoral thesis	i
Abstract	vi
Abstract – Dutch versie	ix
Prošireni rezime	xii
Abbreviations	xxii

1 INTRODUCTION: FROM GRAPHENE TO BOROPHENE – UNLOCKING THE WORLD OF ELEMENTAL TWO-DIMENSIONAL (2D) MATERIALS	1
1.1 Introduction to 2D materials	1
1.1.1 History of 2D materials and future perspective	2
1.1.2 Design and fabrication of 2D materials	4
1.1.2.1 <i>Top-down</i> fabrication techniques	4
1.1.2.2 <i>Bottom-up</i> fabrication techniques	6
1.1.3 Materials characterization techniques	8
1.1.4 Transfer techniques	11
1.1.5 Film patterning	13
1.1.6 Tuning materials properties	16
1.2 2D boron crystal structure (<i>borophene</i>)	19

1.2.1	Tracing the evolution of boron: from early discoveries to complex bulk and 2D phases (borophenes)	19
1.2.2	Borophene synthesis techniques and structural characterization combined with the density functional theory (DFT) approach	26
1.2.2.1	<i>Bottom-up</i> approaches	26
1.2.2.2	Transfer of borophene and growth techniques on non-metallic substrates	38
1.2.2.3	<i>Top-down</i> approaches	40
1.2.3	Tunable properties and potential application of borophene	44
1.2.3.1	Brief overview	44
1.2.3.2	Magnetic properties of borophene	48
1.2.3.3	Superconducting properties of borophene	50
2	THEORETICAL MODELS AND METHODOLOGY	53
2.1	Density functional theory (DFT)	53
2.1.1	Simplifying the problem of many-body system	53
2.1.2	The Hohenberg-Kohn theorems	55
2.1.3	The Kohn-Sham equations	57
2.1.4	Approximations in electronic structure calculations	61
2.1.4.1	Plane wave basis set	61
2.1.4.2	Pseudopotentials	64
2.1.4.3	Projector-augmented wave method	65
2.2	Spin-dependent density functional theory (SDFT)	66
2.2.1	Basic concept	66
2.2.2	Relativistic DFT approach – the role of spin-orbit coupling (SOC)	68
2.2.3	The magnetic ground state	69
2.3	Microscopic theory of magnetism	71
2.3.1	Origin of magnetism	72
2.3.2	Mapping SDFT results to Heisenberg’s spin hamiltonian	78
2.3.2.1	Four-state method (4SM)	80
2.3.2.2	TB2J - Green’s function method	81
2.3.3	Monte Carlo simulations	83
2.4	Density functional perturbation theory (DFPT)	84

2.4.1	Basic concept of the linear response	84
2.4.2	Phonon calculations	86
2.4.3	Electron-phonon coupling	90
2.5	Microscopic theory of superconductivity	91
2.5.1	The 2D limit and the comparison of different <i>ab initio</i> methods (ME, MAD, SCDFE)	94
2.5.2	The Migdal-Eliashberg (ME) theory	95
2.5.2.1	General formalism	95
2.5.2.2	Key approximations and methods in ME theory	98
2.5.2.3	Electron-phonon Wannier (EPW) interpolation	101
3	BOROPHENE AS A PLATFORM FOR 2D MAGNETISM	102
3.1	Fe-based 2D magnets on β_{12} borophene/Ag(111)	102
3.1.1	Structural properties of β_{12} borophene: freestanding and supported by Ag(111) substrate	103
3.1.2	Different Fe nanostructures on β_{12} borophene supported by Ag(111) substrate	104
3.1.3	From Fe chain formation to Fe-based 2D magnetic structures on B-2D/Ag(111)	107
3.1.3.1	Isolated Fe chain	108
3.1.3.2	Closely-packed Fe chains	110
3.1.4	Monte Carlo simulations	113
3.1.5	Conclusions	114
3.2	Microscopic origin of magnetism in Mn-intercalated bilayer β_{12} borophene	116
3.2.1	Screening transition metal intercalants for magnetism and dynamical stability	116
3.2.2	Magnetic properties of Mn-intercalated bilayer β_{12} borophene	120
3.2.2.1	Extraction of magnetic parameters via the 4SM	121
3.2.2.2	Exchange interaction analysis using TB2J	123
3.2.3	Conclusions	127
4	SUPERCONDUCTIVITY IN BARE AND FUNCTIONALIZED BOROPHENES	128
4.1	Superconducting properties of bare and hydrogenated β_{12} borophene	129

4.1.1	Structural, electronic and vibrational properties of bare and hydrogenated β_{12} borophene	130
4.1.2	Exploration of hydrogenated β_{12} borophene configurations: the top and combo sites	133
4.1.3	Vibrational and superconducting properties of bare and hydrogenated β_{12} borophene: the bridge site	136
4.1.3.1	Impact of strain on vibrational and superconducting properties	138
4.1.3.2	Tuning superconducting properties through uniform and nonuniform (FET) electron or hole doping	144
4.1.4	Conclusions	147
4.2	Superconducting properties of bare and intercalated bilayer β_{12} , χ_3 , δ_4 and kagome borophene phases	148
4.2.1	Insights into crystal structures and their stability	148
4.2.2	Electronic, vibrational, and superconducting properties within the isotropic ME framework	156
4.2.2.1	β_{12} phase of bilayer borophene ($\eta = 1/6$)	156
4.2.2.2	χ_3 phase of bilayer borophene ($\eta = 1/5$)	159
4.2.2.3	δ_4 and kagome phases of bilayer borophene ($\eta = 1/4$)	162
4.2.3	Anisotropic ME theory applied to promising candidates	169
4.2.4	Conclusions	170
5	CONCLUSIONS	173
	APPENDIX	175
A1:	Wannier transformations and WANNIER90 code	175
A2:	Technical details for section 3.1	178
A3:	Technical details for section 3.2	179
A4:	Technical details and additional results for section 4.1	180
A5:	Technical details and additional results for section 4.2	193
	BIBLIOGRAPHY	194
	Curriculum Vitae	a
	List of publications	d

Izjava o autorstvu	e
Izjava o istovjetnosti štampane i elektronske verzije doktorskog rada	f
Izjava o korišćenju	g

INTRODUCTION: FROM GRAPHENE TO BOROPHENE – UNLOCKING THE WORLD OF ELEMENTAL TWO-DIMENSIONAL (2D) MATERIALS

*“When one dares to try, rewards are not guaranteed but at least it is an adventure.” –
Andre K. Geim*

1.1 Introduction to 2D materials

The 2004 discovery of graphene [1] marked the beginning of a transformative era in materials science, leading to the emergence of “two-dimensional (2D) materials”.¹ Distinguished by their minimal thickness – often just a few atoms or a single atom – and characterized by stronger in-plane compared to out-of-plane bonds between atoms, these materials exhibit extraordinary physical and chemical properties in contrast to their three-dimensional (3D) counterparts. Over the last twenty years, the field of 2D materials has experienced significant breakthroughs, encompassing the development of novel synthesis methods, exploration of unique intrinsic properties, identification of innovative applications, and progress in commercialization efforts. Ongoing intensive research on these materials aims to synthesize and develop more effective devices with superior characteristics across various sectors of application. Due to its exceptional physical and chemical properties, many scientists believe that the 2D structure of boron – borophene – is exactly that new “*wonder*” material that fulfills these criteria. Hence, in this chapter, we will lead you through the historical journey of 2D material discovery, their fabrication

¹A material is considered zero-dimensional (0D) when all its dimensions are nano-sized, commonly referred to as a “nanoparticle”. If two dimensions are nano-sized while the third is significantly larger, it transforms into a one-dimensional (1D) material, known as a “nanotube/nanowire”. When only one dimension is nano-sized, it takes on a 2D structure resembling a thin sheet, similar to paper. If none of its dimensions meet the nano-sized criteria, it falls into the category of three-dimensional (3D) or “bulk” material.

and integration into devices, and exploration of their novel intrinsic properties, highlighting the latest advancements and persistent challenges faced by scientists in the field of 2D boron structures. We uncovered methods to enhance certain physical properties of various 2D boron structures, opening up possibilities for their practical applications. With that said, let us begin this “scientific journey”!

1.1.1 History of 2D materials and future perspective

“This form of carbon should be characterized by a name marking it as a distinct element. I propose to term it graphon.” – B. C. Brodie

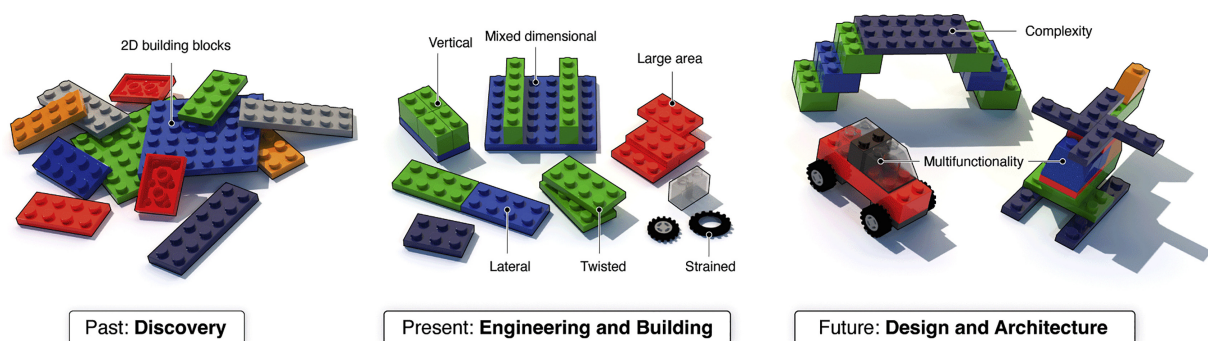


Figure 1.1: The brief history of 2D atomic building blocks and their heterostructures [2].

The history of the first discovered 2D material – graphene – dates back to the year 1859 and it is directly linked to the chemistry of graphite.² In his experiments, British chemist Benjamin C. Brodie treated graphite with acids, which resulted in the creation of a new carbon form that he termed “carbonic acid” or “graphon” [3], which recent research has revealed to be a suspension of tiny crystals of graphene oxide [4]. Following extensive research on the “laminated” structure of graphite oxide, Hanns-Peter Boehm and colleagues made a breakthrough in 1962 by identifying the thinnest fragments of reduced graphite oxide as monolayers [5]. They additionally coined the term *graphene*, formed by blending *graphite* with the suffix that denotes polycyclic aromatic hydrocarbons [6]. Overall, the previous mentioned research predominantly used transmission electron microscopy (TEM) for characterization and was later followed by years of experimental efforts of epitaxial growth of ultra-thin graphitic films on metallic substrates [7, 8, 9, 10]. Another direction of research was established with the unveiling of fullerenes in 1985 which shed light on the existence of numerous other carbon allotropes [11]. The first reports on carbon nanotubes came in 1991 [12], sparking a wave of research that pushed scientists to

²Graphite is a 3D form of carbon, consisting of stacked layers of graphene held together by the van der Waals (vdW) forces.

create thin nanoribbons and extract flat graphite materials. Furthermore, attempts to produce thin graphite films through mechanical exfoliation (MEE) led to the issuance of various patents, yielding multilayer samples as thin as a few nanometers [13]. Finally, in 2004, Andre Geim and Konstantin Novoselov achieved the proper isolation using the Scotch tape method and characterization of graphene, transferring nearly charge-neutral layers onto SiO₂ substrates [1]. Researchers thereafter have developed various methods for preparation of graphene, proving that mono- and few-layer configurations could be synthesized, possessing remarkable physical properties. This breakthrough also opened the way towards the exploration and fabrication of various non-carbon-based 2D materials, including graphene-family materials (e.g., *h*-BN [14]), transition metal dichalcogenides (TMDs) [15, 16], MXenes [17], and metal oxides [18]. However, these discoveries also raised another question:

“Are there elemental 2D materials – that consist of only one type of atom – similar to graphene?”

In 2012, a new 2D form of silicon, known as silicene, was identified on a silver surface under ultra-high vacuum (UHV) conditions, using molecular beam epitaxy (MBE) for its synthesis [19]. This advancement sparked an intensive search for similar 2D materials, yielding positive results. We can now talk about a family of elemental 2D materials, which includes (by the year of experimental production): germanene (2014) [20], phosphorene (2014) [21], stanene (2015) [22], borophene (2015) [23], antimonene (2016) [24], bismuthene (2017) [25], gallenene (2018) [26], plumbene (2019) [27], iodine (2020) [28], arsenene (2020) [29], selenene (2022) [30], tellurene (2023) [31], and beryllene (2023) [32]. Unlike graphene, these materials do not occur naturally and lack a 3D parent crystal (they are “metastable”), ruling out MEE as a production method. Instead, chemical fabrication techniques such as MBE, liquid-phase exfoliation (LPE), epitaxial growth on substrates, or solution-based methods are required. These approaches often demand specific conditions or metallic substrates,³ complicating large-scale production and practical use in ambient environments, which can adversely affect their unique structural and electronic properties. While experimental viable mechanisms – like stacking (and twisting) of different 2D materials to form lateral and vertical heterostructures, their functionalization, or applied controlled strain (see Figure 1.1) – can manipulate these properties, the primary challenge still remains achieving their large-scale and high-quality production.

³They are unsuitable for the production of electronic devices due to their strong chemical interactions with the sample (like charge transfer, surface roughness, contamination, or electronic screening).

1.1.2 Design and fabrication of 2D materials

The production of 2D materials involves a diverse array of fabrication techniques, each with its distinct advantages and limitations. These techniques can broadly be categorized into two main approaches: top-down and bottom-up methods (see Figure 1.2). Top-down techniques involve extraction of 2D materials from a bulk source material. On the other hand, bottom-up methods, which start with the atomic ingredients and ways how to assemble them together, entail the growth of the desired 2D material to specification. Understanding the intricacies of these approaches is crucial for unlocking the full potential of 2D materials in various applications. This section will provide an overview of main top-down and bottom-up fabrication techniques, highlighting their respective merits and challenges.

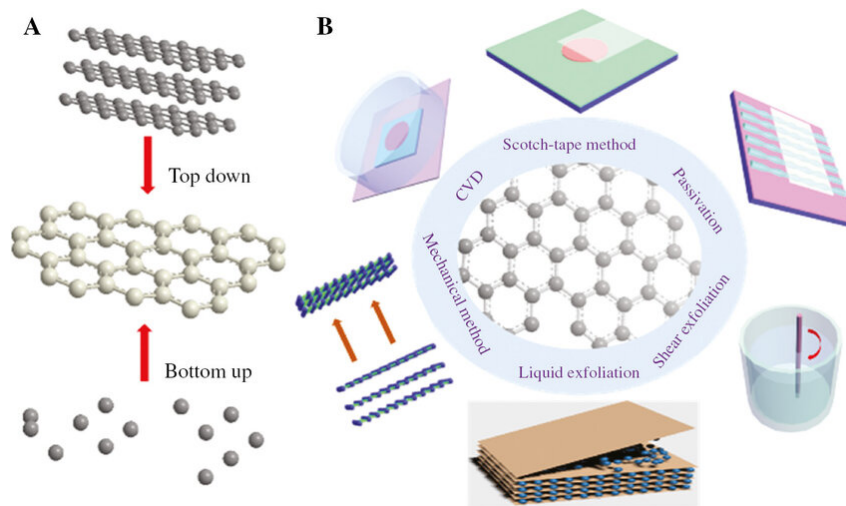


Figure 1.2: The synthesis of 2D materials typically approached through two primary methods: top-down and bottom-up methods [33].

1.1.2.1 Top-down fabrication techniques

Mechanical exfoliation (MEE) – a method used to create thin layers or flakes from bulk materials, typically at the micro- or nano-scale [34]. It is highly effective for producing graphene and other van der Waals (vdW) materials by applying mechanical forces to peel off individual layers from a 3D crystal. MEE is valued for its simplicity and cost-effectiveness, requiring no sophisticated equipment or complex procedures. It can generate high-quality, defect-free nanosheets or thin films, crucial for research where material's purity is paramount. However, MEE lacks control over the size, thickness, and shape of the flakes and may encounter issues like low yield and contamination, limiting its suitability for large-scale fabrication. A widely used MEE method is the “Scotch tape method”, where adhesive tape is employed to peel layers

from a bulk crystal [35]. This adhesive tape, which holds the separated layers, is subsequently pressed onto a substrate (e.g., a silicon wafer) and then removed, leaving behind thin flakes. However, the irregular thickness and small size of the flakes produced by this process limit its use to laboratory settings rather than large-scale production. Efforts to increase the exfoliation yield and the lateral dimensions of the 2D flakes include the use of a polymeric intermediate substrate, employing gold-assisted MEE techniques [36, 37], or utilizing a more general MEE method based on gold tape [38].

Solution processing – a prominent technique in this category is the **liquid phase exfoliation (LPE)** [39], which involves the process of dispersing bulk layered materials into a suitable solvent to weaken the vdW forces holding the layers together. This process allows single- or few-layer flakes to separate and disperse in the liquid. The choice of solvent is crucial, as it significantly impacts the exfoliation efficiency and the stability of the dispersed nanosheets. Common solvents include water, organic solvents, and surfactant solutions. Ultrasonic energy, often referred to as ultrasonic exfoliation, is typically employed to facilitate the exfoliation process and/or shear mixing [40]. Sonication provides the mechanical energy needed to break down bulk materials into smaller flakes by causing tensile stress to separate the layers. To prevent re-aggregation and enhance dispersion quality, surfactants or dispersants are frequently introduced to stabilize the exfoliated nanosheets in the liquid medium. LPE offers several advantages, including scalability, mass production, application to a wide range of bulk materials, and compatibility with various uses. However, the low monolayer yield, sub-100 nm flake size, poor layer control, or high defect and solvent residue density render these flakes generally unsuitable for application.

While traditional exfoliation strategies are effective for delaminating vdW solids into ultrathin nanostructures, they struggle with layered ionic solids due to the strong bonds within the layers. To address this, the **ion-intercalation and exfoliation** method [41] is employed, where ions (e.g., alkali metals) and solvents are inserted between the layers of the bulk material, causing expansion and weakening of the bonds, leading to exfoliation of individual layers into 2D nanosheets. This method is advantageous for its high yield of monolayers and suitability for mass production. However, the main disadvantages include the production of materials with relatively small lateral sizes, potential defects and phase transformations, with high sensitivity to water and oxygen. Related approaches, such as modified Hummer's methods for graphene oxide [42] and chemical-etching-assisted LPE for MXenes [43], have further expanded the "toolkit".

1.1.2.2 *Bottom-up* fabrication techniques

Chemical vapor deposition (CVD) – widely employed technique for synthesis of 2D materials, offering precise control over their quality, lateral dimensions, thickness, and overall performance [44]. In this process, precursor gases containing the atomic components of the desired film are vaporized and introduced into a heated tube furnace (chamber). These gases react with a substrate to form a thin layer of the target 2D material. The process parameters, including gas pressures, compositions, temperature, mass flux, and reaction times, must be carefully controlled as they significantly impact the film's thickness, quality, and composition. After deposition, the material may undergo treatments such as annealing, cooling, or etching to enhance its properties or achieve specific characteristics. Although more complex and more expensive than many *top-down* techniques, CVD is highly scalable and produces films of quality comparable to MEE layers. An advanced version of CVD is the **atomic layer deposition (ALD)** [45]. While CVD introduces a mixture of vapor-phase reactants into the deposition chamber, ALD operates differently. It starts with the introduction of one reactant, which forms a monolayer on the substrate before being evacuated. Subsequently, a second reactant is introduced, reacting precisely with the monolayer of the first reactant adsorbed on the surface. This sequential process forms a solid film, one by one atomic layer at a time, and it can be repeated iteratively to achieve the desired film thickness. ALD's key advantage lies in preventing reactants from reacting in the vapor phase, and ensuring precise control over film composition.

Solution-based chemical synthesis – a diverse array of methods has been established for the synthesis of 2D materials using wet chemical techniques [46]. These encompass high-temperature chemical reactions in solutions, interface-mediated growth (where reactions occur at liquid surfaces), and the fusion of nanoparticles into larger nanosheets, among others. Typically, these methods yield flakes with lateral dimensions less than 100 nm. Similar to LPE, they also contend with residual solvent issues. Nonetheless, the scalability, cost-effectiveness, and versatility of these chemical synthesis methods make them ideal for large-scale production in certain applications. Therefore, let us briefly examine a few of these methods. The *hydro(solvo)thermal* method involves a process of conducting the reaction in a sealed aqueous solution above ambient temperature and pressure [47]. The advantages of *hydro(solvo)thermal* synthesis over other crystal growth methods include lower temperatures and the convenience of adjusting reaction conditions. Another significant method is the *template synthesis*, which involves a mechanism of controlling the morphology of a template for growing crystals confined to its specific dimensions.

Following crystal growth, the template is removed through high-temperature processes [48]. Furthermore, the *sol-gel* technique involves a solution (sol) that gradually undergoes a transition to form a “gel” consisting of a liquid as well as a solid phase [49]. This evolution occurs through the polycondensation or polymerization of metal-containing precursors, often facilitated by carboxylic acids. These acids act as complexing agents, binding metal ions and promoting the formation of a polymeric network within the solution. Subsequent thermal treatment (calcination or annealing), drives the removal of solvent and organic components, leading to the formation of crystal phases and the development of the desired material structure. *Sol-gel* synthesis offers extensive flexibility, enabling precise control over properties through tailored heat treatment conditions and reactant ratios.

Physical vapor deposition (PVD) – employed to deposit thin films of materials onto substrates through physical processes. In this process, materials are vaporized from solid or liquid sources within a vacuum or other plasma-like environments. This vapor is then transported to the substrate, where it condenses, forming thin films with thicknesses ranging from a few nanometers to several micrometers. The most common PVD processes are *sputtering*,⁴ *evaporation*,⁵ *pulsed laser deposition (PLD)*⁶ and so on [50]. In a broader context, one noteworthy PVD technique is the **molecular beam epitaxy (MBE)**. MBE is an advanced method for growing crystal layers with exceptional control and precision. It operates by directing heated atomic or molecular beams towards a heated substrate within an UHV chamber, where they condense and form epitaxial layers [51]. MBE offers several advantages, like atomic layer precision, high purity, and capability of fabricating sophisticated multilayer structures, but is also known to be costly and time-consuming. Additionally, *vdW epitaxial growth on substrates* represents another common variant of the MBE technique. Unlike conventional MBE, where the substrate surface functions as a catalyst, in vdW epitaxy, the substrate frequently serves as a seed crystal. This method is utilized to create atomically thin, high aspect ratio 2D materials [52]. Since these materials are fabricated in vacuum environments, they must also operate under ambient conditions for practical commercial applications. To mitigate this issue, passivation strategies are employed by applying a protective layer or coating to the material’s surface, thereby preventing chemical reactions, oxidation, and degradation [53].

⁴The ion source bombards the bulk material, releasing it into the vacuum environment where it subsequently coalesces onto the substrate surface to form a thin film.

⁵Technique in which the evaporated bulk material condenses onto the substrate in high-vacuum environment.

⁶A high-power pulsed laser beam vaporizes material inside a vacuum chamber allowing to be deposited onto a substrate surface to form thin film.

1.1.3 Materials characterization techniques

Characterization of materials is essential for advancing fabrication processes. Widely used techniques such as transmission electron microscopy (TEM), atomic force microscopy (AFM), Raman spectroscopy, or scanning tunneling microscopy (STM), are employed to determine key properties of 2D crystals such as layer number, defects, crystal orientation, and interfaces. In situ characterization, achieved by controlling temperature, electric fields, or both during film synthesis, allows the study of dynamic growth behaviors. While these high-end methods are effective for small samples, there is a need for faster, in-line monitoring techniques for industrial-scale applications.

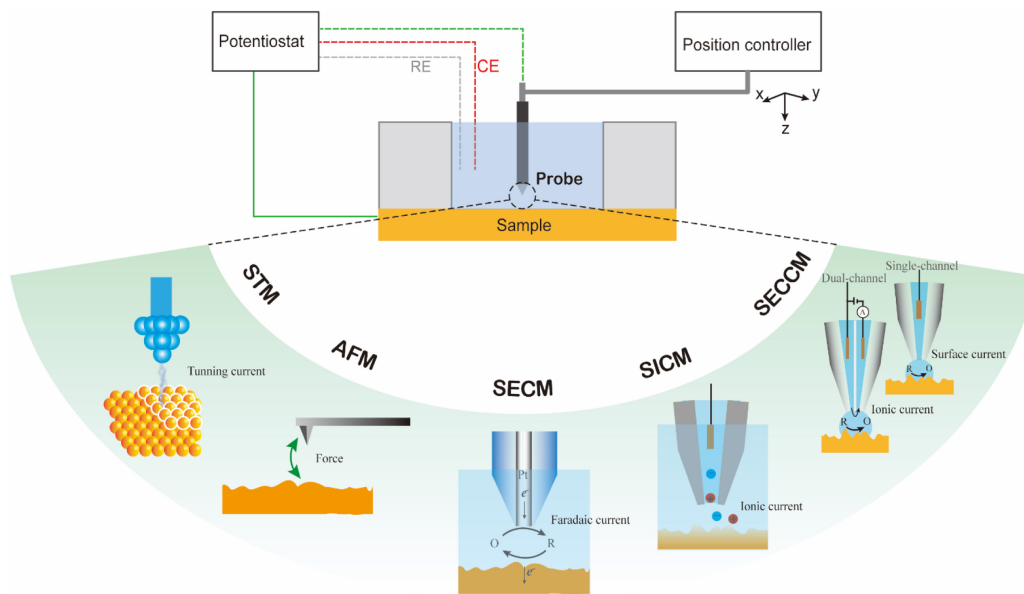


Figure 1.3: Overview of different scanning probe microscopy techniques – part of characterization techniques [54].

Scanning probe microscopies (SPM) are renowned characterization techniques which scan a probe across a surface by measuring the interactions between them, as depicted in Figure 1.3. Some of the most common SPM techniques are: **scanning tunneling microscopy (STM)**, **atomic force microscopy (AFM)**, and **ultrasonic force microscopy (UFM)**. STM and AFM are the two most commonly employed SPM techniques, offering structural insights with atomic-level resolution. **STM** utilizes a sharp metallic tip, as the probe, to scan over the surface of a conducting sample without physical contact, measuring the *tunneling current*. As this tip approaches the sample, applying a voltage causes electrons to tunnel between the tip and the surface barrier, resulting in an exponential increase in tunneling current as the distance decreases. The STM maintains a constant current by adjusting the tip's height and voltage, which maps the surface's topography, and by holding the tip in a constant position above the

surface while varying the voltage between the tip and the sample⁷ one gets insights into the sample's local density of states (LDOS).⁸ STM offers lateral precision of 0.1 nm and vertical precision of 0.01 nm, enabling detailed imaging [55, 56]. One limitation of STM is that it only works with conducting samples due to its reliance on tunneling current, whereas **AFM** can also image insulating materials. In AFM, a sharp nanometer-scale tip attached to a cantilever, as a probe, is used for scanning the sample's surface. As the tip approaches, tip-surface interaction – electrostatic force – causes the bending of cantilever which is monitored via photoelectric sensor, while an “control mechanism” adjusts the sample position to maintain a constant tip height. This allows precise mapping of surface topography, and has been widely used to measure the thickness of 2D layers [56]. Moreover, **UFM** is another powerful technique for measuring material stiffness at the nanometer scale, such as the mechanical coupling between a sample and its substrate. UFM works by vibrating the sample at high-frequency regime which is higher than the AFM cantilever's “resonant” regime [57]. This specific stiffness modifies the sample's restoring force, allowing UFM to detect subsurface features like cavities and interfaces. UFM can be used alongside AFM, converting ultrasonic vibrations into detailed images (different color contrast) of stiffness variations. This method is particularly effective for studying 2D materials by revealing subsurface defects and differences in bonding strength of freestanding sample and onto different substrates. For more details regarding other methods, we suggest the Ref. [54].

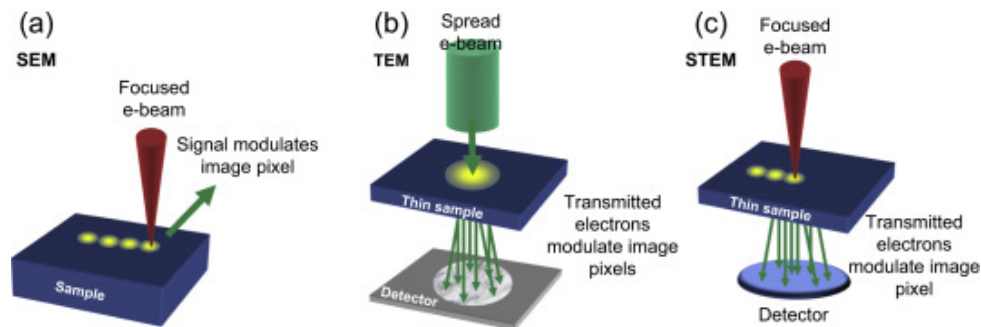


Figure 1.4: Schematic illustration of (a) SEM, (b) TEM, and (c) STEM imaging techniques [58].

Electron microscopy techniques (EMT) commonly include **scanning electron microscopy (SEM)** and **transmission electron microscopy (TEM)**, as shown in Figure 1.4(a-b). In general, light microscopes are constrained by diffraction limits, which restrict their resolution to approximately $1 \mu\text{m}$. In contrast, electron microscopes,⁹ which use electrons and therefore much

⁷Thereby recording the current changes.

⁸Scanning tunneling spectroscopy (STS), used with STM, measures the local electronic density of states (LDOS) of a sample. By applying a bias voltage between the STM tip and the sample, STS reveals detailed information about the material's electronic structure, including variations in electronic states and energy gaps at the atomic scale.

⁹It operates in a vacuum to prevent electron scattering by air molecules en route from source to sample. SEM

shorter de Broglie wavelengths, offer higher resolution. Both SEM and TEM use a focused beam of electrons, generated thermoionically in an ion gun cathode and raster scanned across the sample surface. SEM is designed to examine material surfaces, with secondary electrons emitted from the sample and collected to form an image, typically achieving a resolution of <50 nm. TEM, on the other hand, transmits electrons through a thin sample and uses their deflection to produce high-resolution images, often surpassing SEM due to its higher voltage (200–300 kV) and shorter electron wavelengths, although it requires samples to be very thin (<200 nm) [58, 59]. These techniques offer detailed insights into the crystal structure, elemental composition, inter-layer stacking arrangements, layer dimensions, and by combining it with *selected area electron diffraction (SAED)*,¹⁰ monolayer graphene can be distinguished from its multi-layer configurations. Additionally, *dark-field microscopy*¹¹ has recently been developed to identify the number of layers and stacking order in layered materials [60]. Modern advancements include hybrid SEM/TEM systems, where SEM can be equipped to collect transmitted electrons in *scanning transmission electron microscopy (STEM)* mode (see Figure 1.4(c)) at higher electron energies, enhancing imaging capabilities. STEM is often combined with *electron energy loss spectroscopy (EELS)* which enables high-resolution imaging of individual atoms in thin materials by using a electron beam that scatters upon striking specific atoms. STEM can be performed at low accelerating voltages (<60 keV) to minimize beam damage [58, 59]. Furthermore, **low-energy electron microscopy (LEEM)**¹² enables the study of material's structure, morphology, and dynamics with nanometer-scale resolution. In LEEM, a low-energy electron beam (0-100 eV) is directed onto the sample surface, and the reflected electrons form an image. It is used for real-time observation of surface phenomena such as phase transitions, thin film growth, and surface reconstructions.

Other characterization techniques, which are not previously mentioned, mainly include *diffraction or spectroscopy techniques*. For example, upon irradiation of a sample, a small portion of the incoming light undergoes an inelastic scattering, resulting in a wavelength shift; **Raman spectroscopy** exploits this effect by using monochromatic light to measure the energy difference between the scattered and incident light, revealing the material's vibrational mode

typically uses a low vacuum (0.1 to 10^{-4} Pa), while TEM requires a higher vacuum (10^{-4} to 10^{-7} Pa) [58].

¹⁰By directing a high-energy electron beam through a chosen area, typically a few nm to μm in diameter, SAED produces a diffraction pattern that reveals details about the crystal structure, orientation, defects, and phase.

¹¹Dark-field microscopy is a technique that enhances visibility of fine structures by capturing only the scattered light from the sample, effectively making bright features stand out against a dark background.

¹²Unlike low-energy techniques, high-energy electron microscopy (HEEM) utilizes a high-energy electron beam to achieve ultra-high-resolution imaging of materials, with energies ranging from hundreds of keV to MeV.

spectrum as a unique fingerprint. On the other hand, **X-ray diffraction (XRD)** is used for the identification of crystal phase and configuration by analyzing the interaction of X-rays with a material, thereby resolving the unit cell dimensions and symmetry through resulting diffraction patterns [59]. While these techniques are used to determine the crystallographic structure, **X-ray photoelectron spectroscopy (XPS)** enables the analysis of surface elemental composition and oxidation states by determining the kinetic energy of electrons ejected from a sample upon X-ray irradiation. Additionally, **Auger electron spectroscopy (AES)** is a surface-sensitive technique that uses electron or X-ray beams to ionize atoms, resulting in the emission of Auger electrons.¹³ Examining the energy of emitted electrons yields comprehensive data on the surface's elemental composition and chemical properties. Also, **angle-resolved photoemission spectroscopy (ARPES)** is another pivotal technique for investigating the electronic structure of materials. By utilizing photon-induced emission, it measures the kinetic energy and emission angle of photoemitted electrons, yielding direct access to momentum-resolved band structures. This approach is particularly well-suited for exploring complex systems, such as high-temperature superconductors and topological insulators. On the other hand, in **low-energy electron diffraction (LEED)**¹⁴ a low-energy electron beam (10-200 eV) is directed at the sample surface, where electrons undergo elastic scattering. The resulting diffraction pattern, arising from the interference of scattered electrons, reveals detailed information about the atomic arrangement and periodicity of the surface. LEED is particularly well-suited for investigating surface crystallography and reconstruction, adsorbate structures, and thin films.

1.1.4 Transfer techniques

Integrating 2D materials directly into devices poses significant challenges due to the stringent conditions required for their development. In response, advanced transfer techniques (see Figure 1.5) were created to move 2D materials from their growth surfaces to desired substrates while preserving their properties and quality. This section focuses on how various transfer techniques of 2D materials from their initial substrates are crucial for practical applications.

In the realm of conventional transfer methods, two primary classifications emerge: **wet transfer** and **dry transfer** techniques [61]. Regarding **wet transfer** techniques, the most

¹³When an atom is exposed to an X-ray pulse or electron beam, an inner-shell electron is ejected, creating a vacancy. To restore stability, an outer-shell electron fills the vacancy, and in the process, a second electron, known as the Auger electron, is ejected.

¹⁴Akin to LEED, high-energy electron diffraction (HEED) utilize a high-energy (keV) electron beam.

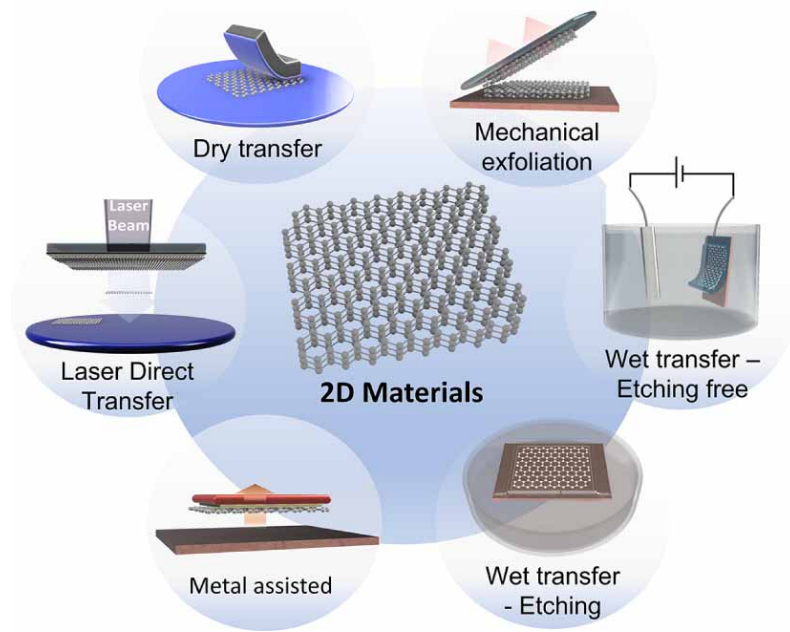


Figure 1.5: The overview of main transfer methods for 2D materials [61].

common method involves the use of polymethyl methacrylate (PMMA) as a transfer film [62]. Initially, PMMA is coated onto the 2D material which was previously synthesized on a substrate. This PMMA/2D material/substrate stack is then dipped in an etchant to dissolve the substrate. The stack is subsequently floated in deionized water to rinse off residual etchant. The floating PMMA/2D material is then carefully transferred onto a target substrate. Finally, the assembly is immersed in a solvent (acetone), to effectively dissolve the PMMA, ensuring that the 2D material remains intact on the new substrate (after washing and drying), with the critical challenge being the complete elimination of any residual PMMA. Another strategy involves directly detaching the polymer/2D material from substrate by employing the electrochemical method – etching free method [63]. The substrate, coated with a polymer/2D material is immersed in an electrolyte solution. By applying an electric current, which induces electrochemical reactions, gas bubbles are generated, typically hydrogen or oxygen, at the interface with substrate. These bubbles create pressure, causing the polymer/2D material stack to detach from the metallic substrate. Although “bubble-free” electrochemical transfer processes are designed to avoid damages from bubbles [64], they typically require more time than conventional electrochemical methods and are limited in terms of compatible donor substrates. Therefore, *wet transfer* techniques enable the transfer of large-area films but face significant drawbacks, including contamination from residual PMMA and solvents, with sample deformation that hinders uniform coating on complex substrates. On the other hand, the **dry transfer** process, crucial for large-scale applications, hinges on

the different adhesion strengths between the *transfer film/2D material* and *2D material/target substrate* interfaces. To achieve a flawless, undamaged transfer, the bond strength between the 2D material and the “receiving” substrate must be greater than that between the 2D material and the *transfer film*. [65]. Also, a preparation process of 2D materials involves a deposition of a thin polymer layer, such as polydimethylsiloxane (PDMS), to serve as a supporting layer – transfer stamp. In the next stage, the growth substrate is removed by immersing the structure in etching solution, followed by rinsing in deionized water to eliminate any remnants from the process. Alternatively, mechanical exfoliation can eliminate the need for chemical processing by adhering a sticky layer to the 2D material while it remains on the original substrate [66]. To transfer the 2D material successfully, the *2D material/transfer stamp* (stack) must be carefully placed onto the target substrate. After “securing” the 2D material onto the desired substrate, the polymer layers acting as the transfer medium are carefully removed. Additionally, the *pick-up* technique was introduced to directly transfer single flakes onto a target substrate. This method employs specialized stamps (polypropylene carbonate coated PDMS blocks or hemisphere PDMS stamps), suitable for precise multidimensional manipulation of flakes, including rotation, stacking, and alignment along specific crystal directions [67]. However, conventional transfer methods are unsuitable for structures smaller than a few μm but the *metal-assisted transfer* method [68], which uses a thin metal film as an intermediary, overcomes this limitation.

1.1.5 Film patterning

Film patterning is a vital technique in material science and hybrid device fabrication, enabling the precise creation of shapes and features on thin films. Techniques such as photolithography, electron beam lithography, and nanoimprinting offer fine control over material's properties and device functionality (see Figure 1.6). This section details various film patterning methods and their effects on advancing technology and enhancing device performance.

One of the most commonly used *top-down* methods for nanoscale device patterning is *nanolithography*. This technique can be divided into two main categories: (i) *direct nanolithography techniques* and (ii) *nanolithography using resists* [70].

Regarding *direct nanolithography techniques*, we will start with **focused helium ion beam (FHIB)** patterning¹⁵ which is a high-precision method used to create nanometer-scale patterns on 2D materials, with resolution of ~ 0.5 nm. In this process, the ion beam can etch away or deposit

¹⁵Commercially available focused ion beam (FIB) systems have predominantly used Ga^+ .

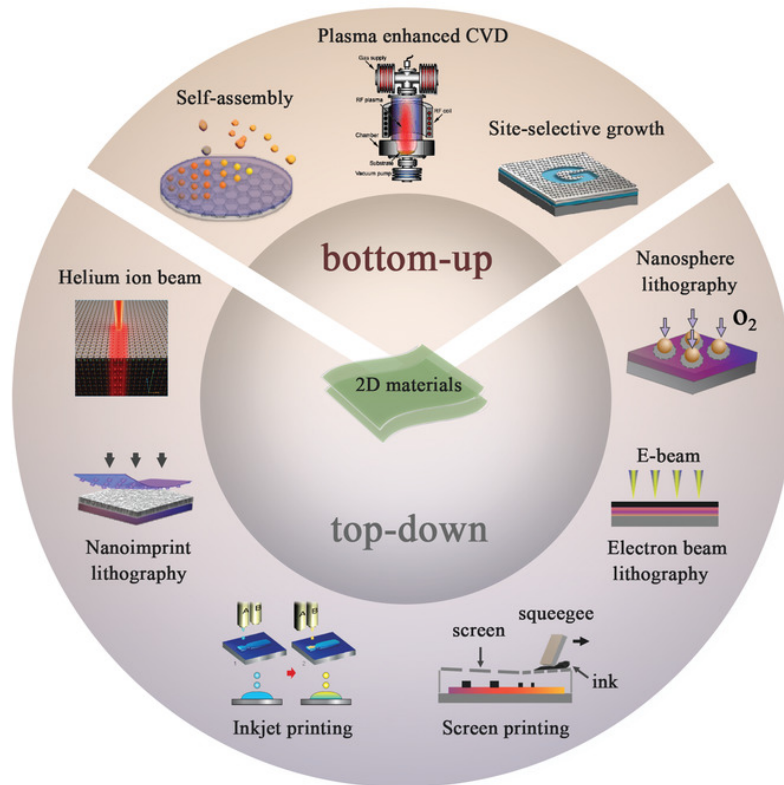


Figure 1.6: Overview of several methods for fabricating patterned 2D materials [69].

material, allowing precise patterning and modification of the surface. It is effective for controlling line width, crystal structure, and edge roughness with minimal subsurface damage. It allows the creation of extremely narrow etched channels (nanoribbons), can introduce point defects to modify material properties (such as altering electrical conduction in graphene or controlling resistivity in MoS₂) but is less suited for large-scale processing [69, 70, 71]. **Scanning probe lithography (SPL)** uses a sharp probe tip to directly write patterns on a substrate by interacting with the material's surface, achieving high resolution (below 20 nm) though it remains inefficient for large-scale production [70, 72]. Another notable patterning technique is **inkjet printing**, which directly deposits (prints) patterns onto surfaces in the way that position and pattern shape can be controlled by programming. It is well-suited for large-area patterns, typically with resolutions above 1 μm [73], and supports a wide range of inks thereby successfully producing photosensors, memory devices, supercapacitors, and various electronic devices [69, 74].

Nanolithography using resists can be divided into three categories: **optical(photo) lithography (O(P)L)**, **electron beam lithography (EBL)**, and **nanoimprint lithography (NIL)**. In standard **O(P)L** process, a layer of photoresist is initially deposited onto the desired 2D material via *centrifugal deposition* and subsequently structured using ultraviolet (UV) exposure, with resolution of 1 μm to 10 nm. This patterned photoresist serves as a mask for subsequent etching

processes, such as reactive ion etching (RIE) or reactive gas etching, thereby transferring the photoresist pattern onto the 2D film. An alternative to conventional etching is the *lift-off* technique, where a substrate is coated with photoresist, patterned with UV light, and then conformally overlaid with a 2D film. The specimen is subsequently submerged in a solvent that selectively dissolves the resist, detaching the undesired 2D layer while preserving the patterned 2D material firmly attached to the target substrate. However, to attain even higher patterning resolution, down to a few nanometers without the diffraction limitations, **EBL** technique is frequently employed. Under precise computational control, a focused electron beam exposes the electron-sensitive resist according to specific requirements, creating regions with different solubility properties.¹⁶ The subsequent development process reveals a electron-sensitive resist pattern, which is then transferred to the material in a manner similar to traditional O(P)L. However, EBL is slower and more expensive, making it less suitable for large-scale production [70]. On the other hand, **nanoimprint lithography (NIL)**, also known as stamp technique, is another patterning technique which involves a process of imprinting a mold with a targeted nanoscale pattern onto a resist-coated substrate without the need for resist exposure. The process uses high imprinting pressure and elevated temperatures to ensure that the resist material adopts the mold's shape. After imprinting, the resist is etched and removed, leaving a pattern on the substrate that complements the mold's design [75]. The quality of the mold in NIL is crucial for achieving high-resolution patterning, as the mold's features define the resolution. NIL allows high-throughput patterning over large areas, though it often requires an additional etching step to remove residual resist. Despite limitations in creating complex patterns, its simplicity, efficiency, and large-area capabilities are suitable for industrial applications. Furthermore, **nanosphere lithography (NSL)** is a cost-effective technique for creating nanoscale patterns using self-assembled arrays of colloidal particles. These particles form a thin, ordered layer with holes on a substrate, which acts as a mask during deposition of the desired material. After deposition through holes, the particles are removed, leaving behind a precise pattern. NSL is valued for its simplicity and large-area patterning with good resolution, but is limited by pattern complexity and challenges in achieving long-range order [70].

Regarding the *bottom-up* patterning techniques, they can be divided into: **self-assembly method**, **plasma enhanced CVD (PECVD)**, and **site-selective growth**. **Self-assembly** involves the spontaneous organization of structural units, such as atoms, molecules, or nanomaterials.

¹⁶EBL is typically carried out within a scanning electron microscope (SEM) or specialized equipment designed for this purpose.

als, into ordered, stable structures. This parallel processing method is suitable for the large-scale formation of nanometric 2D patterns, crucial for device applications [69]. For example, molecular precursors like $C_{38}Br_2N_4H_{22}$ can polymerize into graphene nanoribbons, which, when doped with nitrogen, align into 2D arrays via hydrogen bonding. Self-assembly can also create their 3D stack structures in solution through π -stacking and vdW forces [76]. In general this method has several disadvantages, including limited control over defects, inconsistent long-range order, challenges in designing complex patterns, and the process can be time-consuming. On the other hand, **PECVD** is a technique where a source gas is ionized to form plasma, activating reactive materials to achieve CVD by providing high-energy electrons, enabling the self-assembly growth of materials like vertical graphene nanowalls [69]. For example, under radio-frequency plasma, graphene grows vertically on nanopore alumina membranes, with gold nanoparticles enhancing growth quality and density [77]. However, PECVD is complex and expensive, with challenges in achieving uniformity over large areas. Furthermore, **site-selective growth** improves the traditional CVD (randomly distributed 2D materials onto substrate) by precisely placing 2D materials on predefined areas. This method uses prepatterned substrates or growth seeds to control material deposition, allowing creation of high-quality, large-area films with accurate patterns. Techniques such as *lift-off* and EBL help to achieve targeted growth, enhancing device integration. Despite these advantages, site-selective growth can struggle with uniformity, scalability, and compatibility with different materials [69, 78].

1.1.6 Tuning materials properties

Tuning 2D materials properties is vital for their use in electronics, optoelectronics, sensing, and energy devices. The desired adjustments can be implemented either during material synthesis or after integrating the materials into devices. This section is mainly about post-transfer techniques like gate or strain tuning, carrier doping, etc. (see Figure 1.7). These methods allow precise control over electronic, optical, and mechanical properties, enhancing the materials performance and enabling new applications.

Let us start with **field effect**¹⁷ which is a key mechanism for tuning the physical properties of 2D materials. In a typical *field effect transistor (FET)* configuration, a parallel-plate capacitor structure with materials like highly doped silicon as one electrode, an insulating layer, and a 2D material like graphene as the other electrode is commonly used. Applied gate voltage V_g

¹⁷Gate tuning – electric field is applied perpendicular to the 2D material through a gate dielectric. This field modulates the carrier concentration (increases/decreases) in the 2D material, altering its electronic properties.

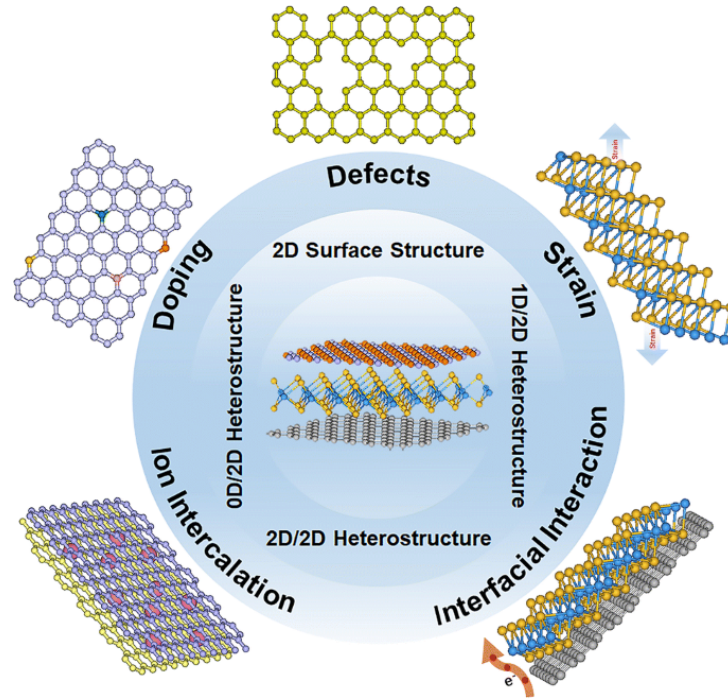


Figure 1.7: Tuning the properties of 2D materials by different methods, including atom doping, defect engineering, strain, ion intercalation, and the construction of heterostructures [79].

modulates the carrier density in the 2D material (graphene in this case), shifting the Fermi level due to the electrostatic doping effect. This method can induce carrier density up to 10^{13} cm^{-2} by using insulated-gate structure,¹⁸ with higher densities achievable using ion liquids as gating materials, which can exceed 10^{14} cm^{-2} in MoS_2 [80]. Interestingly, ferroelectric gates have a spontaneous polarization that remains stable without an external field and can be reversed with applied voltages. Their rewritable and stable ferroelectric polarization, along with a high dielectric constant, makes them ideal for non-volatile memories. Integrating ferroelectric gates with 2D semiconductors allows precise control over doping levels, leading to advancements in memory devices [81]. Another approach to tune the electronic properties of 2D materials involves **carrier doping** by foreign atoms. Depositing atoms such as potassium onto graphene creates ionic bonds that transfer charges to the graphene, shifting its Fermi level and modifying its electronic properties [82]. This method can achieve significantly higher doping densities than electrostatic doping via gate voltage. However, the process is irreversible, limiting its suitability for practical device applications. Additionally, *substitutional doping*¹⁹ of graphene with different elements like nitrogen or boron during growth process can effectively alter its electronic properties [83]. Moreover,

¹⁸In the *back-gate* configuration (commonly used), a gate voltage is applied to the substrate beneath the 2D material; the top-gate configuration places the gate electrode on top for localized tuning, while the dual-gate configuration combines both for precise control and advanced functionalities.

¹⁹Replacing an atom with a different element possessing comparable radii.

while graphene itself is typically inert and lacks electrocatalytic activity, introducing **defects** can significantly enhance its reactivity. *Defects* such as *vacancies* and *edge* disruptions can break electron-hole symmetry and increase the local density of reactive π -electrons [84]. Furthermore, **strain engineering** is another key method for tuning 2D materials by effectively changing their lattice and electronic structures, like enhancing electron mobility in silicon transistors through applied uniaxial or biaxial tensile strains [85]. Unlike traditional bulk materials, which can only tolerate limited strain, 2D materials like graphene exhibit remarkable deformation capacity, withstanding up to 25% elastic strain without breaking [86]. Additionally, strain improves carrier mobility in FET and introduces piezoresistive and piezoelectric effects, expanding potential applications to sensors, photodetectors, and flexible devices [87, 88]. Not only that it can change the phonon structure but also can both alter the magnetism of intrinsic vdW magnets and induce magnetism in otherwise nonmagnetic 2D materials [89]. Experimentally, strain can be induced through lattice mismatch²⁰ by using various methods, including different substrates (flexible, patterned, or piezoelectric) and techniques involving AFM tips. Additionally, the vdW interlayer coupling in 2D materials facilitates the **intercalation** of foreign ions, atoms, and molecules into the large interlayer space instead of substitutional sites. This *intercalation method* has been used to exfoliate 2D materials in solution and is commonly applied in batteries and electrochemical cells. Recently, intercalation has been shown to modulate the crystal lattice and electronic structure of host materials, enabling phenomena such as semiconductor–metal transitions, charge density waves (CDW), and superconductivity [90]. Other important tuning techniques include **optical tuning** (adjusting light interaction), **laser modification** (altering material properties with laser such as bandgap modulation, selective site doping, or enhancing carrier mobility), **ion modification** (tailoring via ion irradiation by creation of vacancies or directly implant dopants) and **tip scanning modification** (local property control with tip-induced reduction, oxidation, and other reactions) [74]. Besides, 2D materials can also serve as fundamental building blocks for constructing various materials. Stacking multiple layers of the same material can create vertical²¹ 2D heterostructures, where changing the stacking order alters both symmetry and its properties. Constructing advanced 2D heterostructures is not limited to same type of material

²⁰Lattice mismatch refers to the relative ratio of the lattice constants (the distances between atoms in a crystal) between two materials. When two materials with different lattice constants are brought into contact, the mismatch can cause strain in the interface or in the layers of material. This is because the atoms in the materials may not align perfectly, leading to compressive or tensile stress in the material layers. This phenomenon is particularly significant in thin films, heterostructures, and when integrating different materials in semiconductor devices.

²¹In contrast, *lateral* heterostructures arrange different 2D materials side by side in the same plane, forming patterned or mosaic structures, as shown in Figure 1.1.

layers; combining different materials into vdW heterostructures introduces charge redistribution, interface strain, or structural modifications in each material, leading to new functionalities. This approach, known as **heterostructure engineering**, demonstrates the potential for innovative material design [91]. A slight rotational misalignment between adjacent 2D crystals, beyond mere layer stacking, can induce novel and remarkable properties like intrinsic unconventional superconductivity in twisted bilayers or so-called *magic-angle*²² graphene systems [92]. On top of that, in vdW heterostructures Moiré patterns arise, from lattice mismatches and/or twisting of layers, with large-scale periodicity also known as a Moiré superlattice. These patterns cause local variations in stacking order, leading to differences in material properties. The study of Moiré patterns, particularly in graphene and *h*-BN heterostructures, is a promising new field in material science. This technique, often called *twistronics* is suitable for the tuning of electronic properties and, in magnetic materials, can break inversion symmetry causing non-collinear spin configurations, and potentially result in exotic magnetic states like *magnetic skyrmions* in CrI₃, useful for spintronic applications [93, 94]. Nevertheless, a production of 2D heterostructures still remains a more intricate process than the fabrication of monolayer materials.

1.2 2D boron crystal structure (*borophene*)

Boron, with its intricate bonding nature, exhibits extraordinary structural complexity, as seen in the prediction of 16 distinct bulk phases, though many remain poorly understood and only 5 have been confirmed. This complexity extends to borophene, a 2D boron allotrope, whose flexible bonding arrangements result in remarkable polymorphism and a wide range of potential properties. However, the synthesis of borophene remains a significant challenge, with current methods limited by difficulties in large-scale production and oxidation prevention. Despite these challenges, borophene has garnered considerable attention due to its theoretically predicted superior physical properties compared with graphene.

1.2.1 Tracing the evolution of boron: from early discoveries to complex bulk and 2D phases (borophenes)

The journey towards the discovery of *borophene* (2D structure of boron), one of the most promising 2D materials of the modern era, can be traced back to the ancient recognition of borate

²²The “magic angle” in twisted bilayer graphene, approximately 1.1 degrees, induces a flat electronic band structure and leads to unconventional superconductivity.

compounds (boron oxyanions), most notably *borax* ($\text{Na}_2\text{B}_4\text{O}_7 \cdot 10\text{H}_2\text{O}$).²³ Although much of borax's ancient history is unverified, it is believed that the Babylonians used it around 6000 years ago as a flux in goldsmithing, while the Egyptians employed it in mummification, medicine, and metallurgy. The earliest solid evidence of borax mineral ("tincal") use comes from the 8th century, when Arab traders sourced it from Tibetan dry lakes, calling it "buraq" which means *white* [95, 96]. However, the first crucial step towards discovery and isolation of pure boron began with Wilhelm Homberg, who in 1702 treated natural borax with acid to produce a substance he called "sedative salt" (also known as boric acid). This early work set the stage for two significant independent discoveries in 1801. On one side, Louis J. Gay-Lussac and Louis J. Thénard extracted a new element that they called "*bore*" (*boron*) by decomposing boric acid ($\text{B}(\text{OH})_3$) using fused potassium [97]. On the other side, Humphry Davy heated potassium with boric acid in a copper tube, and successfully produced a new substance, which he named "*boracium*" (later called *boron*) [98]. In 1856, Henry Sainte-Claire Deville and Friedrich Wöhler refined the method for producing boron, substituting potassium with sodium which yielded large quantities of amorphous boron, and by using aluminum, they produced crystalline boron, known as *adamantine* (diamond) boron [99]. Subsequently, Henri Moissan (1906 Nobel laureate) showed that the earlier methods of Gay-Lussac, Thénard, and others, yielded boron with only 50–60% purity. His refined process, which involved reducing boric anhydride with magnesium, was initially thought to produce 99% pure boron but subsequent analysis revealed it was actually only 90% pure [100]. Ultimately, in 1909, Ezekiel Weintraub achieved nearly 99% pure boron by reducing boron trichloride with hydrogen using an electric arc on a cold copper anode [101].

Despite significant advances in boron research, the first bulk phase of pure boron was identified by Donald E. Sands and J. L. Hoard in 1957 [102]. The complex crystal structure, characterized as high-temperature low-pressure β -rhombohedral or β - $\text{B}_{105-108}$ ²⁴ phase, was resolved later, in 1963 [103, 104]. In 1958, a new, low-temperature bulk phase of boron was discovered [105], and its crystal structure was subsequently determined to be α -rhombohedral (α - B_{12}) in the following year [106]. Later, in 1960, a new complex high-temperature tetragonal boron ($\text{T-B}_{190-192}$) phase was discovered [107, 108]. In 1964, Robert Wentorf, a pioneer in high-pressure material synthesis, investigated boron's behavior under extreme conditions. By subjecting standard boron allotropes to pressures over 100 kbar and temperatures 1773–2273 K,

²³Also, boron occurs in several forms, including borax, kernite, and tincalconite (hydrated sodium borates), which are the predominant commercial boron minerals located in California's dry areas. Natural boric acid, known as sassolite, is primarily found in Italy.

²⁴The notation $\text{B}_{105-108}$ refers to a unit cell that contains 105-108 boron atoms.

he produced a novel phase with a distinctive Debye-Scherrer diffraction pattern [109]. The crystal structure of this phase remained unknown until 2009, when *ab initio* calculations revealed it to be an ionic phase, named γ -B₂₈. This phase exhibits extreme hardness, with a Vickers value of 50 GPa, making it the toughest boron allotrope identified so far [110, 111].

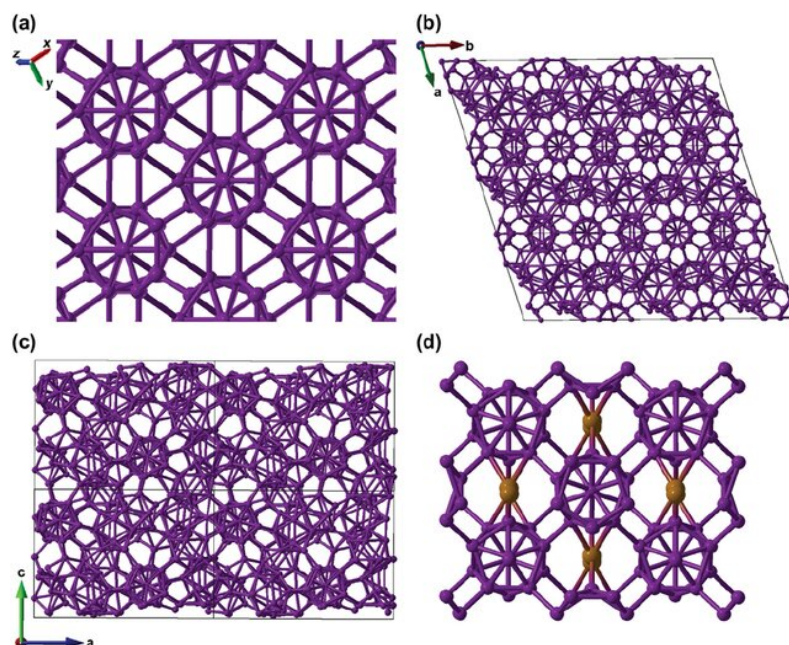


Figure 1.8: Crystalline arrangements of boron polymorphs: (a) α -B₁₂, (b) β -B₁₀₆, (c) T-B₁₉₂, and (d) γ -B₂₈ [96, 111].

Regardless of substantial progress, the relative stability of four boron phases under ambient conditions remains experimentally unresolved, making boron a persistently challenging element to fully understand. This prompts the question: “*What underlies its complex chemical behavior?*”

With three valence electrons ([He] $2s^2 2p^1$)²⁵ but four available valence orbitals, boron experiences an inherent electron deficiency, which drives it to adopt different bonding configurations, such as sp^2 hybridization, where it forms *tri*-coordinated structures with an empty *p* orbital. Additionally, the interplay of localized $2s$ and $2p$ orbitals gives rise to diverse bonding modes in bulk boron, from strong two(three)-center covalent bonds to metallic-like multi-center bonds which are crucial for forming polyhedral structures,²⁶ particularly the dominant B₁₂ icosahedra in the role of the basic structural unit, as depicted in Figure 1.8. The well known Wade’s rule states that an icosahedral cluster with n vertices needs $n + 1$ pairs of skeletal electrons to stabilize

²⁵Boron possesses only three valence electrons, which would typically favor metallic behavior. However, these electrons are sufficiently localized, leading to the emergence of insulating states. This delicate balance between metallic and insulating characteristics is readily influenced by pressure, temperature, and impurities.

²⁶All boron phases feature icosahedral B₁₂ clusters, where three-center metallic-like bonds are found within the clusters with covalent two- and three-center bonds linking them. While this bonding typically yields an insulating state, the introduction of impurities can shift the material to a metallic state.

its multi-centered bonding. In the case of an icosahedral B_{12} cluster, 36 valence electrons are present, so that 26 are used to fill 13 bonding orbitals within the icosahedron, and the remaining 10 electrons contribute to bonding between different icosahedrons. Each icosahedron forms six 2-center-2-electron bonds with adjacent atoms, using 6 electrons, and six 3-center-2-electron bonds with other neighbors, using 4 electrons. These bonds, both two- and three-centered, are responsible for the exceptional hardness of boron crystal and its compounds. Besides B_{12} icosahedra, boron crystal structures also include other unit building blocks such as B_2 dumbbell units, B_{21} , B_{28} , or B_{84} .

While the stability of boron phases under ambient conditions remained unresolved, *ab initio* calculations offered improved insights into this issue. The stability debate between α - B_{12} and β - B_{106} was resolved around 2007, with different studies favoring disordered β - B_{106} over α - B_{12} boron phase [112, 113]. On the other hand, experiments on ambient-temperature compression of β - B_{106} boron phase demonstrated metastable amorphization at 100 GPa [114] and even the emergence of superconductivity at 160 GPa, with critical temperature (T_c) reaching up to 7 K [115]. Furthermore, by employing laser heating to overcome kinetic barriers, β - B_{106} undergoes a phase transition to T- B_{192} at temperatures around 2280 K and pressures exceeding 10 GPa [116]. However, the discovery of γ - B_{28} filled a key gap in boron's phase diagram, revealing its large stability field that persists up to 89 GPa before transforming into the highly anisotropic α -Ga-type²⁷ phase [111] – theoretically predicted in 2004 with interesting superconducting properties [117, 118] – providing therefore new insights into boron's intricate phase behavior, as depicted in Figure 1.9.

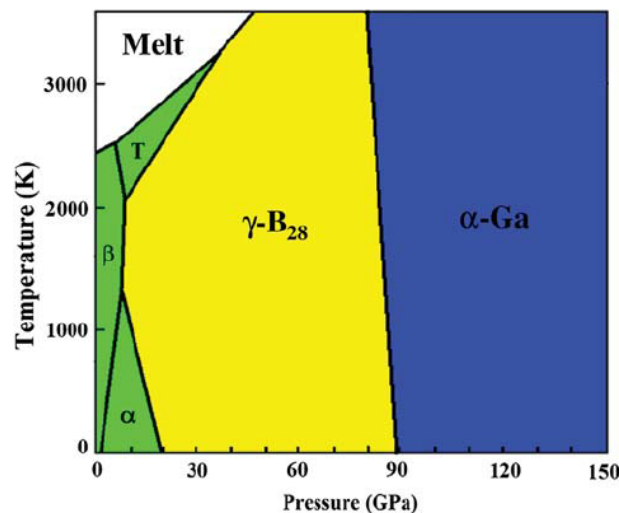


Figure 1.9: Phase diagram of boron, including both theoretical and experimental data [96, 111].

²⁷This boron phase does not contain B_{12} icosahedra.

Following the discovery of these five boron bulk phases, an intriguing question arises: “*Could 2D boron structure, analogous to graphene, be synthesized?*”

In 1995, Ihsan Boustani’s groundbreaking study revolutionized boron research, demonstrating via density functional theory (DFT) simulations that boron clusters containing up to 14 atoms preferentially adopt convex or “semi-planar” geometries rather than icosahedral arrangements [119]. Moreover, he found that the high stability of quasi-planar boron clusters is driven by strong π -hybrid interactions, forming electron clouds on both sides of the plane, akin to graphite. His initial findings on double layers suggest an exceptionally stable system, pointing to the potential existence of a boron lattice with graphite-like properties [120]. He proposed the *formation rule*, called “**Aufbau principle**”,²⁸ which employs hexagonal pyramidal units for quasi-planar and convex stable boron clusters, and pentagonal pyramidal units for 3D *cage*-like clusters [121]. In 1997, using this formation rule, he predicted a new class of clusters called *tubules*, visualized as quasi-planar surfaces rolled into cylinders, with the first experimental evidence of boron nanotubes reported in 2004 [122, 123]. In 2007, a cluster resembling the well-known C_{60} fullerene was identified, named B_{80} , whose structure contains also hexagons but with additional atoms at their centers [124]. This research paved the way for predicting 2D boron sheet analogous to graphene, with the unfolding of B_{80} onto a plane revealing a stable flat crystal composed of a triangular lattice with isolated hexagonal voids (HH), also known as α -sheet [125, 126] (see Figure 1.10(a)).

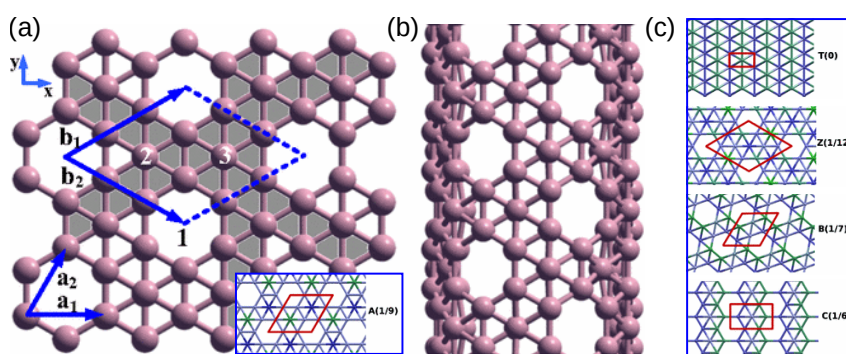


Figure 1.10: The structure of (a) α boron layer, (b) the corresponding nanotube structure, as well as (c) structures of additional four different boron 2D configurations. Adapted from [126, 127].

In 2010, Hui Tang and collaborators proposed multiple boron sheet configurations with

²⁸Convex boron clusters, which can be seen as segments of infinite tubules or spheres, tend to form closed polyhedra and are predicted to be spherical with sizes exceeding 90 atoms, such as B_{92} and B_{122} . Quasi-planar clusters resemble stable surfaces which stability increases with size. In contrast, open 3D structures are less stable and tend to close the open spheres with fewer atoms. The structural units used as building blocks in all cases are mainly B_6 and B_7 .

varying patterns and density of HHs (η)²⁹ (see Figure 1.10(c)), revealing that some have cohesive energies comparable to the α -sheet, thereby prompting further exploration into the polymorphism of 2D boron structure. However, the most stable boron sheet structure in their study is A($\eta = \frac{1}{9}$) because electrons fully occupy the in-plane bonding states (B- σ) and leave the antibonding states empty (B- σ^*),³⁰ achieving an optimal balance between two-center and three-center bonding [127]. However, in 2012, Evgeni S. Penev and collaborators, using cluster expansion with DFT results as the input, predicted that the $\eta = \frac{1}{8}$ boron sheet is slightly more stable than the $\eta = \frac{1}{9}$ phase [129]. The stability of the $\eta = \frac{1}{9}$ boron sheet arises from B atoms at hexagon centers acting as electron “donors” while the empty HHs act as electron “acceptors”, balancing thereby the electronic deficiency [127, 128, 130], with vacancy-vacancy interactions slightly shifting the ground state towards the $\eta = \frac{1}{8}$ phase [128]. This intrinsic doping mechanism suggests that borophene attains an electron configuration equivalent to graphene when the vacancy ratio is $\eta = \frac{1}{9}$. However, on substrates, charge transfer alters this balance, leading to $\eta \neq \frac{1}{9}$.

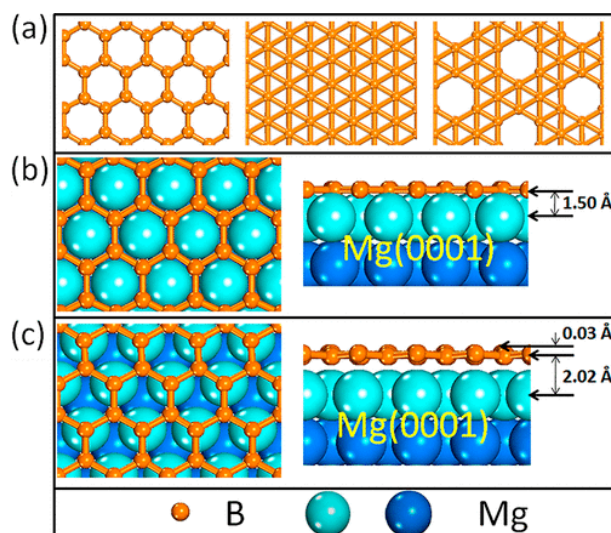


Figure 1.11: (a) Schematic representations of three different 2D boron structures, together with top and side views of the hexagonal sheet (h-BS) on Mg(0001) substrate for (b) top, (c) hcp site [131].

Although 2D boron remains less energetically favorable than 3D phases – unlike graphene which has stable, naturally occurring bulk counterpart – its synthesis challenges, rooted in instability and polymorphism, have been advanced through essential theoretical insights guiding further experimental progress. The synthesis of silicene on Ag(111) substrate in 2012 [19]

²⁹The HH density is given by $\eta = \frac{n}{N}$ parameter, where n is representing the number of hexagonal voids in a supercell containing N triangular lattice sites.

³⁰Boron sheets with $\eta < \frac{1}{9}$ are electron-rich and exhibit off-plane buckling due to mixing of B- $s + p_{x,y}$ and B- p_z orbitals, while those with $\eta > \frac{1}{9}$ remain flat and tend to accept electrons in order to stabilize their structure [128].

sparked a new wave of research, leading to theoretical predictions that 2D boron structure could be realized on certain metallic substrates. L. Z. Zhang and collaborators examined three types of monolayer boron sheets (BSs), as shown in Figure 1.11(a). Their findings show that *h*-BS is the most stable phase compared to triangular and mixed hexagonal-triangular boron sheets, with “charge migration” from metallic substrates to *h*-BS occurring due to its inherent electron imbalance [131]. In 2013, Yuanyue Liu and colleagues proposed that BSs (using boron clusters B_n with number of atoms $n < 20$) could be grown on Ag(111) or Au(111) surfaces via CVD, with a high nucleation barrier preventing the formation of 3D structures. They also proposed that BSs may form by immersing a boron-covered MgB_2 surface in a boron-enriched surrounding. These sheets were predicted to be weakly bound to the substrates, making post-synthesis separation into freestanding forms feasible [132]. Additionally, Hongsheng Liu and colleagues demonstrated two methods for boron monolayer growth on Cu(111) substrate: (i) depositing boron atoms directly or (ii) by landing small B_n (with $n < 20$) clusters on it, both resulting in a mixed hexagonal-triangular boron sheet after nucleation and thermal annealing [133]. In 2014, Zachary A. Piazza and colleagues provided both experimental and theoretical evidence that B_{36} is a highly stable, quasi-planar boron cluster with a “middle” hexagonal void, marking the pioneer demonstration that single boron layers with such voids are attainable and could serve as fundamental building blocks for 2D boron configurations. In light of their potential large-scale synthesis, they proposed the name “*borophene*”, drawing an analogy to graphene [134]. Furthermore, in 2015, Guoan Tai and colleagues synthesized atomically thin γ -orthorhombic boron (γ - B_{28}) films on copper foils via low-pressure CVD [135]. In the same year Zhuhua Zhang and colleagues demonstrated,

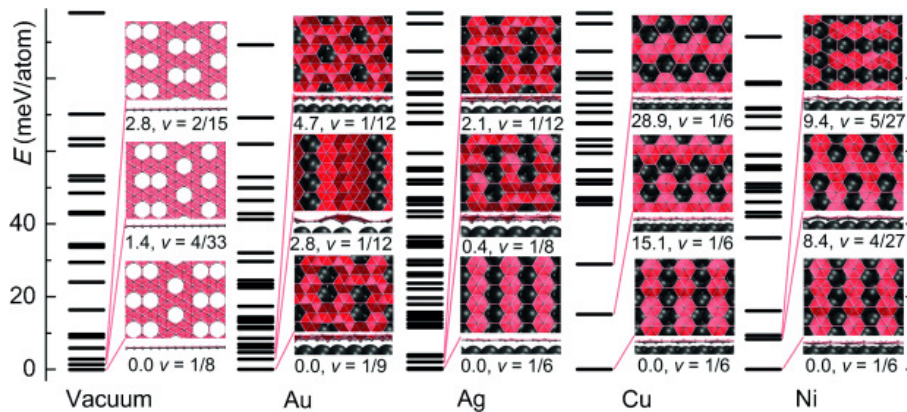


Figure 1.12: Energy differences among distinct 2D boron structures, both in the isolated state and on various metallic substrates (black spheres), with insets showing the most stable configurations for each case [136].

using cluster expansion and a surface structure-search method, that 2D boron configuration

strongly depends on the “nature” of its interaction with metallic substrates. On less reactive substrates like Au, 2D boron forms nonplanar, buckled structures with multiple polymorphs, while on more reactive metals like Ag, Cu, and Ni, increased electron donation enhances the η value, stabilizing the 2D boron structure. This substrate-dependent structural variation arises from the interplay between two key factors: (i) the strain energy associated with buckling, and (ii) the chemical hybridization between boron and the metal. Their overall analysis indicate that a planar $\eta = \frac{1}{6}$ sheet is the most stable structure on a range of different metallic substrates (see Figure 1.12), highlighting the need for immediate experimental confirmation [136]. Finally, in the same year, guided by theoretical predictions and their own insights Andrew J. Mannix and colleagues achieved a major breakthrough by synthesizing borophene on a pristine single-crystal Ag(111) surface in a UHV chamber [23]. This breakthrough provided the basis for advancing the synthesis of various borophene phases in the years that followed.

1.2.2 Borophene synthesis techniques and structural characterization combined with the density functional theory (DFT) approach

Borophene has garnered significant interest due to its outstanding physical properties but its synthesis remains challenging, primarily due to its reactive nature and structural complexity. Current efforts rely on bottom-up methods, which offer exact control over borophene growth on metallic substrates but require ultra-high vacuum and high-temperature conditions. Recently, modified top-down approaches have been explored to expand synthesis possibilities and enable growth under more accessible conditions. Together with advanced characterization techniques and DFT modeling, deeper insights into borophene’s structural and electronic properties are obtained, which are crucial for realizing its full potential under ambient conditions and driving progress in its technological integration and scalable production.

1.2.2.1 Bottom-up approaches

We will summarize the synthesis of borophene on various substrates, highlighting the experimental methods used for controlled growth, as illustrated in Figure 1.13. The synthesis primarily employs MBE and advanced versions of CVD, with structures analyzed through comparison of simulated and real experimental STM or LEED data for the most stable configurations. Despite advancements, achieving true atomic resolution with STM or other characterization techniques, remains challenging for borophene, even with enhanced tip modifications. In this context, DFT

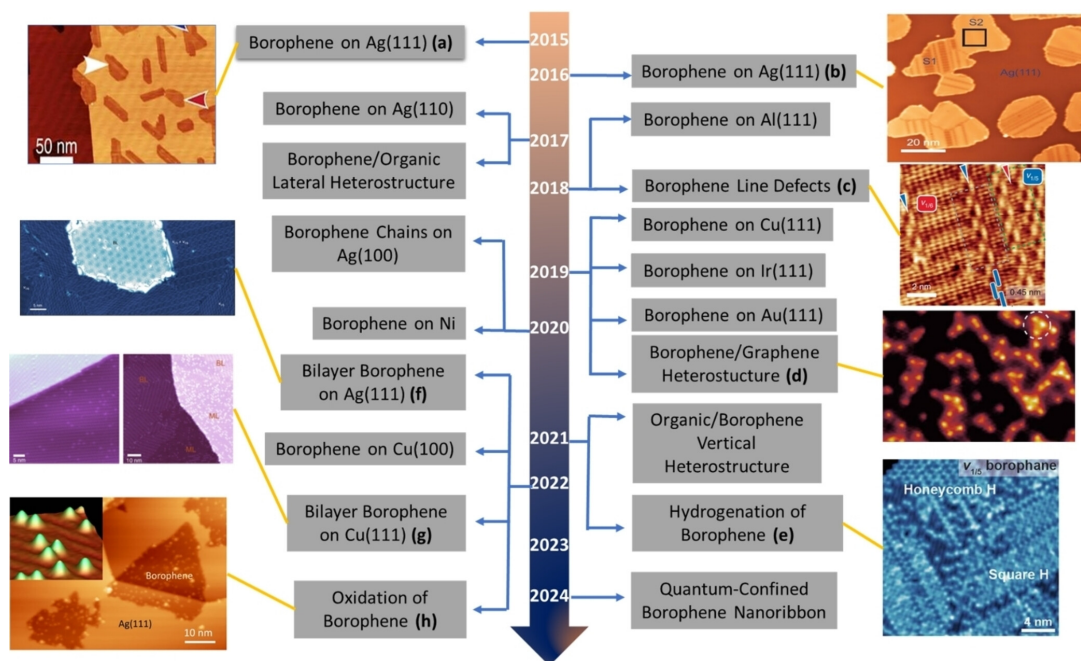


Figure 1.13: Timeline of experimental bottom-up borophene synthesis [137].

calculations are useful for gaining deeper insight into the true structures of the synthesized borophenes. However, many DFT-predicted stable structures have similar energies, complicating the selection based solely on cohesion energy. Variability in structure due to growth temperature, deposition rate, and substrate orientation underscores the need for better understanding of borophene's metastable phases. To address these challenges and bridge existing gaps, novel techniques are urgently needed to provide clearer insights into the true structure and properties of borophene.

Year 2015 – we will briefly present the work by Andrew J. Mannix and colleagues. They employed a high-purity solid boron source, effectively bypassing the challenges associated with toxic precursors. The temperature of the substrate was controlled in the range of 723–973 K throughout the deposition, while the boron flux was set between 0.01 and 0.1 monolayers per minute, as depicted in Figure 1.14(a). Following deposition, *in situ* AES detected a boron KLL peak at 180 eV (see Figure 1.14(b)), while STM topography at 823 K revealed two distinct boron phases: (i) a homogeneous phase and (ii) a corrugated striped phase, indicated by red and white arrows in Figure 1.14(c), respectively. Furthermore, $\frac{dI}{dV}$ maps of LDOS (see Figure 1.14(d)) revealed strong electronic contrast between these two phases. Namely, low deposition rates favored transition from striped islands to striped nanoribbons (blue arrow), while higher rates and temperatures promoted homogeneous islands, suggesting the latter is more metastable. Building on this, STM/STEM images reveal pronounced anisotropic properties of both phases, while

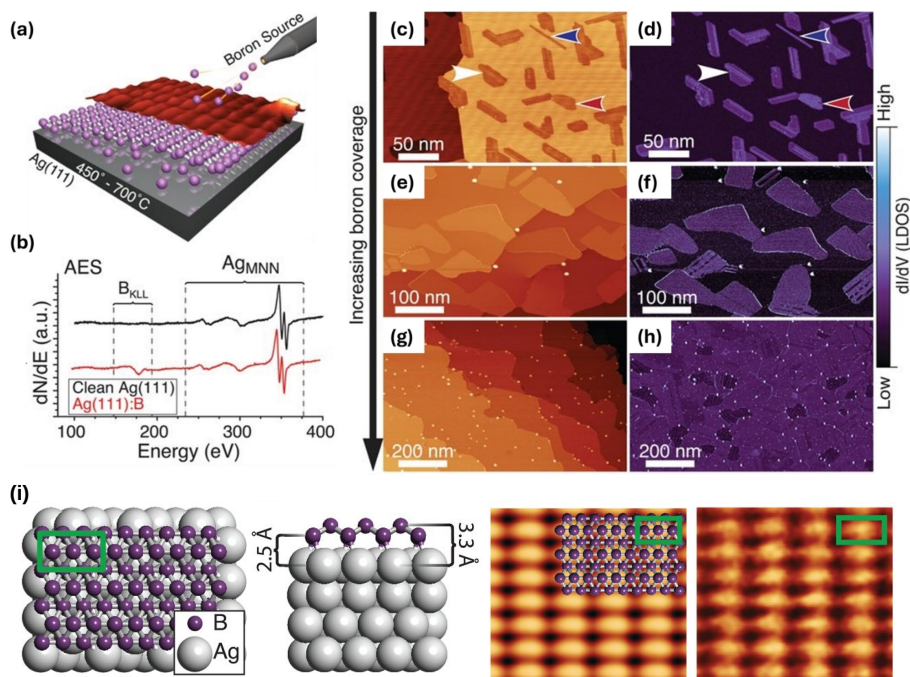


Figure 1.14: (a) Illustration of borophene growth on an Ag(111) substrate, with (b) the corresponding Ag(111)-AES spectra prior to and post borophene formation. (c, e, g) STM topography (left) and closed-loop $\frac{dI}{dV}$ images (right - d, f, h) at different boron coverage. (i) Top and side views of the low-energy monolayer structure, alongside DFT simulated and experimental STM images. Adapted from [23, 137].

XPS demonstrates that bare borophene samples oxidize within hours, whereas an amorphous Si/SiO₂ capping layer markedly delays this process. Using DFT approach it was shown that the lowest-energy monolayer structure is derived from distorted B₇ clusters using Boustani's *Aufbau principle*, with space group *Pmnm* and lattice parameters of 0.500 and 0.289 nm.³¹ This $\eta = 0$ borophene phase aligns well with STM data and electron diffraction results, as shown in Figure 1.14(i). The calculated electronic DOS confirms metallic behavior and strong mechanical anisotropy, with the Young's modulus potentially rivaling that of graphene [23].

Year 2016 – however, the previous predicted $\eta = 0$ structure did not align well with the theoretically predicted $\eta = \frac{1}{6}$ phase as a ground state on a metallic substrates. Under UHV conditions, Baojie Feng and colleagues grew two distinct and perfectly ordered monolayer islands – referred to as the S₁ and S₂ phases – on an Ag(111) substrate at approximately 570K, via MBE, as illustrated in Figure 1.15. The high-contrast STM image in Figure 1.15(b) shows parallel stripes on the island surface aligned with the [110] axis of the Ag(111), with a division of 1.5 nm (solid lines). On the other hand, the high-resolution STM image in Figure 1.15(c) reveals ordered protrusions aligned along the [112] direction, with nearest-neighbor distances of 3.0 Å along

³¹The experimental derived rectangular unit cell is defined by vectors **a** and **b**, with lengths of 0.51 nm (± 0.02 nm) and 0.29 nm (± 0.02 nm), respectively.

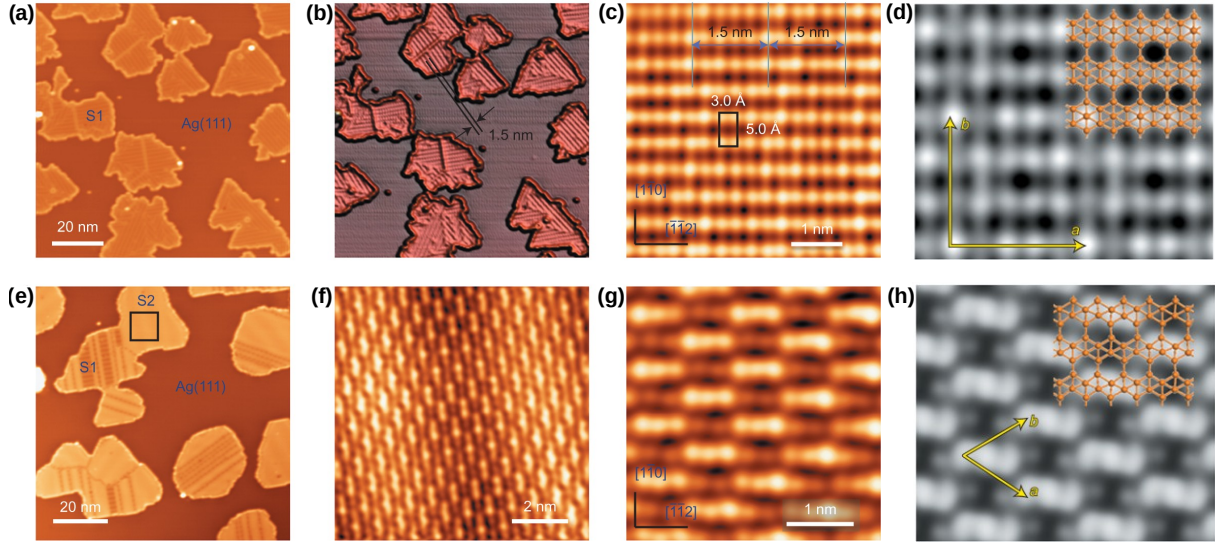


Figure 1.15: Scanning probe visualization of S_1 boron formations atop $Ag(111)$ (~ 570 K), with (b) a depth-enhanced view emphasizing 1.5 nm stripe separations. (c) Sharpened atomic-scale scan of S_1 , with (d) computed STM of β_{12} phase. (e) Thermal processing at 650 K yields predominant S_2 while traces of S_1 still persist. (f) Zoomed-in scan from marked region, with (g) refined atomic imaging of S_2 , and (h) computed STM of χ_3 phase. Adapted from [138].

the rows and 5.0 Å across (black rectangle), and this specific phase is named S_1 . Furthermore, the S_2 phase, often coexisting with the S_1 phase between 650 and 800 K, dominates at higher temperatures and can nucleate on $Ag(111)$ via direct deposition at ~ 680 K. High-resolution STM images (see Figure 1.15(f–g)) reveal how S_2 phase is composed of aligned protrusions extending along the $[112]$ axis, with a nearest-neighbor spacing of 3.0 Å along the rows and 4.3 Å across. DFT calculations revealed that the S_1 phase corresponds to the planar $\eta = \frac{1}{6}$ (β_{12}) structure,³² characterized by chains of holes separated by rows of hexagonal boron units, as shown in Figure 1.15(d), which is in a perfect agreement with the previous theoretical prediction. The S_2 phase is likely associated with the $\eta = \frac{1}{5}$ (χ_3) sheet model (see Figure 1.15(h)) characterized by narrower zig-zag boron rows interspersed with arrays of holes. The “striped phase” (δ_6) reported in the previous study is thermodynamically less stable compared to these phases and requires specific conditions for formation, such as precise boron flux control. Additionally, DOS calculations reveal their metallic character, and XPS measurements confirm that while the edges of the boron sheets oxidize, the interior atoms remain more inert to oxidation [138]. Therefore, the naming of the distinct phases of borophene (like β_{12} , χ_3 , or δ_6) is completely based on their unique structural features. Hence the question arises: “How can different borophene sheets be

³²Due to lattice mismatch, the fivefold lattice constant of the boron sheet (15.0 Å) aligns with three times the $Ag(111)$ periodicity (15.06 Å), leading to the formation of a 1.5 nm Moiré pattern along the boron row direction, which accounts for the 1.5 nm stripes observed in the STM image [138].

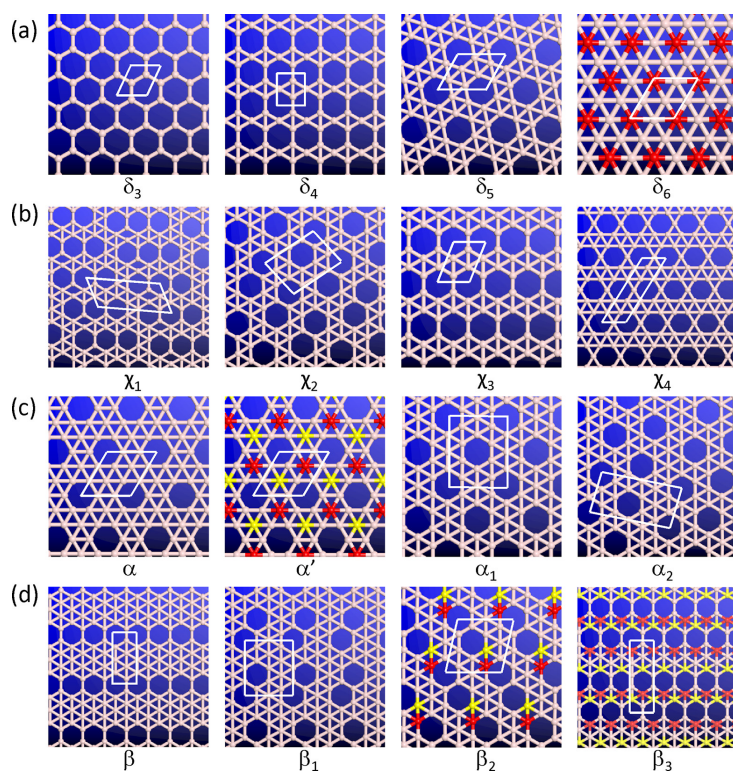


Figure 1.16: Top views of (a) δ -, (b) χ -, (c) α -, and (d) β -type borophene. Red and yellow spheres indicate boron atoms displaced either outward or inward from the plane, creating buckled sheet structures [139].

classified most effectively?” In addition to the global η parameter, which quantifies the area density of hexagonal voids, the local coordination number (CN) of boron atoms (as well as their number in the unit cell) is used to classify monolayer boron sheets. The classifications include: (i) α -type ($CN = 5, 6$), (ii) β -type ($CN = 4, 5, 6$), (iii) χ -type ($CN = 4, 5$), (iv) ψ -type ($CN = 3, 4, 5$), and (v) δ -type (single CN value). For instance, a buckled triangular sheet with $CN = 6$ is designated as a δ_6 -sheet, while a graphene-like honeycomb sheet with $CN = 3$ is termed a δ_3 -sheet (see Figure 1.16(a)) [139].

Year 2017 – the *sixfold symmetry* of Ag(111) leads to the formation of triangular boron structures, prompting exploration of boron growth on an anisotropic substrate. Qing Zhong with collaborators studied borophene growth on anisotropic Ag(110) substrate via MBE, revealing two key findings: (i) the spontaneous formation of borophene nanoribbons (BNRs) oriented in the $[-110]$ direction, and (ii) the identification of four periodic structures on the surfaces comprising boron chains interspersed with rows of hexagonal voids. STM and DFT calculations have shown that these structures consist of linear motifs with varying widths, corresponding to the β , β_8 , β_{12} and χ_3 phases [140]. Additionally, Xiaolong Liu and colleagues reported the first experimental demonstration of lateral interfaces between borophene and PTCDA³³ on Ag(111) surface [141].

³³Perylene-3,4,9,10-tetracarboxylic dianhydride.

Year 2018 – another phase – graphene-like honeycomb (δ_3) borophene – on an Al(111) surface using MBE was fabricated by Wenbin Li and colleagues. STM imaging revealed a perfect monolayer with a honeycomb lattice, stabilized by substantial charge transfer – nearly one electron per boron atom – from the Al(111) substrate. Theoretical calculations further confirmed the structure’s stability, highlighting its potential to control borophene’s electronic properties, such as Dirac states and superconductivity, through substrate-induced charge transfer [142]. Also, Xiaolong Liu and colleagues examined atomic-scale line imperfections in borophene using UHV–STM/STS and DFT. Under specific growth conditions, borophene phases (corresponding to the $\eta = \frac{1}{6}$ and $\eta = \frac{1}{5}$ phases) intermixed, with line defects adopting structures that aligned well with the neighboring phase’s constituent units. Due to anisotropy, these line defects favored periodic self-assembly, generation of novel borophene phases, merging crystal and defect boundaries, with low-temperature data showing CDW-like electronic behavior influenced by line defects, offering prospects for future borophene uses [143].

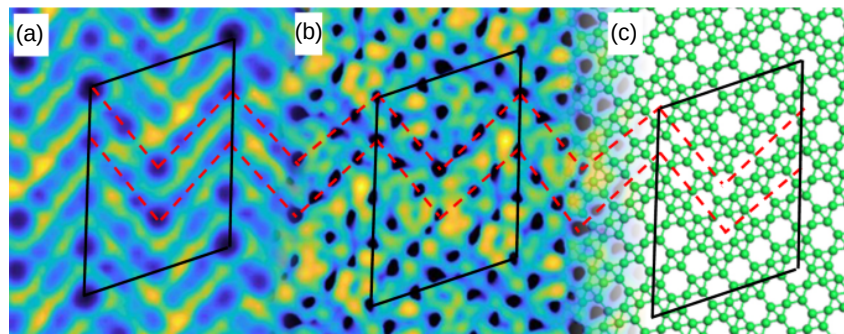


Figure 1.17: (a) High-resolution STM data showing the borophene unit cell and zig-zag pattern. (b) DFT-calculated isosurface of borophene, with (c) its visual representation, showing atomic positions and bonding [144].

Year 2019 – the first larger (above nanometer scale), *device-scale* borophene islands with related but modified structures were synthesized on Cu(111) substrate (see Figure 1.17), also via MBE [144]. By using Cu(111) substrates at 770 K, which are less inert than Ag but not reactive enough to form metal-borides, the researchers achieved the nucleation and growth of large-area ($100 \mu\text{m}^2$) monolayer borophene. Using LEEM, the team monitored real-time dynamics of borophene nucleation and growth, while LEED, STM, and DFT revealed a charge-transfer-stabilized $\eta = \frac{1}{5}$ phase on Cu(111) with minimal covalent bonding, as shown in Figure 1.17(c). The study also demonstrates that the growth of atomically thin borophene sheets is self-limiting on different substrates and shows how substrate choice significantly impacts growth dynamics, adhesion, and film properties, which is crucial for fabricating large domains and heterostructures.

Beyond achieving large-scale growth, Nikolay A. Vinogradov and colleagues synthesized a defect-free, metallic χ_6 borophene phase on Ir(111) via boron deposition and annealing in UHV (see Figure 1.18), achieving *decoupling* from substrate through Au intercalation without altering borophene's structure. LEED, STM, and DFT confirmed minimal charge transfer (hole doping of ~ 0.08 electrons per B atom) compared to electron-doped borophene on Cu(111), with stable adjacent sites offering catalytic potential and ordered adsorption for applications in catalysis, sensing, and nanotechnology [145]. Additionally, Brian Kiraly and colleagues

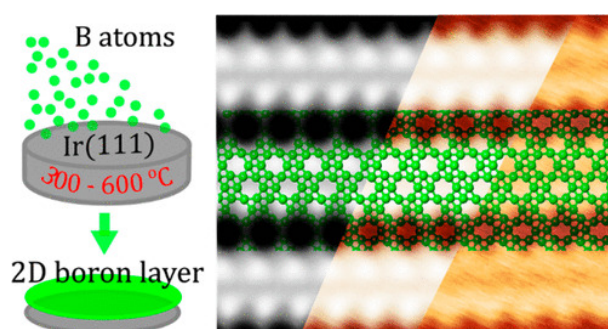


Figure 1.18: Schematic of boron deposition on Ir(111) with DFT-calculated tunneling current isosurface for the χ_6 borophene configuration [145].

synthesized metallic $\eta = \frac{1}{12}$ borophene on Au(111) in UHV, revealing that at low temperatures, boron forms clusters on the surface. At ~ 823 K, boron diffuses onto the Au bulk and reemerges as 2D borophene upon cooling, a process confirmed by energy path calculations and XPS. Higher boron doses are needed for production of nanoscale borophene islands on Au(111) compared with Ag(111) substrate [146]. Furthermore, Xiaolong Liu and colleagues demonstrated the integration of borophene into 2D heterostructures with graphene on Ag(111) using UHV deposition. Despite lattice and symmetry mismatches, carbon and boron sequentially deposited create nearly atomically sharp lateral and rotationally commensurate vertical heterointerfaces, as revealed by STM/STS. Carbon monoxide (CO) functionalized STM tips show atomically resolved covalent boron-carbon bonds at the borophene-graphene junctions [147].

Year 2020 – beyond the previously emphasized factors of lattice compatibility and charge transfer, the *alignment of boron chains with respect to the substrate* plays a crucial role in determining phase formation. Yu Wang and colleagues successfully synthesized borophene on an Ag(100) surface via MBE, identifying three distinct phases (two of them exhibited long-range order with varying proportions of boron chains) with different and interesting “*nature*” confirmed by STM in combination with DFT calculations. Two types of borophene islands were observed on Ag(100): type I, with chains along the [110] direction with two sub-phases (*A* and *B*) with

distinct chain arrangements, and type II (sub-phase C), where chains are rotated by 74° . Minimal charge transfer indicated weak interaction with the Ag surface, and the A and B sub-phases resembled the freestanding β_{12} phase, suggesting that their mixed-chain structure on Ag(100) retains predicted intrinsic properties – with less strain – of bare phases [148]. Furthermore, Zenghui Wu reported a novel phase of boron sheets, quasicubic c -B₄₈, synthesized on Ni foil using CVD in a mixed H₂ and Ar environment [149].

Year 2021 – marked a series of groundbreaking studies in the borophene field, like reducing the oxidation by hydrogenation or fabrication of bilayer configurations. However, let us start with a pivotal study that revisited the reported δ_3 phase on Al(111) [142], finding that it reconstructs the top metal layer into a stoichiometric AlB₂ sheet, thus supporting its classification as a 2D boride rather than borophene [150]. Additionally, by using tip-enhanced Raman spectroscopy (TERS)³⁴ with its sub-nanoscale spatial resolution the first experimental realization of a vertical tetraphenyldibenzoperiflanthene(DBP)/borophene heterostructure by self-assembling under UHV conditions was reported [151]. Using UHV-TERS and DFT, they identified strain in borophene induced by DBP molecules, compressing and slightly undulating the lattice, with STM manipulation demonstrating reversible strain control – a novel approach for tuning 2D material properties. Building on borazine-based (B₃N₃H₆) h -BN synthesis, Marc G. Cuxart and colleagues utilized diborane (B₂H₆) from commercial borazine as a precursor to achieve high-quality, large-area borophene layers via CVD on Cu(111) and Ir(111), enabling even stable borophene/ h -BN heterostructures that resist oxidation at room temperature [152]. In parallel, a separate team employed CVD on heated Ir(111), using high-temperature borazine dosing (at 1373 K) to yield a nitrogen-free, boron-rich surface, forming large-scale χ_6 -polymorph through segregation-enhanced epitaxy, with LEED and STM/STS confirming Dirac-like electronic properties – addressing thereby the prior limitations in borophene synthesis for device applications [153]. Yet, another two major breakthroughs in the field of borophene have significantly advanced its potential applications: (i) the first successful fabrication of **hydrogenated** borophene (*borophane*) [154] and the creation of the first **bilayer** configurations, specifically on Ag(111) [155] and Ru(0001) substrates [156]. Chemical functionalization enables tunable electronic properties in 2D materials, beyond mere passivation, exemplified by hydrogenated borophene (*borophane*), synthesized via UHV hydrogen exposure. This process produced eight *borophane*

³⁴It combines the chemical specificity of plasmon-enhanced Raman spectroscopy with the spatial resolution of a scanning probe microscope, providing simultaneous chemical and topographic information. Under UHV conditions, TERS can reveal subnanoscale chemical details, making it an ideal tool for characterizing highly localized structural and chemical properties in low-dimensional materials and heterostructures, including strain, defects, and doping.

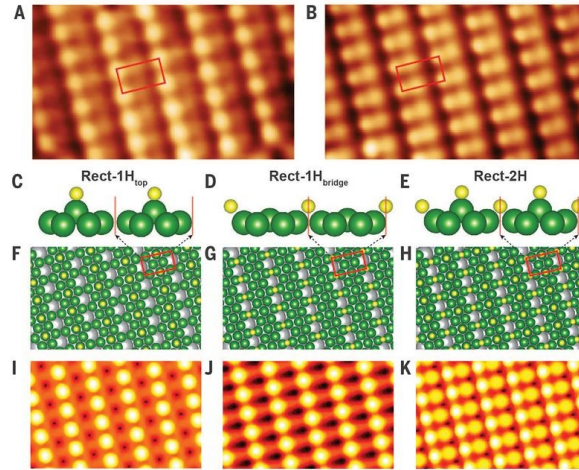


Figure 1.19: (A, B) CO-functionalized STM maps of $rect-(\eta = \frac{1}{6})-30^\circ$ hydrogenated borophene with a 0.50×0.30 nm unit cell (highlighted in red) at varying bias voltages. Side (C, D, E) and top views (F, G, H) for the $rect-H_{top}$ structure (H atom at the top site), the $rect-H_{bridge}$ (H atom at the “bridge” site), and $rect-2H$ with two H atoms at both sites, respectively. (I, J, K) Simulated STM images within 100 meV above the Fermi level for each configuration [154].

polymorphs, with the $rect-(\eta = \frac{1}{6})-30^\circ$ structure noted for its well-ordered high hydrogen coverage and stability (see Figure 1.19). STM and DFT identified three stable hydrogen adsorption configurations: $rect-1H_{top}$ (forming B–H bond), $rect-1H_{bridge}$ (forming B–H–B – “banana” like – bonds), and $rect-2H$. Covalent B–H bond lengths, akin to those in borane, confirmed stability against oxidation by XPS for over a week, with reversibility back to bare borophene upon annealing at 573 K, highlighting *borophane’s* potential for reconfigurable applications [154]. Although bilayer borophene was first synthesized as small (<50 nm) domains on Ag(111) in 2021, the results were published later, in 2022 [155]. Nevertheless, Peter & Eli Sutter demonstrated layer-by-layer growth on Ru(0001), like in their work with graphene, reaching configuration of two monolayers in thickness via boron segregation [156]. Utilizing Ru’s high boron solubility, boron was stored at high temperatures and released upon cooling. LEEM and LEED confirmed that both the monolayer and bilayer (BL) borophene are highly crystalline, forming well-ordered superlattice structures on the metal substrate but with unknown structure.

Year 2022 – marked significant advancements in the synthesis of large-scale bilayer borophene and the understanding of oxidation process in borophene. Let us start with the synthesis of nanometer-scale BL borophene on Ag(111) via MBE under UHV conditions by Xiaolong Liu and colleagues, utilizing large, atomically flat Ag terraces to facilitate random monolayer nucleation [155]. By extending deposition from 623 to 723 K, they achieved a well-ordered BL structure with a lattice constant of 5.7 ± 0.2 Å, indicative of bilayer formation. CO-functionalized STM pro-

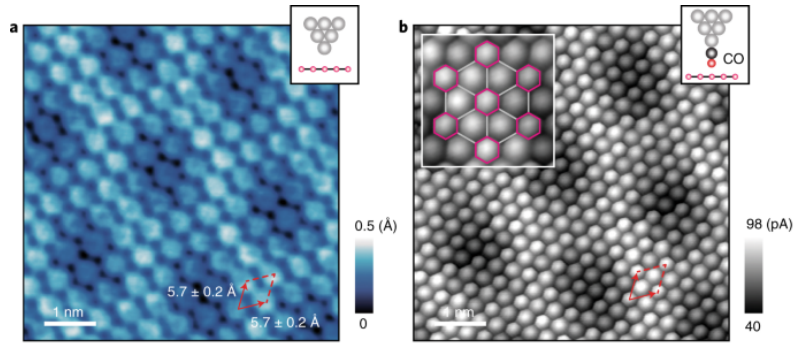


Figure 1.20: (a) STM image of bilayer borophene obtained using a bare PtIr tip, with lattice directions indicated by red arrows. (b) STM scan, with CO tip, of the same region demonstrating significantly enhanced spatial resolution. The inset provides a magnified view, revealing a distorted honeycomb lattice overlay [155].

vided high-resolution images, as depicted in Figure 1.20(b), that revealed covalent bonding within the BL- α phase, corroborated by matching experimental STM (or AFM) and DFT-simulated data. Notably, BL borophene retains the metallic properties of monolayer borophene while demonstrating enhanced crystallinity and electronic performance. However, Caiyun Chen and colleagues synthesized uniform, **millimeter-scale BL** borophene on Cu(111) via MBE [157]. After forming a monolayer, further boron deposition revealed a new ordered phase, confirmed as BL through STM imaging, which showed consistent height across all bias voltages. Annealing at approximately 750 K produced large, uniform BL domains with continuity across the substrate steps. STM analysis identified two mirror-symmetric BL domains composed of parallel chains with alternating bright and dark ellipsoidal protrusions, exhibiting a nearest-neighbor distance of about 5 Å. A stable structural model, based on first-principles calculations and STM data, consisted of two flat β_{12} boron sheets with periodic zig-zag modulation, closely matching experimental lattice parameters ($a = 16.2$ Å, $b = 33$ Å, $\Theta = 69.2^\circ$)³⁵ and showing less than 0.3% lattice mismatch relative to Cu(111) (see Figure 1.21). The temperature range for its formation (600–750 K) is narrower than that for monolayer (600–850 K). Energy calculations indicated that BL borophene is more thermodynamically stable than monolayer borophene, with Bader charge analysis showing significant charge redistribution around interlayer-bonded boron atoms. XPS characterization showed that bilayer borophene has enhanced chemical stability, with only 23% of boron oxidized after air exposure, compared to complete oxidation of monolayer borophene. Furthermore, the Cu(111) substrate not only facilitated the formation of BL borophene but also indicates its potential for *decoupling process* in future studies, and

³⁵ $a = 16.1$ Å, $b = 34.2$ Å and $\Theta = 69^\circ$.

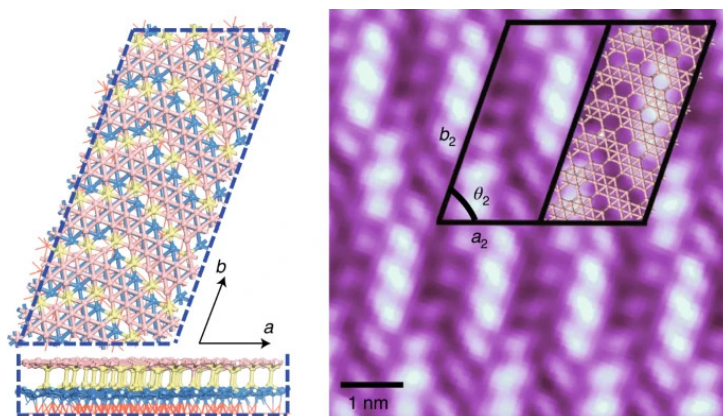


Figure 1.21: Simulated atomic configuration of bilayer borophene, shown from top (above) and side perspectives together with its high-resolution STM image with mirror symmetric orientations on the Cu(111) substrate [157].

BL is anticipated to exhibit enhanced flexibility and greater resistance to strain compared to its monolayer counterpart. Overall, BL borophene demonstrates enhanced stability and resistance to oxidation, positioning it as a strong candidate for potential device use. Additionally, the Cu(100) substrate serves as an ideal platform to investigate the influence of substrate *symmetry* on borophene's structure and properties, addressing the challenge of balancing the substrate-borophene interaction. To tackle this, Rongting Wu and colleagues utilized MBE combined with real-time monitoring via LEEM and LEED to synthesize extensive, monocrystalline borophenes on Cu(100). Micro-LEED and dark-field LEEM revealed four rotational domains, while high-resolution CO-STM tips, supported by DFT calculations, identified a new borophene phase with a small rectangular unit cell ($5 \times 6 \text{ \AA}$) comprising ten boron atoms and two HFs (see Figure 1.22). This phase, labeled as β_{13} , is self-limiting, preventing the formation of a second layer even at temperatures of 753–873 K. DFT simulations suggest that β_{13} is the most stable freestanding structure, with an optimized unit cell size of $5.04 \times 5.82 \text{ \AA}$. Notably, β_{13} phase on Cu(100) exhibits a flatter geometry and experiences anisotropic tension (averaging 5%), alongside a lower electron doping of 0.21 e/B mainly from copper 4s orbitals, indicating a weaker B-Cu interaction than on Cu(111). This characteristic enhances the material's suitability for exfoliation and transfer in device applications [158]. On top of that, a significant progress was made that year in understanding borophene's **oxidation** mechanism, which is a key factor for stabilizing it in ambient conditions. Xiaolong Liu and colleagues investigated borophene's reactivity with air and molecular oxygen under UHV using STM/STS, XPS, and DFT calculations, finding that while borophene degrades rapidly in air, it oxidizes more predictably under molecular oxygen in UHV [159]. Oxidation primarily affects the edges rather than the basal plane, where oxygen

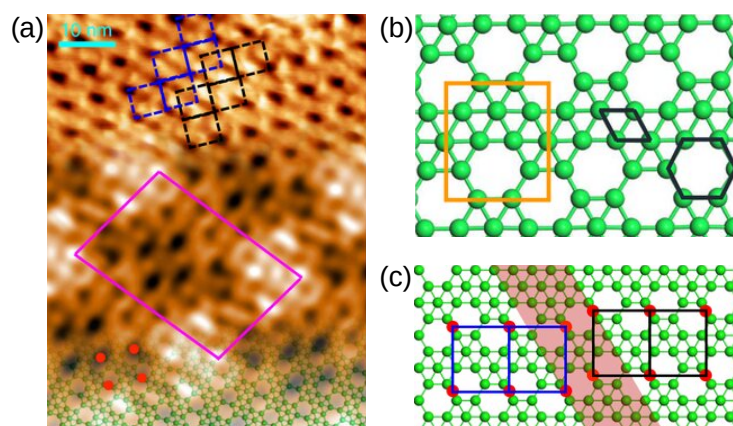


Figure 1.22: The atomic configuration of β_{13} borophene derived from (a) STM data and (b,c) DFT simulations. Adapted from [158].

adsorption forms atomically ordered structures. They found that specific edge orientations, such as zig-zag edges of the $\text{rect}(\eta = \frac{1}{6})\text{-}30^\circ$, are more resistant to oxidation. Additionally, both experimental and DFT findings indicate that molecular oxygen adsorbed on the surface breaks apart at room temperature, with atomic oxygen diffusing across the surface and chemisorbing on basal and edge sites, resulting in irreversible oxidation up to 773 K. These findings suggest that covalent hydrogenation or noncovalent molecular layers may block oxidation, especially on specific edges. Another complementary UHV-TERS study revealed a spatial resolution of $\sim 4.8 \text{ \AA}$ with single B–O bond sensitivity, showing that atomic oxygen selectively adsorbs at “bridge” sites, forming stable B–O–B bonds that can be thermally reversed at 633 K [160]. In contrast, molecular oxygen spontaneously dissociates, highlighting borophene’s edge reactivity and phase-dependent oxidation patterns: the $\eta = \frac{1}{6}$ phase forms stronger bonding between B and O than the $\eta = \frac{1}{5}$, which favors weaker B–O–B ring epoxide configurations. This findings are also in line with previous studies on hydrogenated borophene and bilayer borophenes which have demonstrated increased stability against oxidation stemming from active-site shielding through hydrogen-mediated bonding or electron redistribution via interlayer boron connections, respectively. These insights enhance our understanding of borophene’s reactivity and establish UHV-TERS as an essential technique for atomic-level surface chemistry with implications for catalysis, molecular engineering, and low-dimensional materials.

Year 2023 – Hao Li and colleagues investigated B-rich transformations on Cu(111) under gradual UHV post-annealing [161]. Their study revealed a transformation sequence from amorphous B-clusters to striped-phase borophene, ultimately leading to the more stable β -class borophene as the annealing temperature increased. The [110] Cu(111) step edges, with voids,

defects, and Cu islands, serve as nucleation sites for striped-phase borophene, which transitions into β -type borophene due to enhanced buckling and electron transfer from the substrate. These insights provide a path for controlled borophene synthesis on Cu(111) and suggest a strategy for using substrates with 1D defects to tune borophene properties. Further, selective boron cluster formation was achieved by evaporating boron onto Cu(111) pre-covered with monolayer borophene [162]. DFT calculations reveal that the periodic B₅ clusters on borophene arise from in-plane charge distribution and electron delocalization, with dense B₅ clustering predicted to spontaneously transform into bilayer borophene, suggesting a *domino-like* mechanism for bilayer growth. Also, in a pioneering approach combining CVD and UHV annealing, Matteo Jugovac and colleagues synthesized graphene/borophene vertical heterostructures with atomically sharp interfaces and high chemical purity [163]. LEED data supported XPS and LEEM findings, confirming commensurate borophene χ_6 islands at the graphene/Ir interface. This heterostructure exhibits enhanced stability, oxidation resistance, and retained metallicity of borophene, with distinct graphene Dirac cones and a parabolic borophene band crossing the Fermi level, boosting electronic DOS [163]. Lastly, Karim M. Omambac and colleagues examined the selective CVD deposition of *h*-BN and borophene on Ir(111) from a borazine precursor, addressing challenges in bi-elemental 2D material synthesis [164]. They found that low temperatures led to dense nucleation of *h*-BN, while higher temperatures favored nitrogen desorption and boron dissolution, promoting borophene growth. By tuning temperature and pressure, high-quality *h*-BN, borophene, or even both materials could be selectively grown, offering an optimized CVD approach for these 2D materials.

Year 2024 – recent advances have enabled significant progress in controlled nanoscale synthesis of BNRs. Qiucheng Li and colleagues fabricated BNR polymorphs with precise edge configurations on Ag(977) terraces, revealing unique quantum-confined states [165]. Similarly, Xiao-Ji Weng and colleagues characterized Cu–B₈ metalloborophene nanoribbons formed on Cu(110) [166], and Haochen Wang and colleagues achieved sub-2 nm BNRs [167].

1.2.2.2 Transfer of borophene and growth techniques on non-metallic substrates

Metallic substrates create short current paths, reducing thereby accuracy of borophene transport measurements. Additionally, interaction with substrates, presence of surface defects, and state hybridization distort borophene's intrinsic electronic properties, limiting its potential in nanoscale devices. Decoupling borophene from the substrate is essential to accurately characterize its

electronic structure and to advance its use in electronics. First significant step towards this goal – as previously mentioned – was done by intercalating gold at the borophene/Ir(111) interface at room temperature [145]. Gold’s low reactivity allowed it to be deposited without disrupting borophene’s structure, as STM images showed the material’s striped pattern remained intact. Gold atoms migrated along borophene’s stripes, with intercalation process occurring especially near edges and lattice defects, preserving its symmetry and structural integrity. This suggests that borophene can maintain its structure independently from the Ir substrate, though producing uniform, high-quality layers for transfer was still a challenge.

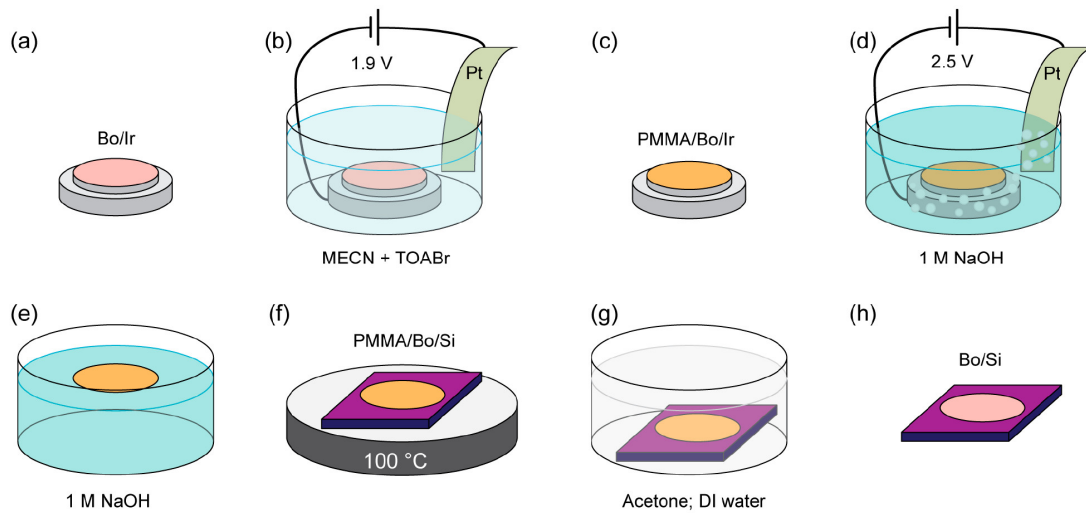


Figure 1.23: Steps involved in transferring borophene: (a) borophene deposited on Ir, (b) after which together with Pt foil is immersed in a MECN and TOABr solution for the first electrochemical step. (c) The borophene is then supported by PMMA on Ir, and (d) in the second electrochemical step placed in a NaOH solution, so that (e) the PMMA/borophene is separated from the Ir substrate. (f) PMMA/borophene/Si is then heated, and (g) PMMA is removed using acetone and DI water, resulting in (h) clean borophene on Si [168].

It was not until 2021 that Borna Radatović and colleagues successfully transferred macroscopic, single-layer χ_6 borophene from Ir(111) to a SiO_2 -coated Si wafer (but other solid substrates are equally viable) using an *electrochemical bubbling technique* [168]. This method generates hydrogen bubbles that gently lift borophene from the Ir substrate for transfer process. First, borophene on Ir is immersed in a solution of methylcyanide (MECN) and tetra-*n*-octylammoniumbromide (TOABr) ions that weaken the borophene-Ir bond by intercalation of TOA^+ ions at voltage of 1.9 V. A PMMA layer is applied as support film, and in a NaOH solution, a voltage of 2.5 V creates bubbles to separate the PMMA/borophene from Ir substrate. The PMMA/borophene layer is then carefully rinsed with deionized water and transferred onto the silicon wafer. After heating the sample at 373 K to minimize wrinkles and remove residual

chemicals, the PMMA is dissolved in acetone, leaving behind a clean borophene layer on the Si wafer. The entire transfer process is illustrated in detail through sequential steps in Figure 1.23. Further, microscopy showed a largely uniform borophene layer with minor defects like quasi-1D lines and folds, mainly coming from the original Ir substrate. Raman spectroscopy confirmed borophene's structural integrity on the new substrate, with minor peak shifts due to substrate effects. DFT calculations aligned well with Raman results, suggesting that substrate interactions slightly modify borophene's vibrational properties.

Based on previous results, a logical question arises: “*Is it possible to synthesize borophene directly on another non-metallic substrate?*”

Borophene growth has been observed on various functional substrates which is crucial for its potential applications in advanced electronic devices, including optoelectronics and integrated circuits. Utilizing vdW epitaxy, borophene can be synthesized on these substrates after partial hydrogenation, particularly on fluorophlogopite mica (F-mica) in a hydrogen-rich environment through CVD at 923 K [169]. Characterization techniques such as SEM, AFM, and TEM confirmed that the borophene is uniform, with a thickness of about 1.7 nm and a crystal structure consistent with the predicted α' -2H-borophene. After growth, the wet transfer of borophene – using PMMA to silicon substrates – is executed, and XPS analysis further confirms the absence of post-transfer sodium contaminants. Applying the same method, the α' -2H-borophene (“borophene glass”) was fabricated on quartz (SiO_2) with the thickness of 3.4 nm and was further used to create novel borophene hydroelectric generator [170].

1.2.2.3 *Top-down approaches*

Previous *bottom-up* borophene synthesis methods face major limitations: they require ultra-high vacuum, high temperatures, specific substrates, yield low quantities, and possess limiting scalability. Further *transfer steps* additionally degrade borophene's structure. Developing efficient, scalable production of high-quality mono- and few-layer borophene remains challenging. Advanced versions of *top-down* methods – mechanical and liquid-phase exfoliation – offer promising alternatives.

Year 2018 – Hongling Li and colleagues developed a scalable sonication-assisted LPE method to produce high-purity, few-layer borophenes from boron powder, demonstrating excellent solubility in DMF³⁶ and IPA³⁷ [171]. Different solvents and centrifugation rates were

³⁶Dimethylformamide.

³⁷Isopropyl alcohol.

used to control the size and thickness of the exfoliated sheets, as shown in Figure 1.24. AFM,

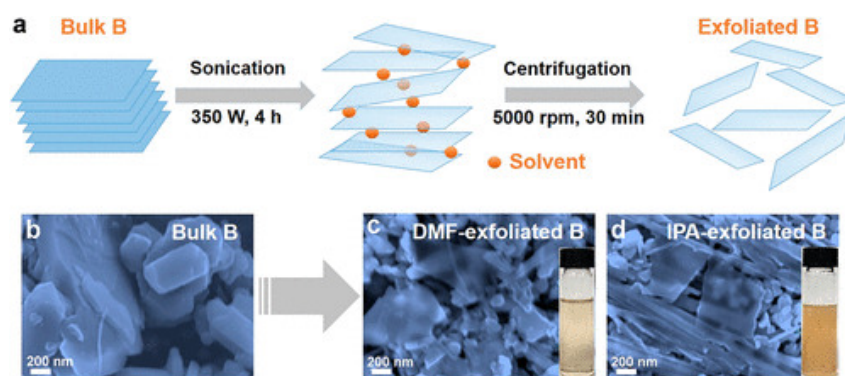


Figure 1.24: (a) Diagram of the sonication-driven LPE method, with (b) SEM images of bulk boron powder and (c) exfoliated boron sheets in DMF (d) and IPA[171].

high-resolution TEM, XRD, and XPS analyses confirmed that the DMF-exfoliated borophene exhibited a crystal structure related to the [104] orientation of the bare B- β -rhombohedral crystal. The DMF-exfoliated sheets were thinner (~ 1.8 nm, ~ 4 layers) and had larger lateral dimensions, while the IPA-exfoliated sheets were thicker (~ 4.7 nm, ~ 11 layers) and showed lattice spacings corresponding to the [015] and [202] planes of β -rhombohedral boron. The borophene sheets remained stable and intact for over 50 days and were successfully applied in fabricating high-performance supercapacitor electrodes. Further, Xiaoyuan Ji and colleagues developed a scalable *top-down* approach combining LPE and thermal oxidation etching to produce high-quality, ultrathin 2D boron nanosheets [172]. Oxidation forms B₂O₃ in thicker layers, which dissolves in a second exfoliation step. Using the mixture of NMP³⁸ and ethanol, the bulk boron could be exfoliated in dispersed sheets with reduced lateral size (~ 250 nm) and thickness (~ 20 nm). TEM, AFM, and XPS confirmed its [104] plane of β -rhombohedral crystal structure. After modification with positively charged amine functionalized polyethylene glycol (PEG-NH₂) the 2D boron nanosheets demonstrated high photothermal conversion effectiveness (42.5%) and potential as therapeutic and imaging agents for cancer.

Year 2019 – Pranay Ranjan and colleagues achieved a scalable synthesis of freestanding borophene sheets (up to 1.2 μm lateral size and 2-18 nm thick) via sonochemical LPE [173]. Acetone was particularly effective, producing high-quality monolayers confirmed by TEM, AFM, and Raman spectroscopy (see Figure 1.25). They also synthesized borophene oxide using modified Hummer’s method and successfully reduced it to borophene, challenging the longstanding belief that borophene requires a substrate, by demonstrating freestanding β_{12} and

³⁸N-methyl-2-pyrrolidone.

χ_3 phases and an intermediate phase production. XPS and thermogravimetric (TGA) analyses confirmed minimal oxidation and ambient stability up to 673 K. SAED showed phase diversity, and they explored borophene's applications in sensing and creation of hybrids with boron nitride and MoS_2 , expanding its potential for electronics and energy storage.

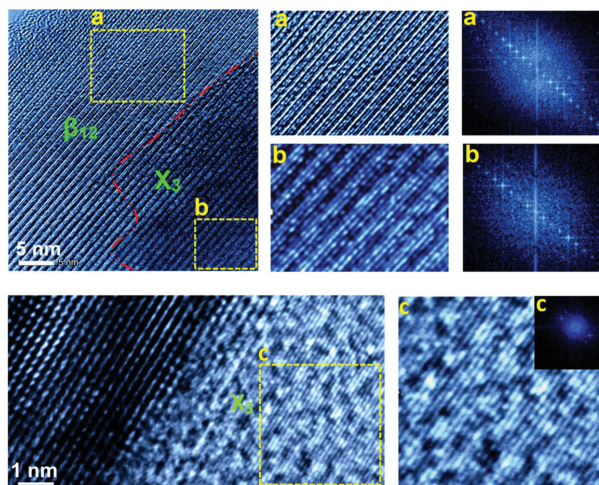


Figure 1.25: High-resolution TEM images of (a) β_{12} , (b) intermediate, and (c) χ_3 borophene phase [173].

Year 2020 – Feng Zhang and colleagues developed a novel acetone solvothermal-assisted LPE technique to synthesize borophene with few layers and large flake sizes. This method combines ball milling, solvothermal swelling, and ultrasonic delamination. The choice of solvent significantly affects exfoliation efficiency, with lower surface tension solvents enhancing the process. Using acetone, they produced four-layer boron sheets with a lateral dimension of $5.05 \mu\text{m}$, surpassing the previously reported maximum of $1.2 \mu\text{m}$. This study highlights the effectiveness of the acetone solvothermal-assisted LPE method in generating high-quality borophene with larger flake sizes [174].

Year 2021 – recent advances using sonochemical and modified Hummer's methods have successfully dispelled the myth that borophene could not be exfoliated but LPE often introduces defects. This poses a challenge: *while UHV methods are costly and substrate-grown borophene alters its electronic properties, LPE borophene may carry solvent-induced surface functionalities. For practical applications, large high-quality, defect-free borophene crystals are essential.* Sumit Chahal and colleagues achieved the first micromechanical exfoliation of borophene, using double-sided tape, from boron crystals, transferring it to thermally oxidized Si/SiO₂ and indium tin oxide (ITO) substrates (see Figure 1.26) [175]. The exfoliated sheets displayed both signatures from the parent crystal and new XRD peaks that indicated structural changes. As interlayer coupling in boron sheets weakens during exfoliation, they tend to adopt configurations that minimize

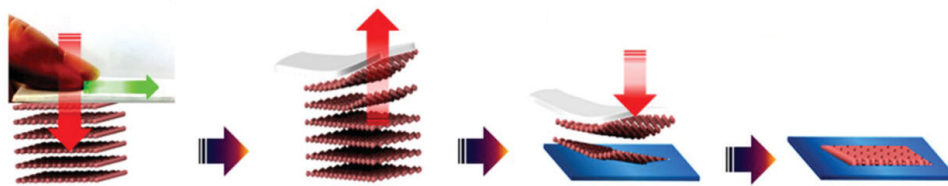


Figure 1.26: Schematic illustration of micromechanical exfoliation process by applying normal and shear forces with double-sided foam tape to peel layers from a boron crystal, transferring them to a SiO₂ substrate, with the bottom layer being adhered to the substrate [175].

energy, so that the final configuration depends on the interaction with substrate. The new peaks became more pronounced with further exfoliation, suggesting layer reorganization into stable structures. Techniques like SEM, AFM, TEM, Raman spectroscopy, and XPS confirmed the crystal structure of the β_{12} phase, with some χ_3 phase presence. Raman peaks for thinner sheets matched those of the β_{12} phase, with exfoliation energies exceeding those of graphene and boron nitride. Intentional oxidation revealed borophene oxide as a semiconductor, while pristine borophene remained metallic. However, compared to the millimeter-scale lateral dimensions reported in Ref. [168], the micrometer-scale lateral dimensions achieved in this study highlight the need for further progress. Furthermore, by using low-temperature LPE, optimized sonication and NMP as the solvent Haojian Lin and colleagues produced freestanding few-layer borophene sheets with high yield (up to 20%) and improved crystallinity [176]. This low-temperature method enhanced exfoliation by increasing bond anisotropy, yielding freestanding uniform sheets (2–5 μm wide, 1.32–2.32 nm thick). XRD and Raman spectroscopy confirmed the presence of β_{12} -borophene with minimal oxidation, while XPS showed over 98% pure boron content. The sheets demonstrated stability for 60 days, and the LTLPE method offers a scalable, efficient route for producing metallic borophene suitable for applications such as Li–S batteries.

Year 2022 – another study examined how electrolyte type, current, and metal mesh (Ni vs. Cu) affect borophene electrochemical exfoliation (see Figure 1.27), particularly flake thickness and size [177]. Using 1 M LiCl in dimethyl sulfoxide (DMSO) at 1 A, Li⁺ ions intercalated more effectively, producing 5–15 layer sheets (1.32–2.32 nm thick). In contrast, Na₂SO₄ in deionized water yielded thinner flakes (0.4–0.9 nm), especially with Cu mesh. Flake sizes ranged from 0.6 to 2.5 μm . TEM showed that Cu mesh favored β -rhombohedral structures, while Ni produced β_{12} and χ_3 phases. Lowering the current, to 0.1 A, improved flake uniformity, with Cu mesh outperforming Ni due to its conductivity. Zeta potential analysis highlighted Li⁺'s superior exfoliation efficiency, offering insights into borophene formation mechanisms. A novel

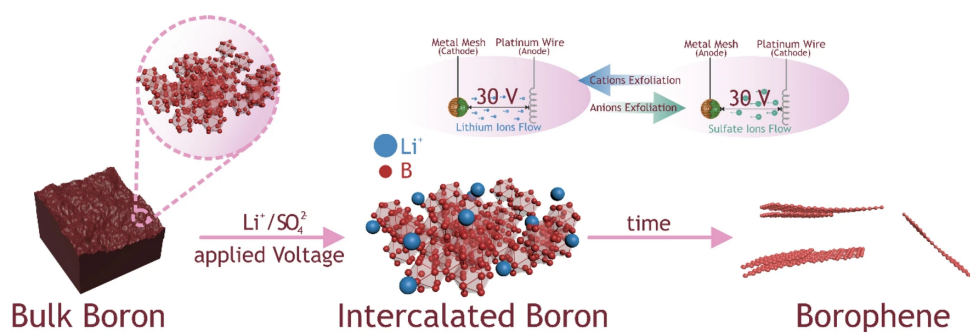


Figure 1.27: Suggested process for exfoliating bulk boron into thin borophene sheets [177].

method inspired by graphene electrochemical exfoliation achieved borophene synthesis using boron as a heated cathode [178]. While boron's low conductivity typically hinders exfoliation at room temperature, this technique utilized a hollow boron rod with an embedded heating coil to overcome this limitation. The heated boron cathode and platinum anode in an electrolyte solution enabled borophene exfoliation, with flakes collected through vacuum filtration, then sonicated in acetone and centrifuged to yield few-layer sheets. This scalable, vacuum-free approach, effective at 873–1273 K, showed promising borophene production, confirmed by Raman spectroscopy, though further refinement is needed for optimal temperature and electrolyte control.

1.2.3 Tunable properties and potential application of borophene

While significant progress has been made in developing synthesis methods for borophene in recent years, its promising properties – such as metallic conductivity, potential superconductivity, and unique optical characteristics – are largely theoretical, with only a few confirmed through experimental study. Continued research is crucial to unlock its full potential in areas such as catalysis, energy storage or superconducting devices. As borophene research advances, it stands poised to become a key player in the next generation of 2D materials, building on the foundations laid by its well-studied counterpart, graphene, with properties that even surpass it.

1.2.3.1 Brief overview

Chemical properties – as previously mentioned, borophene's key chemical property is its high reactivity and therefore relative oxidation resistance, being better than bulk boron phases but still less stable than graphene. Encapsulation with Si/SiO₂, *h*-BN, or graphene, along with reversible hydrogen passivation – and bilayer structures – significantly enhances borophene's air stability. Also, borophenes on metal surfaces can effectively act as catalysts for hydrogen evolution reactions [136]. Advancements in borophene research hold great potential for transforming energy

storage and reducing dependence on fossil fuels, particularly in hydrogen storage applications. Optimizing borophene's hydrogen storage relies on interactions like chemisorption, physisorption, and Kubas-type bonding. The current emphasis on theoretical models underscores the need for experimental validation to enhance the understanding of its hydrogen-binding capabilities [179]. Also, borophene has emerged as a leading candidate for next-generation supercapacitors, outperforming graphene in key electrochemical properties, including a stable voltage window of up to 3.0 V, fast charge/discharge rates, and a high specific capacitance of $147.6 \cdot \text{g}^{-1}$. It retains 88.7% of its capacitance after 6000 cycles and achieves high energy and power density, emphasizing its capability to enhance energy storage technologies [171, 180].

Mechanical properties – borophene showcases remarkable mechanical properties that make it a formidable alternative to graphene and other 2D materials due to a combination of conventional covalent bonds and metallic-like multicenter bonds. These bonds provide both significant strength and flexibility, positioning borophene as a strong competitor to graphene. For instance, the in-plane stiffness of borophene's β_{12} phase reaches 218 N/m along the HHs rows and 205 N/m across, compared to graphene's 342 N/m. When no HHs are present (δ_6 phase) borophene shows strong anisotropy, with in-plane stiffness measuring 398 N/m along the ridges, and only 163 N/m in the orthogonal direction, with a breaking strain at 8% when applied along the ridges. Where borophene truly stands out is in its off-plane flexibility, with a bending modulus of 0.39 eV along row of HHs – approximately one-fourth of graphene's – and 0.56 eV across them. This combination of stiffness and flexibility gives borophene potential for use in advanced composites. In terms of strength, the β_{12} phase exhibits ideal strengths of $\sim 15 \text{ N/m}^{39}$ in both directions, comparable to MoS_2 and higher than materials like phosphorene and silicene. Although its critical strain (10-21%)⁴⁰ is lower than graphene's ($\sim 25\%$), borophene resists structural breaking by being prone to undergo a structural phase transition under high strain. This allows the material to reorganize its pattern, increase HH concentration, and relieve tension, preventing structural damage and making borophene more resilient under extreme conditions. In conclusion, while graphene is stronger, borophene's flexibility, high strength-to-weight ratio, and tunability make it ideal for flexible electronics and advanced composites [128, 180, 181].

Electronic properties – as previously mentioned the boron's electron deficiency, compared to carbon, leads to a more complex range of allotropes with diverse and superior physical properties, including superconductivity and topological features. Unlike carbon's stable honey-

³⁹Graphene exhibit ideal strengt of 34 N/m.

⁴⁰Uniaxial or biaxial strain depending of the borophene phase under consideration.

comb structure, boron's bonding involves both two-center and three-center bonds, resulting in a completely different structural landscape. Furthermore, borophene possesses unique electronic features, such as the presence of Dirac fermions and tunable bandgap, making it an attractive material for nano- and opto-electronics, as its band structure can display metallic, semimetallic but in some cases also semiconducting behaviors with potential for creating transistors and diodes [139, 149, 182]. Theoretical predictions indicated that β_{12} and χ_3 borophenes exhibit metallic properties which was later supported by ARPES measurements [183]. Experimental investigations have indicated Dirac-like electronic characteristics for the χ_6 borophene through STS analysis [153], while DFT calculations suggest that the β_{13} configuration has the potential to support type-II Dirac and Weyl fermions [158]. Finally, ARPES measurements confirmed the presence of Dirac cones in the β_{12} and χ_3 borophene sheet on an Ag(111) substrate [184, 185] providing therefore compelling proof that this elemental 2D material is possessing massless Dirac fermions. By introducing periodic perturbations one can further split these Dirac cones as depicted in Figure 1.28. Furthermore, the described Dirac fermions play a significant role in the remarkable charge carrier mobility and elevated thermal conductivity exhibited by borophene. Also, it is predicted that fully hydrogenated borophene exhibits twisted Dirac cones with high Fermi velocity of 3.5×10^6 m/s – four times higher than graphene – primarily due to the in-plane σ orbitals of boron atoms, resulting in direction-dependent Dirac cones [186].

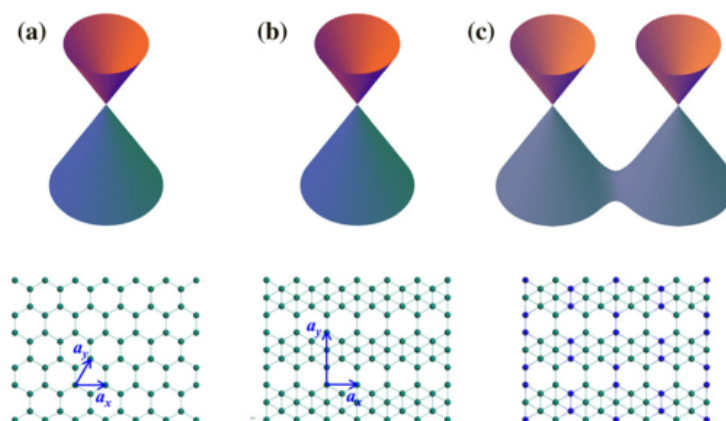


Figure 1.28: Schematic representations of Dirac cones and lattice structures are shown for various configurations: (a) the honeycomb lattice, (b) the unperturbed, and (c) perturbed β_{12} sheet [184].

Thermal properties – first-principles calculations combined with phonon Boltzmann transport equation indicated that isotropic α' borophene has a room-temperature lattice thermal conductivity of $14.34 \text{ Wm}^{-1}\text{K}^{-1}$, which is lower than graphene's $\text{Wm}^{-1}\text{K}^{-1}$ [187]. Interestingly, over 70% of this conductivity arises from high-frequency phonon modes, in contrast with

the typical dominance of low-frequency acoustic modes in other 2D materials. This unusual behavior is attributed to borophene’s unique phonon interactions, which lead to enhanced group velocities and extended phonon relaxation times. Distinct thermal transport properties were also found mainly driven by borophene’s atomic structure and strong phonon-phonon scattering with anisotropic thermal behavior and enhanced near-field thermal radiation, making borophene a prime candidate for advanced thermal management applications. For example, non-equilibrium Green’s function simulations and *ab initio* calculations revealed superior thermal conductance in the ballistic regime of δ_6 and β_{12} (see Figure 1.29) borophene phases, surpassing that of graphene due to their light atomic mass, short B–B bonds, and structural anisotropy [188]. While low-frequency phonon transmission remains nearly isotropic, high-frequency phonons travel in a one-dimensional manner, enhancing thermal conductance.

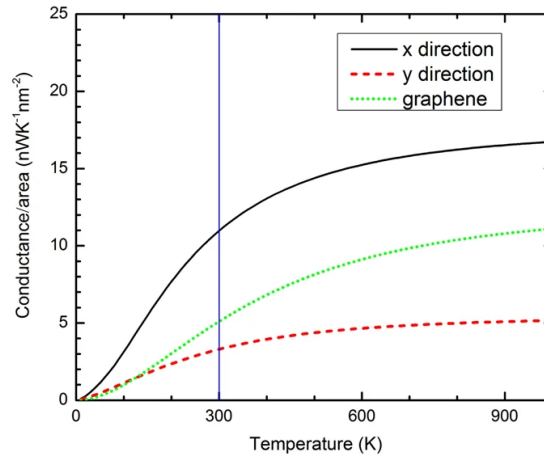


Figure 1.29: The temperature-dependent thermal conductance of β_{12} borophene and graphene is compared, where the thickness of borophene is defined as the diameter of a boron atom, while for graphene, it is based on the interlayer spacing ($\delta = 3.4 \text{ \AA}$) [188].

Hydrogenated δ_3 borophene exhibits exceptional thermal conductance, with first-principles calculations and non-equilibrium Green’s function theory revealing its electron thermal conductance being nearly ten times higher than graphene’s, resulting in total thermal conductance that is twice that of graphene, the highest among 2D materials [189]. This efficiency is due to its hexagonal boron network with hydrogen atoms on “bridge” sites, while tensile strain further enhances electron density and thermal performance, making hydrogenated δ_3 borophene a standout material for heat dissipation and thermal management.

Optical properties – borophene exhibits unique optical properties due to its anisotropic electronic structure, with a broad absorption spectrum spanning from visible to ultraviolet regions. Its tunable bandgap and atomic arrangement make it ideal for optoelectronic applications,

including photodetectors and solar cells. When reduced to just a few atomic layers, borophene shows near-zero reflectance and nearly 100% light transmission, making it highly transparent for touch displays. Its strong metallic nature supports intrinsic plasmons, and effective light manipulation. Unlike graphene, its high electron density allows plasmon energies to extend into the near-visible range which is crucial for the use in sensors and photonics [128]. Additionally, recent studies reveal borophene's potential as a highly sensitive refractive index sensor with near-perfect absorption in the near-infrared regime (NIR), with potential for label-free biosensing, THz photonics, biomedical fields [190], and positioning it as a promising alternative to conventional materials like graphene and gold in telecommunications and renewable energy [190].

Other possible applications – borophene, with its low density, metallic conductivity, and strong interaction with polysulfides, is a promising candidate for Li–S battery electrodes [176], as well as for other types of batteries like metal-ion batteries (such as Li, Na, K, Mg, Ca, and Al ion batteries), or Na-O₂ batteries [181]. Also, borophenes could be used for gas sensing [191, 192], or for drug delivery and cancer therapy [172].

1.2.3.2 Magnetic properties of borophene

Bare borophene is generally non-magnetic, but *defects* like vacancies or transition metal *doping*, without formation of clusters like in graphene, can introduce localized magnetic moments, enabling spin-polarized behavior. Further exploration of these tunable magnetic properties may establish borophene's role in next-generation technologies.

Namely, it is revealed that β_{12} borophene is ferromagnetic by introducing A-type vacancies, as depicted in Figure 1.30. These vacancies, primarily influenced by the *p* orbital electrons,

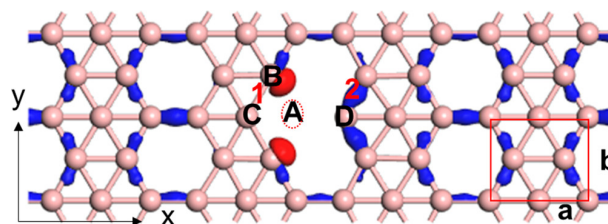


Figure 1.30: β_{12} borophene structure, blue-colored charge density difference, and red-colored spin density for the A-vacancy system are shown, with isovalues of $0.35 \text{ e}/\text{\AA}^3$ for the charge density and $0.03 \text{ e}/\text{\AA}^3$ for the spin density. Boron atoms are depicted as pink spheres.[193]

led to magnetic moments ($<0.5 \mu_B$) that were closely tied to the asymmetrical occupation of electronic states near the Fermi surface. The unique magnetic behavior arises from variation of localized electronic states and the reduced dispersion of bands, which resulted in Stoner

instability and a transition towards a ferromagnetic state. The magnetic moment was found to be significantly dependent on the vacancy configuration and carrier density. The substitution/doping with nonmetallic elements, such as H, N, and C, did not significantly alter the magnetism. Furthermore, the exchange interactions in double-vacancy systems displayed a ferromagnetic coupling, with the Curie temperature of 100 K. Another study investigated the electronic structure and magnetism induced by D-type vacancy defects⁴¹ in χ_3 borophene (see Figure 1.31), revealing that the projected DOS of atoms surrounding the vacancies, particularly the D₂ atom, leads to an asymmetric DOS near the Fermi surface [194]. Spin polarization arises from energy level splitting, and further doping with charge carriers enhances the magnetic moment. The

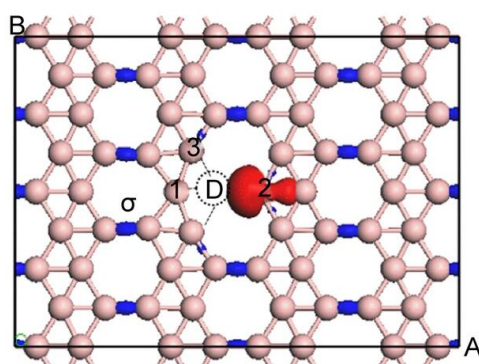


Figure 1.31: χ_3 borophene structure, blue-colored charge density difference, and red-colored spin density for the D-type vacancy system. The isovalues for the blue and red regions are 0.3 and $0.05 e/\text{\AA}^3$, respectively, with pink spheres representing boron atoms [194].

long-range ferromagnetic coupling is mediated by p orbital itinerant electrons described by the Ruderman-Kittel-Kasuya-Yosida (RKKY) like interaction model, where magnetic coupling oscillates as a function of the distance between magnetic atoms. Lower vacancy concentrations maintained a magnetic moment of approximately $1 \mu_B$, while higher concentrations caused broken spin states due to structural distortions. Complex defect systems with zig-zag edges exhibited both ferromagnetic and antiferromagnetic coupling, depending on the distance between magnetic atoms, further validating the RKKY-like behavior. Furthermore, passivation of dangling bonds through H, N, and C substitution/doping modified the magnetic properties, with H doping reducing magnetism by neutralizing dangling bonds and C(N) substitution rendering the system nonmagnetic. Another approach to modulate the magnetic properties of borophenes is through the adsorption of $3d$ transition metals. Adsorption of Cr and Mn on β_{12} borophene induced magnetism, while adsorption of elements from the 4th period, ranging from Sc to Zn, resulted in

⁴¹D-type defects are breaking the σ bond and forming a dangling bond with one unpaired electron with local magnetic moment of $1 \mu_B$.

non-magnetic states [195]. Strong hybridization between Mn and β_{12} borophene is indicated by an high adsorption energy, short adsorption distances, and a charge transfer of $0.71 e$, leading to a reduced magnetic moment of $3.49 \mu_B$ compared to isolated Mn. In contrast, Cr exhibited magnetism through the proximity effect, with Mn showing stronger interaction due to a lower adsorption height. Further, by using DFT+ U approach ($U = 4$ eV, $J = 0.9$ eV), all $3d$ adatoms can be stably adsorbed on β_{12} borophene, with spin polarization emerging in case of Ti, V, Cr, Mn, Fe, Co, and Ni [196]. Notably, Cr, Mn, Fe, and Co adatoms exhibit significant magnetism (from 3.6 up to $4.5 \mu_B$). The magnetic moments are reduced compared to isolated counterparts due to charge transfer and strong hybridization between $3d$ orbitals and boron $2p$ orbitals, which rearranges the electron spins. Moreover, when bilayer β_{12} borophene is intercalated with Mn it possess magnetic moment of $1 \mu_B$ with Curie temperature of 286.5 K [197].

1.2.3.3 Superconducting properties of borophene

According to Bardeen-Cooper-Schrieffer (BCS) theory, metals made of lightweight elements tend to exhibit higher superconducting transition temperatures (T_c) due to their typically high Debye temperatures [198]. 2D materials such as graphene, silicene, and phosphorene, possess semimetallic or semiconducting nature and weak electron-phonon ($e-ph$) coupling (λ), and are therefore not ideal candidates for high- T_c superconductivity. On top of that, in graphene superconductivity is only achieved by metal decoration (with Li the T_c is 8 K) [199], and in silicene ($T_c = 16$ K) [200] and phosphorene ($T_c = 12$ K) [201] by applying tensile strain and electron doping. In contrast, borophene's intrinsic metallicity, coupled with its potentially strong λ , presents a promising pathway towards intrinsic and conventional, phonon-mediated superconductivity. In 2001, superconductivity was observed in bulk MgB_2 with a T_c of 39 K [202] which sparked a wave of research into boron-based superconductors. This, combined with the successful experimental synthesis of borophene, has significantly fueled interest in exploring superconducting states of elemental boron systems. Therefore, in 2016 by combining density functional perturbation theory (DFPT) with the McMillan-Allen-Dynes (MAD) formula it was predicted that β_{12} and χ_3 borophene phase reach the isotropic λ_{iso} of ~ 0.8 and ~ 0.6 (see Figure 1.32) with T_c^{iso} of 16 and 12 K,⁴² respectively [203]. However, the considered structural models have shown phonon instabilities (around the Γ point) and softening at certain \mathbf{q} points, which could be resolved by stabilization through substrate effects (such a strain or doping). On

⁴²An uniform tensile strain of 1% was applied in order to achieve dynamical stability of the structures.

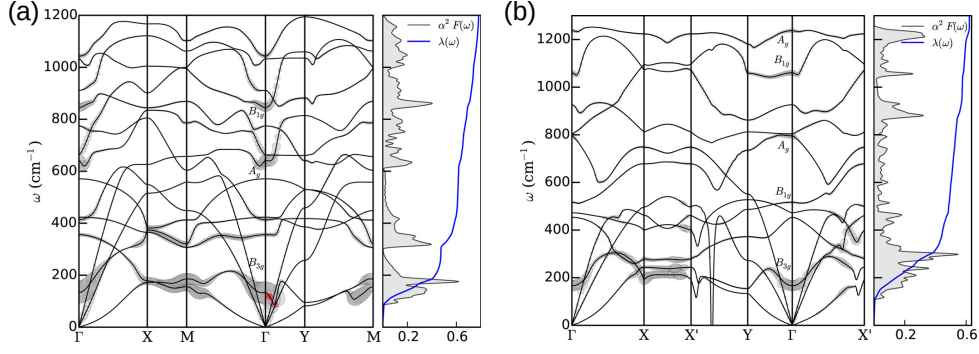


Figure 1.32: Phonon dispersions with the momentum-resolved (λ_{qv}), total ($\lambda(\omega)$) e - ph coupling, and the Eliashberg spectral function for (a) β_{12} , and (b) χ_3 phase. Adapted from [203].

the other hand, Yinchang Zhao and colleagues studied different phases of borophene proving that T_c^{iso} exhibits a gradual increase as the η parameter deviates from $1/9$, where $\eta = \frac{1}{9}$ (α -sheet) is associated with the lowest total energy and DOS at the Fermi level ($N(E_F)$). The trend in T_c^{iso} and λ_{iso} aligns closely with the variation in total energy and $N(E_F)$ as a function of η . For triangular δ_6 borophene (zero η value) the Fermi surface shows strong nesting, resulting in a total λ_{iso} of 0.86 and a T_c^{iso} of 19.7 K. However, when borophene is supported by the Ag(111) substrate, the Fermi surface is significantly modulated despite minimal charge transfer (0.02 e/B , based on Bader analysis). This modification in the nesting of Fermi surface and the suppression of out-of-plane vibrational modes lead to a reduced $\lambda_{\text{iso}} = 0.58$ and a lower logarithmic average phonon frequency ($\omega_{\text{log}} = 7.52$ THz). Consequently, by the support of Ag(111) substrate the T_c^{iso} is ~ 5.2 K, much lower than in freestanding form [204]. However, the tensile strain of 3% or hole doping can boost its T_c^{iso} up to 27.4 and 34.8 K, respectively [205]. Furthermore, Miao Gao and colleagues reported that the calculated T_c^{iso} of freestanding β_{12} and χ_3 are 18.7 K and 24.7 K, respectively [206]. They also found that the electron doping or tensile strain, as well as their combination can further decrease the observed T_c^{iso} in considered compounds. Also when supported by one layer of Ag(111), the T_c^{iso} in χ_3 is reduced to 10.0 K, close to 14.5 K of freestanding form by simultaneously applying electron doping of 0.03 e/B and 3.3% tensile strain. The impact of electron or hole doping, as well as tensile or compressive strain, on the superconducting properties of borophenes remains a key topic that requires further investigation to fully understand its effects. For example, suppression of T_c^{iso} is observed in freestanding β_{12} borophene by applying tensile strain of 2% (to 3 K) or electron doping of 0.1 e/B (close to 0 K) [207]. Borophenes also exhibit a highly anisotropic Fermi surface, and by solving fully anisotropic Migdal-Eliashberg (ME) equations it was found that triangular δ_6 borophene phase, due to strong hybridized σ and π bonds, possesses a single-gap nature with T_c^{aniso} of 27 K [208].

Also, χ_3 borophene was identified as a two-gap superconductor reaching T_c^{aniso} of 26 K, while β_{12} is a strong anisotropic single-gap superconductor with T_c^{aniso} reaching up to 33 K.

Therefore, a compelling question emerges: “*Is there a concrete experimental evidence to validate the numerous theoretical predictions of superconductivity in borophenes?*”

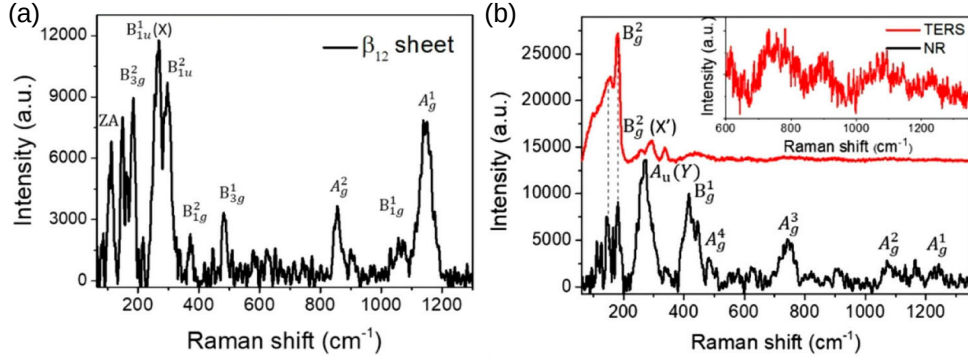


Figure 1.33: In situ Raman spectrum of monolayer (a) β_{12} , and (b) χ_3 borophene [209].

A partial result was achieved through a combination of experimental and theoretical approaches. A Raman spectroscopy study of borophene on Ag(111) examined the β_{12} and χ_3 phases (see Figure 1.33), finding λ values, from phonon line width, of 0.53 and 0.59, respectively [209]. These values theoretically suggest T_c of 7.1 K and 9.8 K for β_{12} and χ_3 borophenes, respectively, which are much lower than previously theoretically predicted T_c for borophenes. However, direct experimental evidence remains elusive, as none of the measurements to date have shown clear signatures of superconductivity, prompting a critical reassessment of theoretical models with particular focus on environmental factors, such as substrate effects, oxidation, and so on. One way to overcome this issue is by chemical passivation. The hydrogenation of δ_6 borophene resulted in the absence of superconductivity [210], while for β_{12} borophene, hydrogenation does not enhance T_c values compared to the parent borophene, especially at higher hydrogen coverage [211]. Bilayer borophenes, with reduced substrate interaction and enhanced oxidation resistance, present promising avenues for tuning superconducting properties through favorable intercalation and property modification. Theoretical studies have supported this approach, predicting superconductivity in Mg-intercalated β_{12} , χ_3 , δ_4 , and kagome bilayer borophene, with T_c^{iso} reaching 13 K [212, 213]. However, a higher T_c^{iso} values of 23 and 36 K were reported when Ca intercalant was used in kagome and δ_3 bilayer configurations, respectively [214, 215]. For some bare bilayer borophenes, like B_8 , it is predicted to possess T_c^{iso} of 12 K [216], and when some phases are stacked into 3D vdW structures, they may offer a platform for phonon-mediated superconductivity with T_c^{iso} values up to 10 K [217].

THEORETICAL MODELS AND METHODOLOGY

2.1 Density functional theory (DFT)

In condensed matter physics, the many-body problem poses significant challenges due to the complex interactions among numerous particles. Density functional theory (DFT) provides a powerful framework to address this complexity by focusing on the ground state electron density instead of the many-electron wavefunction, simplifying calculations while preserving accuracy. As a first-principles method rooted in quantum mechanics, DFT enables precise predictions of electronic structure without the need for empirical parameters. This section reviews the theoretical aspects of DFT alongside practical implementation approaches and key computational tools for modeling material's physical properties.

The literature sources used for this section are provided as Refs. [218, 219, 220, 221, 222, 223].

2.1.1 Simplifying the problem of many-body system

The theoretical examination of the electronic structure and properties of crystals involves addressing the complex quantum mechanical many-body problem, by solving the time-dependent Schrödinger equation,¹ which serves as the cornerstone of non-relativistic quantum mechanics:

$$i\hbar \frac{\partial \Psi_{Total,m}}{\partial t} = \hat{H}_{Total} \Psi_{Total,m}, \quad (2.1)$$

Where $\Psi_{Total,m}$ describes the quantum state of the electron-nuclei system, typically relying on both the spin² and spatial coordinates, and H_{Total} is the corresponding hamiltonian. However,

¹The N -particle Schrödinger equation, where $m \in \{1, \dots, N\}$.

²For the sake of simplicity, the notation for spin coordinates in the following discussions will be omitted.

the time-independent Schrödinger equation, where the hamiltonian remains constant due to a time-invariant potential $V(\mathbf{r}_i)$, offers a simpler and more appropriate framework, by describing stationary states:

$$\hat{H}_{Total}\phi_{Total,m} = E_{Total,m}\phi_{Total,m}. \quad (2.2)$$

The equation (2.2) can be expressed in a more detailed form, grouping the terms that correspond to the interactions between electrons, nuclei, and between electrons and nuclei, so that by taking into account that $4\pi\epsilon_0 = 1$ one gets:

$$\begin{aligned} \hat{H}_{Total} &= -\frac{\hbar^2}{2m_e} \sum_i \nabla_i^2 + \frac{1}{2} \sum_{i \neq j} \frac{e^2}{|\mathbf{r}_i - \mathbf{r}_j|} - \sum_I \frac{\hbar^2}{2M_I} \nabla_I^2 + \frac{1}{2} \sum_{I \neq J} \frac{Z_I Z_J e^2}{|\mathbf{R}_I - \mathbf{R}_J|} - \sum_{i,I} \frac{Z_I e^2}{|\mathbf{r}_i - \mathbf{R}_I|} \\ &= \hat{T}_e + \hat{V}_{ee} + \hat{T}_n + \hat{V}_{nn} + \hat{V}_{en}, \end{aligned} \quad (2.3)$$

with $i \in \{1, \dots, N\}$, and where $\hat{T}_e = -\frac{\hbar^2}{2m_e} \sum_i \nabla_i^2$ is the total kinetic energy of electrons; $\hat{V}_{ee} = \frac{1}{2} \sum_{i \neq j} \frac{e^2}{|\mathbf{r}_i - \mathbf{r}_j|}$ is the Coulomb interaction between electrons; $\hat{T}_n = -\sum_I \frac{\hbar^2}{2M_I} \nabla_I^2$ is the total kinetic energy of nuclei; $\hat{V}_{nn} = \frac{1}{2} \sum_{I \neq J} \frac{Z_I Z_J e^2}{|\mathbf{R}_I - \mathbf{R}_J|}$ is the Coulomb interaction between nuclei; and $\hat{V}_{en} = -\sum_{i,I} \frac{Z_I e^2}{|\mathbf{r}_i - \mathbf{R}_I|}$ is the Coulomb interaction between electrons and nuclei.

In order to simplify the equation, the *Born-Oppenheimer approximation* (BO)³ is applied by recognizing the notable mass difference between nuclei and electrons ($m_e/M_n \sim 10^{-3} - 10^{-5}$), which justifies the assumption that the nuclei remain nearly stationary. As a result, the positions of the fixed nuclei serve as parameters in the hamiltonian that governs the electronic motion,⁴ simplifying the problem by focusing on the electrons behavior within the external field created by the nuclei. This approach is a baseline for perturbation theory (DFPT) which is widely used and proven, particularly in complex calculations involving lattice vibrations and *e-ph* interactions, which are essential for understanding the superconducting and transport properties of materials.

The total wave function can now be factored into two distinct components:

$$\phi_{Total}(\mathbf{r}_i, \mathbf{R}_i) = \phi(\mathbf{r}_i, \mathbf{R}_i) = \sum_m \Omega_m(\mathbf{R}_i) \Psi_{e,m}(\mathbf{r}_i, \mathbf{R}_i), \quad (2.4)$$

the wave function of the nuclei, denoted as $\Omega_m(\mathbf{R}_i)$, and that of the electrons, represented as $\Psi_{e,m}(\mathbf{r}_i, \mathbf{R}_i)$, for a specific fixed configuration of the nuclei. Consequently, the dynamics of electrons within the potential generated by fixed nuclei can now be described, thus enabling the

³Adiabatic approximation.

⁴It is implicitly assumed that the system is electroneutral.

determination of the system's ground state energy (adiabatic potential energy). Utilizing the BO approximation, the total hamiltonian for the electronic subsystem in equilibrium is expressed as:⁵

$$\hat{H}_e = -\frac{\hbar^2}{2m_e} \sum_i \nabla_i^2 + \frac{1}{2} \sum_{i \neq j} \frac{e^2}{|\mathbf{r}_i - \mathbf{r}_j|} + \sum_i v_{ext}(\mathbf{r}_i) = \hat{T}_e + \hat{V}_{ee} + \hat{V}_{ext}, \quad (2.5)$$

where $v_{ext}(\mathbf{r}_i)$ is the *external potential* caused by the nuclei and experienced by the i -th electron. A careful analysis of equation (2.5) reveals that the kinetic energy operator \hat{T}_e is independent of nuclei coordinates and relies solely on the number of electrons (N_e), as well as the Coulomb term \hat{V}_{ee} but its proper description is challenging. On the other hand, the only variable component of the \hat{H}_e is the operator of external potential \hat{V}_{ext} , whose expectation value is the external potential V_{ext} . However, even with a well defined external potential, the exact solution for even the simplest systems remains a big challenge.

2.1.2 The Hohenberg-Kohn theorems

Fortunately, the Hohenberg-Kohn (HK) theorems, which serve as the basic foundation of DFT, redefine these complex quantum-mechanical problems by focusing on electron density $n(\mathbf{r})$ ⁶ rather than using the more complicated wave functions. Initially rooted in the Thomas-Fermi approach of 1927 [224, 225], the modern formulation by Hohenberg and Kohn in 1964 [226] demonstrated how ground state properties of many-electron systems are reliably derived from a variational principle by systematically minimizing the energy functional $E[n_{v_{ext}}(\mathbf{r})]$. Nonetheless, a key challenge persists in effectively characterizing electron-electron interactions, which are essential for precise modeling of electronic behaviors.

We will start by considering a system of N interacting electrons within an external potential. The HK approach posits that the external potential is a functional of the ground state electron density, and, up to an additive constant, it is uniquely determined by this electron density.

- **Theorem I:** *The ground state density $n_o(\mathbf{r})$ of a bound system of interacting electrons in some external potential $v_{ext}(\mathbf{r})$ determines this potential uniquely.*

The electronic hamiltonian, derived from solving the Schrödinger equation for a many-electron system, determines the ground state wave functions $\Psi_{o(e,m)}$ of the system. Thus, a clear connec-

⁵In BO approximation there is also an additional term $E_{nn}(\mathbf{R}_i)$, which represents the classical electrostatic interaction between nuclei. Along with any other contributions to the total energy of the system that are not directly relevant to the description of the electrons, will be omitted in this expression for the sake of simplicity.

⁶In general $n_\sigma(\mathbf{r}) = \frac{\langle \Psi_{e,n} | \hat{n}_\sigma(\mathbf{r}) | \Psi_{e,n} \rangle}{\langle \Psi_{e,n} | \Psi_{e,n} \rangle}$, where $\hat{n}_\sigma(\mathbf{r}) = \sum_{i=1,N} \delta(\mathbf{r} - \mathbf{r}_i) \delta_{\sigma\sigma_i}$ is the electron density operator.

tion exists linking the ground state electron density to the wave function (*one-to-one* mapping), such that the wave function is expressed as a functional that depends of the ground state electron density, $\Psi_{o(e,m)}[n_o(\mathbf{r})]$. In other words, the ground state electron density specifies the total number of electrons and the external potential, which in turn dictate the system's properties, as both the hamiltonian and the ground state wave function depend on these factors. The original proof was applicable only on non-degenerate ground states but was further extended through Levy–Leib (LL) formulation⁷ to include degenerate cases, as well as to non-interacting electron systems.

• **Theorem II:** *For any quantum system of interacting particles in an external potential $v_{ext}(\mathbf{r})$, there exists a universal energy functional $F[n(\mathbf{r})]$, which depends solely on the electron density $n(\mathbf{r})$. This functional reaches its global minimum at the exact ground state density $n_o(\mathbf{r})$, and this minimum value corresponds to the exact ground state energy of the whole system.*

↔ *The proof of the HK theorems can be found in the mentioned literature.*

Therefore, according to the HK theorems, the energy functional $E[n_{v_{ext}}(\mathbf{r})]$ ⁸ can be expressed as:

$$E[n(\mathbf{r})] = F[n(\mathbf{r})] + \int n(\mathbf{r})v_{ext}(\mathbf{r})d\mathbf{r}, \quad (2.6)$$

Where $F[n(\mathbf{r})] = T_e[n(\mathbf{r})] + V_{ee}[n(\mathbf{r})]$ represents the Fock functional,⁹ which is independent of the external potential. Now, according to the II HK theorem, the fundamental condition that must be satisfied is that $E[n_o(\mathbf{r})] < E[n(\mathbf{r})]$, where $n_o(\mathbf{r})$ represents the exact electron density of the ground state. To impose the constraint of total number electron conservation ($\delta N_e = \int \delta n(\mathbf{r})d\mathbf{r} = 0$), a Lagrange multiplier (μ) is introduced, so that the stationary condition for minimizing the HK energy functional is derived:

$$\begin{aligned} \delta E[n_o(\mathbf{r})] &= E[n_o(\mathbf{r}) + \delta n(\mathbf{r})] - E[n_o(\mathbf{r})] = \delta \left\{ E[n(\mathbf{r})] - \mu \int n(\mathbf{r})d\mathbf{r} \right\} \\ &= \int \left\{ \frac{\delta E[n(\mathbf{r})]}{\delta n(\mathbf{r})} - \mu \right\} \delta n(\mathbf{r})d\mathbf{r} = 0. \end{aligned} \quad (2.7)$$

⁷The LL functional differs from the HK functional in that it is defined for any electron density derived from an N -electron wavefunction (“ N -representability”), whereas the HK functional is limited to electron densities generated by an external potential (“ V -representability”), and at the system's energy minimum in a given potential, both functionals are equivalent.

⁸ $n_{v_{ext}}(\mathbf{r})$ represents all possible values of electron density corresponding to a specific external potential. For simplicity, these values will be denoted as $n(\mathbf{r})$, and the true ground state with $n_o(\mathbf{r})$.

⁹The consequence of I HK theorem is that $F[n_o(\mathbf{r})] = \langle \Psi_{o(n,e)}[n_o(\mathbf{r})] | \hat{F} | \Psi_{o(e,n)}[n_o(\mathbf{r})] \rangle$.

This leads to the Euler-Lagrange equation, derived from the variational principle:

$$\mu = \frac{\delta E[n(\mathbf{r})]}{\delta n(\mathbf{r})} = v_{ext}(\mathbf{r}) + \frac{\delta F[n(\mathbf{r})]}{\delta n(\mathbf{r})}. \quad (2.8)$$

The Lagrange multiplier μ , used to ensure electron number conservation, also carries physical significance as it represents the chemical potential, coinciding with the Fermi energy of the system at $T = 0$ K. For the exact form of $F[n(\mathbf{r})]$, equation (2.7) would correspond to the exact electron density of the system's ground state. Therefore, HK approach enables the replacement of the difficult task of describing a system through a many-electron wave function, which depends on $3N$ spatial coordinates (when ignoring spin), with a simpler framework based on electron density, which depends on only three spatial coordinates. In any case, the exact form of $F[n(\mathbf{r})]$ was unknown, and prior direct approximations were insufficiently accurate, especially in describing the kinetic energy component.

2.1.3 The Kohn-Sham equations

The Kohn-Sham (KS) approach [227] then offered a practical solution by replacing the problem of interacting electrons with a system of independent electrons in an effective potential designed to produce an electron density identical to that of the interacting system in ground state. The hamiltonian of such “auxiliary” system also includes the standard kinetic term and an effective potential. Hence, the corresponding many-electron wave function is represented by a Slater determinant composed of single-electron KS orbitals:

$$\Psi_o(\mathbf{r}) = \frac{1}{\sqrt{N!}} \begin{vmatrix} \psi_1(\mathbf{r}_1) & \psi_2(\mathbf{r}_1) & \dots & \psi_N(\mathbf{r}_1) \\ \psi_1(\mathbf{r}_2) & \psi_2(\mathbf{r}_2) & \dots & \psi_N(\mathbf{r}_2) \\ \vdots & \vdots & & \vdots \\ \psi_1(\mathbf{r}_N) & \psi_2(\mathbf{r}_N) & \dots & \psi_N(\mathbf{r}_N) \end{vmatrix}, \quad (2.9)$$

which correspond to the N lowest eigenstates that fulfill the Schrödinger single-electron equation in the following form:

$$\left\{ -\frac{\hbar^2}{2m} \nabla^2 + v_{eff}^{KS}(\mathbf{r}) \right\} \psi_i(\mathbf{r}) = \varepsilon_i \psi_i(\mathbf{r}). \quad (2.10)$$

This method enables the substitution of the electron density of interacting electrons with that of a non-interacting system in its ground state $n_{KS}(\mathbf{r}) = n(\mathbf{r}) = \sum_{i=1}^{occupied} |\psi_i(\mathbf{r})|^2$, as well as the determination of universal functional $F[n(\mathbf{r})]$ (see equation (2.6)), which can be expressed as a sum of three distinct components, yielding the following form for the energy functional:

$$E_{KS}[n(\mathbf{r})] = T_{KS}[n(\mathbf{r})] + \iint \frac{e^2 n(\mathbf{r}) n(\mathbf{r}')}{2|\mathbf{r} - \mathbf{r}'|} d\mathbf{r} d\mathbf{r}' + E_{XC}[n(\mathbf{r})] + \int v_{ext}(\mathbf{r}) n(\mathbf{r}) d\mathbf{r}, \quad (2.11)$$

where $T_{KS}[n(\mathbf{r})] = \sum_{i=1}^N \int \psi_i^*(\mathbf{r}) \left(-\frac{\hbar^2}{2m} \nabla^2\right) \psi_i(\mathbf{r}) d\mathbf{r}$ represents the KS kinetic energy term. The total energy of the auxiliary system must match that of the fully interacting system and therefore the term that encapsulates all many-body exchange-correlation effects ($E_{XC}[n(\mathbf{r})]$) in the KS equation (2.11) essentially represents the difference between the kinetic and potential energies of the interacting electrons, and its corresponding independent (fictitious) electron system:

$$E_{XC}[n(\mathbf{r})] = T_e^{inter.}[n(\mathbf{r})] - T_{KS}[n(\mathbf{r})] + V_{ee}^{inter.}[n(\mathbf{r})] - \iint \frac{e^2 n(\mathbf{r}) n(\mathbf{r}')}{2|\mathbf{r} - \mathbf{r}'|} d\mathbf{r} d\mathbf{r}'. \quad (2.12)$$

Now, using the variational principle, the Euler-Lagrange equation (2.8) becomes:

$$\mu = v_{ext}(\mathbf{r}) + \int \frac{e^2 n(\mathbf{r}')}{|\mathbf{r} - \mathbf{r}'|} d\mathbf{r}' + V_{XC}(\mathbf{r}) + \frac{\delta T_{KS}[n(\mathbf{r})]}{\delta n(\mathbf{r})} = v_{eff}^{KS}(\mathbf{r}) + \frac{\delta T_{KS}[n(\mathbf{r})]}{\delta n(\mathbf{r})}, \quad (2.13)$$

where $V_{XC}(\mathbf{r}) = \frac{\delta E_{XC}[n(\mathbf{r})]}{\delta n(\mathbf{r})}$ is the exchange-correlation functional. Since $T_{KS}[n(\mathbf{r})]$ is actually explicitly dependent on the KS orbitals, the variational principle is directly applied to an arbitrary functional of orbitals:

$$\Omega[\psi_i(\mathbf{r})] = E_{KS}[n(\mathbf{r})] - \sum_i \sum_j \int \varepsilon_{ij} \psi_i^*(\mathbf{r}) \psi_j(\mathbf{r}) d\mathbf{r}, \quad (2.14)$$

where ε_{ij} represents the Lagrange multipliers used to enforce the constraint that the KS orbitals are orthonormalized $\int \psi_i(\mathbf{r})^* \psi_j(\mathbf{r}) d\mathbf{r} = \delta_{ij}$. To ensure that the energy functional $E_{KS}[n(\mathbf{r})]$ reaches its minimum value, it is necessary to minimize the equation (2.14) with respect to KS

orbitals, so that the condition $\delta\Omega[\psi_i(\mathbf{r})] = 0$ ¹⁰ leads to KS equations:

$$\left\{ \begin{aligned} \hat{h}_{eff}^{KS}\psi_i(\mathbf{r}) &= \left\{ -\frac{\hbar^2}{2m}\nabla^2 + v_{eff}^{KS}(\mathbf{r}) \right\} \psi_i(\mathbf{r}) = \sum_{j=1}^N \varepsilon_{ij}\psi_j(\mathbf{r}), \end{aligned} \right. \quad (2.15)$$

$$\left\{ \begin{aligned} v_{eff}^{KS}(\mathbf{r}) &= v_{ext}(\mathbf{r}) + \int \frac{e^2 n(\mathbf{r}')}{|\mathbf{r} - \mathbf{r}'|} d\mathbf{r}' + V_{XC}(\mathbf{r}); \end{aligned} \right. \quad (2.16)$$

$$\left\{ \begin{aligned} n(\mathbf{r}) &= \sum_{i=1}^N |\psi_i(\mathbf{r})|^2. \end{aligned} \right. \quad (2.17)$$

The effective potential $v_{ext}(\mathbf{r})$ acts as a local operator, while the single-electron hamiltonian $\hat{h}_{eff}^{KS}\psi_i(\mathbf{r})$ is a hermitian operator. Consequently, the ε_{ij} matrix is hermitian and can be diagonalized. The KS equations are solved using an *iterative method* called the *self-consistent field* (SCF) approach. In each iteration, the input electron density $n_{in}^k(\mathbf{r})$ of the k -th cycle generates new $v_{eff}^k(\mathbf{r})$. Solving the KS equation (2.15) within this potential gives the eigenvalues ε_{ij}^k and orbitals $\psi_i^k(\mathbf{r})$. These orbitals are then used to calculate the updated electron density from equation (2.17) $n_{out}(\mathbf{r}) = \sum_{i=1}^N |\psi_i^k(\mathbf{r})|^2$, which becomes the input for the next $k + 1$ -th iteration cycle.¹¹ This procedure is iterated until the difference between the input and output electron densities falls below a predefined threshold.

If we want to determine the *equilibrium geometry* of a system within the KS framework, the Hellmann-Feynman theorem is applied to calculate forces acting on the nuclei. According to this theorem, the force on each nucleus \mathbf{R}_i is given by:

$$\mathbf{F}_I = -\frac{\partial E(\mathbf{R}_I)}{\partial \mathbf{R}_I} = -\int \frac{\partial v_{ext}(\mathbf{r})}{\partial \mathbf{R}_I} n_o(\mathbf{r}) d\mathbf{r} - \frac{\partial E_{nn}}{\partial \mathbf{R}_I} = 0. \quad (2.18)$$

When forces are non-zero, the nuclei are repositioned, and the KS equations are re-solved iteratively. This iterative process continues until forces on the nuclei are sufficiently small, marking the minimum-energy configuration.

At this point, a suitable approximation for the exchange-correlation functional $E_{XC}[n(\mathbf{r})]$ must be proposed. The strength of the KS method actually lies in its ability to separate the kinetic energy $T_{KS}(\mathbf{r})$ of the non-interacting electrons and long-range Hartree terms from the

¹⁰For example, $\frac{\delta T_{KS}}{\delta \psi_i^*(\mathbf{r})} = -\frac{\hbar^2}{2m}\nabla^2\psi_i(\mathbf{r})$, and for other terms the “*chain rule*” can be used, and $\frac{\delta n(\mathbf{r})}{\delta \psi_i^*(\mathbf{r})} = \psi_i(\mathbf{r})$.

¹¹However, using solely the output density as input would lead to numerical issues and violate the SCF procedure. Hence, the input density for the $k + 1$ -th iteration is constructed as mixture of $n_{in}^k(\mathbf{r})$ and $n_{out}^k(\mathbf{r})$ so that $n_{in}^{k+1}(\mathbf{r}) = \alpha n_{out}^k + (1 - \alpha)n_{in}^k(\mathbf{r})$, where $\alpha = 0.01 - 0.1$ is called the *linear mixing parameter*. Besides, *Broyden mixing*, which uses information from multiple past iterations to construct an optimal update, dynamically adapts and significantly accelerates SCF convergence.

more complex many-body exchange-correlation energy $E_{XC}[n(\mathbf{r})]$. This separation allows $E_{XC}[n(\mathbf{r})]$ to be effectively represented by a (semi-)local functional of the electron density. In such an approximation, the exchange-correlation energy at any point depends primarily on $n(\mathbf{r})$ in the local neighborhood, making it easier to calculate while still capturing essential many-body effects:

$$E_{XC}[n(\mathbf{r})] = \int n(\mathbf{r})\varepsilon_{XC}([n(\mathbf{r})], \mathbf{r})d\mathbf{r}, \quad (2.19)$$

so that $\varepsilon_{XC}([n(\mathbf{r})], \mathbf{r})$ represents the exchange-correlation energy per electron at position \mathbf{r} , which depends only on the electron density $n(\mathbf{r})$ within a local area around that point \mathbf{r} .¹² This forms the basis for the implementation of non-empirical functionals like the *local density approximation* (LDA), which has been shown to yield reliable results.

The LDA provides a practical yet powerful framework by approximating the $\varepsilon_{XC}([n(\mathbf{r})])$ at each position \mathbf{r} based on the properties of a uniform interacting electron gas. Within the framework, equation (2.19) becomes:

$$E_{XC}^{LDA}[n(\mathbf{r})] = \int n(\mathbf{r})\varepsilon_{XC}^{uniform}(n(\mathbf{r}))d\mathbf{r}, \quad (2.20)$$

and $\varepsilon_{XC}^{uniform}(n(\mathbf{r})) = \varepsilon_X(n(\mathbf{r})) + \varepsilon_C(n(\mathbf{r}))$, where the exchange term $\varepsilon_X(n(\mathbf{r})) = -\frac{3}{4\pi}(3\pi^2n(\mathbf{r}))^{\frac{1}{3}}$ is known, and correlation term $\varepsilon_C(n(\mathbf{r}))$ is accurately determined from Quantum Monte Carlo (QMC) simulations. While LDA performs well in slowly varying density regions, it is less accurate for systems with strong inhomogeneities. Therefore, the semi-local *generalized gradient approximation* (GGA) offers significant improvements, making it highly effective for modeling complex molecules and materials. In this approach, $\varepsilon_{XC}(n(\mathbf{r}))$ is influenced not only by the electron density $n(\mathbf{r})$ but also by its spatial variation, particularly the gradient $\nabla n(\mathbf{r})$:

$$E_{XC}^{GGA}[n(\mathbf{r})] = \int n(\mathbf{r})\varepsilon_{XC}^{GGA}[n(\mathbf{r}), \nabla n(\mathbf{r})]d\mathbf{r}. \quad (2.21)$$

In constructing the exchange-correlation energy $E_{XC}^{GGA}[n(\mathbf{r})]$, certain conditions are typically imposed: (i) fulfilling the sum rule for exchange-correlation hole: $\int n_{xc}(\mathbf{r}, \mathbf{r}')d\mathbf{r}' = -1$; (ii) minimizing the leading terms in the gradient expansion whenever $\xi(\mathbf{r}) \ll 1$ (*high density limit*);¹³

¹²A useful connection between $\varepsilon_{XC}([n(\mathbf{r})], \mathbf{r})$ and the exchange-correlation hole $n_{xc}(\mathbf{r}, \mathbf{r}')$ can be established through the ‘‘coupling constant integration formula’’ – the ‘‘adiabatic connection’’ by Harris [228]. The $n_{xc}(\mathbf{r}, \mathbf{r}')$ refers to the reduction in the probability of finding a second electron at a position \mathbf{r}' given that there is already an electron at \mathbf{r} , particularly when the distance between the two electrons decreases, due to the combined effects of quantum exchange and e - e correlation.

¹³ $\varepsilon_{XC}^{GGA}[n(\mathbf{r}), \nabla n(\mathbf{r})]$ is typically expanded in terms of the dimensionless quantity $\xi(\mathbf{r}) = \frac{1}{2k_F(n(\mathbf{r}))}|\frac{\nabla n(\mathbf{r})}{n(\mathbf{r})}|$

and (iii) dampening contributions from regions where $\xi(\mathbf{r}) > 1$ (*low density limit*). A notable example of good parametrization is given by Perdew, Burke and Ernzerhof, the so-called PBE functional,¹⁴ which effectively balance accuracy and computational efficiency. For further details on the PBE functional construction, we refer the reader to the original work by its developers – Ref. [229].

2.1.4 Approximations in electronic structure calculations

2.1.4.1 Plane wave basis set

We begin by considering the expansion of KS orbitals using a basis set comprised of functions $\{f_\alpha(\mathbf{r})\}$. Although constructed in real space, this set of functions allows expansion in any chosen representation of $f_\alpha(\mathbf{r})$:

$$\psi_i(\mathbf{r}) = \sum_{\alpha} k_{i,\alpha} f_{\alpha}(\mathbf{r}), \quad (2.22)$$

where coefficients $k_{i,\alpha}$ represent the expansion terms that must be determined in order to express the KS orbitals in the chosen basis set. Now, by inserting equation (2.22) in equation (2.15) one obtains:

$$\sum_{\alpha} k_{i,\alpha} [h_{\alpha,\beta}^{KS} - \varepsilon_i \mathcal{A}_{\alpha,\beta}] = 0, \quad (2.23)$$

where elements $h_{\alpha,\beta}^{KS}$ and $\mathcal{A}_{\alpha,\beta}$ belong to the KS matrix \mathcal{H}^{KS} and the overlap matrix \mathcal{A} , respectively. The homogeneous linear system described in equation (2.23) will have nontrivial solutions for the unknown coefficients $k_{i,\alpha}$ only if the determinant of the matrix in the square brackets equals zero:

$$\text{Det} [\mathcal{H}^{KS} - \varepsilon_i \mathcal{A}] = 0. \quad (2.24)$$

This approach reformulates the N -KS equations as a set of simpler relations, where finding the orbitals $\psi_i(\mathbf{r})$ is achieved through standard diagonalization techniques. For computational efficiency, the basis set $\{f_\alpha(\mathbf{r})\}$ must be finite, and the elements of both the \mathcal{H}^{KS} and \mathcal{A} need to be simple to calculate, requiring a balance between accuracy and performance. The ideal basis set for expanding a electron's wave function should exhibit both spatial localization near the

and few other parameters like local Seitz radius r_s , spin polarization factors ζ etc. Different limits of this quantities can determine the exchange and correlation part of $E_{XC}^{GGA}[n(\mathbf{r})]$.

¹⁴In PBE formalism, through $\xi(\mathbf{r})$ one can obtain the exchange part, while the correlation part is expressed by another adimensional parameter $t = \frac{1}{2\phi(\zeta)k_{TF}} \left| \frac{\nabla n(\mathbf{r})}{n(\mathbf{r})} \right|$, where $\phi(\zeta)$ is the spin-scaling factor with $\zeta = \frac{n_{\uparrow}(\mathbf{r}) - n_{\downarrow}(\mathbf{r})}{n(\mathbf{r})}$, and k_{TF} as the Thomas-Fermi screening wave number. Also, the $\xi(\mathbf{r})$ is connected with t through relation: $\xi(\mathbf{r}) = \left(\frac{r_s m e^2}{\hbar^2} \right)^{1/2} \frac{\phi(\zeta)t}{1.2}$ [229].

nuclei, and being smooth as well as delocalized in the interstitial regions in order to mimic the true nature of the system. Achieving this balance is challenging, leading to the development of numerical methods categorized into three primary types: (i) localized functions such as *atomic orbitals* and *Gaussians*, (ii) delocalized functions, like *plane waves (PW)*, and hybrid methods that incorporate both approaches, like *projector-augmented wave (PAW)* method.

For DFT calculations of crystal structures and properties, plane-wave (PW) method is highly effective due to its precision in representing electronic states in periodic systems. A crystal structure, with atoms arranged in a regular lattice, exhibits long-range order through *translational symmetry*, allowing the entire crystal to be described by a single *unit cell* that can be repeated in space (*supercell*) to deal with aperiodic systems (slab, defects, etc.). Also, an ideal crystal not only possesses translational symmetry but also remains unchanged under specific *point group* transformations, with their combination forming the crystal's *space group*. The DFT calculation are typically done in the *irreducible Brillouin zone (IBZ)* which represents the reduced portion of the first BZ – the reciprocal counterpart to the unit cell in direct space – that through space group operations can generate the entire BZ. This reduction not only simplifies electronic structure calculations but also provides deeper insight into the crystal's symmetries and physical properties.

Now, according to Bloch's theorem, the eigenstates of the single-electron hamiltonian can be expressed as the product of a function that satisfies the lattice's periodic conditions and plane wave with wavevector \mathbf{k} :¹⁵

$$\psi_{\mathbf{k}}(\mathbf{r}) = u_{\mathbf{k}}(\mathbf{r})e^{i\mathbf{k}\mathbf{r}} = u_{\mathbf{k}}(\mathbf{r} + \mathbf{R})e^{i\mathbf{k}\mathbf{r}}, \quad (2.25)$$

for all vectors \mathbf{R} from Bravais lattice. Now, the KS orbitals can be written in plane wave basis set by expanding $u_{\mathbf{k}}(\mathbf{r})$ in a sum taken over all distinct reciprocal lattice vectors:

$$\psi_{m,\mathbf{k}} = \sum_{\mathbf{G}} c_{m,\mathbf{k}}(\mathbf{G})e^{i(\mathbf{k}+\mathbf{G})\mathbf{r}}, \quad (2.26)$$

where $c_{m,\mathbf{k}}(\mathbf{G})$ are actually Fourier coefficients. Thus, the plane wave basis forms a complete basis set, enabling the expansion of functions as a Fourier series, with the key advantage that fast Fourier transform (FFT) enable efficient switching between direct and reciprocal space. Also, to make the plane wave expansion in equation (2.26) feasible for numerical computations, a *cutoff*

¹⁵The energy spectrum is also periodic in the reciprocal space. As a result, the entire energy spectrum can be described within the BZ. This periodic representation of energy levels is known as the *band structure*.

energy E_{cut} is introduced, restricting the expansion to wave vectors:

$$\frac{1}{2}|\mathbf{k} + \mathbf{G}|^2 \leq E_{cut}. \quad (2.27)$$

Furthermore, in a finite system with N unit cells, Born-von Kármán (BvK) boundary conditions are applied to simulate an infinite periodic system: $\psi_{m,\mathbf{k}}(\mathbf{r}) = \psi_{m,\mathbf{k}}(\mathbf{r} + \mathbf{R})$. Due to BvK conditions, there are $N_{\mathbf{k}}$ wave-vectors in the BZ, and the volume per \mathbf{k} -point is $\Omega_{cell}/(2\pi)^3$. As the system size increases, the \mathbf{k} -points become denser, approximating an infinite crystal. However, computational limits require optimal BZ sampling, or by using symmetry operation, the IBZ sampling. In practice, unless the dependence on a specific \mathbf{k} -point is needed, one typically computes averages of \mathbf{k} -dependent functions over the IBZ as:

$$\langle f \rangle = \sum_{m=1}^{N_{\mathbf{k}}} \omega_{\mathbf{k}_m} F_{\mathbf{k}_m}^{occ} f(\mathbf{k}_m) + error(\{\mathbf{k}_m\}), \quad (2.28)$$

where $\sum_{m=1}^{N_{\mathbf{k}}} \omega_{\mathbf{k}_m} = 1$ represents the normalized *weights*,¹⁶ $F_{\mathbf{k}_m}^{occ}$ is the occupation factor, and for a specific value of $N_{\mathbf{k}}$, the *special* points $\{\mathbf{k}\}$ are chosen so to minimize the error, which is the difference between the exact integral over the BZ and the approximation using finite \mathbf{k} -sampling. In methods like the *tetrahedron* approach, weights are determined based on the geometry of the BZ.¹⁷ In contrast, special point sampling methods, such as the Monkhorst-Pack scheme [230], generate \mathbf{k} -point sets (equidistant (uniform) grid) where the weights are pre-calculated or derived from the crystal's symmetry. This method is efficient for integrating smooth functions (differentiable), especially in insulators and semiconductors where the count of filled bands remains constant across all \mathbf{k} -points. In metals, however, band crossings and a complex Fermi surface lead to discontinuities associated with partial band filling. These functions are not differentiable at certain points, complicating the integration process and leading to slow SCF convergence when computing physical quantities on a uniform \mathbf{k} -mesh, although slightly better SCF convergence can be achieved using the tetrahedron method. To address this issue, the sharp transition at the Fermi surface, represented by the $F_{\mathbf{k}_m}^{occ}$ step function, is smoothed using a *smearing* approach, such as the Methfessel-Paxton (MP) method [231] employed in this thesis.

¹⁶When calculating physical quantities like electron density or total energy, integrals over continuous \mathbf{k} -space are needed: $\langle f \rangle = \Omega_{cell}/(2\pi)^3 \int_{BZ} F_{\mathbf{k}}^{occ} f(\mathbf{k}) d\mathbf{k}$. Since only a finite set of \mathbf{k} -points can be used, each point is assigned a weight based on the portion of reciprocal space it covers. Therefore, by applying symmetry operations, we can reduce the total number of \mathbf{k} -points required. These weights ensure that the sum over the \mathbf{k} -sampled BZ accurately approximates the integral.

¹⁷Tetrahedra are formed by four adjacent \mathbf{k} -points.

Smearing methods can be also used for other type of materials to enhance numerical stability and convergence near the Fermi level and to mimic finite temperature effects. Ultimately, physical quantities should be calculated in the limit of no smearing ($T \rightarrow 0$ K) to avoid dependence on the smearing method. Finally, we can calculate the electron density as:

$$n(\mathbf{r}) \cong \sum_{m=1}^{N_k} \omega_{\mathbf{k}_m} F_{\mathbf{k}_m}^{occ} n_{\mathbf{k}_m}(\mathbf{r}). \quad (2.29)$$

2.1.4.2 Pseudopotentials

In PW methods, Fourier expansions require prohibitively high E_{cut} near atomic cores due to rapid oscillations in wave function caused by deep potentials. To overcome this, core states are often “frozen”, meaning their form is precomputed from isolated atoms and assumed unchanged, as they do not contribute to bonding. This leads to the development of the *pseudopotential* method, where the core potential is replaced by a smoother, screened potential (see Figure 2.1), allowing for efficient treatment of valence electrons with smaller plane wave basis sets, compared with *all-electron* methods (like *augmented plane wave method* (APW) or *linearized augmented plane wave method* (LAPW)), which explicitly treat both core and valence electrons. Therefore,

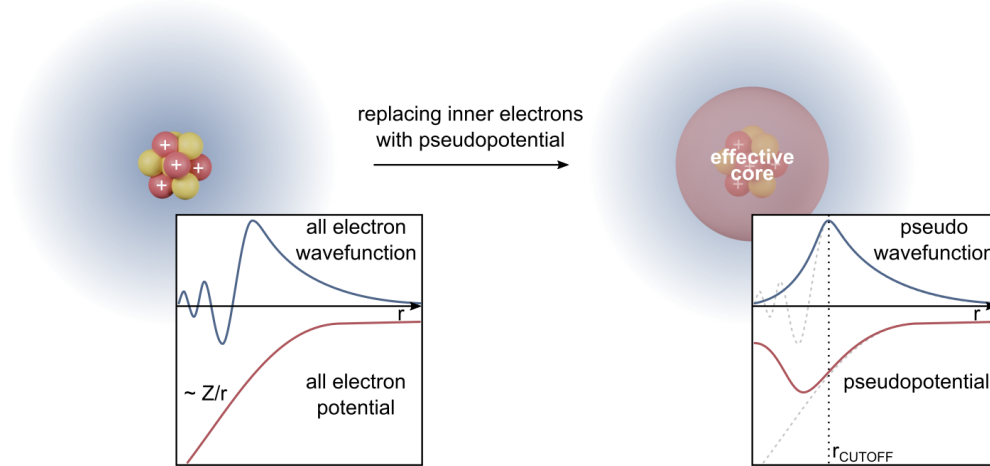


Figure 2.1: Schematic illustration of pseudopotential method <https://creativecommons.org/licenses/by-sa/4.0/>.

the all-electron KS orbital can be written as a linear combination of valence ϕ_v , and core ϕ_c wave functions:

$$\psi_{m,\mathbf{k}}^{PP} = \phi_v^{PP} = \phi_v + \sum_c \kappa_{vc} \phi_c, \quad (2.30)$$

with appropriate coefficients $\kappa_{vc} = \langle \phi_c | \phi_v^{PP} \rangle$ to maintain orthogonality between them. Now, the conventional KS hamiltonian can be expressed as:

$$[H^{KS} + \sum_c (\epsilon_c - \epsilon_v) \langle \phi_c | \phi_c \rangle] | \phi_v^{PP} \rangle = \epsilon_v | \phi_v^{PP} \rangle. \quad (2.31)$$

For example, in *norm-conserving* pseudopotentials (NCPs), the pseudopotential depends on the angular momentum quantum numbers l because the all-electron wave functions for different l -channels exhibit different behaviors near the core. For each l , the pseudopotential must reproduce the scattering properties of the all-electron wave function outside the cutoff radius r_{cut} , ensuring norm conservation within that region. This leads to the construction of semilocal pseudopotentials, where each l -channel has its own pseudopotential and cutoff radius. The norm-conservation condition for each l -channel is given by:

$$\int_0^{r_c} |\phi_{PP}^l(\mathbf{r})|^2 r^2 dr = \int_0^{r_c} |\phi_{ALL}^l(\mathbf{r})|^2 r^2 dr. \quad (2.32)$$

In contrast, *ultrasoft pseudopotentials* (USPPs) are applicable for larger r_c , making them “softer”, thereby reducing the required PW cutoff for calculations.

2.1.4.3 Projector-augmented wave method

The *projector augmented-wave* (PAW) method [232] is designed so to reduce computational costs while preserving the accuracy of presenting the true all-electron wave function. Like the PP method, PAW aims to differentiate between the rapidly oscillating core orbitals and the smoother valence orbitals. In PAW, the true atomic orbitals ψ_i are first obtained through an all-electron calculation. These orbitals are then transformed into smoother *pseudo wavefunction* $\tilde{\psi}_i$, which match the true orbitals ($\psi_i = \tilde{\psi}_i$) beyond a cutoff radius ($r > r_c^a$). The linear transformation, $\psi_i = \hat{T} \tilde{\psi}_i$, recovers the true wavefunctions. It is also useful to expand the pseudo wavefunction into pseudo *partial waves* $\tilde{\psi}_i = \sum_j c_j \tilde{\phi}_j$. Using projectors p_i^a that operate within the core region ($\langle p_i^a | \tilde{\phi}_j^a \rangle = \delta_{ij}, r < r_c^a$, and 0 for $r > r_c^a$), the transformation operator \hat{T} is defined as:

$$\hat{T} = 1 + \sum_i \left(| \phi_i^a \rangle - | \tilde{\phi}_i^a \rangle \right) \langle p_i^a |. \quad (2.33)$$

The final electron wavefunction can be expressed as:

$$|\psi_i\rangle = \hat{T}|\tilde{\psi}_i\rangle = |\tilde{\psi}_i\rangle + \sum_i \left(|\phi_i^a\rangle - |\tilde{\phi}_i^a\rangle \right) \langle p_i^a | \tilde{\psi}_i \rangle. \quad (2.34)$$

Based on this approach, the all-electron wavefunction is reconstructed from the smooth pseudo wavefunction by correcting the discrepancies between the true orbitals and the pseudo partial waves of the atoms within the *augmented sphere*, characterized by r_c^a . To preserve all-electron accuracy, the PAW method “*augments*” the pseudo wavefunctions within this region. Crucially, the augmented spheres for different types of atoms are designed to not overlap, ensuring that each type of atom’s core region is treated independently, and the augmentation remains localized. The electron density is therefore defined as:

$$n(\mathbf{r}) = \tilde{n}(\mathbf{r}) + \sum_a (n^a(\mathbf{r}) - \tilde{n}^a(\mathbf{r})). \quad (2.35)$$

Various software packages implement PAW method in DFT numerically, including Quantum ESPRESSO (QE) [233] or Vienna Ab initio Simulation Package (VASP) [234], which are mainly used in this thesis. Also all-electron DFT software package WIEN2k was used in this thesis [235].

2.2 Spin-dependent density functional theory (SDFT)

The literature sources used for this section are provided as Refs. [236, 237, 238, 239, 240].

2.2.1 Basic concept

For magnetic systems, in addition to the previously defined scalar (spin) $n(\mathbf{r})$, the vector of magnetization density $\mathbf{m}(\mathbf{r})$, must also be considered:

$$\mathbf{m}(\mathbf{r}) = -\mu_B \sum_{i=1}^N \langle \phi_i(\mathbf{r}) | \underline{\sigma} | \phi_i(\mathbf{r}) \rangle; \phi_i(\mathbf{r}) = \begin{pmatrix} \phi_i^\uparrow(\mathbf{r}) \\ \phi_i^\downarrow(\mathbf{r}) \end{pmatrix}, \quad (2.36)$$

where $\underline{\sigma}$ are the Pauli matrices.¹⁸ Also, the hermitian spin electron density matrix is defined as:

¹⁸In the following text, underlined symbols represent 2×2 matrices.

$$\underline{n}(\mathbf{r}) = \frac{1}{2}(n(\mathbf{r})\underline{\mathbb{I}} + \underline{\boldsymbol{\sigma}}\mathbf{m}(\mathbf{r})) = \begin{pmatrix} n(\mathbf{r}) + m_z(\mathbf{r}) & m_x(\mathbf{r}) - im_y(\mathbf{r}) \\ m_x(\mathbf{r}) + im_y(\mathbf{r}) & n(\mathbf{r}) - m_z(\mathbf{r}) \end{pmatrix}, \quad (2.37)$$

where $\underline{\mathbb{I}}$ is a unit matrix, and the elements of $\underline{n}(\mathbf{r})$ can be also written as $n_{\alpha\beta}(\mathbf{r}) = \sum_{i=1}^N \phi_i^{*\alpha} \phi_i^\beta$, so that $\alpha, \beta = (\uparrow, \downarrow)$. Now using the concept of spin-polarization in DFT method introduced by Barth and Hedin in 1972, we can write the KS equation (2.15) as:

$$\left[\left(-\frac{\hbar^2}{2m} \nabla^2 + \int \frac{e^2 n(\mathbf{r}')}{|\mathbf{r} - \mathbf{r}'|} d\mathbf{r}' \right) \underline{\mathbb{I}} + \underline{v}_{ext}(\mathbf{r}) + \underline{V}_{XC}(\mathbf{r}) \right] \begin{pmatrix} \phi_i^\uparrow(\mathbf{r}) \\ \phi_i^\downarrow(\mathbf{r}) \end{pmatrix} = \varepsilon_i \begin{pmatrix} \phi_i^\uparrow(\mathbf{r}) \\ \phi_i^\downarrow(\mathbf{r}) \end{pmatrix}, \quad (2.38)$$

so that the hamiltonian is invariant under spin rotations, and $\underline{v}_{ext}(\mathbf{r}) = v_{ext}(\mathbf{r})\underline{\mathbb{I}} + \mu_B \underline{\boldsymbol{\sigma}} \cdot \mathbf{B}(\mathbf{r})$, with $\mathbf{B}(\mathbf{r})$ as the applied magnetic field. Now, the $\underline{V}_{XC}(\mathbf{r})$ can be written as:

$$\underline{V}_{XC}(\mathbf{r}) = \frac{\delta E_{XC}}{\delta \underline{n}(\mathbf{r})} = V_{XC}(\mathbf{r})\underline{\mathbb{I}} + \mu_B \underline{\boldsymbol{\sigma}} \cdot \mathbf{B}_{XC}(\mathbf{r}). \quad (2.39)$$

If $\underline{v}_{ext}(\mathbf{r})$ and $\underline{V}_{XC}(\mathbf{r})$ matrices are diagonal, then equation (2.38) can be split into two separate equations, each corresponding to spin-up (\uparrow) and spin-down (\downarrow) case. In fact, this corresponds to the case where the magnetic moments are uniformly aligned along a single magnetization axis – typically the global z -axis (along the direction of magnetic field) – leading to what is known as *collinear* magnetization (such as ferromagnetic, or antiferromagnetic states). This results in a simplification where all physical quantities are expressed as functionals of $n(\mathbf{r})$ and the magnitude of $\mathbf{m}(\mathbf{r})$, so that the local *integral magnetic (spin) moment* of an atom becomes:¹⁹

$$M_a^{spin} = \left| \int_{\Omega_{atom}} \mathbf{m}(\mathbf{r}) d\mathbf{r} \right| = \int_{\Omega_{atom}} (n_\uparrow(\mathbf{r}) - n_\downarrow(\mathbf{r})) d\mathbf{r}. \quad (2.40)$$

In this approximation, the *local spin density approximation* (LSDA) functional – used instead of the local density approximation (LDA) (see equation (2.20)) – includes the spin-polarization effects:

$$E_{XC}^{LSDA} = \int n(\mathbf{r}) \varepsilon_{XC}^{uniform}([n_\uparrow(\mathbf{r}), n_\downarrow(\mathbf{r})]) d\mathbf{r}, \quad (2.41)$$

resulting in $V_{XC}^{\uparrow\uparrow} \propto [n_{\uparrow\uparrow}(\mathbf{r})]^{1/3}$ and $V_{XC}^{\downarrow\downarrow} \propto [n_{\downarrow\downarrow}(\mathbf{r})]^{1/3}$. While spin polarization improves calculations of lattice constants for 3d transition metals, LSDA still yields values lower than

¹⁹In units of μ_B .

experimentally observed. Gradient corrections are essential for accurately predicting lattice constants and magnetic moments, as demonstrated for ferromagnetic bulk Fe, where LSDA predicts a non-magnetic fcc ground state, while the inclusion of gradient corrections in the GGA results in a correct bcc structure but with a slightly higher magnetic moment compared to experimental values. Despite challenges in describing magnetic properties of some systems, SDFT remains a powerful tool for predicting magnetic behaviors in materials, and can be even expanded to derive the Stoner model of magnetism.

2.2.2 Relativistic DFT approach – the role of spin-orbit coupling (SOC)

The hamiltonian in equation (2.38) has limitations because it is derived from the spin-independent Schrödinger equation, meaning spin effects only enter indirectly through the wavefunction and the exchange-correlation potential via the Pauli exclusion principle, with interactions included in V_{XC} that are isotropic in space. This approach can predict magnetic order of the bulk system and the spin magnetic moment of an atom, but without a preferred magnetization axis, since there is no coupling between the spin space and lattice. Only by adding explicit spin-dependent terms to the hamiltonian one can describe magnetic anisotropy in the system, which is crucial for achieving long-range magnetic order in 2D systems that can not exist under the constraints of isotropic short-range interactions at non-zero temperature (Mermin-Wagner theorem) [241]. That means that the provided formulation captures Heisenberg-type interactions between two classical spins $H_H = \sum_{i<j} \mathbf{S}_i \mathbb{J}_{ij} \mathbf{S}_j$ ²⁰ were only trace of \mathbb{J}_{ij} can be derived neglecting thereby the full complexity of spin interactions. To extend this description, a more general relativistic DFT framework was introduced by Jansen, emphasizing the importance of spin-orbit coupling (SOC) for existence of magnetic anisotropy in systems [242]. To gain a general idea about SOC one can begin with the simple approach using the single-particle Pauli equation derived from relativistic Dirac equation, to obtain the term that couples the spin to the orbital angular momentum \mathbf{L} , so that the total magnetic moment is $\mathbf{M}_a^{tot} = \mathbf{M}_a^{spin} + \mathbf{M}_a^{orb}$. We can start with the hamiltonian of the Pauli equation written as:

$$H = H_{NR} + N_{SR} + \mathcal{C}_1 \underline{\sigma} \cdot (\nabla V(\mathbf{r}) \times \mathbf{p}) - \mathcal{C}_2 \underline{\sigma} \cdot \mathbf{B}(\mathbf{r}); \quad (2.42)$$

²⁰ \mathbb{J}_{ij} is the 3×3 exchange interaction tensor.

where $\mathcal{C}_1 = \hbar/(2mc)^2$, $\mathcal{C}_2 = e\hbar/2mc$, and the third term of H represents the spin-orbit interaction:

$$H_{SOC} = \mathcal{C}_1 \underline{\sigma} \cdot (\nabla V(\mathbf{r}) \times \mathbf{p}) = \mathcal{C}_1 \frac{1}{r} \frac{\partial V}{\partial r} \underline{\sigma} \cdot (\mathbf{r} \times \mathbf{p}) = \lambda^{SOC} \underline{\sigma} \cdot \mathbf{L}, \quad (2.43)$$

with λ^{SOC} as a SOC constant, and $M_a^{orb} = -\mu_B \sum_i \langle \phi_i | \mathbf{L} | \phi_i \rangle_a$. Thus, SOC is the result of relativistic effects where the spin of an electron interacts with its orbital movement within the electric potential created by the “shielded” nucleus. In electron’s reference frame, this electric field is perceived as a magnetic field, which interacts with the electron’s spin leading to its preferential orientation.

The inclusion of the H_{SOC} term in equation (2.38) not only couples the spin-up and spin-down states but also challenges the assumption that total energy remains invariant under spin rotations. Namely, the orientation of magnetization within a solid is not anymore arbitrary; instead, certain orientations become energetically favored. Such preference arises because the *crystal field* affects the electron’s orbital motion, imposing specific orientations for \mathbf{L} , which in turn influences the alignment of the spin \mathbf{S} through SOC. To calculate *magnetic anisotropy energy* (MAE), methods such as the *magnetic force theorem* and the *four-state method* (4SM) can be employed, both of which analyze the energy differences associated with varying directions of magnetization in a material. However, practical calculations using LSDA or GGA tend to underestimate orbital angular moments, resulting in lower-than-expected MAEs. Incorporating the Hubbard U correction for materials with localized d or f orbitals effectively addresses the limitations by capturing strong correlation effects, and also enhancing the magnetic moments, band gaps and other electronic properties. In addition, SOC contributes to the anisotropy in the interactions between magnetic moments, influencing both the symmetric (can lead to pseudodipolar interaction) and antisymmetric components (Dzyaloshinskii-Moriya interaction) of the \mathbb{J}_{ij} , with the latter arising as a first-order effect of SOC while the former appears as a second-order effect, which will be later discussed in more details.

2.2.3 The magnetic ground state

Determining the true magnetic ground state of a system with given structural properties requires the minimization of the total energy functional $E[\{\mathbf{e}_i\}]$, where \mathbf{e}_i represents the direction of the magnetic moments at each atomic position i in the unit/super cell. This process is complex due to the potential for multiple local minima on a high-dimensional energy landscape. In SDFT, one

starts with an “relaxation” of initial spin configuration and iteratively allowing the directions of e_i to change during SCF calculation, optimizing towards a lower energy state. However, reaching the true ground state can depend on the starting conditions, necessitating advanced techniques to efficiently explore configuration space and avoid getting stuck in a local energy minimum. The given SDFT results can be further mapped to classical Heisenberg model, in order to capture the magnetic interactions and further analyze both collinear and non-collinear configurations.

To consider an equation of motion for the atom’s magnetization while keeping the framework simple, one focuses on cases where the magnetization remains collinear within the atom’s vicinity. Beginning with equation (2.38) and assuming that $v_{ext}(\mathbf{r})$ is diagonal, with $V_{XC}(\mathbf{r})$ being divided into diagonal and off-diagonal parts, one derives a time-dependent – Antropov [243] – equation:

$$i \frac{d}{dt} \begin{pmatrix} \phi_i^\uparrow(\mathbf{r}) \\ \phi_i^\downarrow(\mathbf{r}) \end{pmatrix} = i \frac{d}{dt} \Phi(\mathbf{r}) = [H_d - \underline{\sigma} \cdot \mathbf{B}(\mathbf{r}, t)] \begin{pmatrix} \phi_i^\uparrow(\mathbf{r}) \\ \phi_i^\downarrow(\mathbf{r}) \end{pmatrix}, \quad (2.44)$$

where H_d is hamiltonian with diagonal parts. Also, at any particular moment t , the solution to equation (2.44) that does not depend on time can be derived for a given magnetization arrangement $\{e_i\}$. The equation of motion for $\mathbf{m}(\mathbf{r}, t)$ is then derived by multiplying equation (1.33) from the left by $-\mu_B \Phi^*(\mathbf{r}) \underline{\sigma}$ and adding the complex conjugate form to it:

$$\frac{d\mathbf{m}(\mathbf{r}, t)}{dt} = 2\mathbf{m}(\mathbf{r}, t) \times \mathbf{B}(\mathbf{r}, t) + \frac{i}{2} \nabla(\Phi^*(\mathbf{r}) \underline{\sigma} \cdot \nabla \Phi(\mathbf{r}) - c.c.). \quad (2.45)$$

Neglecting the complex second term, equation (2.45) can be simplified to describe the precession of atom’s magnetization direction due to the magnetic field from itself and surrounding atoms:

$$\frac{d\mathbf{e}_i}{dt} = \frac{2}{\mu_B} \mathbf{e}_i \times \mathbf{E}_i, \quad (2.46)$$

where $\mathbf{E}_i = -\mu_B \mathbf{B}$, so that the contributions stemming from the SOC – magnetic anisotropy – can be added to this term. Now, it is necessary to determine these terms for a given set of $\{\hat{e}_i\}$. Arbitrary magnetic configurations characterized by local magnetization directions $\{e_i\}$ of atoms typically do not yield stationary solution of $E[\underline{n}(\mathbf{r})]$. However, specific cases, such as high-symmetry magnetic arrangements – like collinear states or certain spin-spiral configurations – do present such stationary solutions. The *constrained* SDFT framework, introduced by Dederichs and colleagues [244], offers a generalized energy functional $\tilde{E}[\underline{n}(\mathbf{r})|\{e_i\}]$, ensuring that the

average local magnetization $\langle \mathbf{m} \rangle_i$ aligns with the specified direction \mathbf{e}_i , so that $\mathbf{e}_i \times \langle \mathbf{m} \rangle_i = 0$. This alignment is achieved through a constrained magnetic field \mathbf{B}_c^i , playing the role of the Lagrange multiplier so that:

$$\tilde{E}[\underline{n}(\mathbf{r})|\{\mathbf{e}_i\}] = E[\{\mathbf{e}_i\}] + \mu_B \sum_i \mathbf{B}_c^i \cdot \langle \mathbf{m} \rangle_i, \quad (2.47)$$

where $\underline{n}(\mathbf{r})$ and \mathbf{B}_c^i are determined through SCF calculation. This Lagrange multiplier method, combined within a penalty term in the energy functional [245], enables the generation and analysis of non-collinear magnetic states while allowing the relaxation of atomic and magnetic degrees of freedom. This approach introduces an effective potential that guides local magnetic moments toward specified orientations. By integrating this technique with a classical Heisenberg model, one can extract interatomic exchange parameters and anisotropy terms. This provides a robust framework for exploring magnetic interactions and understanding the behavior of complex systems, applicable to both ground and excited magnetic states.

2.3 Microscopic theory of magnetism

Since the 1960s, studies on quasi-2D magnetic systems, like layered K_2NiF_4 with in-plane long-range magnetic order, have paved the way for investigating magnetic interactions in low-dimensional systems using Ising, XY, and Heisenberg models (see Figure 2.2). Later, thin magnetic films, like NiFe and elemental films, led to advances in giant and tunneling magnetoresistance applications in hard drives and memory devices, respectively. The discovery of graphene and the emergence of tunable 2D vdW magnets like FePS_3 and CrI_3 transformed the field, providing platforms for spintronic applications. Recent efforts focus on Moiré magnetism in twisted 2D magnets, where spatially modulated exchange couplings due to Moiré patterns in systems like twisted CrI_3 generate complex alternating layered anti- and ferromagnetic domains, including noncollinear textures and skyrmions. Beyond traditional intrinsic 2D vdW magnets, other materials are being explored as platforms for inducing magnetism artificially. This approach, seen in studies on borophene and similar 2D materials, provides an alternative pathway to design tunable magnetic properties. Such artificially induced magnetism hold promise for applications in data storage and new spintronic devices, expanding the versatility and functionality of 2D magnetic systems.

The literature sources used for this section are provided as Refs. [247, 248, 249, 250, 251,

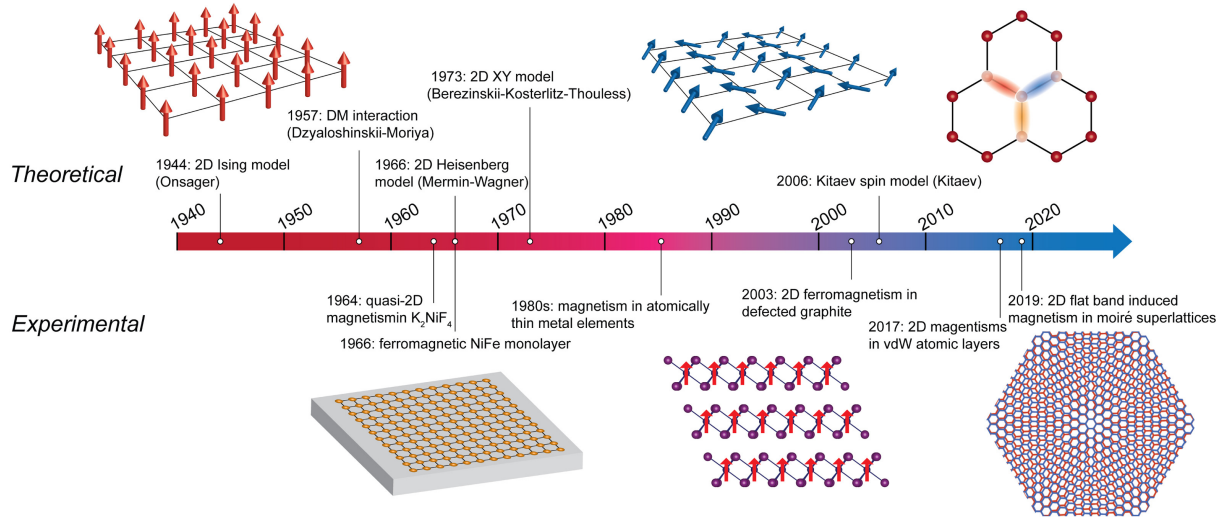


Figure 2.2: Timeline of key developments in 2D magnetism research, with the top panel showing theoretical milestones and the bottom panel highlighting experimental advances [246].

252, 253, 246]

2.3.1 Origin of magnetism

Magnetism is understood through quantum mechanics, as the Bohr–van Leeuwen theorem shows that thermal agitation in classical systems would cancel any equilibrium macroscopic *magnetic order*. At the atomic scale, magnetic moments (\mathbf{M}) arise from both the orbital motion ($\mathbf{M}^{orb} = -\mu_B \mathbf{l}$), and spin of electrons ($\mathbf{M}^{spin} = -g\mu_B \mathbf{s}$), each quantified by the Bohr magneton $\mu_B = \frac{e\hbar}{2m}$. When the quantization axis is chosen along the z -axis, an electron with state $|\phi_i\rangle$ described by quantum numbers n, l, m_l, m_s , has an orbital magnetic moment $M_{l_z} = -\mu_B m_l$, and a spin magnetic moment $M_{s_z} = -g\mu_B m_s$, with g -factor being ~ 2 . However, when a magnetic field is applied, the energy levels split according to $E = g\mu_B m_s B$, what is also known as *Zeeman splitting*.

In atoms with completely filled electron shells, zero net angular momentum is expected, as contributions from individual electrons cancel each other out: $\mathbf{J} = \sum_i \mathbf{l}_i + \sum_i \mathbf{s}_i = 0$, resulting in no atomic magnetic moment $\mathbf{M}_a^{tot} = 0$. Consequently, only unfilled electron shells contribute to a non-zero total angular momentum ($\mathbf{J} \neq 0$) and therefore also magnetic moment ($\mathbf{M}_a^{tot} \neq 0$). In these cases, the overall orbital angular momentum ($\mathbf{L} = \sum_i \mathbf{l}_i$), and spin ($\mathbf{S} = \sum_i \mathbf{s}_i$), are weakly coupled through SOC ($\lambda^{SOC} \mathbf{L} \cdot \mathbf{S}$). Due to SOC, the total angular momentum \mathbf{J} is conserved, and states with given values of L and S split into multiple levels with different J ($J \in \{|L - S|, \dots, L + S\}$), known as the *fine structure*. When an external magnetic field

is applied, these fine structure levels split further due to the Zeeman effect, with the splitting obeying the Landé interval rule, with $\Delta E = \lambda^{SOC} J$. However, to find the ground state of an isolated atom, Hund's rules are applied: (1) the electron wave function is arranged to maximize the total spin quantum number S , minimizing thereby Coulomb repulsion via the Pauli exclusion principle; (2) Then, the orbital angular momentum L is maximized to further reduce Coulomb repulsion through spatial distribution; (3) Finally, the total angular momentum J is determined based on electron occupancy within the shell: J equals $|L - S|$ for shells with occupancy below half and $L + S$ for those exceeding half-filled.

To study the impact of a crystal's local environment on an atom's energy levels it is essential to consider both the symmetry of the nearby point-charge arrangement and the "way" orbitals overlap. In a crystal, surrounding atoms (ligands) create an electric field that perturbs the energy of the metal ion's atomic orbitals. This *crystal field*, which depends on the local (point) symmetry (such as octahedral (O_h) or tetrahedral (T_h) arrangements), splits the otherwise degenerate d -orbitals (in spherically symmetric environment) due to differences in overlap with ligand orbitals, as depicted in Figure 2.3(a). In an octahedral environment, t_{2g} triplet (d_{xy}, d_{xz}, d_{yz}) points between the axes, experiencing less direct overlap and thus lower electrostatic repulsion, resulting in lower energy. Conversely, e_g doublet ($d_{z^2}, d_{x^2-y^2}$), which aligns along the axes toward the ligands, exhibit stronger overlap and higher energy due to increased electrostatic repulsion (see Figure 2.3(b)). Therefore, the electron configuration within the $3d$ orbitals depends on the competition between crystal field splitting energy (Δ_O) and *pairing energy*, adhering to Hund's rule within each orbital set. When Δ_O is less than the pairing energy (weak-field case), electrons occupy each t_{2g} orbital singly, before pairing, resulting in a *high-spin state* with maximal unpaired electrons. Conversely, when Δ_O exceeds the pairing energy (strong-field case), electrons pair within the lower t_{2g} orbitals, leading to a *low-spin* configuration. In a tetrahedral field, the symmetry changes the pattern: e_g orbitals avoid direct ligand alignment and thus have lower energy compared to t_{2g} orbitals. Furthermore, in cases where d -electrons in a transition metal ion partially occupy degenerate orbitals in a symmetric configuration, such as the O_h , the system itself tends to spontaneously lower the energy by lifting the degeneracy through lattice distortion, reducing thereby the symmetry, referred to as the Jahn-Teller (JT) effect. Conversely, when considering the influence of SOC (seen now as a weak perturbation) for ions with an e_g doublet, the orbital moment is quenched $L \rightarrow 0$, and SOC contributes only as a second-order perturbation term (single ion anisotropy or anisotropic g). In contrast, for ions with partially

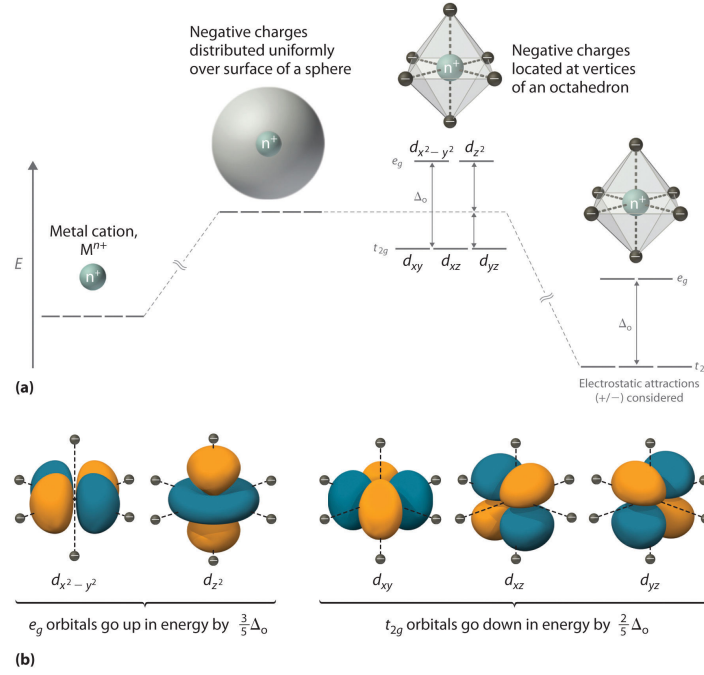


Figure 2.3: (a) An uniform distribution of charge raises the energy of all d orbitals equally, while an octahedral charge distribution causes the d_{z^2} and $d_{x^2-y^2}$ orbitals to increase in energy, while the d_{xy} , d_{xz} , and d_{yz} orbitals decrease in energy. (b) The e_g orbitals, pointing directly at the ligands, have higher energy, while the t_{2g} orbitals, oriented between the ligands, have lower energy <https://creativecommons.org/licenses/by-nc-sa/4.0/>.

asymmetric filled t_{2g} levels, the orbital moment remains active (particularly for heavier ions), with SOC contributing as first-order perturbation (splitting of states), with effective magnetic moment magnitude $\tilde{g}_J \mu_B \sqrt{\tilde{J}(\tilde{J} + 1)}$. The effective $\tilde{\lambda}^{SOC}$, opposite in sign to λ^{SOC} , reverses the energy ordering of t_{2g} states for less and more than half-filled shells. Furthermore, as SOC increases with atomic number (e.g., $\lambda \sim Z^4$), the JT effect is stronger for lighter $3d$ elements, while SOC dominates in heavier $3d$ elements.

So far, we have focused on understanding the origins and behaviors of atomic magnetic moments within crystal fields. However, to fully explain the collective magnetic behavior that results in long-range magnetic order, we need to consider the interactions between magnetic atoms. Although the magnetic dipolar interaction is always present, it is generally too weak to drive ordering in most materials, as it only significantly influences systems below 1 K. Instead, stronger interactions rooted in quantum mechanics – the Pauli exclusion principle, Coulomb interaction, or electron hopping (kinetic exchange) – create the effective *exchange coupling mechanism* as the main source of macroscopic magnetism. As we previously mentioned, Hund’s first rule (*intraatomic-exchange*) postulates that electrons occupy atomic orbitals to maximize spin, reducing Coulomb repulsion and stabilizing the system’s energy through the

Pauli exclusion principle. If we consider a simple *two-electron problem* in single atom ($H_{12} = \hat{h}_0(\mathbf{r}_1) + \hat{h}_0(\mathbf{r}_2) + \frac{e^2}{|\mathbf{r}_1 - \mathbf{r}_2|}$), the total wave function $\phi_{a,b}(\mathbf{r}) = \varphi_{a,b}(\mathbf{r})\chi$ – with φ_a and φ_b being orthogonal eigenstates of $\hat{h}_0(\mathbf{r})$, and $\chi \in \{\alpha, \beta = (\uparrow, \downarrow)\}$ being the spin part – must be antisymmetric with respect to the exchange of both electrons, thus deriving:

$$\begin{cases} |\uparrow\uparrow\rangle = \frac{1}{\sqrt{2}}\alpha_1\alpha_2[\varphi_a(\mathbf{r}_1)\varphi_b(\mathbf{r}_2) - \varphi_a(\mathbf{r}_2)\varphi_b(\mathbf{r}_1)]; & (2.48) \\ |\uparrow\downarrow\rangle = \frac{1}{\sqrt{2}}[\varphi_a(\mathbf{r}_1)\varphi_b(\mathbf{r}_2)\alpha_1\beta_2 - \varphi_a(\mathbf{r}_2)\varphi_b(\mathbf{r}_1)\alpha_2\beta_1]. & (2.49) \end{cases}$$

In the absence of electron-electron interaction all four configurations $\{|\uparrow\uparrow\rangle, |\uparrow\downarrow\rangle, |\downarrow\uparrow\rangle, |\downarrow\downarrow\rangle\}$ are degenerate eigenstates of H_{12} with eigenvalue $\epsilon_a + \epsilon_b$, while in its presence we have:

$$H_{12} = (\epsilon_a + \epsilon_b)\mathbb{1} + \begin{pmatrix} U_{ab} - J_{ab} & 0 & 0 & 0 \\ 0 & U_{ab} & -J_{ab} & 0 \\ 0 & -J_{ab} & U_{ab} & 0 \\ 0 & 0 & 0 & U_{ab} - J_{ab} \end{pmatrix}, \quad (2.50)$$

where U_{ab} and J_{ab} are *Coulomb* and *exchange integrals*, respectively. They are defined as:

$$\begin{cases} U_{ab} = \langle\uparrow\downarrow|\frac{e^2}{|\mathbf{r}_1 - \mathbf{r}_2|}|\uparrow\downarrow\rangle = e^2 \iint \frac{|\varphi_a(\mathbf{r}_1)|^2|\varphi_b(\mathbf{r}_2)|^2}{|\mathbf{r}_1 - \mathbf{r}_2|} d\mathbf{r}_1 d\mathbf{r}_2 > 0; & (2.51) \\ J_{ab} = \langle\uparrow\downarrow|\frac{e^2}{|\mathbf{r}_1 - \mathbf{r}_2|}|\downarrow\uparrow\rangle = e^2 \iint \frac{\varphi_a^*(\mathbf{r}_1)\varphi_b(\mathbf{r}_1)\varphi_b^*(\mathbf{r}_2)\varphi_a(\mathbf{r}_2)}{|\mathbf{r}_1 - \mathbf{r}_2|} d\mathbf{r}_1 d\mathbf{r}_2 > 0. & (2.52) \end{cases}$$

By diagonalizing the hamiltonian, the resulting eigenstates are obtained as follows:

$$\begin{cases} |\phi_s\rangle = \frac{1}{\sqrt{2}}(|\uparrow\downarrow\rangle - |\downarrow\uparrow\rangle), \text{ with } \epsilon_s = \epsilon_a + \epsilon_b + U_{ab} + J_{ab}; & (2.53) \\ |\phi_t\rangle = \frac{1}{\sqrt{2}}(|\uparrow\downarrow\rangle + |\downarrow\uparrow\rangle), |\uparrow\uparrow\rangle, |\downarrow\downarrow\rangle \text{ with } \epsilon_t = \epsilon_a + \epsilon_b + U_{ab} - J_{ab}, & (2.54) \end{cases}$$

thus, the triplet states $|\phi_t\rangle$ have lower energy than the singlet states $|\phi_s\rangle$ due to $J_{ab} > 0$, reflecting the ferromagnetic intraatomic exchange ($S = 1$) as dictated by Hund's first rule.²¹

Let us now consider the general case of non-orthogonal orbitals on atoms with nuclei at positions \mathbf{R}_a and \mathbf{R}_b , where each electron can be localized on either \mathbf{R}_a or \mathbf{R}_b – *interatomic exchange*.

Thus, we define the orbitals as $\varphi_a = \varphi_{at}(\mathbf{r} - \mathbf{R}_a)$ and $\varphi_b = \varphi_{at}(\mathbf{r} - \mathbf{R}_b)$. The overlap integral

²¹In the triplet state ($S = 1$), the spatial wavefunction is antisymmetric, and the spin wavefunction is symmetric, and the possible spin projections are $m_s = -1, 0, 1$. In contrast, the singlet state ($S = 0$) has an antisymmetric spin wavefunction paired with a symmetric spatial wavefunction.

is given by $l = \int \varphi_a(\mathbf{r})\varphi_b(\mathbf{r})d\mathbf{r}$. For the hamiltonian $H_{at}(\mathbf{r} - \mathbf{R})\varphi_{at}(\mathbf{r} - \mathbf{R}) = \epsilon_{at}\varphi_{at}(\mathbf{r} - \mathbf{R})$, we obtain six eigenstates: four correspond to electrons on different orbitals representing *covalent* states $\{|\uparrow, \uparrow\rangle, |\uparrow, \downarrow\rangle, |\downarrow, \uparrow\rangle, |\downarrow, \downarrow\rangle\}$, and two represent *ionized* configurations in which both electrons occupy the same orbital on the same atom $\{|\uparrow\downarrow, 0\rangle, |0, \uparrow\downarrow\rangle\}$. For covalent states, one can again obtain singlet and triplet eigenstates, with:²²

$$\epsilon_t - \epsilon_s = 2 \frac{l^2 U_{ab} - J_{ab}}{1 - l^4}, \quad (2.55)$$

so that for $l = 0$, a ferromagnetic interaction occurs, yielding an energy difference $\epsilon_t - \epsilon_s = -2J_{ab}$. In contrast, for $l \neq 0$, the interaction can become antiferromagnetic, with $\epsilon_t > \epsilon_s$. At moderate interatomic distances, chemical bonding arises in the singlet state (bonding orbitals) due to the attraction of electrons to both nuclei, which outweighs repulsion between them. The triplet states, with the same spin alignment, do not form a bond due to the Pauli principle. The Heitler-London scheme, using two-electron wavefunctions, successfully captures bonding effects and many-body interactions better than molecular orbital theory. However, it has limitations at extreme distances: ionized states disrupt accuracy at small separations, while dynamic correlations stabilize the triplet at large separations ($l \rightarrow 0$), inconsistent with exact solutions. Therefore, for the ionized configurations with $l = 0$, one obtains:

$$\begin{cases} |\phi_a\rangle = \frac{1}{\sqrt{2}}[\alpha_1\beta_2 - \beta_1\alpha_2]\varphi_a(\mathbf{r}_1)\varphi_a(\mathbf{r}_2); \\ |\phi_b\rangle = \frac{1}{\sqrt{2}}[\alpha_1\beta_2 - \beta_1\alpha_2]\varphi_b(\mathbf{r}_1)\varphi_b(\mathbf{r}_2), \end{cases} \quad (2.56)$$

$$\begin{cases} |\phi_a\rangle = \frac{1}{\sqrt{2}}[\alpha_1\beta_2 - \beta_1\alpha_2]\varphi_a(\mathbf{r}_1)\varphi_a(\mathbf{r}_2); \\ |\phi_b\rangle = \frac{1}{\sqrt{2}}[\alpha_1\beta_2 - \beta_1\alpha_2]\varphi_b(\mathbf{r}_1)\varphi_b(\mathbf{r}_2), \end{cases} \quad (2.57)$$

with the on-site Coulomb repulsion²³ $U = \langle \varphi_a | \frac{e^2}{|\mathbf{r}_1 - \mathbf{r}_2|} | \varphi_a \rangle$ taken to be strong ($U > U_{ab}$, as well as $U > J_{ab}$). These configurations are symmetrized into parity-even $|\phi_1\rangle = \frac{1}{\sqrt{2}}(|\phi_a\rangle + |\phi_b\rangle)$, and parity-odd $|\phi_2\rangle = \frac{1}{\sqrt{2}}(|\phi_a\rangle - |\phi_b\rangle)$ states with parity determined by the inversion center located at the midpoint of the bond.²⁴ Let us consider two electrons of opposite spin with basis states $\{|\uparrow, \downarrow\rangle, |\downarrow, \uparrow\rangle, |\uparrow\downarrow, 0\rangle, |0, \uparrow\downarrow\rangle\}$ while assuming a large Coulomb repulsion U , so that condition $t \ll U$ holds (*Mott insulators – localized magnetic moments*), where t is the transfer integral²⁵ representing the probability of electron hopping between sites. The strongly correlated systems are difficult to describe and the total hamiltonian can not be fully diagonalized if U is not large,

²²The expressions for U_{ab} and J_{ab} differ from the previous definitions but retain the same physical meaning.

²³Also known as the Hubbard effective repulsion.

²⁴ $|\phi_s\rangle$ is parity-even and $|\phi_t\rangle$ is parity-odd.

²⁵ $-t = \int \varphi_{at}^*(\mathbf{r} - \mathbf{R}_a) \frac{e^2}{|\mathbf{r} - \mathbf{R}_b|} \varphi_{at}(\mathbf{r} - \mathbf{R}_b)$.

so in general case it is good to use the *downfolding* technique to partition the Hilbert space into low-energy covalent states of interest and high-energy ionic states that are effectively projected out:

$$\left(\begin{array}{cc|cc} 0 & 0 & -t & -t \\ 0 & 0 & t & t \\ \hline -t & t & U & 0 \\ -t & t & 0 & U \end{array} \right) \rightarrow \begin{pmatrix} -t & -t \\ t & t \end{pmatrix} \begin{pmatrix} \epsilon - U & 0 \\ 0 & \epsilon - U \end{pmatrix}^{-1} \begin{pmatrix} -t & t \\ -t & t \end{pmatrix} \approx -\frac{2t^2}{U} \begin{pmatrix} 1 & -1 \\ -1 & 1 \end{pmatrix}, \quad (2.58)$$

with $\epsilon = 0$ for covalent states. This approximation describes an effective interaction between the covalent states, with singlet state being energetically lower than the one triplet state by $\frac{4t^2}{U}$, a result of the *kinetic exchange* process driven by electron hopping. The other triplet states $\{|\uparrow, \uparrow\rangle, |\downarrow, \downarrow\rangle\}$ have also zero energy because hopping is not possible due to the Pauli principle. Also, in highly correlated electron systems, the energy associated with ionized states is typically higher than that of covalent states by an amount proportional to the U . Now, the equation (2.55) can be rewritten as:

$$\epsilon_t - \epsilon_s = \frac{4t^2}{U} + 2\frac{l^2 U_{ab} - J_{ab}}{1 - l^4}, \quad (2.59)$$

with first term being *kinetic exchange* favoring antiferromagnetic ordering, and the second term being *potential exchange* favoring ferromagnetic ordering. Magnetic interactions in most insulating transition-metal compounds arise from the interplay of these two terms, described by the Goodenough–Kanamori–Anderson (GKA) rules [254, 255, 256], as depicted in Figure 2.4. The GKA rules are explaining exchange interactions in terms of ligand (L) mediated couplings between magnetic ions (TM). In 180° configuration, virtual hopping between TM–L–TM is allowed only for antiparallel spins, leading to antiferromagnetic coupling if both TMs have half-filled orbitals. In contrast, 90° configuration involves the overlap of d -orbitals with two different p -orbitals, where Hund’s coupling favors parallel spins in the ligand, leading to a weakly ferromagnetic coupling. The exchange interactions are stronger for the 180° geometry and weaker for the 90° case. Anderson’s approach, which uses Wannier functions (see **APPENDIX A1**) to describe the overlap of d -orbitals with ligand p -orbitals, clarifies this interaction by reducing the complex TM–L–TM process to a simpler two-electron model. In the 180° case, the Wannier functions overlap significantly, leading to a large t and therefore strong kinetic exchange, while in the 90° geometry, the Wannier functions are orthogonal ($t = 0$), and potential

exchange dominates. In the multi-orbital case, Anderson’s approach is more suitable for treating

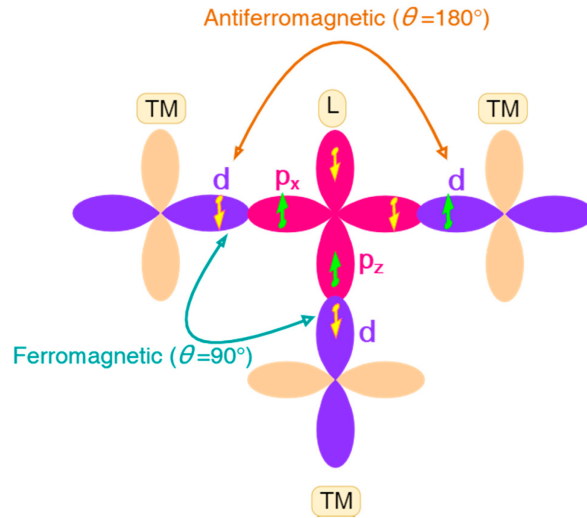


Figure 2.4: A schematic diagram illustrating exchange interactions between TMs with more than half-filled d-shells according to the GKA rules [253].

interactions between half-filled, fully filled, and empty orbitals. In contrast to the one-orbital case, the multi-orbital scenario allows for electron hopping between a half-filled and an empty orbital. This hopping lowers the energy in a ferromagnetic configuration due to Hund’s coupling (J_H), and the energy gain is described by $\frac{4t_e^2}{U-J_H}$, so that $\epsilon_t - \epsilon_s \cong -\frac{4t_e^2}{U} \frac{J_H}{U}$. This leads to a ferromagnetic kinetic exchange, smaller than the antiferromagnetic kinetic exchange because $J_H \ll U$, yet, multiple unoccupied orbitals might be accessible, potentially enhancing the ferromagnetic effect leading to so called *weak ferromagnetism*. However, if one atom possesses a half-occupied orbital and the other an unoccupied one with identical symmetry, the hopping term to the empty orbital $t_e > t$, changes the usual GKA rules: now 180° geometries become ferromagnetic, and 90° ones become antiferromagnetic. Anderson’s approach consolidates the concepts of direct (direct overlap of TM orbitals) and super-exchange²⁶ (TM–L–TM) by introducing kinetic and potential exchange. This framework applies uniformly, regardless of whether ligands mediate the interactions, and in practice it is also difficult to distinguish between magnetic interactions due to orbital overlap or ligand mediation.

2.3.2 Mapping SDFT results to Heisenberg’s spin hamiltonian

Having discussed the exchange interactions as the quantum mechanism for spin alignment, the Heisenberg’s spin hamiltonian precisely models these interactions by quantifying the energy

²⁶Often called indirect, and if more ligands mediate the interaction super-super-exchange interaction.

of spin coupling between neighbors. This formalism directly captures magnetic phenomena enabling detailed analysis of spin order and dynamics. The Heisenberg's spin hamiltonian²⁷ is written as:

$$H_H = \left\{ \sum_{i<j} J_{ij} \hat{\mathbf{S}}_i \hat{\mathbf{S}}_j + H_{Zeeman} + H_{sym}^{ani} + \sum_{i<j} \mathbf{D}_{ij} \cdot (\hat{\mathbf{S}}_i \times \hat{\mathbf{S}}_j) + \sum_i A_{ii} \hat{\mathbf{S}}_i^2 \right\} + H_{biquadratic} + H_{ring} + \dots = \{ H_{sym}^{iso} + H_{Zeeman} + H_{sym}^{ani} + H_{asym}^{DMI} + H_{SIA} \} + H_{h.o.}, \quad (2.60)$$

where the terms in $\{ \}$ are part of the conventional Heisenberg model, which account for pairwise interactions, while higher-order interactions (beyond bilinear such as biquadratic terms or ring interactions) arise as corrections that can refine the model. The quantum spin hamiltonian in equation (2.60) applies to both spin and angular momentum operators, which can represent pure spin moments, orbital moments, or their combinations. For weak SOC, the spin moment is modified by a small orbital contribution, while for strong SOC, the total angular momentum is used. In classical approximations, spin operators are replaced by spin vectors ($\hat{\mathbf{S}} \rightarrow \mathbf{S}$), which simplifies the problem, especially in ferromagnetic systems where energy does not depend on the quantum nature of spins. However, for antiferromagnetic systems, quantum effects are crucial, with quantum behavior becoming more pronounced as spin decreases. The previously described exchange interaction between the i -th and j -th spin sites, in its *symmetric* and isotropic Heisenberg form, is responsible for ferromagnetic ($J_{ij} < 0$) and antiferromagnetic ($J_{ij} > 0$) ordering. However, due to SOC, magnetic anisotropy is induced, with the Dzyaloshinskii-Moriya interaction (DMI) [257, 258] strength scaling as $|\mathbf{D}| \sim \lambda^{SOC}$, and symmetric anisotropy scaling as λ_{SOC}^2 . This scaling is particularly valid in systems where $L \ll S$, such as 3d transition metals.

The DMI arises from the interplay between SOC and the underlying crystal symmetry, particularly in systems that lack spatial inversion symmetry. The DMI is typically considered as the *antisymmetric* exchange term H_{asym}^{DMI} in equation (2.60). The vector \mathbf{D}_{ij} ($|\mathbf{D}_{ij}| \sim \frac{\lambda^{SOC}}{\Delta_0} J_{ij}$) is pointed perpendicular to the plane containing both spins. It favors non-collinear spin configurations by inducing a slight canting of spins, aligning them nearly orthogonal to each other and to DMI vector. This mechanism competes with the Heisenberg's symmetric exchange

²⁷The Heisenberg model ($O(n=3)$) describes spins as 3D vectors, accounting for full rotational symmetry in spin space. Without anisotropy, the 2D isotropic Heisenberg model has no phase transition at finite temperatures, as continuous symmetry breaking is forbidden by the Mermin-Wagner theorem. When the spin dimensionality reduces to $O(n=2)$, the system transitions to the XY model. Such systems experience the Berezinskii-Kosterlitz-Thouless (BKT) "topological" phase transition, leading to quasi-long-range order at finite temperatures and the formation of spin vortex-antivortex pairs. For $O(n=1)$ the system follows the Ising model, where spins are constrained to a single axis. Onsager's solution of the 2D Ising model predicts long-range magnetic order at finite temperatures.

interaction. The relative magnitude of the DMI to the Heisenberg symmetric exchange ($\frac{|D_{ij}|}{|J_{ij}|}$) determines whether chiral spin structures, such as skyrmions and helices, can emerge, as well as weak ferromagnetism and magnetoelectric effect in multiferroic materials. Also, by combining H_{sym}^{iso} with H_{asym}^{DMI} one gets $H_H^{EX} = \sum_{i<j} J_{ij} \mathbf{S}_i \mathbf{S}_j$. Unlike DMI, the *symmetric anisotropic exchange* ($H_{sym}^{ani} = \sum_{i<j} J_{ij}^{ani} \mathbf{S}_i \mathbf{S}_j$) introduces direction-dependent exchange interactions, due to crystal symmetry and SOC, that remain symmetric under spin reversal and prefer specific crystallographic axes. And finally we will describe the *single ion anisotropy* H_{SIA} term, which is lowest order contribution to the MAE, so that: $E_{MAE} \propto \frac{\lambda_{SOC}^2}{\Delta_0} + \frac{\lambda_{SOC}^4}{\Delta_0^3} + \dots$, where for octahedral geometry the quadratic contribution would vanish [259].

Now we can focus on methods for mapping SDFT results to the Heisenberg hamiltonian, specifically using the 4SM and TB2J approach. These methods, based on energy-mapping techniques and Green's functions by taking the local spin rotation as a perturbation, respectively, allow for the extraction of spin interaction parameters, assuming periodic boundary conditions, and are essential for understanding exchange couplings in magnetic materials.

2.3.2.1 Four-state method (4SM)

In order to describe the 4SM we will present the main points of the the work of Denis Šabani and colleagues [260]. The methodology for calculating all elements of J_{ij} is demonstrated using the magnetic exchange element J_{12} for two arbitrarily chosen spin sites ($i = 1$, and $j = 2$), specifically the J_{12}^{xz} element, which is linked to the y -component of the DMI vector. To isolate J_{12}^{xz} , the energy values of the four unique magnetic states of the lattice must be evaluated:

$$\left\{ \begin{array}{l} \text{State 1 : } \mathbf{S}_1 = (+S, 0, 0), \mathbf{S}_2 = (0, 0, +S); \\ \text{State 2 : } \mathbf{S}_1 = (+S, 0, 0), \mathbf{S}_2 = (0, 0, -S); \\ \text{State 3 : } \mathbf{S}_1 = (-S, 0, 0), \mathbf{S}_2 = (0, 0, +S); \\ \text{State 4 : } \mathbf{S}_1 = (-S, 0, 0), \mathbf{S}_2 = (0, 0, -S); \\ \text{Other spins : } \mathbf{S}_{i \neq 1,2} = (0, +S, 0) \text{ or } \mathbf{S}_{i \neq 1,2} = (0, -S, 0). \end{array} \right.$$

Subtracting the energies of states 2 and 3 from states 1 and 4, leaves a term proportional to the parameter of interest:

$$J_{12}^{xz} = \frac{E_1 + E_4 - E_2 - E_3}{4S^2} \rightarrow J_{ij}^{\alpha\beta} = \frac{E_1 + E_4 - E_2 - E_3}{4S^2}, \quad (2.61)$$

with the derivation for other matrix elements being analogous, where $\alpha, \beta = x, y, z$ and $J_{ij}^{\alpha\beta} \neq J_{ij}^{\beta\alpha}$ for $\alpha \neq \beta$. In the special case, when the matrix is antisymmetric ($J_{ij}^{\alpha\beta} = -J_{ij}^{\beta\alpha}$), the DMI components can be simplified to: $D_{ij}^x = J_{ij}^{yz} = -J_{ij}^{zy}$, $D_{ij}^y = J_{ij}^{zx} = -J_{ij}^{xz}$, and $D_{ij}^z = J_{ij}^{xy} = -J_{ij}^{yx}$. To complete the analysis, the SIA parameters are considered, which govern spin interactions within a single ion. Unlike J_{ij} , the SIA matrix A_{ii} must be symmetric due to the equivalent nature of interactions between, e.g. S_i^α and S_i^β , and S_i^β and S_i^α . Additionally, each component can be expressed in terms of the total spin S and other components. As a result, only three upper (or lower) elements need to be calculated for the off-diagonal SIA terms, and two reduced terms suffice for the diagonal elements. By following the same procedure, for off-diagonal element A_{11}^{xy} by choosing 4 states $\{(\pm S\frac{\sqrt{2}}{2}, \pm S\frac{\sqrt{2}}{2}, 0)\}$, with other spins $\mathbf{S}_i = (0, 0, +S)$, and for diagonal $A_{11}^{yy} - A_{11}^{xx}$ the following states $\{(0, +S, 0), (0, -S, 0), (S, 0, 0), (-S, 0, 0)\}$, with other spins $\mathbf{S}_i = (0, 0, +S)$, one can obtain the general formula for off-diagonal and diagonal SIA elements, respectively:

$$A_{ii}^{\alpha\beta} = \frac{E_1 + E_4 - E_2 - E_3}{4S^2}; \quad A_{ii}^{\alpha\alpha} - A_{ii}^{xx} = \frac{E_1 + E_2 - E_3 - E_4}{2S^2}. \quad (2.62)$$

In general material analysis, all five elements of the SIA matrix must be determined. However, for (quasi-)2D materials with 3-, 4-, or 6-fold rotational symmetry with respect to an axis perpendicular to the plane, the SIA can be described by a single term $A_{zz} - A_{xx}$. Therefore, for systems with four-state configurations, constrained SDFT calculations are used to enforce specific magnetic orderings, allowing the accurate determination of magnetic interaction parameters.

2.3.2.2 TB2J - Green's function method

TB2J can calculate exchange terms, and higher-order interactions like biquadratic terms, however, unlike 4SM it does not directly provide the SIA because the formalism is based on localized and orthogonal Wannier functions, which require SOC to be incorporated separately during the Wannierization process, as handled by tools like Wannier90 code (see **APPENDIX A1**). In the Green's function approach of Xu He and colleagues [261], rooted in magnetic-force linear response theory, localized basis functions $\phi_{il\sigma}(\mathbf{r})$ (like Wannier functions) are used, where i , l , and σ represent the site, orbital, and spin indices, respectively. These basis functions are included within the framework of the tight-binding model. After defining tight-binding hamiltonian $\mathbb{H}_{ilj'l'\sigma\sigma'}(\mathbf{R}) = \langle \phi_{il\sigma}(\mathbf{r}) | H | \phi_{il'\sigma'}(\mathbf{r} + \mathbf{R}) \rangle$, the overlap matrix

$\mathbb{S}_{ilj'l'\sigma\sigma'}(\mathbf{R}) = \langle \phi_{il\sigma}(\mathbf{r}) | \phi_{il'\sigma'}(\mathbf{r} + \mathbf{R}) \rangle$,²⁸ and Green's function $\mathbb{G}(\mathbf{R}, \epsilon) = \int_{BZ} \mathbb{G}(\mathbf{k}, \epsilon) e^{-i\mathbf{k}\mathbf{R}} d\mathbf{k}$, for each atom i , the intraatomic component of the \mathbb{H} is $\mathbb{P}_i = \mathbb{H}_{ii}(\mathbf{R} = 0)$, so that each 2×2 spin matrix $\mathbb{P}_{il'}$ is decomposed into scalar and vector part, respectively: $\mathbb{P}_{il'} = p_{il'}^0 I + p_{il'} \mathbf{e}_{il'} \boldsymbol{\sigma}$. By assuming strong intraatomic exchange, the local spin moment \mathbf{S}_i is parallel to the \mathbf{p}_i , hence the unit orientation vector $\mathbf{e}_{il'} = \mathbf{S}_i$. In the same way it is possible to decompose the Green's function for each inter-site orbital pair $\mathbb{G}_{ilj'l'} = G_{ilj'l'}^0 I + \mathbf{G}_{ilj'l'} \boldsymbol{\sigma}$. Using the magnetic force theorem, the change in total energy caused by a perturbation – specifically the spin rotation – can be expressed as the difference in single-particle energies, while keeping the ground state potential fixed:

$$\delta E = \int_{-\infty}^{E_F} \epsilon \delta n(\epsilon) d\epsilon = - \int_{-\infty}^{E_F} \delta N(\epsilon) d\epsilon, \quad (2.63)$$

where $n(\epsilon) = -\frac{1}{\pi} \text{Im Tr}(\mathbb{G}(\epsilon))$ is DOS, and $N(\epsilon) = -\frac{1}{\pi} \text{Im Tr}(\epsilon - \mathbb{H})$ is integrated DOS. Now, the energy variation due to the interaction between spins at sites i and j is given by:

$$\delta E_{ij} = -\frac{2}{\pi} \int_{-\infty}^{E_F} \text{Im Tr}(\delta \mathbb{H}_i \mathbb{G} \delta \mathbb{H}_j \mathbb{G}) d\epsilon, \quad (2.64)$$

where the $\delta \mathbb{H}$ due to spin rotation is given by $\delta \boldsymbol{\theta} \times \overrightarrow{\mathbb{P}}_i$. The expression for δE_{ij} can be further simplified in order to match the form given by the Heisenberg's spin hamiltonian, extracting thereby relevant parameter expressions, like: $J_{ij}^{iso} = \text{Im}(A_{ij}^{00} - A_{ij}^{xx} - A_{ij}^{yy} - A_{ij}^{zz})$, $J_{ij}^{ani,u,v} = \text{Im}(A_{ij}^{uv} - A_{ij}^{vu})$, and $D_{ij}^u = \text{Re}(A_{ij}^{0u} - A_{ij}^{u0})$, where $u, v \in (0, x, y, z)$, and $A_{ij}^{uv} = -\frac{1}{\pi} \int_{-\infty}^{E_F} \text{Tr}\{\mathbb{P}_i^z \mathbb{G}_{ij}^u \mathbb{P}_j^z \mathbb{G}_{ij}^v\} d\epsilon$. If the SOC is neglected, the isotropic exchange is $J_{ij}^{iso} = \text{Im}(A_{ij}^{00} - A_{ij}^{zz})$, and by defining $\Delta_i = \mathbb{P}_i^\uparrow - \mathbb{P}_i^\downarrow = 2\mathbb{P}_i^z$, one can obtain the Liechtenstein-Katsnelson-Antropov-Gubanov [262] expression for isotropic exchange:

$$J_{ij}^{iso} = -\frac{1}{4\pi} \int_{-\infty}^{E_F} \text{Im Tr}(\Delta_i \mathbb{G}_{ij}^\uparrow \Delta_j \mathbb{G}_{ij}^\downarrow). \quad (2.65)$$

Therefore, to calculate exchange parameters using TB2J, a SDFT calculation is performed to obtain the system's electronic structure, from which Wannier functions are constructed to generate a tight-binding hamiltonian that describes the orbital decomposed magnetic interactions.

²⁸For simplicity, we omit all orbital and spin indices in the subsequent discussion.

2.3.3 Monte Carlo simulations

In statistical physics, the partition function $Z_n(\beta)$ for $O(n)$ -symmetric spin models is a central quantity that encapsulates the system's thermodynamic behavior. It is typically expressed as:

$$Z_n(\beta) = \sum_{\mathbf{S}_i} \exp(-\beta H_n), \quad (2.66)$$

with $H_n = J \sum_{\langle ij \rangle} \mathbf{S}_i \mathbf{S}_j$ being the hamiltonian of Ising ($n = 1$), XY ($n = 2$), and Heisenberg ($n = 3$) systems, with spins \mathbf{S}_i of n -dimensional cubic lattice of volume $\Omega = L^n$. The key thermodynamical observables in $O(n)$ spin models are: *internal energy per site* ($e = -\text{dln}(Z_n/\text{d}\beta)/\Omega$), *specific heat* ($C/k_B = \beta^2(\langle H_n^2 \rangle - \langle H_n \rangle^2)/\Omega$), *magnetization* ($m = \langle |\mathbf{S}_{av}| \rangle$), *susceptibility* ($\chi = \beta\Omega(\langle \mathbf{S}_{av}^2 \rangle - \langle \mathbf{S}_{av} \rangle^2)$), and *spin-spin correlation function* ($G(x_i - x_j) = \langle \mathbf{S}_i \cdot \mathbf{S}_j \rangle$), with correlation length at large distances being $\xi = -\lim_{x \rightarrow \infty} |x|/\text{ln}G(x)$. For related observables, the *second-order phase transition* characterized by divergent ξ at $T_c = 1/\beta_c$ could be identified, so that for $T \geq T_c$ one obtains $\xi = \xi_0 + |1 - T/T_c|^{-\nu} + \dots$, and $\xi = \xi_0 - (1 - T/T_c)^{-\nu} + \dots$ for $T \leq T_c$, with critical exponent ν . In finite systems, ξ can not diverge, so divergences in other quantities are rounded and shifted. Near T_c , the linear system size L replaces the role of ξ , modifying scaling laws to describe *finite size* effects and enabling the study of critical phenomena. In numerical simulations of spin systems, the expectation values of key observables are calculated using the Metropolis algorithm, a Markov chain Monte Carlo (MC) method. This algorithm performs local random updates of single spins in the sampled configurations, ensuring that the resulting states follow the Boltzmann distribution. By iteratively accepting or rejecting proposed changes with defined probability transition rate based on energy differences,

$$P(\mathbf{S}_i \rightarrow \mathbf{S}'_i) = \begin{cases} \exp\{-\beta(E - E')\}, & (E' \geq E) \\ 1, & (E' \leq E) \end{cases} \quad (2.67)$$

with E and E' being the energies before and after spin flip, the Metropolis algorithm effectively explores equilibrium properties and critical phenomena in models such as the Ising and Heisenberg systems [263]. Also, other algorithms are often used such as *cluster* or *multicanonical*. Furthermore, in order to determine the statistical behavior of 2D anisotropic Heisenberg's model some improved algorithms are used, based on change of the individual spin directions [264], and root-mean-square value of the three components of magnetization per spin [265].

2.4 Density functional perturbation theory (DFPT)

The literature sources used for this section are provided as Refs. [266, 267, 268, 269, 270]

2.4.1 Basic concept of the linear response

DFPT extends DFT method by providing a systematic approach to calculate response properties of materials under small perturbations. Through the evaluation of the first and second derivatives of the BO energy surface, DFPT determines equilibrium geometries (see equation (2.18)) and vibrational frequencies, with the latter derived from the eigenvalues of the mass-weighted Hessian matrix:

$$\text{Det} \left| \frac{1}{\sqrt{M_I M_J}} \frac{\partial^2 E(\mathbf{R})}{\partial \mathbf{R}_I \partial \mathbf{R}_J} - \omega^2 \right| = 0. \quad (2.68)$$

This method, grounded in the Hellmann-Feynman theorem, enables precise modeling of phonons and other related phenomena. The Hessian in equation (2.68) is obtained by differentiating equation (2.18) with respect to nuclei coordinates (second-order energy derivatives – *harmonic approximation*):²⁹

$$\frac{\partial \mathbf{F}_I}{\partial \mathbf{R}_J} = \frac{\partial^2 E(\mathbf{R})}{\partial \mathbf{R}_I \partial \mathbf{R}_J} = - \int \frac{\partial n_o(\mathbf{r})}{\partial \mathbf{R}_J} \frac{\partial v_{ext}(\mathbf{r})}{\partial \mathbf{R}_I} d\mathbf{r} - \int \frac{\partial^2 v_{ext}(\mathbf{r})}{\partial \mathbf{R}_I \partial \mathbf{R}_J} n_o(\mathbf{r}) d\mathbf{r} - \frac{\partial^2 E_{nn}}{\partial \mathbf{R}_I \partial \mathbf{R}_J}, \quad (2.69)$$

with $\frac{\partial n_o(\mathbf{r})}{\partial \mathbf{R}_J}$ being the *linear response* to a distortion of the nuclei geometry. Within the KS framework, this response is derived using conventional perturbation techniques, in which the effective potential is adjusted iteratively to match the first-order change in the ground state density, ensuring a seamless connection between electronic structure and induced perturbations [271, 272]. To make it clearer, one can start by the linearization of equation (2.17):

$$\frac{\partial n_o(\mathbf{r})}{\partial \mathbf{R}_J} = 4 \text{Re} \sum_{i=1}^{N/2} \psi_i^*(\mathbf{r}) \frac{\partial \psi_i(\mathbf{r})}{\partial \mathbf{R}_J}. \quad (2.70)$$

To obtain the derivations $\frac{\partial \psi_i(\mathbf{r})}{\partial \mathbf{R}_J}$, one can linearize the equations (2.15) and (2.16), leading to the *Sternheimer* equation:

$$(\hat{h}_{eff}^{KS} - \varepsilon_i) \frac{\partial \psi_i(\mathbf{r})}{\partial \mathbf{R}_J} = - \left(\frac{\partial v_{eff}^{KS}(\mathbf{r})}{\partial \mathbf{R}_J} - \frac{\partial \varepsilon_i}{\partial \mathbf{R}_J} \right) \psi_i(\mathbf{r}), \quad (2.71)$$

²⁹Known also as the matrix of the interatomic force constants (IFC).

so that $\frac{\partial \varepsilon_i}{\partial \mathbf{R}_J} = \left\langle \psi_i(\mathbf{r}) \left| \frac{\partial v_{eff}^{KS}(\mathbf{r})}{\partial \mathbf{R}_J} \right| \psi_i(\mathbf{r}) \right\rangle$. These equations outline a SCF methodology for describing the perturbed system, analogous to the KS equations in the unperturbed case, where the connection to the first-order correction (linear response) emerges naturally by expressing equation (2.71) like a sum over the eigenstates of the unperturbed hamiltonian:

$$\frac{\partial \psi_i(\mathbf{r})}{\partial \mathbf{R}_J} = \sum_{j \neq i} \psi_j(\mathbf{r}) \frac{1}{\varepsilon_i - \varepsilon_j} \left\langle \psi_j(\mathbf{r}) \left| \frac{\partial v_{eff}^{KS}(\mathbf{r})}{\partial \mathbf{R}_J} \right| \psi_i(\mathbf{r}) \right\rangle, \quad (2.72)$$

running over valence and conduction states. Now, the equation (2.70) can be rewritten in the form:

$$\frac{\partial n_o(\mathbf{r})}{\partial \mathbf{R}_J} = 4 \operatorname{Re} \sum_{i=1}^{N/2} \sum_{j \neq i} \psi_i^*(\mathbf{r}) \psi_j(\mathbf{r}) \frac{1}{\varepsilon_i - \varepsilon_j} \left\langle \psi_j(\mathbf{r}) \left| \frac{\partial v_{eff}^{KS}(\mathbf{r})}{\partial \mathbf{R}_J} \right| \psi_i(\mathbf{r}) \right\rangle, \quad (2.73)$$

so that the density response contributions from products of valence states cancel each other, allowing the j -index to be restricted to conduction states only. However, the density response can be efficiently computed without the full conduction band spectrum by using the projection onto the valence-state manifold resolving thereby the singularity (case of near-degeneracy) in the left-hand side of equation (2.71):

$$(\hat{h}_{eff}^{KS} + \alpha P_v - \varepsilon_i) \frac{\partial \psi_i(\mathbf{r})}{\partial \mathbf{R}_J} = -(1 - P_v) \frac{\partial v_{eff}^{KS}(\mathbf{r})}{\partial \mathbf{R}_J} \psi_i(\mathbf{r}), \quad (2.74)$$

with $P_v = \sum_v |v\rangle \langle v|$ and α parameter that is larger than the valence bandwidth. Furthermore, DFPT decouples responses to different wavelengths, allowing phonon frequency calculations at any wave vector \mathbf{q} without the use of supercells (necessary in the *frozen*³⁰ method) and with wavelength-independent workload – *monochromatic perturbations*. To demonstrate this, one rewrites the equation (2.74) by directly incorporating \mathbf{k} vector and band index n of the unperturbed wavefunction $\psi_n^{\mathbf{k}}$, decomposing the perturbing potential $\frac{\partial v_{eff}^{KS}(\mathbf{r})}{\partial \mathbf{R}_J}$ into Fourier components, and projecting both sides of equation (2.74) onto the $\mathbf{k} + \mathbf{q}$ manifold, where translational

³⁰This method simulates small, static atomic displacements (“frozen configurations”) to compute phonon frequencies by using supercells, however it is restricted to specific \mathbf{q} -point becoming therefore computationally expensive for dense BZ sampling.

invariance ensures that the $P_{\mathbf{k}+\mathbf{q}}$ projector commutes with \hat{h}_{eff}^{KS} , P_v and P_c , which results in:

$$\left(\hat{h}_{eff}^{\mathbf{k}+\mathbf{q}} + \alpha \sum_{n'} |u_{n'}^{\mathbf{k}+\mathbf{q}}\rangle \langle u_{n'}^{\mathbf{k}+\mathbf{q}}| - \varepsilon_n^{\mathbf{k}} \right) \frac{\partial u_n^{\mathbf{k}+\mathbf{q}}}{\partial \mathbf{R}_J} = - \left(1 - \sum_{n'} |u_{n'}^{\mathbf{k}+\mathbf{q}}\rangle \langle u_{n'}^{\mathbf{k}+\mathbf{q}}| \right) \frac{\partial v_{\mathbf{q}}^{KS}}{\partial \mathbf{R}_J} u_n^{\mathbf{k}}, \quad (2.75)$$

where n' is a summation over valence states, and $\frac{\partial u_n^{\mathbf{k}+\mathbf{q}}}{\partial \mathbf{R}_J}$ represents the Fourier component of the first-order correction to the periodic part of the unperturbed wavefunction. Also, this formalism was extended to metals by Gironcoli, utilizing the smearing function $f(\epsilon) = (1/\sigma)\tilde{\delta}(\epsilon/\sigma)$ with smooth approximation to the step function $\tilde{\Theta} = \int_{-\infty}^x \tilde{\delta}(y)dy$ to handle Fermi surface effects [273], so that equation (2.73) becomes:

$$\frac{\partial n_o(\mathbf{r})}{\partial \mathbf{R}_J} = 2 \sum_{i,j} \psi_i^*(\mathbf{r}) \psi_j(\mathbf{r}) \frac{\tilde{\Theta}_{F,i} - \tilde{\Theta}_{F,j}}{\varepsilon_i - \varepsilon_j} \tilde{\Theta}_{i,j} \left\langle \psi_j(\mathbf{r}) \left| \frac{\partial v_{eff}^{KS}(\mathbf{r})}{\partial \mathbf{R}_J} \right| \psi_i(\mathbf{r}) \right\rangle, \quad (2.76)$$

and with a few additional steps, one can derive the equivalent of equation (2.75). Moreover, in metals, the vanishing energy denominator for charge density perturbations in equation (2.76) causes divergences in screening of perturbations at wavevectors $|\mathbf{q}| = 2k_F$, which can be smeared in 2D, however when *nesting* – two parallel Fermi surface sections are connected by e.g., $2k_F$ – is present, it will diverge even in 3D. This divergence, known as *Kohn anomaly*, strongly impacts phonon dispersion by emergence of dips or softening, and a fine BZ sampling is necessary near $2k_F$ to accurately capture this effects. On top of that, the $2n + 1$ theorem, which follows from the variational principle, provides a powerful framework for efficiently computing up to the $2n + 1$ -th order energy derivatives from wavefunction and density derivatives up to the n -th order. For instance, in *anharmonic* studies, third-order force constants – key to understanding phonon linewidths and nonlinear optical responses – can be determined using only first-order derivatives of the wavefunction, significantly reducing computational complexity.

2.4.2 Phonon calculations

Phonons are quantized lattice vibrations, emerging from the atomic motion modeled as simple independent harmonic oscillators³¹ (normal modes), constructing thereby the dynamical matrix whose eigenvalues correspond to phonon frequencies $\omega_\nu(\mathbf{q})$,³² with eigenvectors representing the

³¹In the harmonic approximation, phonons behave like atoms connected by springs following Hooke's law ($\mathbf{F} = -k\mathbf{r}$), with potential energy $E_p = k|\mathbf{r}|^2/2$, where k is the spring constant. Imaginary phonon modes signal structural instability.

³² ν is the corresponding phonon mode (branch) index.

corresponding atomic displacements in the unit cell. They are classified as *acoustic* (A) or *optical* (O), based on atomic displacement patterns from their equilibrium positions. A -phonons involve in-phase atomic motion and are crucial for sound propagation, with their frequencies approaching zero as $\mathbf{q} \rightarrow 0$, reflecting the translational symmetry of the 3D crystal. In contrast, O -phonons exhibit out-of-phase motions and interact strongly with light, making them detectable in Raman and infrared spectroscopies. The interplay of atomic masses (M_{light} , and M_{heavy}) and their bonding (spring constant k between them) dictates the dynamical behavior, with heavier atoms governing acoustic modes ($\omega_A \sim \sqrt{k/M_{heavy}}$) and lighter atoms dominating optical modes ($\omega_O \sim \sqrt{k/M_{light}}$). The simple *diatomic chain* model ($N = 2$) provides a easy understanding of these dynamics, where alternating masses and spring constants can also lead to a frequency gap between the A and O phonon branches, emphasizing the role of mass and interatomic bonding in phonon dispersion $\omega_\nu(\mathbf{q})$. Also, for a material containing N atoms per unit cell, the phonon spectrum consists of $3A$ - and $3N - 3O$ -modes. They can be further categorized into longitudinal (L) and transverse (T) modes, with L modes having atomic displacements along the wave propagation direction and T modes having displacements perpendicular to it. For 3D materials, the A modes consist of one longitudinal (LA) mode and two transverse (TA) modes, while the O -modes consist of $N - 1$ longitudinal optical (LO) modes and $2N - 2$ transverse optical (TO) modes. However, phonon behavior in 2D materials differs significantly due to the lack of atomic neighbors in the direction perpendicular to the crystal plane. Specifically, 2D materials feature one out-of-plane – along z -axis – ZA mode, one TA mode, and one LA mode, as well as $N - 1$ ZO , TO , LO modes, respectively (see Figure 2.5) [274, 275].

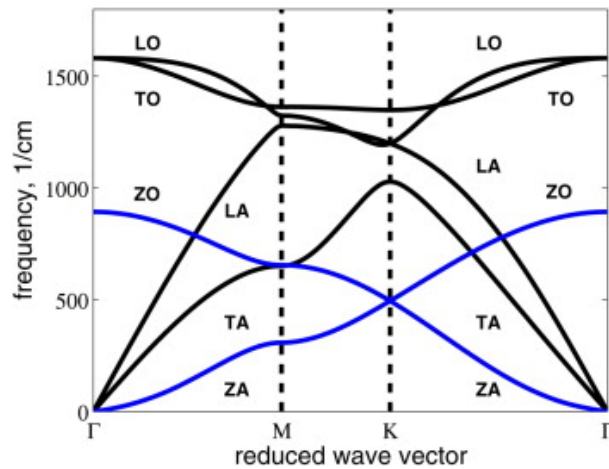


Figure 2.5: The calculated phonon dispersion for graphene ($N = 2$) [276].

Now, let us explore the connection to DFPT and its application in phonon calculations. The

position of the I -th atom, \mathbf{R}_I , is expressed as $\mathbf{R}_I = \mathbf{R}_l + \boldsymbol{\tau}_s + \mathbf{u}_s(l)$, where \mathbf{R}_l is the coordinate of the l -th unit cell (u.c.) within the Bravais lattice, $\boldsymbol{\tau}_s$ refers to the s -th atom's equilibrium position inside the u.c., and $\mathbf{u}_s(l)$ represents the deviation from this equilibrium. Therefore, two atomic indices in the BvK supercell are denoted by $\kappa = \{l, s\}$ and $\kappa' = \{m, t\}$. Due to translational invariance, the IFC matrix, as expressed in equation (2.69), depends on the u.c. indices l and m only through their relative displacement $\mathbf{R} = \mathbf{R}_l - \mathbf{R}_m$, so that:

$$\Phi_{\kappa\kappa'}^{\alpha\beta} = \frac{\partial^2 E}{\partial u_{\kappa}^{\alpha} \partial u_{\kappa'}^{\beta}} = \Phi_{\kappa\kappa'}^{\alpha\beta}(\mathbf{R}), \quad (2.77)$$

where $\alpha, \beta = x, y, z$. The Fourier transform of $\Phi_{\kappa\kappa'}^{\alpha\beta}(\mathbf{R})$, denoted as $\tilde{\Phi}_{\kappa\kappa'}^{\alpha\beta}(\mathbf{q}) = \sum_{\mathbf{R}} e^{-i\mathbf{q}\mathbf{R}} \Phi_{\kappa\kappa'}^{\alpha\beta}(\mathbf{R})$, represents the second-order Taylor expansion term of the BO energy surface $E = E_0 + \sum_{\kappa\alpha} \tilde{\Phi}_{\kappa}^{\alpha} u_{\kappa}^{\alpha} + \frac{1}{2} \sum_{\kappa\alpha, \kappa'\beta} \tilde{\Phi}_{\kappa\kappa'}^{\alpha\beta} u_{\kappa}^{\alpha} u_{\kappa'}^{\beta}$, with respect to an amplitude of lattice distortion $\mathbf{u}(\mathbf{q})$ (displacement patterns), forming thereby the *dynamical matrix*:

$$\tilde{\Phi}_{\kappa\kappa'}^{\alpha\beta}(\mathbf{q}) = \frac{1}{N_{cell}} \left. \frac{\partial^2 E}{\partial u_{\kappa}^{*\alpha}(\mathbf{q}) \partial u_{\kappa'}^{\beta}(\mathbf{q})} \right|_{u=0}, \quad (2.78)$$

where N_{cell} is number of unit cells. The corresponding phonon frequencies $\omega_{\nu}(\mathbf{q})$ are actually the solutions of secular equation:

$$\text{Det} \left| \frac{1}{\sqrt{M_{\kappa} M_{\kappa'}}} \tilde{\Phi}_{\kappa\kappa'}^{\alpha\beta}(\mathbf{q}) - \omega_{\nu}^2(\mathbf{q}) \right| = 0, \quad (2.79)$$

having the same form as equation (2.68). Translational invariance ensures that a lattice distortion at wavevector \mathbf{q} does not induce forces at $\mathbf{q}' \neq \mathbf{q}$. In DFPT, this property is exploited by computing the dynamical matrix in reciprocal space for a grid of \mathbf{q} -points in BZ. A Fourier transform then converts these results to real space, yielding IFCs while preserving crystal's periodicity and symmetry. However, numerical errors coming from finite $\mathbf{k}(\mathbf{q})$ -point sampling of BZ and the limitation of interactions to a finite distance can violate these symmetries, leading to unphysical results such as non-zero acoustic phonon frequencies at $\mathbf{q} \rightarrow 0$ or distorted phonon dispersions. To address these issues, *acoustic sum rules* (ASRs) are enforced by adjusting IFCs to satisfy symmetry constraints, which include permutation and space group symmetry, as well as Born-Huang global invariance conditions [277, 278, 279] for translational and rotational

symmetries:

$$\left\{ \begin{array}{l} \sum_{\kappa} \Phi_{\kappa}^{\alpha} = 0, \\ \sum_{\kappa} \Phi_{\kappa}^{\alpha} \tau_{\kappa}^{\beta} = \sum_{\kappa} \Phi_{\kappa}^{\beta} \tau_{\kappa}^{\alpha}, \\ \sum_{\kappa'} \Phi_{\kappa\kappa'}^{\alpha\beta} = 0, \\ \sum_{\kappa'} \Phi_{\kappa\kappa'}^{\alpha\beta} \tau_{\kappa'}^{\gamma} + \delta_{\alpha\gamma} \Phi_{\kappa}^{\beta} = \sum_{\kappa'} \Phi_{\kappa\kappa'}^{\alpha\gamma} \tau_{\kappa'}^{\beta} + \delta_{\alpha\beta} \Phi_{\kappa}^{\gamma}. \end{array} \right. \quad \begin{array}{l} (2.80) \\ (2.81) \\ (2.82) \\ (2.83) \end{array}$$

Translational invariance ensures that a uniform displacement of all atoms does not produce a net force, resulting in acoustic phonons with zero frequency when $\mathbf{q} \rightarrow 0$. Angular momentum conservation, tied to rotational invariance, guarantees that the lattice potential remains unchanged under infinitesimal rotations of all atoms. Also, for a bulk in equilibrium, the stress tensor ($\sigma = (1/\Omega) \sum_{\kappa} \Phi_{\kappa}^{\alpha} \tau_{\kappa}^{\beta}$) for volume Ω of a finite lattice disappears, removing surface effects, and providing additional 36 Huang conditions from the fourth-rank tensor $T_{\alpha\beta,\gamma\delta}^{sym} = T_{\gamma\delta,\alpha\beta}^{sym}$:

$$\sum_{\kappa\kappa'} \Phi_{\kappa\kappa'}^{\alpha\beta} \tau_{\kappa\kappa'}^{\gamma} \tau_{\kappa\kappa'}^{\delta} = \sum_{\kappa\kappa'} \Phi_{\kappa\kappa'}^{\gamma\delta} \tau_{\kappa\kappa'}^{\alpha} \tau_{\kappa\kappa'}^{\beta}, \quad (2.84)$$

which can be reduced to 15 by using the following symmetry condition: $T_{\alpha\beta,\gamma\delta}^{sym} = T_{\beta\alpha,\gamma\delta}^{sym} = T_{\alpha\beta,\delta\gamma}^{sym}$. Now we will see how to implement this in practical calculations. As we already know, IFCs in real space are obtained by fitting DFPT forces via the small displacement method and then by interpolating them into reciprocal space via Fourier transformation to obtain the dynamical matrices. The small displacement method expresses forces as $\mathbf{F} = \mathbb{A}\Phi = \mathbb{A}\mathbb{C}\phi$, where \mathbb{A} is the displacement matrix, \mathbb{C} encodes symmetry constraints, and ϕ are independent IFC parameters, determined via least-squares or compressive sensing, with $\Phi = \mathbb{C}\phi$. These IFCs are corrected to satisfy invariance conditions before Fourier interpolation. Two correction methods are used: (i) projection onto the subspace of invariance conditions, minimizing deviations from the original IFCs ($\Phi^c = \Phi - \sum_i (\Phi g_i) g_i$), as implemented in QE, or (ii) direct minimization, which adjusts IFCs while staying close to the originals [278]. In 2D limit, these invariance constraints are essential for describing acoustic vibrations at low frequencies. Unlike bulk materials, where all three acoustic branches are linear ($\omega_{\nu}(\mathbf{q}) \sim q$) at long-wavelength limit $\mathbf{q} \rightarrow 0$, 2D systems exhibit distinct behavior. The LA and TA modes remain linear, while the ZA mode follows a quadratic dispersion $\omega_{ZA}(\mathbf{q}) \sim q^2$, attributed to the symmetry and rotational invariance of 2D structures [277, 278]. This mode, also known as the *flexural* mode, represents out-

of-plane rippling of the 2D sheet [280]. Using the Huang conditions and symmetry of the internal relaxation tensor $T_{\alpha\gamma,\beta\delta}^{int}$,³³ it follows that $T_{z\beta,\gamma\delta}^{sym} + T_{z\gamma,\beta\delta}^{int} = T_{\gamma\delta,z\beta}^{sym} + T_{\gamma z,\delta\beta}^{int}$. When rotational invariance is maintained and the system is stress-free, this results in bending condition: $T_{\gamma\delta,z\beta}^{sym} = -T_{\gamma z,\delta\beta}^{int}$, which can be applied to mitigate numerical noise in computations while preserving the quadratic nature of flexural mode dispersion [278].

2.4.3 Electron-phonon coupling

To proceed, we will examine the dynamical coupling of electronic and phononic subsystems, described by the standard hamiltonian:

$$H = \underbrace{\sum_{n\mathbf{k}} \epsilon_{n\mathbf{k}} \hat{c}_{n\mathbf{k}}^\dagger \hat{c}_{n\mathbf{k}}}_{\text{electronic part}} + \underbrace{\sum_{q\nu} \hbar\omega_{q\nu} \left(\hat{a}_{q\nu}^\dagger \hat{a}_{q\nu} + \frac{1}{2} \right)}_{\text{phononic part}} + \underbrace{\frac{1}{\sqrt{N_{\text{cell}}}} \sum_{\mathbf{k}mnq\nu} g_{\mathbf{k},\mathbf{q}}^{mn\nu} \hat{c}_{m\mathbf{k}+\mathbf{q}}^\dagger \hat{c}_{n\mathbf{k}} (\hat{a}_{q\nu} + \hat{a}_{-q\nu}^\dagger)}_{\text{coupled electron-phonon subsystems}}, \quad (2.85)$$

to the first-order in the atomic displacements. The matrix elements $g_{\mathbf{k},\mathbf{q}}^{mn\nu}$ quantify the strength of electron-phonon (*e-ph*) coupling and have the physical dimension of energy [281]. The primary challenge now lies in determining the parameters entering in the equation (2.85). While electronic excitations were modeled using the free-electron gas approximation, and lattice vibrations as acoustic waves in the Debye model, the determination of the *e-ph* interaction matrix elements $g_{\mathbf{k},\mathbf{q}}^{mn\nu}$ with realistic approximations remained challenging for many years. The first approximation, introduced by F. Bloch [282], described the electron scattering process mediated through acoustic phonon from $|\mathbf{k}\rangle$ to $|\mathbf{k} + \mathbf{q}\rangle$ state:

$$g_{\mathbf{k},\mathbf{q}}^{mn\nu} = -i \sqrt{\frac{\hbar}{2N_{\text{cell}} M_\kappa \omega_{q\nu}}} \mathbf{q} \cdot \mathbf{e}_{\kappa\nu}(\mathbf{q}) V_0, \quad (2.86)$$

where $\mathbf{e}_{\kappa\nu}(\mathbf{q})$ represents the eigenmode of the κ -th atom, and V_0 represents the unit cell averaged effective potential experienced by electrons in the crystal lattice. However, this model has significant limitations. It neglects ‘‘umklapp’’ processes, where we have transition from state $|\mathbf{k}\rangle$ to $|\mathbf{k} + \mathbf{q} + \mathbf{G}\rangle$, which is necessary for describing resistivity in metals. Even the *rigid-ion*³⁴ approximation used for this model leads to a divergence in the Fourier transform of the potential as $1/q^2$ for $\mathbf{q} \rightarrow 0$, predicting unrealistically strong *e-ph* interactions [281]. These shortcomings

³³The contribution arising from the adjustment of internal atomic positions due to external stress fields [279].

³⁴The effective potential felt by the electrons is essentially the cumulative sum of the individual ionic potentials from each nucleus.

necessitated refinements, such as inclusion of electronic screening of the nuclear potential, as done by Mott and Jones [283]. J. Bardeen followed this in 1937 with a complementary approach that replaced the potential V_0 with a screened form [284], offering additional insights into the role of electron screening:

$$V_0 \rightarrow \frac{V_\kappa(\mathbf{q})}{1 + \left(\frac{k_{TF}}{q}\right)^2 F\left(\frac{q}{2k_F}\right)}. \quad (2.87)$$

It is a self-consistent field method for calculating e - ph matrix elements using linearized Hartree theory. However, his approach neglected exchange and correlation effects, a limitation partially addressed later by him and Pines in 1955 through screened exchange interactions [285], although their formalism's complexity hindered further progress. However, the DFPT transformed the field, enabling precise and reliable predictions of e - ph interactions (see Figure 2.6) that were previously out of reach.

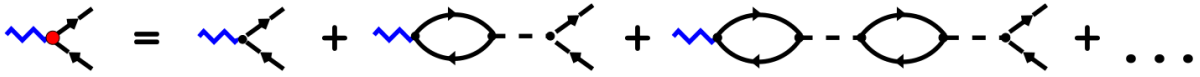


Figure 2.6: Electron propagators (black lines), phonons (blue zig-zags), and effective electron-electron interactions (dashed lines) define the screened e - ph vertex in DFPT, with the KS charge susceptibility representing the electron-hole bubble [267].

In DFPT, the screened e - ph matrix elements depend on the variation in effective potential:

$$g_{\mathbf{k},\mathbf{q}}^{mn\nu} = \langle u_{m\mathbf{k}+\mathbf{q}} | \nabla_{\mathbf{q}\nu} v_{eff}^{KS} | u_{n\mathbf{k}} \rangle_{cell}, \quad (2.88)$$

with SOC that can be taking into account: $\nabla v_{eff}^{KS} \rightarrow \nabla v_{eff}^{SR} + \nabla v^{SOC}$. In the following section, we will present the methodology for calculating the spectral Eliashberg function using e - ph matrix elements from DFPT within the Migdal approximation, and its application to investigating the superconducting properties of materials.

2.5 Microscopic theory of superconductivity

Following the identification of superconductivity in mercury by K. Onnes in 1911, the field has advanced through the exploration of various families of superconductors (see Figure 2.7), driven by the pursuit of higher T_c values – ultimately to “survive” at ambient conditions – and promising new avenues for both fundamental physics and practical applications. However, the first microscopic explanation for superconductivity was provided in 1957 within the BCS theory,

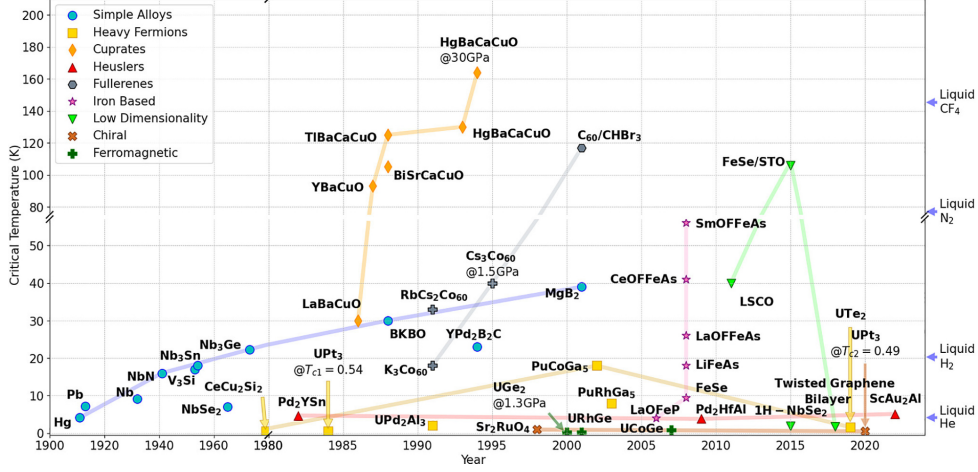


Figure 2.7: A historical overview of superconducting materials, categorized by families and their respective critical temperatures [286].

which established a formalism for *pairing* electrons with opposite momentum and opposite spin – Cooper pairs (*bound state*) – via an attractive interaction mediated by acoustic phonons,³⁵ leading to the formation of a superconducting condensate able to conduct current without energy loss (*superfluid*) [198]. The Cooper pairs’ energy spectrum features a gap, meaning that there is a minimum energy required to break the pairs and create excitations which are in correspondence with one in the free-electron model. To proof this, let us start with the reduced (*pairing*) BCS hamiltonian which simplifies the problem by focusing on the weak attractive interaction between electrons $V_{kk'}$ that leads to the formation of Cooper pairs:

$$H_{BCS} = \sum_{k\sigma} \epsilon_k \hat{c}_{k\sigma}^\dagger \hat{c}_{k\sigma} - \sum_{kk'} V_{kk'} \hat{c}_{k\uparrow}^\dagger \hat{c}_{-k\downarrow}^\dagger \hat{c}_{-k'\downarrow} \hat{c}_{k'\uparrow}, \quad (2.89)$$

with non-interacting electron energy ϵ_k relative to the Fermi level. In order solve the problem, one can use the Hartree-Fock decoupling, which corresponds to electron pairing in the mean-field approach:

$$H_{BCS}^{MF} = \sum_{k\sigma} \epsilon_k \hat{c}_{k\sigma}^\dagger \hat{c}_{k\sigma} - \sum_{\mathbf{k}} \left(\Delta_{\mathbf{k}}^* \hat{c}_{\mathbf{k}\uparrow} \hat{c}_{-\mathbf{k}\downarrow} + \Delta_{\mathbf{k}} \hat{c}_{-\mathbf{k}\downarrow}^\dagger \hat{c}_{\mathbf{k}\uparrow}^\dagger \right) + \sum_{\mathbf{k}} \frac{|\Delta_{\mathbf{k}}|^2}{\tilde{V}}, \quad (2.90)$$

where \tilde{V} denotes the effective interaction that attracts the electron pairs, and $\Delta_{\mathbf{k}} = \tilde{V} \sum_{\mathbf{k}'} \langle \hat{c}_{-\mathbf{k}\downarrow} \hat{c}_{\mathbf{k}'\uparrow} \rangle$ is the superconducting gap. We can further rewrite the equation (2.90) using the Nambu-Gor’kov

³⁵The interaction between electrons in a Cooper pair involves a dynamical polarization of the lattice. As an electron passes through the lattice, it causes a temporary distortion by attracting positively charged ions, creating a region of localized positive charge. This distortion acts as a polarization “wake”, which attracts a second electron with opposite momentum and spin. This mechanism is therefore mediated by phonons within the energy range $(-\hbar\omega_D \leq \epsilon_{\mathbf{k}} \leq +\hbar\omega_D)$, also known as the Debye window.

formalism as:

$$H_{BCS}^{MF} = \sum_{\mathbf{k}} \hat{\psi}_{\mathbf{k}}^{\dagger} h_{\mathbf{k}} \hat{\psi}_{\mathbf{k}} + \sum_{\mathbf{k}} \left(\epsilon_{\mathbf{k}} + \frac{|\Delta_{\mathbf{k}}|^2}{\tilde{V}} \right), \quad (2.91)$$

where $\hat{\psi}_{\mathbf{k}} = \begin{pmatrix} \hat{c}_{\mathbf{k}\uparrow} \\ \hat{c}_{-\mathbf{k}\downarrow}^{\dagger} \end{pmatrix}$, and $\hat{\psi}_{\mathbf{k}}^{\dagger} = \begin{pmatrix} \hat{c}_{\mathbf{k}\uparrow}^{\dagger} & \hat{c}_{-\mathbf{k}\downarrow} \end{pmatrix}$ are Nambu spinors, and $h_{\mathbf{k}} = \begin{pmatrix} \epsilon_{\mathbf{k}} & \Delta_{\mathbf{k}} \\ \Delta_{\mathbf{k}}^* & -\epsilon_{\mathbf{k}} \end{pmatrix}$. To diagonalize $h_{\mathbf{k}}$, its eigenvalues must first be determined, as they define the diagonal elements in the transformed matrix. They are quasiparticle energies $E_{\mathbf{k}\pm} = \pm E_{\mathbf{k}}$, with $E_{\mathbf{k}} = \sqrt{\epsilon_{\mathbf{k}}^2 + |\Delta_{\mathbf{k}}|^2}$, defining the so called *Bogoliubov spectrum* which shows *particle-hole* symmetry, as its eigenvalues are symmetric around zero energy, reflecting solutions for both electrons (+) and holes (-). By using the unitary transformation we can diagonalize the given 2×2 $h_{\mathbf{k}}$ matrix as $U_{\mathbf{k}}^{-1} h_{\mathbf{k}} U_{\mathbf{k}} = \text{diag}(E_{\mathbf{k}}, -E_{\mathbf{k}})$, which is also known as the *Bogoliubov transformation*:

$$\begin{pmatrix} \hat{c}_{\mathbf{k}\uparrow} \\ \hat{c}_{-\mathbf{k}\downarrow}^{\dagger} \end{pmatrix} = \begin{pmatrix} u_{\mathbf{k}} & -v_{\mathbf{k}}^* \\ v_{\mathbf{k}} & u_{\mathbf{k}}^* \end{pmatrix} \begin{pmatrix} \hat{\gamma}_{\mathbf{k}\uparrow} \\ \hat{\gamma}_{-\mathbf{k}\downarrow}^{\dagger} \end{pmatrix}, \quad (2.92)$$

with eigenvectors that satisfy the normalization condition $|u_{\mathbf{k}}|^2 + |v_{\mathbf{k}}|^2 = 1$, so that equation (2.91) becomes:

$$H_{BCS}^{MF} = \sum_{\mathbf{k}\sigma} E_{\mathbf{k}} \hat{\gamma}_{\mathbf{k}\sigma}^{\dagger} \hat{\gamma}_{\mathbf{k}\sigma} + \sum_{\mathbf{k}} \overbrace{\left(\frac{|\Delta_{\mathbf{k}}|^2}{\tilde{V}} + \epsilon_{\mathbf{k}} - \sqrt{\epsilon_{\mathbf{k}}^2 + |\Delta_{\mathbf{k}}|^2} \right)}^{E_0 \text{ (ground state energy)}}, \quad (2.93)$$

with $\langle \hat{\gamma}_{\mathbf{k}\sigma}^{\dagger} \hat{\gamma}_{\mathbf{k}\sigma} \rangle = f(E_{\mathbf{k}})$ – Fermi function, and corresponding BCS wave function $\Psi_{BCS} = \prod_{\mathbf{k}} \left[u_{\mathbf{k}}^* + v_{\mathbf{k}} \hat{c}_{\mathbf{k}\uparrow}^{\dagger} \hat{c}_{-\mathbf{k}\uparrow}^{\dagger} |0\rangle \right]$, where $|0\rangle$ is the vacuum state. By minimizing E_0 with respect to $\Delta_{\mathbf{k}}$ at $T = 0$, one can obtain the nontrivial solution in weak *e-ph* coupling limit ($\lambda = N(E_F) \tilde{V} \ll 1$) for superconducting gap:

$$\Delta_{\mathbf{k}}(T = 0) \approx 2\hbar\omega_D e^{-\frac{1}{\lambda}}. \quad (2.94)$$

To determine the superconducting critical temperature T_c (pair breaking), one needs to find the conditions $\Delta_{\mathbf{k}} \rightarrow 0$, where the quasiparticle spectrum matches that of the normal state $E_{\mathbf{k}} \rightarrow |\epsilon_{\mathbf{k}}|$, leading, after some algebra, to:

$$k_B T_c \approx 1.13 \hbar \omega_D e^{-\frac{1}{\lambda}}. \quad (2.95)$$

By dividing equation (2.94) by equation (2.95), the *universal ratio* (material independent) can be derived $2\Delta_{\mathbf{k}}(T = 0)/k_B T_c = 3.53$ [287, 288]. This formalism effectively describes conventional superconductors with weak to moderate *e-ph* interactions which are instantaneous and restricted to acoustic phonons but becomes inadequate for systems with strong coupling, as reflected in deviations from the *universal ratio*. This limitations are addressed by the Migdal-Eliashberg (ME) formalism [289, 290, 291], which refines the *e-ph* interaction by considering it to be local in space and by taking into account the *retardation effects*. It also incorporates Coulomb repulsion, which competes with the phonon-mediated attraction between electrons.

2.5.1 The 2D limit and the comparison of different *ab initio* methods (ME, MAD, SCDFT)

Before advancing to ME theory, a fundamental question arises: “*Is superconductivity even possible in the 2D limit?*” In 2D dimensional systems, reduced spatial interactions among electrons lead to significant fluctuations in the order parameter, potentially suppressing phase transitions. Furthermore, the Mermin–Wagner theorem prevents the existence of true long-range superconducting order in the 2D limit, however the BKT transition enables quasi-long-range correlations – bound vortex-antivortex pairs – and thus the emergence of superconductivity. On top of that, even in the absence of the BKT transition, Cooper pairs can still be formed at the mean-field level through the BCS mechanism when $T_c^{BCS} > T_c^{BKT}$, provided the order parameter correlations are sufficiently strong at low temperatures. Despite this, 2D superconductivity is inherently delicate and prone to the effects of disorder, which can trigger a superconductor–insulator transition. Overcoming these challenges requires highly ordered and well-controlled samples, along with advanced experimental methods to probe their superconducting properties [292]. In summary, superconductivity is even favorable in 2D limit due to increased $N(E_F)$, and because Cooper pairing in 2D \mathbf{k} -space at the Fermi surface occurs without a threshold for the attractive interaction.

Moreover, the anisotropic ME theory and DFT for superconductors (SCDFT) [293]³⁶ – which is based on effective KS equations having the same form as the Bogoliubov–de Gennes (BdG) equations – show good agreement between predicted and experimentally measured T_c . However, the ME theory is generally preferred over SCDFT because it directly provides the physical

³⁶In SCDFT, the anomalous superconducting density $\chi_s(\mathbf{r}, \mathbf{r}') = \langle \hat{\psi}_\uparrow(\mathbf{r})\hat{\psi}_\downarrow(\mathbf{r}') \rangle$ is introduced as an additional density alongside the electronic density, explicitly capturing the broken symmetry of the superconducting ground state, with a decoupling approximation employed to separately describe the normal and superconducting states.

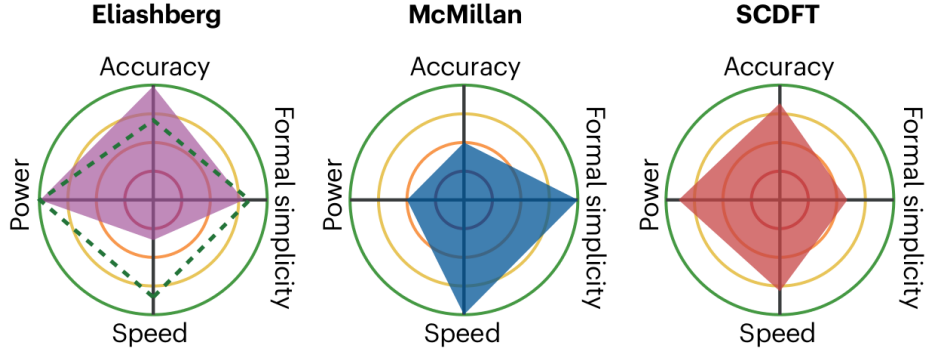


Figure 2.8: Comparison of theories for superconductivity: the ME theory offers high accuracy at high computational cost, MAD formulas provide fast T_c estimates with lower accuracy, and SCDFT balances accuracy and efficiency while enabling anisotropic characterization of materials [294].

superconducting gap and more accurate quasiparticle excitation energies, while SCDFT involves additional approximations, leading to discrepancies between the KS and physical gaps, greater complexity, and less accurate predictions of T_c (see Figure 2.8) [294].

2.5.2 The Migdal-Eliashberg (ME) theory

The literature sources used for this section are provided as Refs. [295, 296, 297, 298].

2.5.2.1 General formalism

Let us rewrite equation (2.85) by using $\hat{\varphi} = (\hat{a}_{q\nu} + \hat{a}_{-q\nu}^\dagger)$ in Nambu-Gor'kov formalism:

$$\begin{aligned}
 H = & \sum_{\mathbf{k}} \epsilon_{\mathbf{k}} \hat{\psi}_{\mathbf{k}}^\dagger \hat{\tau}_3 \hat{\psi}_{\mathbf{k}} + \sum_{q\nu} \hbar\omega_{q\nu} \left(\hat{a}_{q\nu}^\dagger \hat{a}_{q\nu} + \frac{1}{2} \right) + \sum_{\mathbf{k}q\nu} g_{\mathbf{k},\mathbf{k}+\mathbf{q}}^\nu \hat{\psi}_{\mathbf{k}+\mathbf{q}}^\dagger \hat{\tau}_3 \hat{\psi}_{\mathbf{k}} \hat{\varphi}_{q\nu} + \\
 & + \frac{1}{2} \sum_{\mathbf{k}_1 \mathbf{k}_2 \mathbf{k}_3 \mathbf{k}_4} \langle \mathbf{k}_3 \mathbf{k}_4 | V_C | \mathbf{k}_1 \mathbf{k}_2 \rangle \left(\hat{\psi}_{\mathbf{k}_3}^\dagger \hat{\tau}_3 \hat{\psi}_{\mathbf{k}_1} \right) \left(\hat{\psi}_{\mathbf{k}_4}^\dagger \hat{\tau}_3 \hat{\psi}_{\mathbf{k}_2} \right), \quad (2.96)
 \end{aligned}$$

with the Coulomb interaction represented by the last term, and constraint of translational invariance given by $\mathbf{k}_1 + \mathbf{k}_2 - \mathbf{k}_3 - \mathbf{k}_4 = 0 \vee \mathbf{G}$, and:

$$\hat{\tau}_0 = \begin{pmatrix} 1 & 0 \\ 0 & 1 \end{pmatrix}, \quad \hat{\tau}_1 = \begin{pmatrix} 0 & 1 \\ 1 & 0 \end{pmatrix}, \quad \hat{\tau}_2 = \begin{pmatrix} 0 & -i \\ i & 0 \end{pmatrix}, \quad \hat{\tau}_3 = \begin{pmatrix} 1 & 0 \\ 0 & -1 \end{pmatrix}, \quad (2.97)$$

being the notation for Pauli matrices in Nambu space. In order to describe the quasiparticles and Cooper pairs the generalized Green's function $\hat{G}(\mathbf{k}, \tau)$ in a 2×2 matrix form, with the average

over the grand canonical ensemble, is used:

$$\hat{G}(\mathbf{k}, \tau) = - \begin{pmatrix} \langle T_\tau \hat{c}_{\mathbf{k}\uparrow}(\tau) \hat{c}_{\mathbf{k}\uparrow}^\dagger(0) \rangle & \langle T_\tau \hat{c}_{\mathbf{k}\uparrow}(\tau) \hat{c}_{-\mathbf{k}\downarrow}(0) \rangle \\ \langle T_\tau \hat{c}_{-\mathbf{k}\downarrow}^\dagger(\tau) \hat{c}_{\mathbf{k}\uparrow}^\dagger(0) \rangle & \langle T_\tau \hat{c}_{-\mathbf{k}\downarrow}^\dagger(\tau) \hat{c}_{-\mathbf{k}\downarrow}(0) \rangle \end{pmatrix}, \quad (2.98)$$

where diagonal elements correspond to “normal”, and the off-diagonal to Gor’kov’s anomalous Green’s functions. Also, due to the periodicity of $\hat{G}(\mathbf{k}, \tau)$ in imaginary time, it admits a Fourier series expansion:

$$\hat{G}(\mathbf{k}, \tau) = \frac{1}{\beta} \sum_{i\omega_n} e^{-i\omega_n \tau} \hat{G}(\mathbf{k}, i\omega_n), \quad (2.99)$$

where $i\omega_n = i(2n+1)\pi/\beta$ are the Matsubara frequencies, so that equation (2.98) can be rewritten as:

$$\hat{G}(\mathbf{k}, i\omega_n) = \begin{pmatrix} G(\mathbf{k}, i\omega_n) & F(\mathbf{k}, i\omega_n) \\ F^*(\mathbf{k}, i\omega_n) & -G(-\mathbf{k}, -i\omega_n) \end{pmatrix}. \quad (2.100)$$

Now, using the Dyson equation one obtains:

$$\hat{G}(\mathbf{k}, i\omega_n) = \hat{G}_0^{-1}(\mathbf{k}, i\omega_n) - \hat{\Sigma}(\mathbf{k}, i\omega_n), \quad (2.101)$$

where $\hat{G}_0^{-1}(\mathbf{k}, i\omega_n) = i\omega_n \hat{\tau}_0 - \epsilon_{\mathbf{k}} \hat{\tau}_3$ is Green’s function for the normal state, and $\hat{\Sigma}(\mathbf{k}, i\omega_n)$ denotes the self-energy related to the electron pairing mechanism. This term in ME approximation (see

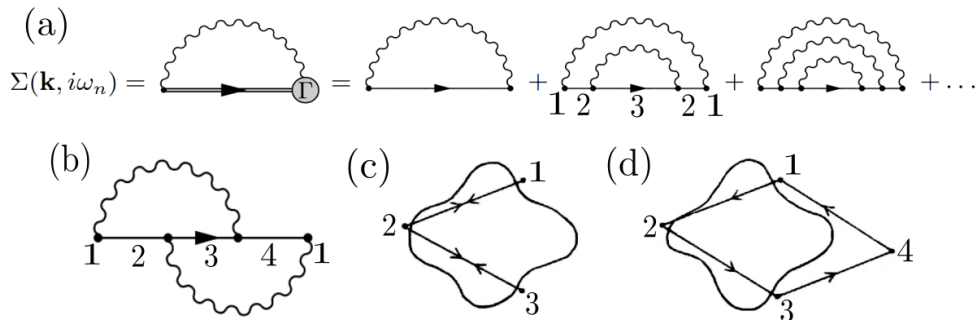


Figure 2.9: (a) The Feynman diagram related to ME theory which depict the renormalized electron self-energy arising from e -ph interactions (Γ denotes vertex, while wavy and thick lines represent the interacting phonon and electron propagators, respectively). (b) The first-order vertex correction omitted in Migdal’s theory. (c,d) Fermi surfaces and \mathbf{k} states that play a role in the second order phonon exchange depicted in (a) and to the vertex correction depicted in (b), respectively. Adapted from [288, 296].

Figure 2.9(a) can be written as:

$$\hat{\Sigma}(\mathbf{k}, i\omega_n) = \overbrace{-T \sum_{\mathbf{k}'n'\nu} \hat{\tau}_3 \hat{G}(\mathbf{k}', i\omega_{n'}) \hat{\tau}_3 |g'_{\mathbf{k}\mathbf{k}'}|^2 D_\nu(\mathbf{k} - \mathbf{k}', i\omega_n - i\omega_{n'})}^{\text{the electron-phonon contribution } \hat{\Sigma}_{ep}(\mathbf{k}, i\omega_n)} - \overbrace{T \sum_{\mathbf{k}'n'} \hat{\tau}_3 \hat{G}^{od}(\mathbf{k}', i\omega_{n'}) \hat{\tau}_3 V_C}_{\text{Coulomb contribution } \hat{\Sigma}_C(\mathbf{k}, i\omega_n)}, \quad (2.102)$$

where $D_\nu(\mathbf{q}, i\omega_n - i\omega'_{n'}) = 2\omega_{q\nu}/[(i\omega_n)^2 - \omega_{q\nu}^2]$ is the *dressed Green's function for phonons*, $g'_{\mathbf{k}\mathbf{k}'}$ are the screened *e-ph* matrix elements, and $V_C = V_C^{\mathbf{k}-\mathbf{k}'}$ is the static screened Coulomb interaction between the electronic states. Therefore, all vertex corrections of the order $\mathcal{O}(\sqrt{m/M}) \sim \omega_D/E_F$ are omitted according to Migdal's theorem, and higher-order terms should be included in the electron self-energy if energies of phonon and electrons are comparable. Furthermore, the self-energy treats the electron band index as diagonal, a valid approximation for nondegenerate bands where the small energy scale of superconducting pairing suppresses band mixing. However, Migdal's theorem is not valid for phonons with small $|\mathbf{q}|$, and for Fermi surface with 1D topology.

Further, the 2×2 $\hat{\Sigma}(\mathbf{k}, i\omega_n)$ matrix can be rewritten as a linear combination of Pauli matrices and scalar functions as coefficients:

$$\hat{\Sigma}(\mathbf{k}, i\omega_n) = i\omega_n[1 - Z(\mathbf{k}, i\omega_n)]\hat{\tau}_0 + \chi(\mathbf{k}, i\omega_n)\hat{\tau}_3 + \phi(\mathbf{k}, i\omega_n)\hat{\tau}_1 + \bar{\phi}(\mathbf{k}, i\omega_n)\hat{\tau}_2, \quad (2.103)$$

like $Z(\mathbf{k}, i\omega_n)$ as *mass renormalization* function, $\chi(\mathbf{k}, i\omega_n)$ as *energy shift*, $\phi(\mathbf{k}, i\omega_n)$ as *order parameter*, and the gauge is chosen where the $\bar{\phi}(\mathbf{k}, i\omega_n) = 0$. By combining equation (2.101) with equation (2.103), after some algebra, one obtains:

$$\hat{G}(\mathbf{k}, i\omega_n) = -\frac{i\omega_n Z(\mathbf{k}, i\omega_n)\hat{\tau}_0 + [\epsilon_{\mathbf{k}} + \chi(\mathbf{k}, i\omega_n)]\hat{\tau}_3 + \phi(\mathbf{k}, i\omega_n)\hat{\tau}_1}{\Theta(\mathbf{k}, i\omega_n)}, \quad (2.104)$$

where $\Theta(\mathbf{k}, i\omega_n) = \det \hat{G}(\mathbf{k}, i\omega_n) = [\omega_n Z(\mathbf{k}, i\omega_n)]^2 + [\epsilon_{\mathbf{k}} + \chi(\mathbf{k}, i\omega_n)]^2 + [\phi(\mathbf{k}, i\omega_n)]^2$. The strategy now is to enforce self-consistency by substituting the Green's function from equation (2.104) into the self-energy terms in equation (2.102). Matching the scalar coefficients of the Pauli matrices in this process the *anisotropic ME equations* can be obtained:

$$\left\{ \begin{array}{l} Z(\mathbf{k}, i\omega_n) = 1 + \frac{T}{\omega_n N(E_F)} \sum_{\mathbf{k}'n'} \frac{\omega_{n'} Z(\mathbf{k}', i\omega'_{n'})}{\Theta(\mathbf{k}', i\omega'_{n'})} \lambda(\mathbf{k}, \mathbf{k}', n - n'); \end{array} \right. \quad (2.105)$$

$$\left\{ \begin{array}{l} \chi(\mathbf{k}, i\omega_n) = -\frac{T}{N(E_F)} \sum_{\mathbf{k}'n'} \frac{\epsilon_{\mathbf{k}'} + \chi(\mathbf{k}', i\omega'_{n'})}{\Theta(\mathbf{k}', i\omega'_{n'})} \lambda(\mathbf{k}, \mathbf{k}', n - n'); \end{array} \right. \quad (2.106)$$

$$\left\{ \begin{array}{l} \phi(\mathbf{k}, i\omega_n) = \frac{T}{N(E_F)} \sum_{\mathbf{k}'n'} \frac{\phi(\mathbf{k}', i\omega'_{n'})}{\Theta(\mathbf{k}', i\omega'_{n'})} [\lambda(\mathbf{k}, \mathbf{k}', n - n') - N(E_F)V_C], \end{array} \right. \quad (2.107)$$

where $\hbar = k_B = 1$ and $\lambda(\mathbf{k}, \mathbf{k}', n - n') = \lambda_{\text{ansio}} = \int_0^\infty \frac{2\omega}{(\omega_n - \omega_{n'})^2 + \omega^2} \alpha^2 F(\mathbf{k}, \mathbf{k}', \omega) d\omega$ is the anisotropic (\mathbf{k} spatial (momentum) dependence) *e-ph* coupling. The Eliashberg spectral function $\alpha^2 F(\mathbf{k}, \mathbf{k}', \omega)$ can be written in the following form:

$$\alpha^2 F(\mathbf{k}, \mathbf{k}', \omega) = N(E_F) \sum_{\nu} |g_{\mathbf{k}\mathbf{k}'}^{\nu}|^2 \delta(\omega - \omega_{q\nu}), \quad (2.108)$$

which can be calculated using the DFPT formalism, specifically the equation (2.88). Also, one can further characterize the superconducting gap as:

$$\Delta(\mathbf{k}, i\omega_n) = \frac{\phi(\mathbf{k}, i\omega_n)}{Z(\mathbf{k}, i\omega_n)}, \quad (2.109)$$

so that the anisotropic critical temperature (T_c^{ansio}) is the maximum temperature at which the superconducting gap function $\Delta(\mathbf{k}, i\omega_n)$ is non-zero, corresponding to the onset of superconductivity and the existence of nontrivial solutions to the ME equations. The ME equations can be simplified by limiting the consideration to electron bands close to the Fermi energy, where the energy shift $\chi(\mathbf{k}, i\omega_n)$ becomes negligible and can be set to zero, with constant electronic DOS, reducing the problem to two coupled nonlinear equations that can be solved self-consistently for each temperature T :

$$\begin{cases} Z(\mathbf{k}, i\omega_n) = 1 + \frac{\pi T}{\omega_n} \sum_{\mathbf{k}'n'} W_{\mathbf{k}'} \frac{\omega_{n'}}{\sqrt{R(\mathbf{k}', i\omega_{n'})}} \lambda_{\text{ansio}}; \\ Z(\mathbf{k}, i\omega_n) \Delta(\mathbf{k}, i\omega_n) = \pi T \sum_{\mathbf{k}'n'} W_{\mathbf{k}'} \frac{\Delta(\mathbf{k}', i\omega_{n'})}{\sqrt{R(\mathbf{k}', i\omega_{n'})}} (\lambda_{\text{ansio}} - N(E_F) V_C), \end{cases} \quad (2.110) \quad (2.111)$$

where $R(\mathbf{k}, i\omega_n) = \omega_n^2 + \Delta^2(\mathbf{k}, i\omega_n)$, $W_{\mathbf{k}} = \delta(\epsilon_{\mathbf{k}})/N(E_F)$, with the cutoff for sum over Matsubara frequencies being ω_c , which is 4–10 times the maximum phonon energy.

2.5.2.2 Key approximations and methods in ME theory

Let us now outline some of the key approximations and methods commonly used in the ME formalism:

Coulomb interaction – in equation (2.111) the Coulomb interaction V_C , expressed as a double average over Fermi surface, can be replaced by a dimensionless parameter μ^* after performing the energy integral up to the cutoff frequency, also known as *Morel-Anderson*

pseudopotential (semiempirical parameter):

$$\mu^* = \frac{\mu}{1 + \mu \ln(E_F)/\omega_c}, \quad (2.112)$$

which takes values between 0.1 and 0.16 for a wide range of superconductors.

Analytic continuation to the real axis – the ME approach offers high computational efficiency when formulated on the imaginary Matsubara frequency axis, enabling the calculation of critical temperatures. However, for computation of spectral properties one needs the superconducting gap along the real frequency axis. While directly solving the equations on the real axis is challenging, the gap and renormalization function can be obtained through analytic continuation of the solutions from the imaginary axis. This continuation is typically performed using Padé approximation or Marsiglio–Schossmann–Carbotte (MSC) iterative procedures [299]. For example, by using the MSC formalism, one can obtain the quasiparticle energy $E_{\mathbf{k}} = \sqrt{[\epsilon_{\mathbf{k}}/Z(\mathbf{k}, E_{\mathbf{k}})]^2 + \Delta^2(\mathbf{k}, E_{\mathbf{k}})}$, and at the Fermi level, $\epsilon_{\mathbf{k}} = 0$, so that the quasiparticle shift is defined as $E_{\mathbf{k}} = \text{Re} \Delta(\mathbf{k}, E_{\mathbf{k}})$, with the *gap edge* being $\text{Re}[\Delta(\mathbf{k}, \Delta_{\mathbf{k}})] = \Delta_{\mathbf{k}}$.

Isotropic ME equations – in materials where Fermi surface anisotropy is minimal or diminished by impurities, the ME equations can be simplified to an isotropic form by averaging over the Fermi surface, so that equations (2.110) and (2.111) become:

$$\begin{cases} Z(i\omega_n) = 1 + \frac{\pi T}{\omega_n} \sum_{n'} \frac{\omega_{n'}}{\sqrt{R(i\omega_{n'})}} \lambda_{\text{iso}}; & (2.113) \\ Z(i\omega_n) \Delta(i\omega_n) = \pi T \sum_{n'} \frac{\Delta(i\omega_{n'})}{\sqrt{R(i\omega_{n'})}} (\lambda_{\text{iso}} - \mu^*), & (2.114) \end{cases}$$

with isotropic Eliashberg spectral function being $\alpha^2 F(\omega) = \sum_{\mathbf{k}, \mathbf{k}'} W_{\mathbf{k}} W_{\mathbf{k}'} \alpha^2 F(\mathbf{k}, \mathbf{k}', \omega)$. Furthermore, the normalized quasiparticle density of states in the superconducting state, $N_S(\omega)$, can be derived from the isotropic superconducting gap on the real axis, giving $N_S(\omega)/N(E_F) = \text{Re}[\omega/\sqrt{\omega^2 - \Delta^2(\omega)}]$.

Isotropic DFPT calculations and McMillan-Allen-Dynes (MAD) formula – instead of performing isotropic ME calculations, one can estimate the T_c^{iso} by combining DFPT with the McMillan-Allen-Dynes (MAD) formula [300, 301]. Therefore, let us start with the harmonic approximation of DFPT, in which phonons are considered as non-interacting lattice vibrations with infinite lifetimes. However, interactions with electrons modify these phonons, introducing a finite linewidth – proportional to the inverse of lifetime – connected to the phonon self-energy's

$$\begin{aligned}
\text{(a) } \Pi(\omega) &= \text{Diagram 1} + \text{Diagram 2} - \text{Diagram 3} \\
&\quad + \text{Diagram 4} - \text{Diagram 5} - \text{Diagram 6} + \dots \\
\text{(b) } \text{Re } \Pi(0) &= \text{Diagram 7} \quad \text{(c) } \text{Im } \Pi(\omega) = \text{Im } \text{Diagram 8}
\end{aligned}$$

Figure 2.10: (a) The Feynman diagram, in ME approximation, of the phonon self-energy ($\hat{\Pi}$) considering second-order contributions in e -ph vertex. By using the screened vertex as defined in Figure 2.6, real (b), and (c) imaginary part of $\hat{\Pi}$ can be calculated. Adapted from [267].

imaginary component ($\text{Im } \hat{\Pi}$), and causing a frequency shift associated with the real part ($\text{Re } \hat{\Pi}$), where $\hat{D}_\nu(\mathbf{q}, i\omega_n) = \hat{D}_{\nu 0}^{-1}(\mathbf{q}, i\omega_n) - \hat{\Pi}_\nu(\mathbf{q}, i\omega_n)$ [267]. As depicted in Figure 2.10(c), using the Migdal approximation, the $\text{Im } \hat{\Pi}$ which corresponds to the phonon half-width at half-maximum (linewidth) $\gamma_{q\nu}$ can be calculated as:

$$\gamma_{q\nu} = \hat{\Pi}_\nu'' = \text{Im } \hat{\Pi}_\nu = \sum_{kmn} w_k |g_{\mathbf{k},\mathbf{q}}^{mn\nu}|^2 \frac{f(\epsilon_{\mathbf{k}n}) - f(\epsilon_{\mathbf{k}+\mathbf{q}m})}{\epsilon_{\mathbf{k}n} - \epsilon_{\mathbf{k}+\mathbf{q}m} - \omega_{q\nu} + i\eta}, \quad (2.115)$$

where e -ph matrix elements can be calculated using DFPT equation (2.88), w_k are specific weights for \mathbf{k} -grid normalized to 2 (to account for spin degeneracy), and η is broadening [302]. A common approximation to equation (2.115) involves small broadening η ($T \rightarrow 0$), leading to “double delta approximation”, as implemented in QE [233] and Electron-Phonon Wannier code (EPW) [302].³⁷ For specific phonon mode ν and \mathbf{q} -point the e -ph coupling can be expressed as:

$$\lambda_{q\nu} = \frac{1}{\pi N(E_F)} \frac{\gamma_{q\nu}}{\omega_{q\nu}^2} = \frac{1}{N(E_F)\omega_{q\nu}} \sum_{kmn} w_k |g_{\mathbf{k},\mathbf{q}}^{mn\nu}|^2 \delta(\epsilon_{\mathbf{k}n})\delta(\epsilon_{\mathbf{k}+\mathbf{q}m}), \quad (2.116)$$

so that the total isotropic e -ph coupling is: $\lambda_{\text{iso}} = \sum_{q\nu} w_q \lambda_{q\nu}$, where w_q are BZ phonon weights normalized to 1 [302]. The Eliashberg spectral function can be calculated as:

$$\alpha^2 F(\omega) = \frac{1}{2} \sum_{q\nu} w_q \omega_{q\nu} \lambda_{q\nu} \delta(\omega - \omega_{q\nu}), \quad (2.117)$$

so that one can also calculate λ_{iso} by using the formula: $2 \int_0^\infty \alpha^2 F(\omega) \omega^{-1} d\omega$. Now using the MAD formula (see Figure 2.8) [300, 301], which is valid for $\lambda_{\text{iso}} < 2$, the T_c^{iso} can be calculated as:

$$T_c^{\text{iso}} = \frac{\omega_{\text{log}}}{1.2} \exp \left[\frac{-1.04(1 + \lambda_{\text{iso}})}{\lambda_{\text{iso}}(1 - 0.62\mu^*) - \mu^*} \right], \quad (2.118)$$

³⁷EPW allows for both precise calculations of e -ph properties by solving the ME equations without simplifications, and computations using the double delta approximation for efficiency or comparison.

where $\omega_{log} = \exp \left[\frac{2}{\lambda_{iso}} \int \alpha^2 F(\omega) \log(\omega) \omega^{-1} d\omega \right]$.

Other approximations – the standard ME equations rely on several key approximations, including the validity of Migdal’s theorem, the use of a single-band model, and an isotropic order parameter. These have been generalized to address more complex systems, such as multi-band superconductors like MgB₂, pairing symmetries beyond the conventional *s*-wave (singlet superconductors), such as *p*-wave and *d*-wave, and unconventional superconductors requiring vertex corrections. Extensions also account for finite bandwidth effects, asymmetric occupation of conduction bands ($\chi(\omega) \neq 0$), nonuniform DOS, and the inclusion of disorder or magnetic impurities, spin fluctuations, critical magnetic fields, and proximity effects [295].

2.5.2.3 Electron-phonon Wannier (EPW) interpolation

The anisotropic ME formalism, combined with electron-phonon Wannier (EPW) interpolation, addresses the computational challenges posed by dense BZ sampling required near the Fermi surface, e.g., determination of electronic states, phonon energies, and *e-ph* matrix elements using standard DFPT formalism [302, 303]. Instead, a set of *e-ph* elements calculated on a coarse grid using DFPT is interpolated in the maximally localized Wannier function (MLWF) representation (see APPENDIX A1), followed by transformation of electronic hamiltonian and phonon dynamical matrices, and then interpolated into the Bloch representation using Fourier techniques. Therefore, the *e-ph* matrix elements in MLWF representation can be computed using the relation:

$$g(\mathbf{R}_e, \mathbf{R}_p) = \frac{1}{N_p} \sum_{\mathbf{k}, \mathbf{q}} w_{\mathbf{k}} w_{\mathbf{q}} e^{-i(\mathbf{k}\mathbf{R}_e + \mathbf{q}\mathbf{R}_p)} U_{\mathbf{k}+\mathbf{q}}^\dagger g_{\mathbf{k}, \mathbf{q}} U_{\mathbf{k}} u_{\mathbf{q}}^{-1}, \quad (2.119)$$

with weights normalized to 1. The electronic hamiltonian in the MLWF representation is formulated as:

$$H_{\mathbf{R}_e, \mathbf{R}'_e}^{el} = \sum_{\mathbf{k}} w_{\mathbf{k}} e^{-i(\mathbf{R}'_e - \mathbf{R}_e) \cdot \mathbf{k}} U_{\mathbf{k}}^\dagger H_{\mathbf{k}}^{el} U_{\mathbf{k}}, \quad (2.120)$$

which elements decay rapidly with the distance $|\mathbf{R}'_e - \mathbf{R}_e|$. On the other hand, the dynamical matrix is transformed as:

$$D_{\mathbf{R}_p, \mathbf{R}'_p}^{ph} = \sum_{\mathbf{q}} w_{\mathbf{q}} e^{-i(\mathbf{R}'_p - \mathbf{R}_p) \cdot \mathbf{q}} e_{\mathbf{q}}^\dagger D_{\mathbf{q}}^{ph} e_{\mathbf{q}}, \quad (2.121)$$

where $e_{\mathbf{q}}$ are the orthonormal eigenvectors [302, 303]. Therefore, EPW efficiently studies superconductivity by leveraging Wannier interpolation – fine BZ sampling – for *e-ph* elements.

BOROPHENE AS A PLATFORM FOR 2D MAGNETISM

In this chapter, we present results on the magnetic properties of Fe nanostructures on β_{12} borophene supported by an Ag(111) substrate and Mn-intercalated β_{12} bilayer borophene, obtained from DFT, SDFT, and other theoretical models, offering insights into the underlying mechanisms for magnetic order in these 2D systems.

3.1 Fe-based 2D magnets on β_{12} borophene/Ag(111)

The discovery of monolayer graphene in 2004 sparked immense interest in 2D materials, unveiling a rich array of exceptional physical and chemical properties, setting thereby the stage for the exploration of other 2D crystals with diverse characteristics. Among these, only a few mechanically exfoliated vdW materials exhibit intrinsic magnetic properties, making them valuable for both fundamental studies of magnetism in the 2D limit and potential applications in spintronics. Recent research highlights the preservation of long-range magnetic order in materials such as CrI_3 , FePS_3 , and $\text{Cr}_2\text{Ge}_2\text{Te}_6$, showcasing ferromagnetic and antiferromagnetic behaviors under specific conditions. Nonmagnetic 2D materials like graphene and h-BN can be magnetized through defect engineering or doping with magnetic atoms. However, the tendency of magnetic adatoms to form clusters poses a significant challenge. When metal adatoms are placed at point defects in graphene or h-BN, they are stabilized and prevented from clustering, as these defects act as “trapping” sites. Despite this, the random distribution of defects prevents the establishment of long-range magnetic order. In contrast, borophene (B-2D) – the new 2D “wonder” material – synthesized on metallic substrates, offers a periodic lattice with well-ordered and closely packed reactive holes, presenting a promising template for stabilizing regular magnetic nanostructures, as shown in our work for well-ordered Fe nanostructures on β_{12} borophene supported by Ag(111) substrate (B-2D/Ag(111)). This work combines DFT, SDFT, Ising & Heisenberg model, and MC simulations in order to investigate the magnetic properties of Fe atoms on B-2D/Ag(111), and potential for achieving long-range magnetic order.

3.1.1 Structural properties of β_{12} borophene: freestanding and supported by Ag(111) substrate

At the beginning, we will refer to the structural properties of β_{12} borophene (B-2D), as depicted in Figure 3.1(a). This specific phase possesses a triangular lattice of boron (B) atoms with periodic rows of empty hexagonal holes (HHs) formed by the absence of B atoms at their center (B_{hollow}). Furthermore, when supported by an Ag(111) substrate, as depicted in Figure 3.1(d), it serves as an excellent template for the growth of well-ordered Fe structures, as will be detailed in the subsequent subsections. To model this B-2D/Ag(111) structure using DFT (see **APPENDIX A2**

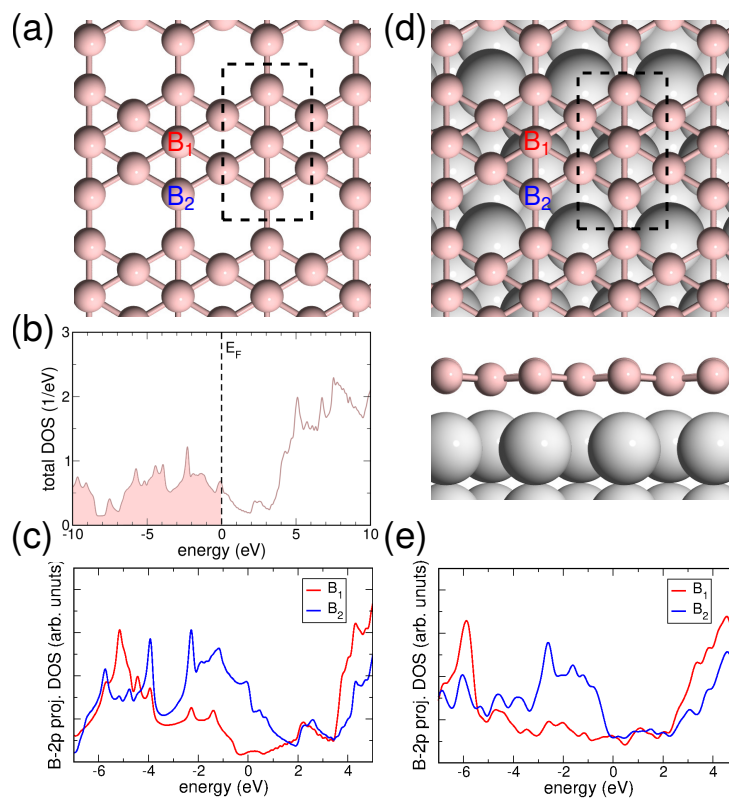


Figure 3.1: (a) Structure of isolated β_{12} borophene from a “top” perspective, followed by (b) its overall electronic DOS and (c) contributions from the 2p orbitals of B_1 and B_2 atoms, each with distinct CN values. (d) Structure of β_{12} borophene placed on an Ag(111) crystal, with (e) the associated electronic DOS projected onto the 2p orbitals of B_1 and B_2 . B and Ag atoms are shown as small ochre and large gray spheres, respectively.

for computational details), it is important to note that the B-2D layer exhibits a close-packed HH arrangement aligned along the [110] direction of the Ag(111) surface, with its lattice parameter closely matching the interatomic spacing of Ag atoms. This minimal lattice mismatch preserves the translational symmetry of the Ag(111) substrate, enabling the system to be described by a compact surface unit cell. The computed lattice parameters, $a = 2.94 \text{ \AA}$ and $b = 5.09 \text{ \AA}$,

align exceptionally well with experimental measurements and prior DFT results. Regarding the electronic properties, the total DOS graphic in Figure 3.1(b) highlights the metallic nature of the B-2D sheet, with variations in the coordination number ($CN = 4, 5, 6$) of B atoms driving its distinct local electronic properties (see Figure 3.1(c)). Notably, the B_2-2p states exhibit a higher DOS near the Fermi level (E_F) compared to B_1-2p states. The weak coupling between B-2D and the Ag surface, characterized by a binding energy of 0.12 eV per B atom, results in charge transfer from Ag to B-2D, shifting the $2p$ states of B_2 below E_F , as depicted in Fig. 3.1(e). The subsequent subsection explores Fe adsorption on B-2D/Ag(111) and the resulting formation of diverse nanostructures.

3.1.2 Different Fe nanostructures on β_{12} borophene supported by Ag(111) substrate

Variations in the local electronic properties of B atoms, driven by differences in their CN values, are also closely tied to their chemical reactivity. Atoms with lower CN values generally exhibit stronger binding of adsorbates compared with their higher- CN counterparts. To validate this statement, we calculated the binding energies (E_b) of Fe atoms on both the freestanding B-2D structure and on the B-2D/Ag(111) configuration, using the following formulas respectively:

$$\begin{cases} E_b^{\text{B-2D}} = \frac{N_{\text{Fe}}E(\text{Fe}) + E(\text{B-2D}) - E(\text{Fe/B-2D})}{N_{\text{Fe}}}, & (3.1) \\ E_b^{\text{B-2D/Ag(111)}} = \frac{N_{\text{Fe}}E(\text{Fe}) + E(\text{B-2D/Ag(111)}) - E(\text{Fe/B-2D/Ag(111)})}{N_{\text{Fe}}}, & (3.2) \end{cases}$$

where, $E()$ denotes the total energy of considered systems, while N_{Fe} specifies the Fe content per unit cell. Further, Figure 3.2(a) shows the most favorable Fe adsorption locations on B-2D/Ag(111), while the related E_b values are provided in Figure 3.2(b) and Table 3.1, which also lists E_b for Fe on freestanding B-2D at corresponding sites. As evident, the HH positions on B-2D/Ag(111) are the most energetically preferred one, with Fe binding energies of 3.70 eV and 3.32 eV for configurations beneath (I) and atop (II) the B-2D layer, respectively, as illustrated in Figure 3.2(c–d). For an Fe atom to diffuse from site II to site I, traversing the HH region, an overcoming of an energy barrier of 1.0 eV is required. While thermodynamics favor Fe atom binding beneath the β_{12} borophene layer, insufficient surface temperature or kinetic energy during deposition can result in Fe adatoms remaining atop the β_{12} borophene, becoming “trapped” in adsorption site II. Furthermore, Table 3.1 presents the binding energies

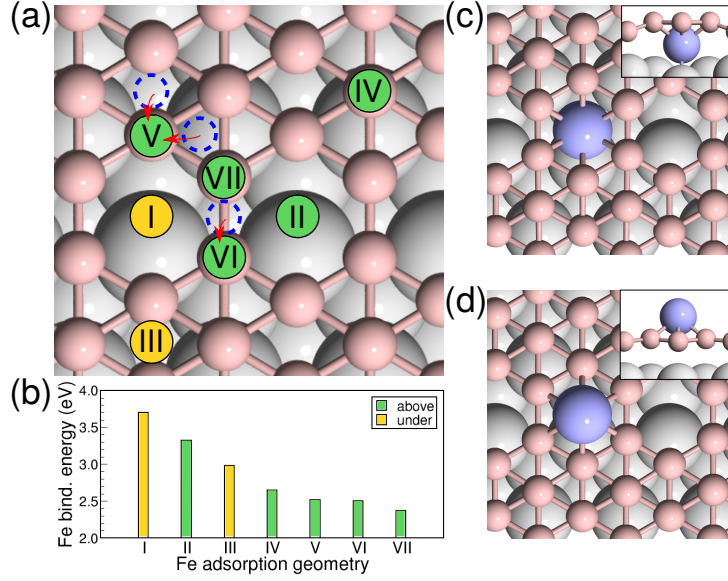


Figure 3.2: (a) Favorable Fe adsorption geometries and (b) associated binding strengths on B-2D/Ag(111). Yellow and green color represent Fe positions beneath and atop β_{12} borophene, while dashed blue ones highlight unstable locations with red arrows indicating nearby stable positions. (c) Top and (d) side views (inset) display the preferred adsorption positions (I, II) from (a). Fe atoms are shown in ice blue, with boron and silver keeping the same color coding as Figure 3.1.

and magnetic moments of Fe atoms across seven adsorption sites on the B-2D/Ag(111) structure, as depicted in Figure 3.2. For comparison, we also included data for the corresponding sites of freestanding β_{12} borophene. The significantly stronger binding of Fe atoms to the freestanding β_{12} borophene compared to the Ag(111)-supported sheet aligns with the anticipated reduction in β_{12} borophene's reactivity upon interaction with the Ag(111) surface. This observation is consistent with studies indicating that the interaction between β_{12} borophene and substrates like Ag(111) can modulate its electronic properties, thereby affecting its reactivity.

Now we will focus more on the results for the adsorption of two or more Fe atoms on the

Table 3.1: For the adsorption structures shown in Figure 3.2(a), the computed adsorption energies and magnetic moments of Fe atoms are present.

Configuration	Freestanding β_{12} borophene		B-2D/Ag(111)	
	Binding energy (eV/atom)	Mag. moment (μ_B /atom)	Binding energy (eV/atom)	Mag. moment (μ_B /atom)
I (Fig. 3.2(a))	-	-	3.70	2.27
II (Fig. 3.2(a))	4.57	1.01	3.32	2.92
III (Fig. 3.2(a))	-	-	2.98	1.52
IV (Fig. 3.2(a))	2.84	2.18	2.65	3.11
V (Fig. 3.2(a))	-	-	2.52	2.81
VI (Fig. 3.2(a))	-	-	2.50	2.74
VII (Fig. 3.2(a))	-	-	2.37	2.71

B-2D/Ag(111) structure. Our results indicate a tendency for adatoms to aggregate into dimers, with the most stable configuration above the β_{12} borophene as shown in Figure 3.3(a). The corresponding binding energy of 3.52 eV per atom, as shown in Table 3.2, is for 0.2 eV per atom greater than that of a single Fe atom located at site II. The Fe–Fe bond length of 2.48 Å, larger than the 2.01 Å observed for gas-phase of Fe₂ but smaller than the 2.93 Å separation between B-2D holes at Ag(111), results from a balance between the holes’ high reactivity, which favors elongation, and strong Fe–Fe interactions, which promote contraction. Furthermore, in line

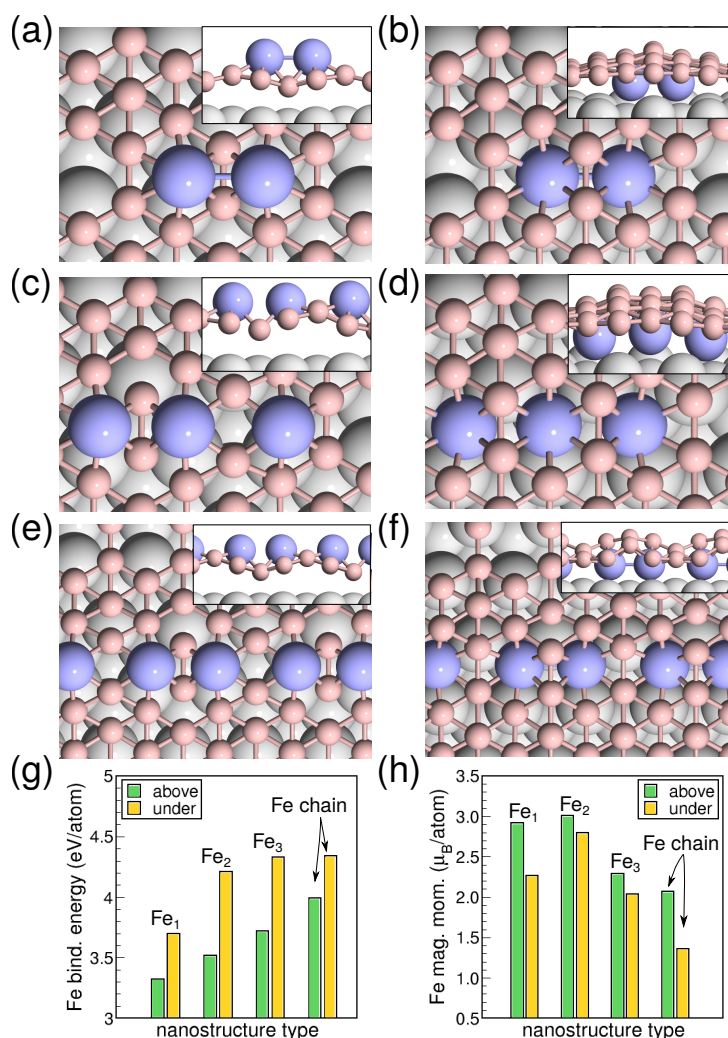


Figure 3.3: Fe (a,b) dimers, (c,d) trimers, and (e,f) infinite chain (above,under) the HHs of B-2D/Ag(111) are shown from top and side perspectives. Panels (g) and (h) display adsorption energies and magnetic moments per Fe atom.

with the single Fe atom case, the configuration beneath the β_{12} borophene (see Figure 3.3(b)) is significantly more stable than the configuration above, with a binding energy of 4.21 eV/atom and a shorter bond length of 2.40 Å due to interaction with the Ag(111) surface. Unlike β_{12} borophene, the flatter potential energy landscape of Ag(111) surface results in weaker site-specific

Table 3.2: Adsorption energies and magnetic moments per Fe atom, computed for the configurations shown in Figure 3.3.

Configuration	Freestanding β_{12} borophene		B-2D/Ag(111)	
	Binding energy (eV/atom)	Mag. moment (μ_B /atom)	Binding energy (eV/atom)	Mag. moment (μ_B /atom)
Fe ₂ -A (Fig. 3.3(a))	4.85	1.07	3.52	3.01
Fe ₂ -U (Fig. 3.3(b))	-	-	4.21	2.80
Fe ₃ -A (Fig. 3.3(c))	4.78	1.24	3.72	2.29
Fe ₃ -U (Fig. 3.3(d))	-	-	4.33	2.04
Fe _{chain} -A (Fig. 3.3(e))	4.88	1.04	3.99	2.07
Fe _{chain} -U (Fig. 3.3(f))	-	-	4.34	1.36

binding preferences of Fe. The trend is also observed for Fe₃, where configurations beneath the β_{12} borophene are more stable, and is further amplified in infinite Fe dimmer chains (Fe_{chain}), where the elongation of the linear nanostructure greatly enhances the stability of Fe adatoms (see Figure 3.3 and Table 3.2). On top of that, all considered Fe adsorption configurations exhibit magnetic properties, with spin moments varying from 1.36 μ_B in the chain (see Figure 3.3(f)) to 3.01 μ_B in the dimer (see Figure 3.3(a)). Also, Fe atoms adsorbed below the β_{12} borophene, close to the Ag(111) surface, show considerably smaller magnetic moments compared to those atop, in line with the expectation that stronger binding enhances Fe-3d state delocalization, thereby decreasing the exchange splitting between spin-majority and spin-minority states.

3.1.3 From Fe chain formation to Fe-based 2D magnetic structures on B-2D/Ag(111)

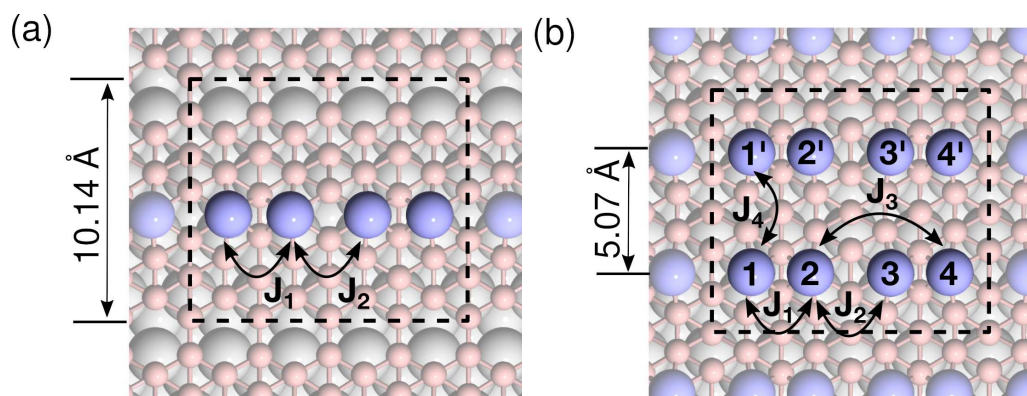


Figure 3.4: Top-down perspectives of (a) well-isolated and (b) densely arranged Fe chains on the B-2D/Ag(111) surface are presented. The black rectangle delineates the 4×2 surface unit cell employed in the computational analysis. Fe atom labeling corresponds to equations (3.3) and (3.4), with exchange coupling constants (J) between Fe atoms indicated by black double-headed arrows.

We now turn our attention to the structural, electronic, and magnetic properties of infinite Fe monoatomic chains positioned either above or beneath the β_{12} borophene on the Ag crystal. This system was modeled using a 4×2 supercell, considering two scenarios: (i) when the interchain distance is 10.14 Å, the Fe chains are assumed to be non-interacting (see Figure 3.4(a)), and (ii) when the distance is reduced by half, the Fe chains are treated as interacting in the closely packed configuration (see Figure 3.4(b)). Furthermore, Figure 3.5 presents the induced electron density

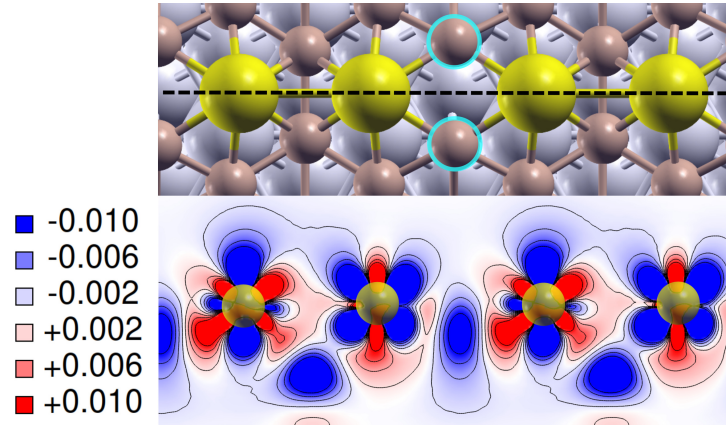


Figure 3.5: The electron charge density induced by the adsorption of an Fe chain on B-2D/Ag(111) is shown in the plane that intersects the Fe atoms (dashed black line). The color map represents the charge density in units of electrons/Bohr³. For clarity, only the Fe atoms, shown as yellow spheres, are displayed in the lower panel.

(ICD) plot, illustrating the redistribution of electrons resulting from the interaction between the Fe chain and the B-2D/Ag(111) configuration. Taken in the plane that intersects the Fe atoms, the plot reveals direct orbital overlap for the nearest Fe atoms in the dimer configuration. In contrast, the interaction between Fe atoms separated by 3.36 Å (between dimmers) occurs via a pair of boron atoms, indicated by pale blue rings in the top section of Figure 3.5. Let us now explore the magnetic properties of two distinct cases in more depth: (i) the isolated Fe chain, and (ii) the closely-packed Fe chains.

3.1.3.1 Isolated Fe chain

Structural analysis reveals significant dimerization in isolated Fe chain, as depicted in Figure 3.6(a). For the chain positioned above B-2D, the nearest neighbor (NN) distances range from 2.60 to 3.26 Å, while for the configuration where the Fe chain is embedded between B-2D and Ag(111), these distances vary between 2.50 and 3.36 Å. Interestingly, the buckling of the β_{12} borophene remains comparable to that observed in the trimer configuration, regardless of whether the Fe chain is situated above or beneath the B-2D sheet. Figure 3.6(b) schematically presents

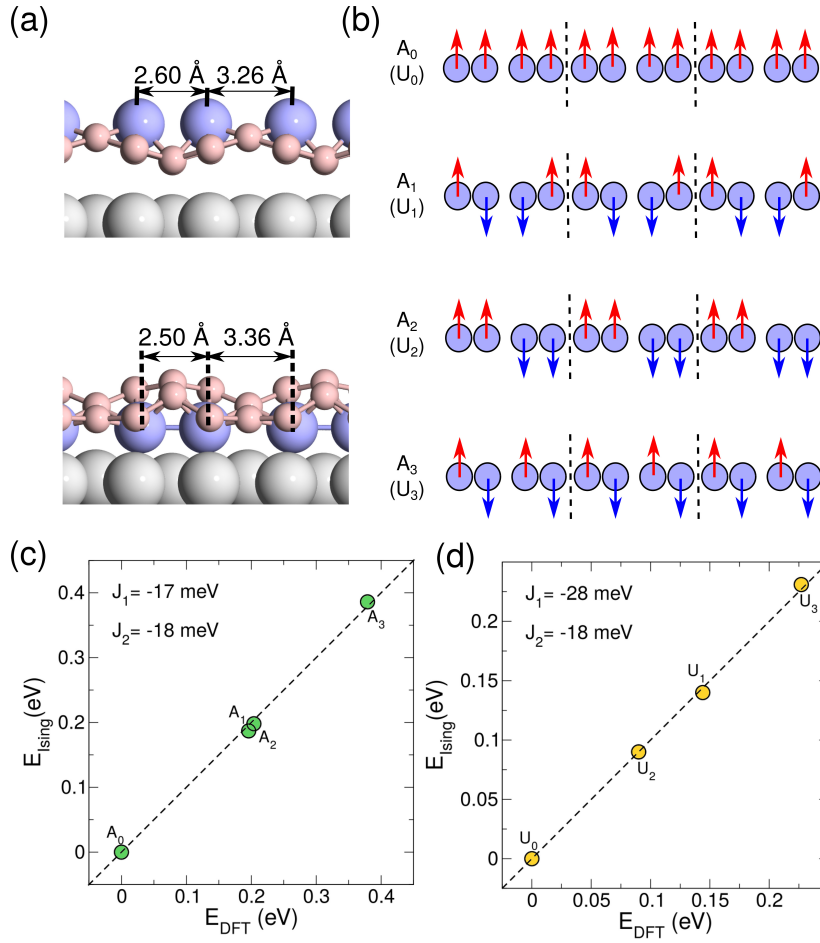


Figure 3.6: (a) Structure of single Fe chains from a “side” perspective, positioned either atop (upper panel) or beneath (bottom panel) the B-2D layer on the Ag(111) substrate. (b) A schematic representation highlighting four distinct spin configurations of Fe atoms in (a). The unit cell along the chain axis, indicated by black dashed lines, was employed in the SDFT calculations. (c) and (d) display the correlation between energy differences derived from SDFT calculations and those obtained by from Ising model (equation (3.3)) for Fe chains located atop and beneath the B-2D sheet, respectively.

four distinct spin configurations of isolated Fe chains, positioned either above (A chains) or under (U chains) the β_{12} borophene. These configurations, labeled as A_i and U_i , where $i \in \{0, 1, 2, 3\}$, correspond to the isolated Fe chains shown in Figure 3.6(a). The energy differences between these configurations, obtained from SDFT calculations, are analyzed within the framework of the Ising model:

$$E_{\text{Ising}} = J_1(M_1M_2 + M_3M_4) + J_2(M_2M_3 + M_4M_1), \quad (3.3)$$

where the exchange interaction is restricted to the NN. The exchange constant J_1 characterizes the interaction between Fe atoms within single dimer, while J_2 describes the exchange coupling between NN Fe atoms belonging to different dimers, as depicted in Figure 3.4(a). The M_i

Table 3.3: SDFT-computed relative energies (E_{SDFT}) of different spin configurations from Figure 3.6(b), compared with values derived from the Ising model using equation (3.3), along with the absolute magnetic moments of Fe atoms.

Spin config.	E_{SDFT} (eV)	E_{Ising} (eV)	Mag. moment ($\mu_{\text{B}}/\text{atom}$)
A ₀	0.00	0.00	1.67
A ₁	0.20	0.19	1.69
A ₂	0.20	0.20	1.66
A ₃	0.38	0.39	1.63
U ₀	0.00	0.00	1.15
U ₁	0.14	0.14	1.19
U ₂	0.09	0.09	1.14
U ₃	0.23	0.23	1.01

represent the magnetic moments associated with the four distinct Fe sites within the unit cell, as obtained from SDFT calculations. Table 3.3 summarizes the results of SDFT calculations, showing the relative energies of various spin configurations with respect to the lowest-energy state, alongside the absolute values of Fe magnetic moments. Figure 3.6(c–d) illustrates the excellent agreement between the SDFT calculations and the Ising model for the exchange constants $J_1 = 17$ meV and $J_2 = 18$ meV for *A* chain, and $J_1 = 28$ meV and $J_2 = 18$ meV for *U* chain. Also this figure reveals that the nearly degenerate antiferromagnetic spin configurations A_1 and A_2 of ferromagnetically coupled dimers in the *A* chain are split in the *U* chain due to enhanced dimerization, which modifies the exchange interactions and results in distinct coupling constants between M_1 and M_2 and between M_2 and M_3 . Furthermore, the difference in energy between the ground state and the most unfavorable setup is significantly smaller in the *U* chain, due to the Fe atoms, positioned beneath the β_{12} borophene, experiencing a stronger interaction with the Ag(111) surface, which leads to their reduced magnetic moments.

3.1.3.2 Closely-packed Fe chains

We now turn to the case of closely-packed Fe chains, examining their structural properties and the potential influence of their reduced interchain spacing on magnetic properties. A strong dimerization of Fe atoms is observed in closely-packed chains, as shown in Figure 3.7(a). The small interchain separation of 5.07 Å leads to notable interactions between the magnetic moments of neighboring chains. To account for these interactions, the system was treated as a 2D magnet, and eight distinct magnetic configurations were examined, as illustrated in Figure 3.7(b). The corrugation of the B-2D layer is reduced compared with that observed for isolated Fe chains, with

values of 1.03 Å and 1.04 Å for chains positioned above and under the B-2D layer, respectively. To fit the SDFT results to a 2D Ising model, additional coupling constants are introduced beyond

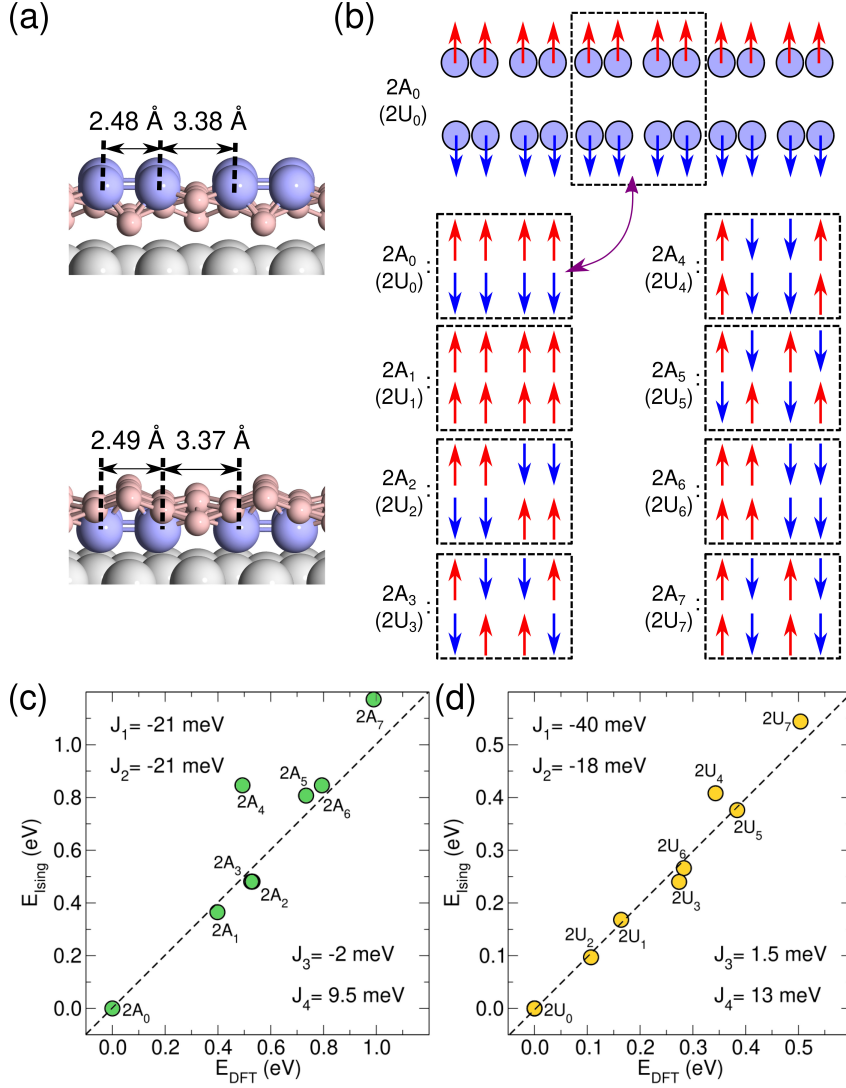


Figure 3.7: (a) Structure of closely-packed Fe chains from a “side” perspective, positioned either atop (upper panel) or beneath (bottom panel) the B-2D layer on the Ag(111) substrate. (b) Schematic representation of the unit cell with eight distinct spin configurations for Fe atoms in (a). (c) and (d) display the correlation between energy differences derived from SDFT calculations and those obtained by from Ising model (equation (3.4)) for Fe chains located atop and beneath the B-2D sheet, respectively.

those used in the 1D model (see equation (3.3)). Specifically, J_3 represents the coupling between next NN within the same chain, while J_4 captures the interaction with the nearest Fe atoms from the adjacent chains (see Figure 3.4(b)). The 2D Ising model is expressed as:

$$E_{\text{Ising}} = J_1(M_1M_2 + M_3M_4 + \dots) + J_2(M_2M_3 + M_4M_1 + \dots) + 2J_3(M_1M_3 + M_2M_4 + \dots) + 2J_4 \sum_{i=1}^4 M_iM_{i'}, \quad (3.4)$$

where the terms denoted by “ r ” refer to analogous interactions described by the first two terms in each bracket, but include interactions with atoms from the neighboring chain. The energies of different spin configurations, as depicted in Figure 3.7(b), relative to the most stable configuration, are calculated using SDFT and are provided in Table 3.4. As with isolated Fe chains,

Table 3.4: SDFT-computed relative energies (E_{SDFT}) of different spin configurations from Figure 3.7(b), compared with values derived from the Ising model using equation (3.4), along with the absolute magnetic moments of Fe atoms.

Spin config.	E_{SDFT} (eV)	E_{Ising} (eV)	Mag. moment ($\mu_{\text{B}}/\text{atom}$)
$2A_0$	0.00	0.00	1.65
$2A_1$	0.40	0.37	1.54
$2A_2$	0.53	0.48	1.56
$2A_3$	0.53	0.48	1.62
$2A_4$	0.49	0.85	1.57
$2A_5$	0.73	0.81	1.47
$2A_6$	0.79	0.85	1.53
$2A_7$	0.99	1.17	1.47
$2U_0$	0.00	0.00	1.10
$2U_1$	0.16	0.17	0.82
$2U_2$	0.11	0.10	1.03
$2U_3$	0.27	0.24	0.99
$2U_4$	0.34	0.41	0.79
$2U_5$	0.38	0.38	0.72
$2U_6$	0.28	0.27	0.88
$2U_7$	0.50	0.54	0.09

ferromagnetic ordering within the closely-packed Fe chains remains the most energetically favorable configuration. However, the interchain exchange interaction promotes antiferromagnetic coupling, resulting in the spins of neighboring chains being aligned oppositely in the most stable spin configurations, corresponding to the $2A_0$ and $2U_0$ arrangements, as shown in Figure 3.7(b). As anticipated from the preferred intra- and interchain spin arrangements, the least favorable magnetic configurations – $2A_7$ and $2U_7$ in Figure 3.7(b) – exhibit antiferromagnetic coupling within the chains and ferromagnetic coupling between them, opposite to the previously mentioned $2A_0$ and $2U_0$ configurations. Overall, Figure 3.7(c–d) demonstrates an excellent agreement between the SDFT and 2D Ising model, apart from the $2A_4$ spin configuration.

3.1.4 Monte Carlo simulations

Standard SDFT calculations are restricted to predicting magnetic properties at zero temperature, while assessing the robustness of extended magnetic order against thermal fluctuations up to the transition temperature (T_c) requires alternative theoretical approaches. To address this, we described our model as a 2D network of classical moments and applied Monte Carlo (MC) method to estimate the T_c for cases where Fe-based 2D magnet is situated atop (A) or beneath (U) the β_{12} borophene on Ag(111) crystal. The isotropic exchange parameters J used for MC simulations were extracted from our SDFT computations. The calculated T_c varies significantly with the spin dimensionality, consistent with observations for CrI_3 , where the Ising approach predicts a T_c three times higher than both the Heisenberg framework and experimental observations.

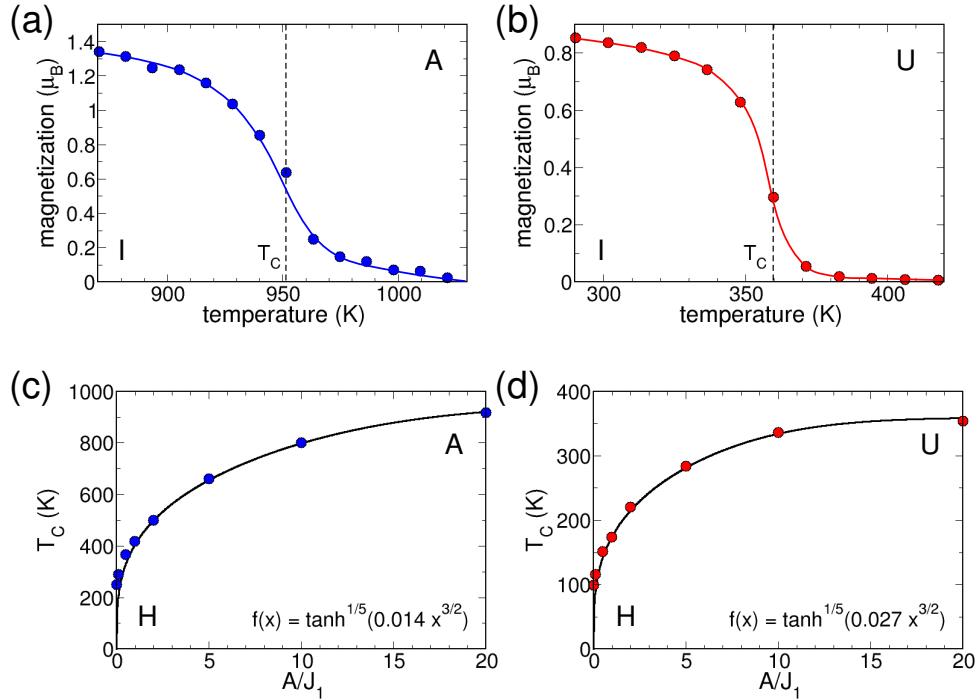


Figure 3.8: Magnetization vs. temperature, obtained via MC simulations, is shown for 2D Fe positioned (a) atop (A), and (b) beneath (U) B-2D on Ag(111), assuming that the classical Ising (I) model describes their magnetic properties. The critical temperature (T_c) of these 2D magnets, as a function of scaled anisotropy (A/J_1), is depicted for configurations (c) atop (A) and (d) beneath (U) B-2D on Ag(111), combining MC simulations with the classical anisotropic Heisenberg model incorporating SIA term.

To estimate the T_c of the Fe-based magnets positioned atop and beneath β_{12} borophene on Ag(111) crystal, we employed MC simulations based on the Ising model. The variation of sublattice magnetization with temperature for these systems is displayed in Figure 3.8(a–b), and the T_c was identified as the temperature corresponding to the peak in the specific heat.

The calculations reveal that the T_c for the Fe structure atop β_{12} borophene is 950 K which is significantly higher compared with 360 K for the Fe configuration beneath the borophene layer.

In the subsequent phase of MC simulations, we replaced the Ising model with a treatment of Fe magnetic moments as classical 3D vectors, while maintaining the same exchange interaction parameters. These simulations were conducted within the anisotropic Heisenberg model, incorporating an additional SIA term into equation (3.4):

$$E_{\text{SIA}} = A \sum_i (M_i^z)^2. \quad (3.5)$$

Now, building on the findings of D. Torelli and T. Olsen [304], who showed that the T_c predicted by the Ising model aligns with the Heisenberg model when incorporating SIA term in the $A/J \rightarrow \infty$ limit, we extended our MC simulations to the anisotropic Heisenberg model. Various A/J_1 values were analyzed in these simulations, with the results depicted in Figure 3.8(c–d). The results of the MC simulations were then analyzed by fitting them to analytical functions of the form:

$$T_C = T_C^{\text{Ising}} f(A/J_1), \quad (3.6)$$

with

$$\begin{aligned} f(x) &= \tanh^{1/5}(0.014x^{3/2}) && (A - \text{magnet}), \\ f(x) &= \tanh^{1/5}(0.027x^{3/2}) && (U - \text{magnet}). \end{aligned} \quad (3.7)$$

By incorporating SOC into our new SDFT calculations, we determined the SIA parameters for Fe-based 2D magnets, finding values of -0.2 meV and -0.1 meV for these magnets atop and beneath β_{12} borophene, respectively. These parameters were then used in the anisotropic Heisenberg model to compute the values of T_c , yielding 105 K for the A -2D magnet and 30 K for the U -2D magnet. These results suggest that the systems can not sustain long-range magnetic order above 105 K and that the Ising model overestimates the critical temperature by about a factor of 10.

3.1.5 Conclusions

By combining SDFT calculations with MC simulations, we explored the magnetic properties of nanostructures formed by Fe adsorption on a borophene layer supported by Ag(111) substrate.

Ab initio calculations revealed that Fe atoms exhibit a strong preference for binding to HH of borophene, effectively filling its periodic 2D void pattern. Structures with Fe situated between the borophene layer and the Ag(111) substrate were found to be more stable compared to configurations where Fe atoms remain adsorbed on the borophene surface. However, due to the significant diffusion barrier for Fe atoms through HHs, metastable surface nanostructures are likely to persist at low or moderate temperatures.

The magnetic ground state of Fe-based 2D magnets shows an antiferromagnetic interaction between chains with ferromagnetic coupling within each chain. Exchange constants were obtained from SDFT-calculated magnetic moments and energy differences between ground state and higher-energy spin arrangements. These constants were subsequently incorporated into MC simulations to evaluate the T_c within the anisotropic Heisenberg model. The simulations yielded T_c values of 105 and 30 K for Fe-based 2D magnets positioned atop and beneath the β_{12} borophene on the Ag(111) substrate, respectively. These results indicate that further optimization is necessary for these systems to operate at room temperature. Substituting Fe with Co may offer a potential route to enhance T_c , given the higher MAE associated with Co-based nanostructures.

- **Publication:** Božidar N. Šoškić, Srdjan Stavrić, and Željko Šljivančanin, Ab-initio and Monte Carlo study of Fe-based two-dimensional magnets at borophene supported by Ag(111) surface. *Physical Review Materials*, 5:074001, 2021.
- <https://link.aps.org/doi/10.1103/PhysRevMaterials.5.074001>

3.2 Microscopic origin of magnetism in Mn-intercalated bilayer β_{12} borophene

As established in the preceding section, monolayer borophene demonstrates immense potential as a template for stabilizing 2D magnetism. However, one of the critical challenges in leveraging structures for practical applications lies in susceptibility of borophene to oxidation under ambient conditions. A promising solution to overcome this limitation involves transitioning from monolayer borophene to functionalized bilayer configurations, such as intercalated borophenes. Among the proposed strategies for inducing magnetism in such systems, the inclusion of transition metal intercalants has garnered significant attention, with Mn emerging as a leading candidate. As already reported in the literature, Mn retains magnetic moment of $1 \mu_B$ with Curie temperature of 287 K [197], in contrast to many other transition metal adatoms that lose magnetism upon intercalation in bilayer β_{12} borophene. Despite the latter realizations, a fundamental question remained unanswered: “What is the microscopic origin of magnetism in such an intercalated system?” To explore the origins and mechanisms of exchange interactions, we employed two advanced theoretical methodologies, namely the 4SM and the TB2J framework. Among the examined d -block elements spanning from Sc to Zn, only four (Cr, Mn, Fe, Co) exhibit a magnetic moment when intercalated. However, Mn-intercalated structure is the only one that retains the dynamical stability. Therefore, in this section we detail the exchange interactions and their origins in Mn-intercalated bilayer β_{12} borophene, shedding light on the emergent magnetic phenomena in this 2D material heterostructure.

3.2.1 Screening transition metal intercalants for magnetism and dynamical stability

We initiate our study with a computational screening to assess the magnetism and dynamical stability of X-intercalated bilayer β_{12} borophene (B_5XB_5), where X denotes d -block elements spanning from Sc to Zn. To identify the optimal adsorption site for intercalation, we computed the binding energies across various intercalation geometries

$$E_X = \frac{NE_X + E_{B_5B_5} - E_{B_5XB_5}}{N_X}, \quad (3.8)$$

even including positions atop the borophene layer as depicted in Figure 3.9(a). Our calculations revealed that for the HH sites X=Mn exhibits the highest binding energy (see Figure 3.9(b)), indicating favorability of Mn for intercalation. To ensure that intercalation of Mn atoms does not induce their dimerization, we employed calculations using a 2×2 supercell and found no evidence of such a processes. Considering that a unit cell is sufficient to describe the system, we

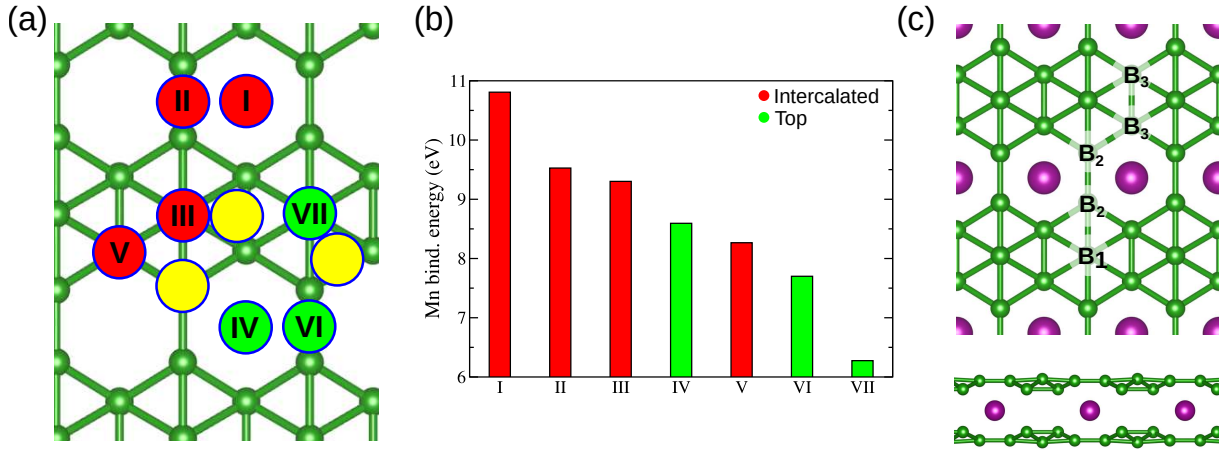


Figure 3.9: (a) Mn adsorption positions and (b) binding energies on the bilayer β_{12} borophene. Red and green circles indicate intercalated and top-layer sites, while yellow circles highlight unstable locations. (c) The structure of Mn-intercalated bilayer β_{12} borophene. The boron atoms with different CN values are denoted as B_1 , B_2 , and B_3 . The boron atoms are visualized by green spheres, while Mn atoms are represented by violet spheres.

computed the magnetic moments of various intercalants using SDFT formalism (see **APPENDIX A3** for computational details). Our results indicate that only four of ten intercalants exhibit magnetic moments: Cr with $0.025 \mu_B$, Mn with $0.956 \mu_B$, Fe with $0.537 \mu_B$, and Co with (negligible) $0.001 \mu_B$. Furthermore, intercalation not only alters the lattice parameters of bare bilayer β_{12} borophene ($a = 2.94 \text{ \AA}$ and $b = 5.07 \text{ \AA}$) but also modifies the interlayer spacing, as shown in Table 3.5. When Mn is intercalated, the B_3 – B_3 bonds in bilayer β_{12} borophene contract significantly, as well as the Mn– B_2 and Mn– B_3 bonds (see Figure 3.9(c) for atomic notation), indicating strong hybridization between Mn- $3d$ and B- $2p$ orbitals and therefore the buckling of the whole structure.

Table 3.5: The B–B distance for B_1 , B_2 , and B_3 atoms, as well as X–B distance for $X \in \{\text{Cr}, \text{Mn}, \text{Fe}, \text{Co}\}$ and the corresponding magnetic moments.

Config. X=	B_1 – B_1 (\AA)	B_2 – B_2 (\AA)	B_3 – B_3 (\AA)	X– B_2 (\AA)	X– B_3 (\AA)	Mag. moment (μ_B/atom)
None	3.042	2.635	2.746	-	-	-
Cr	3.402	3.170	2.186	2.294	2.049	0.025
Mn	3.351	3.161	2.181	2.290	2.032	0.956
Fe	3.312	3.184	2.227	2.298	2.020	0.537
Co	3.300	3.223	2.355	2.317	2.048	0.001

Further, to evaluate the dynamical stability of the four candidates, we applied the “frozen” method for phonon calculations, employing a $3 \times 5 \times 1$ supercell and taking into account the SOC. To confirm the ferromagnetic nature of the systems under consideration, which is important for

phonon calculation setup, we used a 2×2 supercell and explored various spin configurations while allowing the system's geometry to relax. For the case of four Mn atoms in the supercell, we tested five distinct spin arrangements: UU-UU, UU-DD, DU-DU, DU-UD, and DU-DD, where U represents a spin-up state and D represents a spin-down state. Our calculations identified the ferromagnetic arrangement (UU-UU) as the ground state for the systems under study. The results of phonon calculations for four different systems under consideration are presented in Figure 3.10. Our analysis reveals that only Mn-intercalated bilayer borophene is dynamically

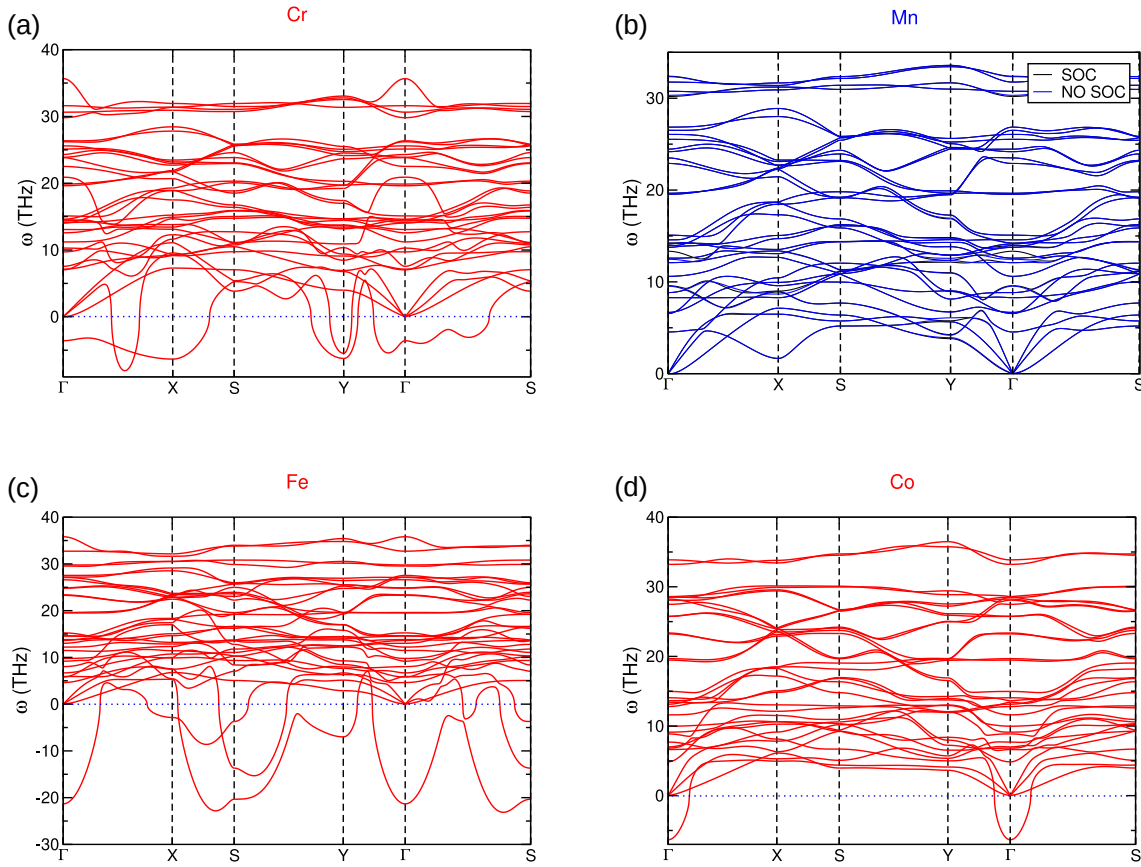


Figure 3.10: Phonon dispersion with SOC included for bilayer β_{12} borophene intercalated with: (a) Cr, (b) Mn (without SOC), (c) Fe, and (d) Co.

stable, characterized by a slight softening of the acoustic phonon branch near the high-symmetry X point, as shown in Figure 3.10(b). Additionally, incorporating SOC results in minimal changes of higher-frequencies around the Γ point compared to the case without SOC. After identifying Mn as the only candidate that meets the criteria for dynamical stability and magnetic induction, we proceed to examine the structural, electronic, and magnetic properties of this system in greater detail.

The Mn-intercalated bilayer β_{12} borophene structure, as depicted in Figure 3.9(c), is belonging to $Pmm2$ (No. 25) space group, with lattice constants of $a = 2.88 \text{ \AA}$ and $b = 5.11 \text{ \AA}$. Due to the differing coordination numbers (CNs) of B_1 , B_2 , and B_3 atoms, the local electronic environment in the bilayer β_{12} borophene varies significantly. This disparity leads to strong hybridization between Mn $3d$ -orbitals on one side, and B_1 and B_2 $2p$ -orbitals on the other side, resulting in the formation of short, robust Mn–B bonds. As the magnetism of Mn is mainly governed by the nature of its $3d$ -electron states, this hybridization between Mn- $3d$ states and the B- $2p$ states significantly impacts system's electronic properties, causing partial delocalization of the $3d$ -states, thereby altering its magnetic moment. In an simple ionic picture, the reduction of Mn magnetic moment from $5 \mu_B$ in isolated form (Mn:[Ar] $4s^23d^5$) to $1 \mu_B$ in bilayer β_{12} borophene (B:[He] $2s^22p^1$) is caused by an electron transfer and the subsequent filling of bonding states, thereby suppressing spin polarization of system, and leaving only one unpaired electron which results in a net magnetic moment of $1 \mu_B$. Figure 3.11(a) shows the calculated

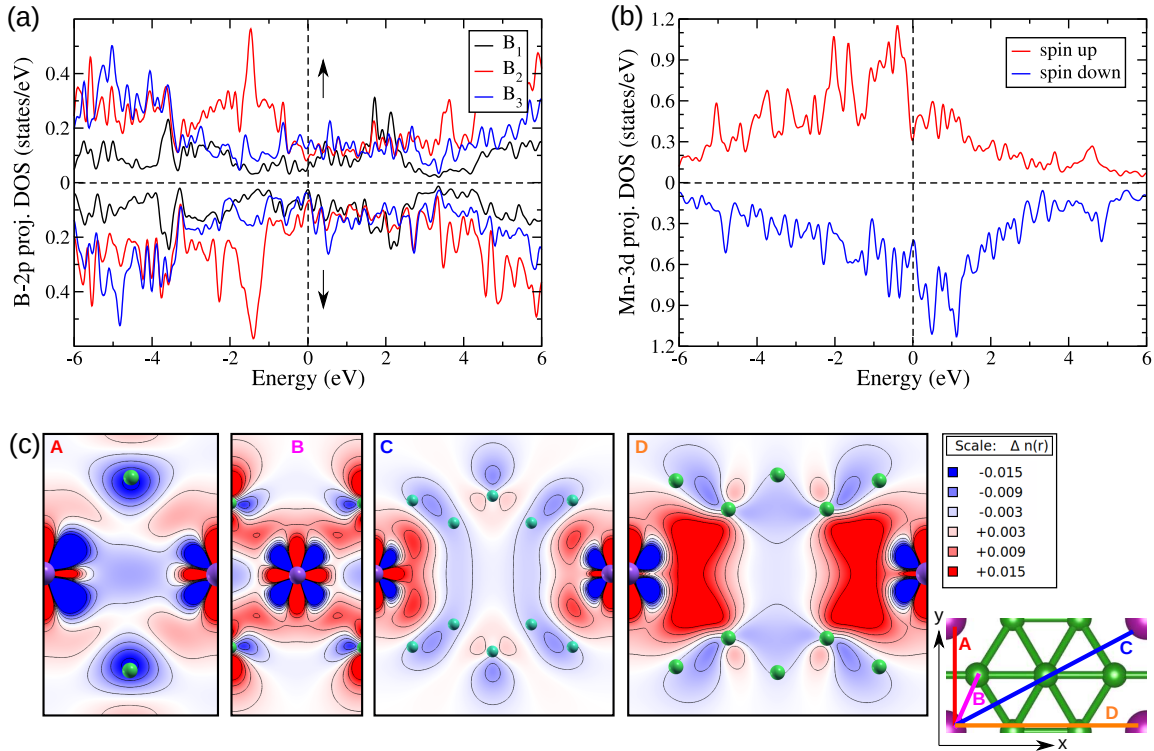


Figure 3.11: Projected DOS on (a) B- $2p$, and (b) Mn- $3d$ orbitals. (c) Electron charge density induced by intercalation of Mn atoms in bilayer β_{12} borophene illustrated in planes A, B, C, D perpendicular to structure as shown in small right panel. The color map represents the charge density in units of electrons/Bohr³.

projected DOS, where the boron atoms display negligible magnetic moments due to the absence of exchange splitting, while Mn exhibits a splitting between spin-majority and spin-minority

states, confirming its magnetic nature, as shown in Figure 3.11(b). Furthermore, Figure 3.11(c) shows the induced charge density (ICD) distribution, highlighting the electron redistribution induced by the interaction between Mn atoms and the bilayer β_{12} borophene structure. The plot, extracted from the A -plane of the Mn atoms and oriented perpendicular to the borophene layers, reveals a significant overlap of $3d$ orbitals between adjacent Mn atoms along the y -direction. Notably, the pronounced interaction between Mn- $3d$ orbitals and B_2 - $2p$ orbitals as shown in B -plane, indicates additional boron-mediated magnetic coupling between Mn atoms. Also, when choosing the D -plane, a clear strong hybridization between Mn- $3d$ states and B_3 - $2p$ states is visible. However, to obtain a deeper insight into magnetic interactions between Mn atoms and their origin we will continue with extraction of exchange parameters using 4SM and TB2J theoretical frameworks.

3.2.2 Magnetic properties of Mn-intercalated bilayer β_{12} borophene

To sustain measurable long-range magnetic order in a system, it is essential not only to have non-zero magnetic moments on the Mn ions but also to establish strong magnetic interactions among them. Therefore, we employed two approaches: (i) mapping the overall energies of different spin arrangements obtained via SDFT onto the Heisenberg's hamiltonian, following the method used in 4SM approach, and (ii) calculating magnetic exchange interactions by analyzing energy variations due to small rotations of magnetic moments on Mn atoms, as implemented in the TB2J methodology. The isotropic exchange coupling constants ($J_{\#NN}^{iso}$) calculated using

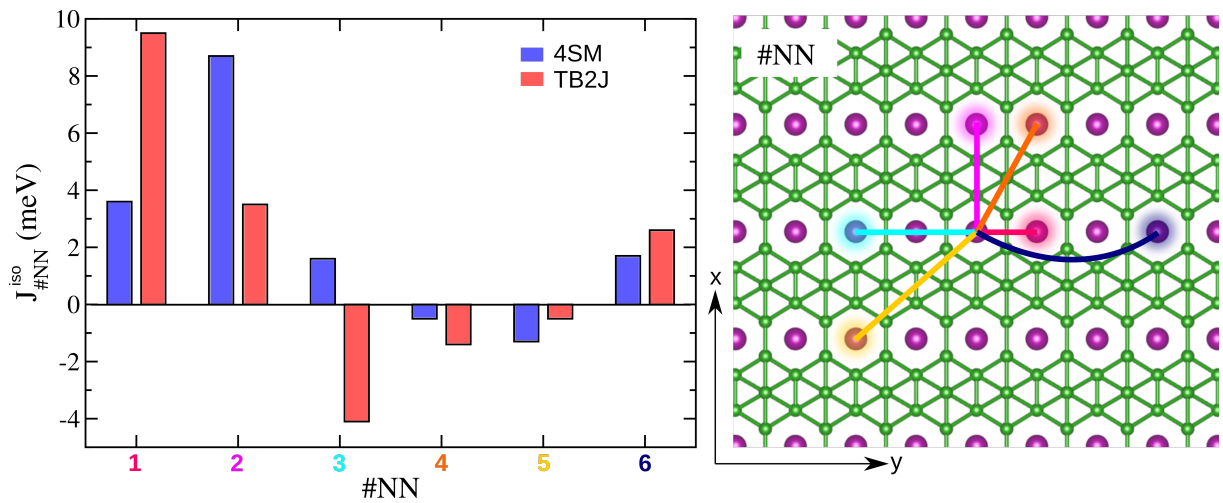


Figure 3.12: The isotropic exchange constants obtained by using 4SM (blue) and TB2J (red) method for 1st, 2nd, 3rd, 4th, 5th, and 6th NN.

both methods, with the spin normalized to 1 in each case, are presented in Figure 3.12 for the

first six NNs. The two strongest ferromagnetic interactions, with the largest magnitudes, occur for the 1st and 2nd NNs. For the 3rd NN, the sign of the isotropic exchange coupling differs for the two used methods. For the 4th and 5th NNs, both methods yield small antiferromagnetic coupling constants, while a ferromagnetic coupling is observed for the 6th NN. The exact isotropic exchange constants for the first six NNs, along with their respective distances, are listed in Table 3.6, as obtained from both 4SM and TB2J methods.

Table 3.6: The values for isotropic exchange constants obtained by using 4SM and TB2J method, as well as the distance of corresponding #NN.

#NN	4SM (meV)	TB2J (meV)	Mn–Mn (Å)
1 st	3.6	9.5	2.9
2 nd	8.7	3.5	5.1
3 rd	1.6	−4.1	5.8
4 th	−0.5	−1.4	5.9
5 th	−1.3	−0.5	7.7
6 th	1.7	2.6	8.6

3.2.2.1 Extraction of magnetic parameters via the 4SM

For the 4SM calculations, we expanded the unit cell to a 3×6×1 supercell and computed all potential exchange parameters for the spin site pairs within the first six NNs. We followed the procedure outlined in subsection 2.3.2.1. We computed the energies of four distinct spin configurations using constrained non-collinear SDFT calculations and mapped them onto the corresponding Heisenberg’s hamiltonian. After that, we derived one exchange matrix element, and by repeating this process for all nine matrix elements, we constructed the full 3×3 exchange interaction tensors \mathbb{J}_{ij} for all the first six NNs:¹

$$\mathbb{J}_{01} = \begin{pmatrix} 3.73 & 0.00 & 0.00 \\ 0.00 & 3.80 & 0.00 \\ 0.00 & 0.00 & 3.20 \end{pmatrix}; \quad \mathbb{J}_{02} = \begin{pmatrix} 9.16 & 0.00 & 0.00 \\ 0.00 & 9.17 & 0.00 \\ 0.00 & 0.00 & 7.61 \end{pmatrix};$$

¹After calculations, we found the anisotropic exchange interaction to be negligible for all pairs, attributed to the very weak spin-orbit coupling on B atoms. Consequently, we effectively set these contributions to zero.

$$\mathbb{J}_{03} = \begin{pmatrix} 1.47 & 0.00 & 0.00 \\ 0.00 & 1.44 & 0.00 \\ 0.00 & 0.00 & 1.97 \end{pmatrix}; \quad \mathbb{J}_{04} = \begin{pmatrix} -0.27 & 0.00 & 0.00 \\ 0.00 & -0.38 & 0.00 \\ 0.00 & 0.00 & -0.80 \end{pmatrix};$$

$$\mathbb{J}_{05} = \begin{pmatrix} -1.39 & 0.00 & 0.00 \\ 0.00 & -1.38 & 0.00 \\ 0.00 & 0.00 & -1.26 \end{pmatrix}; \quad \mathbb{J}_{06} = \begin{pmatrix} 1.53 & 0.00 & 0.00 \\ 0.00 & 1.61 & 0.00 \\ 0.00 & 0.00 & 1.83 \end{pmatrix}, \quad (3.9)$$

where a positive $J > 0$ favors parallel spin alignment, leading to ferromagnetic ordering, while a negative $J < 0$ favors antiparallel alignment, resulting in antiferromagnetic ordering. Also, the values of the isotropic exchange constants presented in Figure 3.12 and Table 3.6 were calculated by using the formula:

$$J_{ij}^{iso} = \frac{1}{3} Tr \mathbb{J}_{ij} = \frac{1}{3} (J_{ij}^{xx} + J_{ij}^{yy} + J_{ij}^{zz}). \quad (3.10)$$

However, these values do not provide information about direction-dependent interactions. To obtain this, we calculate the difference between $\langle J_{ij}^{zz} \rangle$ and $\langle J_{ij}^{xx} \rangle$ or $\langle J_{ij}^{yy} \rangle$, which allows us to extract the symmetric anisotropic exchange interactions, as shown in Table 3.7. It is clear that

Table 3.7: The values of symmetric anisotropic exchange interactions for different NNs.

#NN	$\langle J_{ij}^{zz} \rangle - \langle J_{ij}^{xx} \rangle$ (meV)	$\langle J_{ij}^{zz} \rangle - \langle J_{ij}^{yy} \rangle$ (meV)
1 st	-0.53	-0.60
2 nd	-1.55	-1.56
3 rd	0.50	0.53
4 th	0.53	0.42
5 th	-0.13	-0.12
6 th	0.30	0.22

for the first NN the spin slightly cant more towards the y -direction relative to the z -direction compared to x -direction, while for the second and fifth NNs, both the x - and y -directions are favored equally. For the third, fourth, and sixth NNs, the spins exhibit a preference for the z -direction, indicating alignment along the z -axis with possible slight deviations. Furthermore, our results show that due to the inversion symmetry of the crystal, and in the absence of external forces that break this symmetry, the Mn-intercalated bilayer β_{12} borophene will exhibit a zero DMI value. Therefore, the only additional contribution to the anisotropy arises from the SIA term, which has been explicitly calculated. Since the considered material possesses the $Pmm2$

symmetry, the SIA tensor is fundamentally constrained by the crystal's symmetry elements, which include identity, two mirror planes (perpendicular to the x -axis (m_x) and y -axis (m_y)) and a 2-fold rotational axis (rotation for 180° around the z -axis). Due to mirror symmetry, the diagonal terms of SIA are allowed to be non zero because they correspond to interactions along the x and y axes, which are preserved under mirror symmetry, as well as along z -axis which is not influenced. The off-diagonal terms must vanish because they would change spatial direction under reflection. Also, the diagonal terms stay invariant under a 180° rotation around the z -axis. In our case, the computation of SIA terms is simplified, and only diagonal terms are expected to be non zero. As predicted, our calculations yielded only diagonal elements, with $A_{yyxx} = 0.16$ meV and $A_{zzxx} = 0.19$ meV. While we have gathered here all the relevant exchange parameters, the origin of those magnetic exchange interactions remains unknown. To advance the understanding beyond the 4SM framework, we thus employed the TB2J code and also compared the results to those obtained using 4SM.

3.2.2.2 Exchange interaction analysis using TB2J

After the analysis of 4SM results, we delved deeper into the origin of the exchange interactions in Mn-intercalated bilayer β_{12} borophene. Before proceeding, it was essential to compute all exchange parameters using the TB2J framework, and the results are shown in Figure 3.13. As in the case of 4SM, the sign of the isotropic exchange interaction J remains consistent, except for the third NN, where a deviation is observed. Regarding this problem, it is important to mention that in the case of TB2J calculations, we have included all d orbitals on Mn atoms and only p_z orbitals on B atoms, to facilitate the Wannierization of the complex electronic structure which otherwise reflects strong entanglement between s , p_x , and p_y orbitals throughout the energy spectrum. The successful inclusion of p_x , and p_y orbitals on B into the consideration requires an extensive analytical and computational effort, which remains pending due to limited time and computational resources. At this stage this was warranted to facilitate Wannierization but we cannot claim with certainty if this approximation has caused the 4SM-TB2J discrepancy for the 3^{rd} NN. Additionally, the DMI is effectively found to be zero. Having presented the core results, we can now delve deeper into the origin of the magnetic interactions in this material. Based on the initial insights from the ICD results, we assumed that the majority of the exchange interactions arise from the direct exchange between the $3d$ -orbitals of the interacting Mn atoms ($3d$ - $3d$ exchange) and from the one mediated by B_2 or B_3 atoms (Mn- B_n -Mn) in

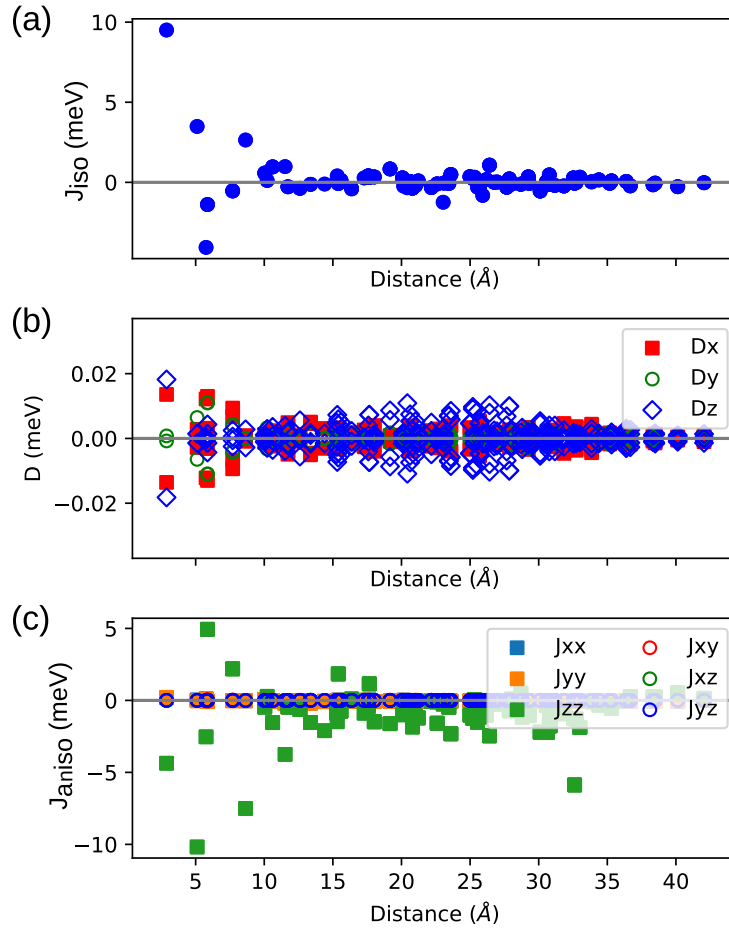


Figure 3.13: Values for (a) isotropic exchange interactions, (b) DMI, and (c) symmetric anisotropic exchange interactions for different NNs.

the form of super-exchange or super-superexchange interaction. Therefore, we decomposed the exchange interactions into contributions from individual $3d$ -orbitals of the interacting pair of Mn atoms, which allowed us to disentangle the key contributors, as presented in Figure 3.14. As seen in the figure, the largest contribution to the 1st NN magnetic interaction stems from the coupling between the d_{xy} -orbital on one Mn atom and the same orbital on the other Mn atom, probably mediated by the B_2-p_z orbital, resulting therefore in the $(d_{xy} - p_z - d_{xy})$ super-exchange interaction. To date, such schematic depictions of super-exchange mechanisms have remained the primary approach in the literature, despite lacking rigorous validation. Namely, the current analyses predominantly focus on specific d -orbital interactions, taking into account all microscopic mechanisms together, without the ability to disentangle them. To move beyond the purely schematic assumptions, we employed the *successive hopping inclusion method* (SHIM), developed by Šabani *et al.* (<https://doi.org/10.48550/arXiv.2502.08273>), providing a systematic approach for capturing the origin of magnetic interactions. The main idea of the method is to resolve magnetic exchange through systematically activating hopping paths

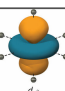
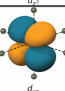
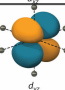
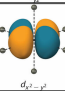
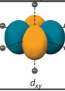
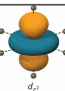
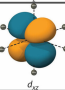
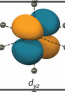
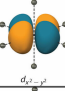
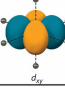
Orbitally decomposed interactions																
		1 st NN					2 nd NN					3 rd NN				
		d_{z^2}	d_{xz}	d_{yz}	$d_{x^2-y^2}$	d_{xy}	d_{z^2}	d_{xz}	d_{yz}	$d_{x^2-y^2}$	d_{xy}	d_{z^2}	d_{xz}	d_{yz}	$d_{x^2-y^2}$	d_{xy}
d_{z^2}		-3.73	0.00	-0.11	-1.39	0.01	1.70	-0.01	-0.01	0.75	-0.01	-1.30	0.00	-0.05	-0.35	0.00
d_{xz}		0.00	1.16	-0.01	0.00	0.01	-0.01	-1.15	0.00	0.00	0.01	0.00	0.30	0.00	0.00	0.00
d_{yz}		-0.11	-0.01	7.90	-0.01	0.01	-0.01	0.00	3.30	0.01	0.00	-0.05	0.00	-0.22	-0.01	0.00
$d_{x^2-y^2}$		-1.39	0.00	-0.01	-0.75	-0.01	0.75	0.00	0.01	-0.35	0.00	-0.35	0.00	-0.01	-0.03	0.00
d_{xy}		0.01	0.01	0.01	-0.01	7.93	-0.01	0.01	0.00	0.00	-1.50	0.00	0.00	0.00	0.00	-1.99
		4 th NN					5 th NN					6 th NN				
		d_{z^2}	d_{xz}	d_{yz}	$d_{x^2-y^2}$	d_{xy}	d_{z^2}	d_{xz}	d_{yz}	$d_{x^2-y^2}$	d_{xy}	d_{z^2}	d_{xz}	d_{yz}	$d_{x^2-y^2}$	d_{xy}
d_{z^2}		-0.12	0.00	0.04	-0.04	-0.04	-0.12	0.00	0.00	-0.07	-0.05	0.71	0.00	0.00	0.10	0.00
d_{xz}		0.00	0.00	-0.16	0.00	0.00	0.00	-0.05	-0.27	0.00	0.00	0.00	0.43	0.00	0.00	0.00
d_{yz}		0.04	-0.16	0.09	0.00	0.00	0.00	-0.27	0.24	0.00	0.01	0.00	0.00	-0.08	0.00	0.00
$d_{x^2-y^2}$		-0.04	0.00	0.00	0.08	0.06	-0.07	0.00	0.00	-0.02	-0.05	0.10	0.00	0.00	-0.02	0.00
d_{xy}		-0.04	0.00	0.00	0.06	-1.19	-0.05	0.00	0.01	-0.05	0.28	0.00	0.00	0.00	0.00	1.37

Figure 3.14: Sub-orbitally-decomposed 3d–3d interactions for first six NNs.

between different orbitals by gradually lowering the threshold for hoppings $|t| > \tau$ in order to isolate the contributions of specific microscopic exchange processes in the orbitally-resolved representation.² Therefore, to confirm the $d_{xy} - p_z - d_{xy}$ super-exchange mechanism, we applied the mentioned method, and for $\tau = 0.51$ eV the contributions drop to zero because the $\text{Mn}-d_{xy}(\downarrow) \leftrightarrow \text{B}_2-p_z(\downarrow)$ hopping parameter is excluded, confirming our assumed dominant super-exchange interaction. The next significant contribution having origin in super-superexchange

²A non-zero magnetic exchange between two d -orbitals on magnetic atoms arises only if at least one continuous hopping path links them through a sequence of non-zero hopping parameters.

mechanism is the antiferromagnetic $d_{z^2} - d_{z^2}$ interaction, for which the main contribution is stemming from $\text{Mn-}d_{z^2}(\uparrow)\leftrightarrow\text{B}_3\text{-}p_z(\uparrow)\leftrightarrow\text{B}_3\text{-}p_z(\uparrow)\leftrightarrow\text{Mn-}d_{z^2}(\uparrow)$ hopping path. However, the second highest contribution comes from the $d_{yz} - d_{yz}$ interaction between Mn atoms, which is mainly explained by the direct overlap of the their dumbbell-shaped orbitals oriented along the bond, as further confirmed in our analysis. By excluding the direct $\text{Mn-}d_{yz}(\uparrow)\leftrightarrow\text{Mn-}d_{yz}(\uparrow)$ hopping parameter, the value of exchange interaction drops from 7.90 meV to 2.93 meV. On the other side, the overall ferromagnetic interaction for the 2^{nd} NNs is primarily driven by the $d_{yz} - d_{yz}$, $d_{z^2} - d_{z^2}$, and $d_{x^2-y^2} - d_{z^2}$ interactions (along with its symmetric counterpart $d_{z^2} - d_{x^2-y^2}$), with additional significant contributions from the antiferromagnetic coupling coming from $d_{xy} - d_{xy}$ and $d_{xz} - d_{xz}$ interactions, making the overall interaction rather complex. However, the largest ferromagnetic contribution is coming from $d_{yz} - d_{yz}$ interaction, for which the exclusion of $\text{Mn-}d_{yz}(\downarrow)\leftrightarrow\text{B}_2\text{-}p_z(\downarrow)$ resulted in zero value for the exchange constant. For the 3^{rd} NNs, the dominant contribution to the antiferromagnetic coupling arises from the $d_{xy} - d_{xy}$ and the $d_{z^2} - d_{z^2}$ interactions. In the case of $d_{xy} - d_{xy}$, when excluding the super-superechange hopping term $\text{Mn-}d_{z^2}(\uparrow)\leftrightarrow\text{B}_2\text{-}p_z(\uparrow)\leftrightarrow\text{B}_1\text{-}p_z(\uparrow)\leftrightarrow\text{B}_2\text{-}p_z(\uparrow)\leftrightarrow\text{Mn-}d_{z^2}(\uparrow)$ there is a strong switching from antiferromagnetic to ferromagnetic coupling which further by using $\tau = 0.51$ eV resulted in a zero contribution, because the $\text{Mn-}d_{xy}(\downarrow)\leftrightarrow\text{B}_2\text{-}p_z(\downarrow)$ hopping term is excluded, same as for the 1^{st} NN. For $d_{z^2} - d_{z^2}$ interaction, there is also a strong switch from antiferromagnetic contribution to a ferromagnetic one for $\tau = 0.11$ eV, by excluding the $\text{Mn-}d_{z^2}(\uparrow)\leftrightarrow\text{B}_3\text{-}p_z(\uparrow)\leftrightarrow\text{B}_3\text{-}p_z(\uparrow)\leftrightarrow\text{Mn-}d_{z^2}(\uparrow)$ hopping path, and dropping to zero when the other paths connecting $\text{B}_2\text{-}p_z(\downarrow)$ and $\text{B}_1\text{-}p_z(\downarrow)$ are excluded. In the case of antiferromagnetic coupling for the 4^{th} and 5^{th} NNs, the dominant contributions arise from the $d_{xy} - d_{xy}$ interaction and the $d_{yz} - d_{xz}$ interaction (along with its symmetric counterpart $d_{xz} - d_{yz}$), respectively. For the 4^{th} NN, when choosing $\tau = 0.38$ eV, the dominant $d_{xy} - d_{xy}$ vanishes because the $\text{Mn-}d_{z^2}(\uparrow)\leftrightarrow\text{B}_2\text{-}p_z(\uparrow)\leftrightarrow\text{B}_1\text{-}p_z(\uparrow)\leftrightarrow\text{B}_2\text{-}p_z(\uparrow)\leftrightarrow\text{Mn-}d_{z^2}(\uparrow)$ hopping path is excluded. However, for the 5^{th} NN there is even a strong ferromagnetic contribution coming from $d_{xy} - d_{xy}$ interaction, so that the small total antiferromagnetic coupling is a consequence of the smaller contribution of the other $d - d$ interactions. Finally, for the 6^{th} NN ferromagnetic coupling, the dominant contribution stems from the $d_{xy} - d_{xy}$ interaction, which is again mediated by the $\text{B}_2\text{-}p_z$ orbital.

3.2.3 Conclusions

Our study provided a detailed understanding and insights into the main sources of the ferromagnetic long-range order in Mn-intercalated bilayer β_{12} borophene. The isotropic exchange parameters obtained from the 4SM and TB2J methods are quite similar. While the DMI is absent, through symmetry constraints and small SOC, we identify that only the diagonal elements of the SIA term play a significant role in anisotropic interactions. Analysis of the TB2J results reveals that for the 1st NN the ferromagnetic interaction is dominated by the direct overlap of d_{yz} orbitals, as well as the $d_{xy} - d_{xy}$ interaction mediated by B_2-p_z orbital i.e. the super-exchange interaction. In general, the interaction along the y direction, beyond the 1st NN, is predominantly dominated by the $d_{xy} - d_{xy}$ coupling, with $d_{z^2} - d_{z^2}$ interactions as the next most important contributor, both underlying different types of super-exchange interactions involved. The 2nd NN interaction (along x -axis) is ferromagnetic but exhibits more complexity, with largest contribution stemming from $d_{yz} - d_{yz}$ super-exchange interaction. For the 4th NN, the antiferromagnetic coupling arises primarily from the super-superexchange $d_{xy} - d_{xy}$ interaction, while the 5th NN interaction is more intricate, involving relevant contributions from multiple terms. These results unveil the complex and intriguing nature of magnetic interactions in Mn-intercalated bilayer β_{12} borophene, worthy of further exploration and possible use in spintronic technology.

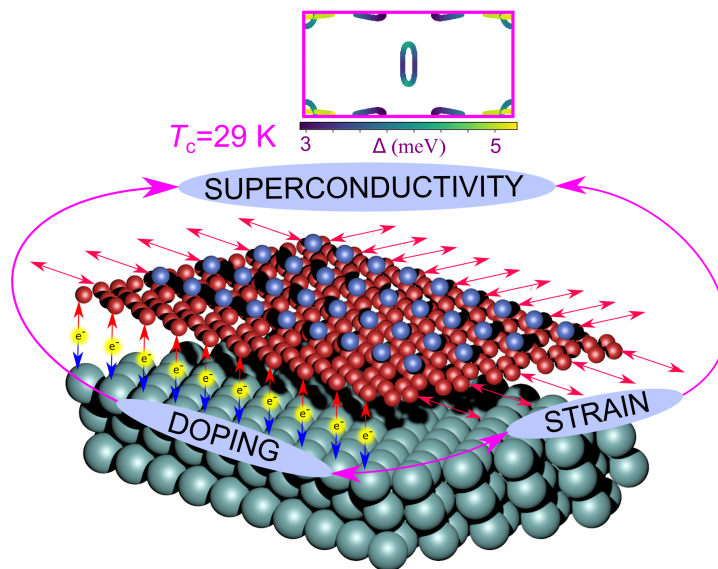
- **Manuscript in preparation:** Božidar N. Šoškić, Denis Šabani, Milorad V. Milošević, and Željko Šljivančanin, Ab-initio study of magnetism in Mn-intercalated bilayer β_{12} borophene.

SUPERCONDUCTIVITY IN BARE AND FUNCTIONALIZED BOROPHENES

While numerous theoretical studies predict superconductivity in bare borophene phases, experimental confirmation remains elusive. This raises a critical question: “Should the bare β_{12} borophene phase still be considered both dynamically stable and superconducting?” Our findings reveal its intrinsic dynamical instability, and although strain acts as a stabilizing mechanism, superconductivity is not induced. In contrast to the bare phase, our investigations demonstrate that hydrogenated borophene is not only dynamically stable but also superconducting, with a critical temperature (T_c) reaching 30 K under influence of uniaxial strain or hole doping. Furthermore, we identify several intercalated bilayer borophene phases – particularly those with alkaline earth metal intercalants – that can achieve T_c values up to 60 K. For all materials studied, we reveal distinct physical trends and uncover the microscopic mechanisms driving their superconductivity, providing deeper insights into the behavior of these compounds. The hydrogenated monolayer and functionalized bilayer borophene configurations emerge as promising candidates for practical applications, exhibiting reduced susceptibility to oxidation in ambient environments.

4.1 Superconducting properties of bare and hydrogenated β_{12} borophene

Borophenes, a novel class of atomically thin boron sheets, exhibit remarkable physical properties such as exceptional mechanical flexibility, high optical transparency, significant hydrogen storage capacity, ultrahigh thermal conductivity, and complex electronic behavior, including metallic Dirac fermions and potential for phonon-mediated superconductivity. These characteristics make borophenes highly promising candidate for applications ranging from battery electrodes to chemical catalysis, gas sensors, and superconductors. However, their tendency to oxidize under ambient conditions poses a significant challenge for practical usage. A notable solution to this issue is surface hydrogenation, a chemical passivation method proven to be effective for stabilizing similar low-dimensional materials like silicene and germanene. Recently, hydrogenated β_{12} borophene structures, known as “borophanes”, have been synthesized, demonstrating enhanced stability under ambient conditions, with the added ability to thermally desorb hydrogen in order to recover the bare phase. In this work we investigated borophanes as candidates for hydrogen-based phonon-mediated superconductors, inspired by the theoretical prediction of high critical temperatures (T_c) in hydrogen-rich compounds. While previous studies reported limited superconductivity in hydrogenated borophenes, our work reveals a substantial enhancement of both dynamical stability and superconducting properties of β_{12} borophane upon careful optimization of computational parameters. Using anisotropic ME theory, we analyzed the microscopic origins of superconductivity in borophane and propose strategies, such as strain engineering and carrier doping, to further increase T_c values, achieving up to 29 K. This work highlights borophane’s potential as a viable low-pressure hydrogen-rich superconductor, bridging a critical gap in the search for practical boron-based devices.



4.1.1 Structural, electronic and vibrational properties of bare and hydrogenated β_{12} borophene

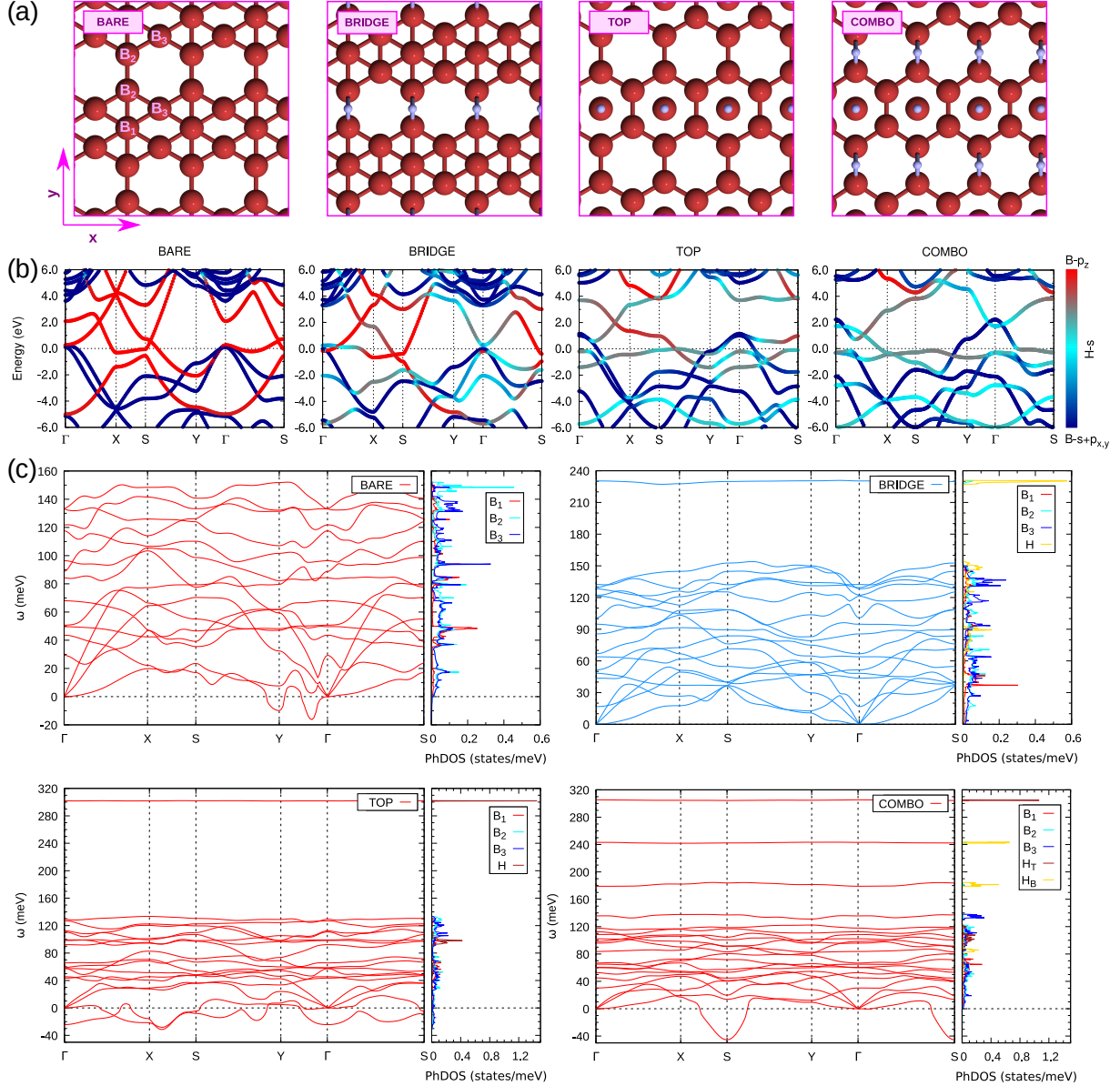


Figure 4.1: Structural, electronic, and vibrational properties of bare and hydrogenated β_{12} borophene. (a) Top views of the crystal structures of bare and hydrogenated borophenes (bridge, top, and combo adsorption site), together with their (b) orbital-resolved electronic band structures, and (c) corresponding phonon dispersions and atom-resolved phonon density of states (phDOS).

We first examined the structural characteristics of both bare and hydrogenated β_{12} borophene, shown in Figure 4.1(a). As previously established, the basic crystal structure consists of a flat arrangement of boron (B) atoms ordered in a triangular pattern. However, a row of hexagonal sites devoid of boron atoms (B_{hollow}) exists, where the remaining B_{hollow} atoms act as electron donors, while these empty vacant sites function as electron acceptors. This arrangement of B

atoms thus gives rise to an interesting electron “self-doping” mechanism. The computed lattice parameters of bare β_{12} borophene phase are $a = 2.92 \text{ \AA}$ and $b = 5.06 \text{ \AA}$, and the structure is classified within the orthorhombic $Pmmm$ (No. 47) space group, featuring three distinct types of boron atoms – B_1 , B_2 , and B_3 – with varying coordination numbers (CN). Computational details are provided in **APPENDIX A4**. The variations in CN values significantly affect the local electronic properties and reactivity of bare phase, creating multiple adsorption sites favorable for hydrogen binding. While the bare phase is intrinsically dynamically unstable, hydrogen adsorption stabilizes the structure. Among the various configurations explored, the “bridge” site ($H_{bridge}-\beta_{12}$) is energetically the most favorable one, with a binding energy of 3.39 eV, making it the preferred adsorption site over others, as depicted in Figure 4.1(a).

Regarding the electronic properties, Figure 4.1(b) shows that the bonding states (σ) derived from in-plane B- $s + p_{x,y}$ orbitals in the bare phase are almost entirely filled, with a gap of over 3 eV separating them from their antibonding counterparts (σ^*). Therefore, the residual electrons are primarily distributed in states from out-of-plane B- p_z orbitals. Bader charge analysis further reveals that hydrogen adsorption withdraws approximately 0.5 e from the borophene layer, significantly modifying its electronic band structure. Concurrently, the lattice constants remain largely unchanged upon hydrogenation ($a = 2.93 \text{ \AA}$ and $b = 5.07 \text{ \AA}$), though hydrogen adsorption induces a symmetry modification, with the $H_{bridge}-\beta_{12}$ structure adopting the $Pmm2$ (No. 25) space group.

Turning to the vibrational properties, the phonon band structure of the bare β_{12} borophene phase, computed using DFPT, reveals a dynamical instability (see Figure 4.1(c)), in contrast to previous reports (see Refs.[203, 208, 211]) that suggest stability for this structure. This discrepancy arises mainly from differences in the electronic smearing parameter used in the calculations. Our test calculations, shown in Figure 4.2, reveal a phonon instability in the bare β_{12} borophene phase, which is resolved by using a smearing parameter of 0.02 Ry, indicating that the observed dynamical stability is artificially induced. To accurately compute the physical properties of both bare and hydrogenated borophenes while retaining observable phonon instabilities, we used a smaller electronic smearing parameter of 0.0025 Ry (approximately 0.03 eV). This parameter selection is physically motivated and significantly impacts the accuracy of the computed results. Although often naively viewed as a mere numerical convergence tool, the use of a large electronic smearing parameter (greater than 0.1 eV or ~ 0.007 Ry) can artificially broaden the electronic distribution near the Fermi level. This distortion can significantly affect

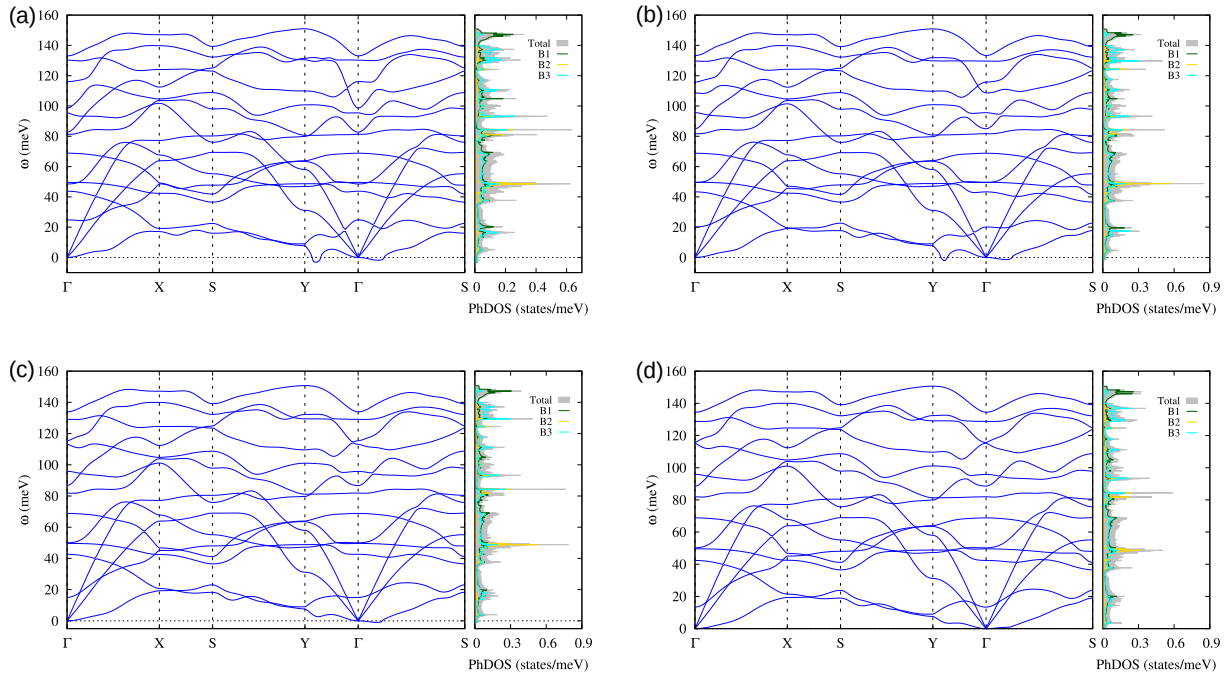


Figure 4.2: Phonon dispersion and atom-resolved phonon DOS of freestanding bare β_{12} borophene by applying different smearing values: (a) 0.005 Ry, (b) 0.01 Ry, (c) 0.015 Ry, and (d) 0.02 Ry.

the electronic properties, thereby altering key physical quantities. Such artificial broadening can stabilize metallic phases or other structures that would otherwise be unstable at lower smearing widths, leading to an inaccurate depiction of the system’s true electronic ground state. Excessive smearing may also suppress or obscure phonon instabilities, charge density wave (CDW) tendencies, and superconducting behavior, all of which rely on precise Fermi surface characterization. In contrast, employing a smaller smearing parameter (0.01–0.05 eV) preserves the sharpness of the electronic distribution, ensuring that instabilities, phase transitions, and phonon softening are accurately captured, thus providing a more faithful representation of the system’s physical properties. Our approach, utilizing a low smearing parameter, clearly revealed an instability in the bare phase which primarily arises from the weak B_2 – B_2 bond, which leads to the presence of unstable out-of-plane phonon modes. Upon hydrogen adsorption at the “bridge” site, the B_2 – B_2 bond is significantly strengthened, resulting in the formation of a stable B_2 –H– B_2 three-center bond. This strengthened bonding formation leads to the dynamical stability of the hydrogenated structure (see Figure 4.1(c)), in stark contrast to the instability observed in its bare phase.

Before proceeding to the next part, it is essential to provide a brief overview of the relevant literature, along with a critical assessment of the key findings. The seminal study presented as Ref. [203] in the thesis investigates potential superconductivity in bare borophene phases and reports a clear phonon instability, even when using a large Gaussian smearing parameter

of 0.02 Ry. Dynamical stability was only achieved upon applying a 1% tensile strain. Furthermore, their electron-phonon ($e-ph$) coupling calculations exhibit considerable sensitivity to different smearing values. In contrast, Ref. [208] used the same smearing parameter, but with a higher plane-wave energy cutoff of 90 Ry (compared to 70 Ry in the earlier study), along with norm-conserving pseudopotentials. This approach successfully removed the instabilities, aligning with our findings shown in Figure 4.2(d). Additionally, Ref. [211], which focuses on hydrogenated borophene, employed the Methfessel-Paxton smearing width of 0.01 Ry for structural optimization and DOS calculations, later switching to Gaussian smearing values ranging from 0.015 to 0.02 Ry for phonon calculations – a somewhat unusual approach. Following structural optimization, the so-called “bridge” configuration places the hydrogen atom closer to a neighboring boron atom, rather than at a high-symmetry site, as opposed to our findings. Notably, a phonon softening is observed along the $X-M$ k -path, even with relatively large smearing values. However, the behavior for smaller smearing values was not explored in this work.

4.1.2 Exploration of hydrogenated β_{12} borophene configurations: the top and combo sites

Another experimentally identified hydrogenated configurations, as outlined in Ref. [154], consist of the top site and a distinct configuration combining the top and bridge adsorption sites, referred to as the “combo” structure. Both configurations are depicted in Figure 4.1(a). Adsorption of hydrogen at the top site of borophene induces significant dynamical instability, as evident from the presence of unstable phonon branches across the entire Brillouin zone (see Figure 4.1(c)), along with pronounced structural buckling. This instability is further reflected in the lattice parameters, where the top configuration exhibits slight compression ($a = 2.89 \text{ \AA}$ and $b = 4.99 \text{ \AA}$) compared with the bare phase. In contrast, the “combo” configuration, characterized by hydrogen adsorption on both the top and bridge sites, shows dynamical instability localized near the S point in the Brillouin zone, which phonon mode encompasses out-of-plane displacements of the B_2 and H_{bridge} atoms, coupled with in-plane movements of the B_3 and H_{top} atoms. The lattice parameters for this structure, $a = 2.80 \text{ \AA}$ and $b = 5.13 \text{ \AA}$, indicate a distinct lattice distortion with a compression along one direction and elongation along the other. These observations highlight the contrasting effects of hydrogen adsorption on structural stability and vibrational properties. The electron deficiency in the “combo” configuration induces a gap between the $B-\pi$ and π^* states, as shown in Figure 4.3. Our findings reveal that introducing additional

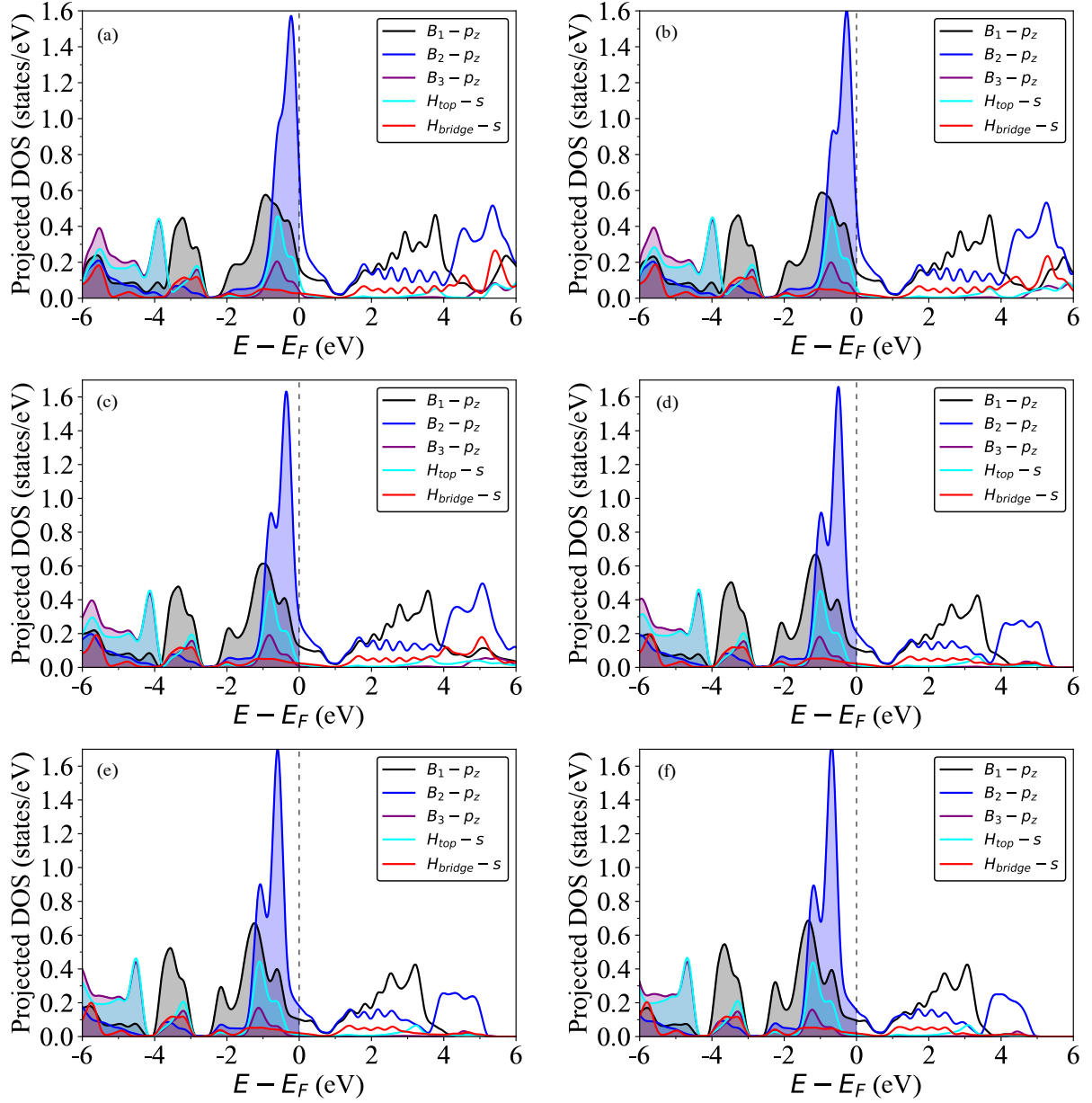


Figure 4.3: The projected DOS onto the B - p_z and H - s orbitals (including H_{top} and H_{bridge} atoms) is illustrated for (a) freestanding $2H$ - β_{12} borophene and under uniform electron doping levels of (b) 0.014 e/B , (c) 0.03 e/B , (d) 0.06 e/B , (e) 0.10 e/B , and (f) 0.15 e/B .

electrons into the system to further populate the π^* states restores dynamical stability. This behavior mirrors that of the dynamically stable bridge configuration, where the π^* states exhibit higher occupancy. Specifically, our simulations indicate that an electron doping level of 0.1 e/B is necessary to stabilize the structure – equivalent to the charge extracted by the additional hydrogen atom from the borophene layer compared to the bridge configuration. Shifting the Fermi level establishes a balanced occupation of the partially filled σ and π^* states, which is essential for the material's dynamical stability. However, the calculated values of isotropic e - ph coupling (λ_{iso}) and T_c^{iso} remain relatively small, with superconductivity completely vanishing

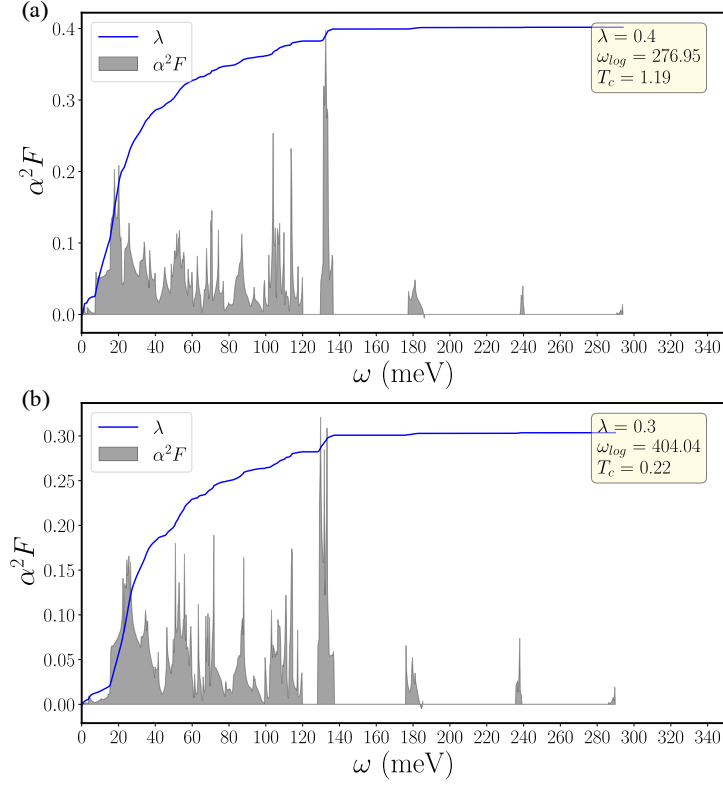


Figure 4.4: The isotropic Eliashberg function for 2H on freestanding β_{12} borophene by applying uniform electron doping of (a) 0.10 e/B and (b) 0.15 e/B.

for doping concentrations above 0.1 e/B, as shown in Figure 4.4. This trend arises from the reduced contributions of the B_1 - p_z , B_2 - p_z , and H- s states at the Fermi level (E_F), while the B- σ states remain the dominant contributors, as shown in Table 4.1. In general, when comparing the top and combo configurations with the H_{bridge} - β_{12} structure, they exhibit relatively weak superconducting properties.

Table 4.1: The values of projected DOS at E_F in units of states/eV of 2H on freestanding β_{12} borophene, and by applying uniform electron doping.

	0.00 e/B	+0.014 e/B	+0.03 e/B	+0.06 e/B	+0.10 e/B	+0.15 e/B
B_1 - σ	0.19	0.19	0.18	0.18	0.22	0.25
B_2 - σ	0.22	0.18	0.14	0.13	0.15	0.17
B_3 - σ	0.10	0.07	0.05	0.04	0.04	0.04
B_{tot} - σ	0.51	0.44	0.37	0.35	0.41	0.46
B_1 - p_z	0.18	0.15	0.13	0.11	0.10	0.09
B_2 - p_z	0.71	0.48	0.30	0.21	0.18	0.16
B_3 - p_z	0.04	0.02	0.01	0.00	0.00	0.00
B_{tot} - p_z	0.93	0.65	0.44	0.32	0.28	0.25
H_{top} - s	0.10	0.06	0.03	0.01	0.01	0.01
H_{bridge} - s	0.03	0.03	0.03	0.02	0.02	0.02
Total	1.57	1.18	0.87	0.70	0.72	0.74

4.1.3 Vibrational and superconducting properties of bare and hydrogenated β_{12} borophene: the bridge site

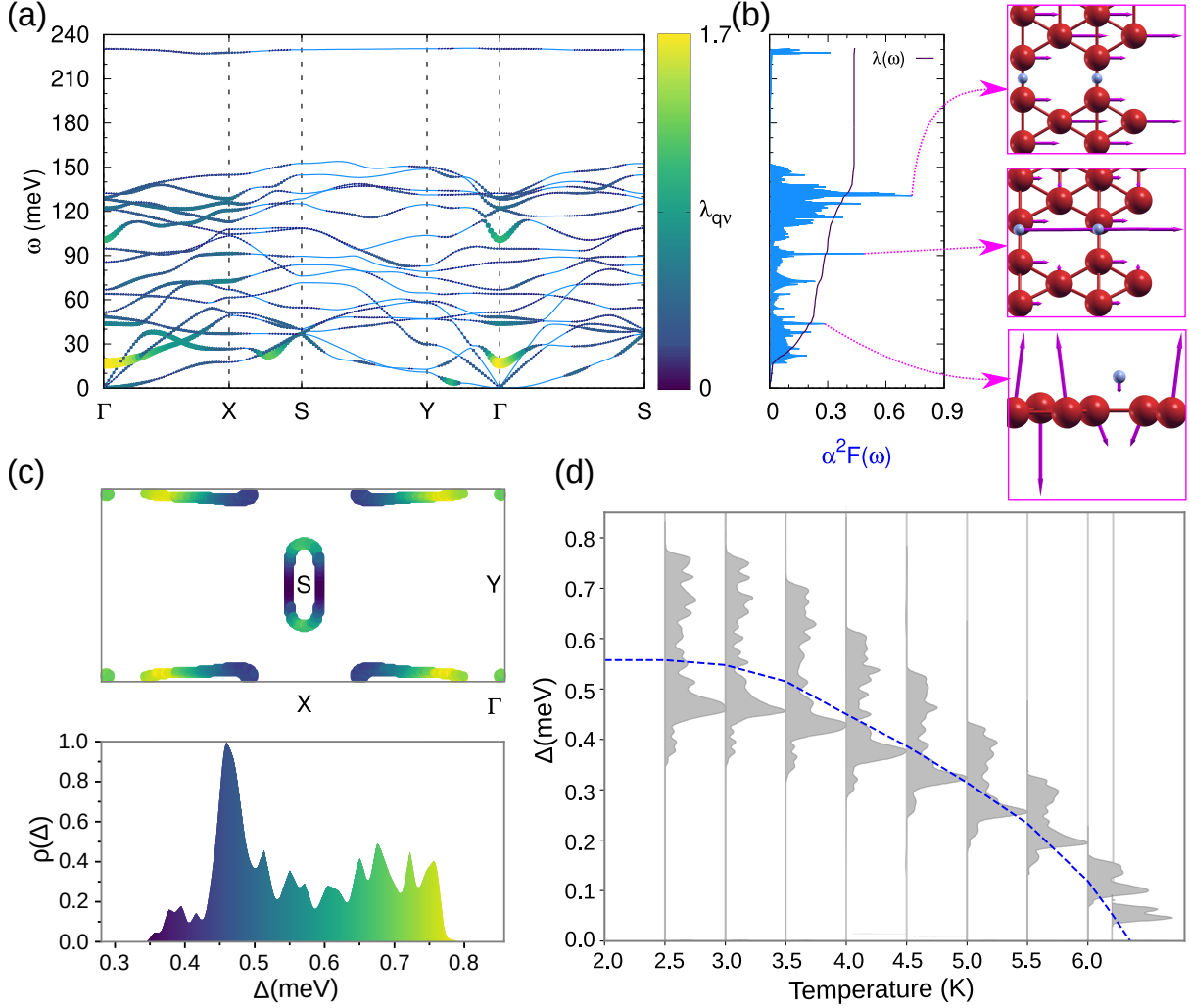


Figure 4.5: The superconducting properties of $H_{\text{bridge}}\text{-}\beta_{12}$ borophene using a fully anisotropic ME approach. Inset (a) shows the phonon dispersion along with the momentum-resolved e - ph coupling ($\lambda_{q\nu}$), depicted by a color scale. Inset (b) presents the isotropic Eliashberg spectral function, highlighting the phonon modes associated with the prominent peaks observed in it. Inset (c) presents the superconducting gap distribution across the Fermi surface at 2.5 K, along with the corresponding $\rho(\Delta)$ map depicted in color. Inset (d) illustrates the temperature-dependent evolution of Δ , with the weighted average (dashed blue line) yielding a T_c^{aniso} of 6.3 K.

Let us now focus on a detailed exploration of vibrational and superconducting properties of the $H_{\text{bridge}}\text{-}\beta_{12}$ borophene configuration, which stands out as the most compelling candidate for hosting superconductivity. Figure 4.5(a) illustrates the phonon band structure of the $H_{\text{bridge}}\text{-}\beta_{12}$ borophene configuration, complemented by the mode(ν)- and momentum(q)-dependent e - ph coupling, $\lambda_{q\nu}$. The strongest e - ph coupling is observed near the Γ point, associated with phonon energy around 20 meV, which corresponds to the softened B_1 optical phonon mode.

In Figure 4.5(b), the Eliashberg spectral function exhibits several prominent peaks, primarily attributed to two key phonon modes. The first peak arises from the in-plane and in-phase motion of B₁, B₂, and H atoms, coupled with a slight out-of-phase and in-plane motion of B₃ atoms, occurring at approximately 90 meV. The second, and most pronounced peak, is linked to the optical A_u phonon mode, characterized by in-plane movements of boron atoms at around 130 meV. Collectively, these contributions result in an isotropic *e-ph* coupling constant of $\lambda_{\text{iso}} = 0.44$, leading to a isotropic critical temperature of $T_c^{\text{iso}} = 4.0$ K, as determined by the McMillan-Allen-Dynes (MAD) formula. To precisely evaluate how hydrogenation impacts the superconducting properties of β_{12} borophene, we utilized first-principles calculations results as inputs to solve the fully anisotropic ME equations. This methodology enables us to compute the superconducting gap $\Delta(\mathbf{k})$ at the E_F , with results shown in Figure 4.5(c). The Fermi surface consists of three distinct sheets: (i) an ellipsoidal sheet centered around the *S* point, characterized by hybridized B-*p_z* and H-*s* orbitals; (ii) an elongated sheet extending along the Γ -*X* direction, where the electronic character transitions from predominantly B-*p_z* near Γ point to a hybridized B-*p_z*/H-*s* state further along; and (iii) a small circular sheet near Γ composed purely of B- σ states. Among these, the sheet around *S* point exhibits the smallest $\Delta(\mathbf{k})$ values, reaching 0.35 meV at 0 K, where the electronic states are primarily B-*p_z*, and slightly larger gap values in regions of hybridized B-*p_z*/H-*s* states. For the elongated sheet along Γ -*X*, the lowest gap values (as low as 0.43 meV) arise from hybridized B-*p_z*/H-*s* states, while the largest gaps (up to 0.78 meV) are associated with pure B-*p_z* states. The gap distribution $\rho(\Delta)$, as depicted in Figure 4.5(c), reveals a smooth profile without distinct domes, indicating that the superconductivity is of an anisotropic single-gap character. On top of that, Figure 4.5(d) displays the temperature dependence of $\Delta(\mathbf{k})$, calculated by solving the anisotropic ME equations, which disappears at a critical temperature of $T_c^{\text{ansio}} = 6.3$ K. To further evaluate the influence of individual elements in the H_{bridge}- β_{12} borophene system, we examined the isotope effect by adjusting the phonon frequencies based on isotope masses, followed by recalculating the anisotropic ME equations. Our results reveal a more pronounced B isotope effect ($\alpha_B = 0.63$) compared with the H isotope effect ($\alpha_H = 0.05$), highlighting the crucial role of hydrogen in improving the stability of bare β_{12} borophene while preserving its inherent superconducting nature.

4.1.3.1 Impact of strain on vibrational and superconducting properties

In the following analysis, we explored the impact of lattice deformation on the superconducting behavior of $H_{bridge}-\beta_{12}$ borophene. Strain engineering in 2D materials, achievable through methods such as substrate selection or utilizing piezoelectric substrates, has emerged as an effective strategy for tuning and optimizing superconductivity. This approach has been widely applied in a broad spectrum of 2D superconducting systems, where controlled strain can induce significant modifications in electronic structure, thereby enhancing their superconducting properties. Our

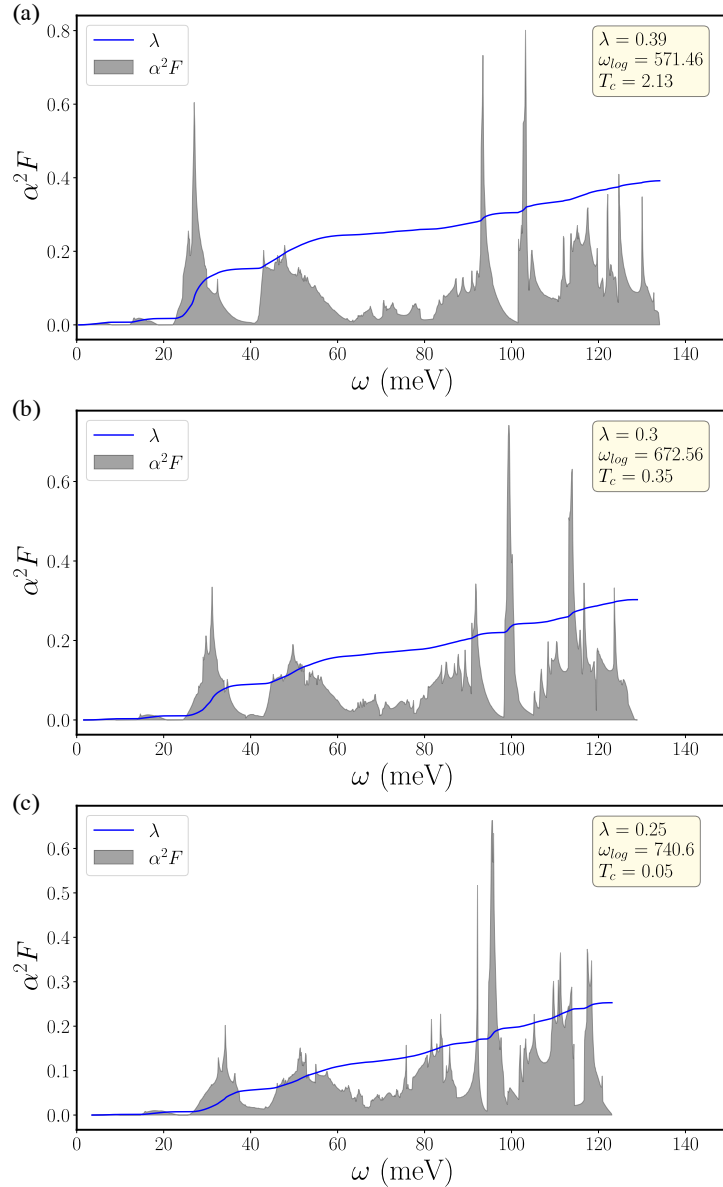


Figure 4.6: The isotropic Eliashberg spectral function of bare β_{12} borophene by applying biaxial tensile strain of (a) +3%, (b) +4%, and (c) +5%.

study applies this concept to $H_{bridge}-\beta_{12}$ borophene, shedding light on how strain can modulate its superconducting properties. Considering the pronounced anisotropic nature of β_{12} borophene,

we introduced in-plane strain (ϵ) with independent variations in the x and y directions (see Figure 4.1(a)). The strain values for ϵ_x and ϵ_y were systematically explored, ranging from -5% (compressive) to $+5\%$ (tensile) with a 1% increment, resulting in a total of 121 distinct strain configurations. First, we evaluated the impact of strain on the bare β_{12} borophene structure by applying biaxial tensile strain and observed that the material achieves dynamical stability at a strain value of $\epsilon_{x,y} = +3\%$. At this level, the material exhibits a T_c^{iso} of 2.13 K (see Figure 4.6). However, further increase of strain values up to $\epsilon_{x,y} = +5\%$ resulted in a marked suppression of superconductivity. This phenomenon is attributed to a sharp reduction in the DOS at the E_F , primarily stemming from B- σ states, as shown in Table 4.2.

Table 4.2: The values of projected DOS at E_F in units of states/eV for bare β_{12} borophene phase and upon applying biaxial tensile strain.

	Bare	$\epsilon_{x,y} = +3\%$	$\epsilon_{x,y} = +4\%$	$\epsilon_{x,y} = +5\%$
$B_1\text{-}\sigma$	0.23	0.15	0.09	0.08
$B_2\text{-}\sigma$	0.19	0.14	0.09	0.09
$B_3\text{-}\sigma$	0.00	0.00	0.00	0.00
$B_{tot}\text{-}\sigma$	0.42	0.29	0.18	0.17
$B_1\text{-}p_z$	0.38	0.41	0.42	0.42
$B_2\text{-}p_z$	0.54	0.54	0.55	0.59
$B_3\text{-}p_z$	0.04	0.04	0.04	0.03
$B_{tot}\text{-}p_z$	0.96	0.99	1.01	1.04
Total	1.38	1.28	1.19	1.21

On the other hand, hydrogenation significantly enhances the stiffness of β_{12} borophene, primarily due to the high intrinsic frequencies of hydrogen-associated phonon modes. This “stiffening effect” limits the material’s ability to withstand compressive strain. Conversely, the phonon spectra remain dynamically stable under tensile strain up to $+5\%$ for most strain configurations, as illustrated in Figure 4.7(a–b). The figure highlights significant variations in λ_{iso} as a function of applied strain, which arise from the interplay of two distinct effects. In the absence of strain along the y direction, the increase of ϵ_x resulted in a reduction of the p_z contributions from B_1 and B_2 atoms, thereby decreasing λ_{iso} . On the other hand, when $\epsilon_x = 0$, an increase in ϵ_y enhances the contribution of σ states from B_1 and B_2 atoms, which leads to a marked increase in λ_{iso} . The behavior for other strain combinations arises from the interplay between these two core mechanisms, which can be seen from the Table 4.3.

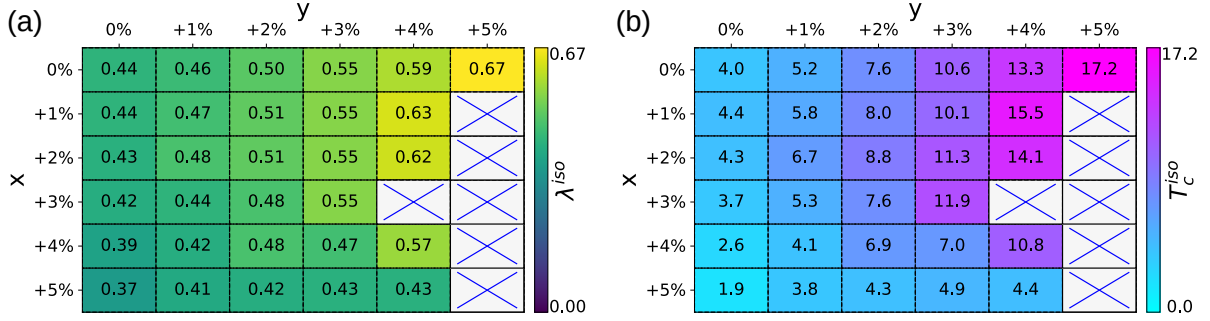


Figure 4.7: Anisotropic superconducting properties of $H_{bridge}-\beta_{12}$ borophene under influence of applied in-plane tensile strain. (a) The isotropic e-ph coupling and (b) the resulting T_c^{iso} values under varying tensile strains applied along the two principal in-plane directions, with the highest values observed for uniaxial tensile strain at $\epsilon_y = +5\%$.

Table 4.3: The values of projected DOS at E_F in units of states/eV for nonuniform tensile strain.

$\epsilon_x = 0\%$	$\epsilon_y = 0\%$	$\epsilon_y = +1\%$	$\epsilon_y = +2\%$	$\epsilon_y = +3\%$	$\epsilon_y = +4\%$	$\epsilon_y = +5\%$
$B_1-\sigma$	0.12	0.13	0.15	0.16	0.17	0.20
$B_2-\sigma$	0.05	0.05	0.06	0.07	0.07	0.11
$B_3-\sigma$	0.01	0.01	0.00	0.00	0.00	0.00
$B_{tot}-\sigma$	0.18	0.19	0.21	0.23	0.24	0.31
B_1-p_z	0.19	0.19	0.18	0.18	0.19	0.20
B_2-p_z	0.28	0.27	0.26	0.25	0.25	0.22
B_3-p_z	0.11	0.11	0.11	0.12	0.12	0.11
$B_{tot}-p_z$	0.58	0.57	0.55	0.55	0.56	0.53
H-s	0.05	0.05	0.05	0.06	0.06	0.06
Total	0.81	0.80	0.81	0.84	0.86	0.90

$\epsilon_x = 1\%$	$\epsilon_y = 0\%$	$\epsilon_y = +1\%$	$\epsilon_y = +2\%$	$\epsilon_y = +3\%$	$\epsilon_y = +4\%$	$\epsilon_y = +5\%$
$B_1-\sigma$	0.13	0.14	0.14	0.15	0.16	0.20
$B_2-\sigma$	0.05	0.05	0.05	0.06	0.06	0.10
$B_3-\sigma$	0.01	0.01	0.00	0.00	0.00	0.00
$B_{tot}-\sigma$	0.19	0.20	0.19	0.21	0.22	0.30
B_1-p_z	0.22	0.21	0.20	0.20	0.20	0.20
B_2-p_z	0.30	0.29	0.28	0.27	0.26	0.24
B_3-p_z	0.11	0.11	0.11	0.12	0.12	0.12
$B_{tot}-p_z$	0.63	0.61	0.59	0.59	0.58	0.56
H-s	0.05	0.05	0.06	0.06	0.06	0.06
Total	0.87	0.86	0.84	0.86	0.86	0.92

$\epsilon_x = 2\%$	$\epsilon_y = 0\%$	$\epsilon_y = +1\%$	$\epsilon_y = +2\%$	$\epsilon_y = +3\%$	$\epsilon_y = +4\%$	$\epsilon_y = +5\%$
$B_{1-\sigma}$	0.14	0.15	0.15	0.16	0.16	0.19
$B_{2-\sigma}$	0.04	0.05	0.05	0.05	0.05	0.09
$B_{3-\sigma}$	0.00	0.00	0.00	0.00	0.00	0.00
$B_{tot-\sigma}$	0.18	0.20	0.20	0.21	0.21	0.28
B_{1-p_z}	0.21	0.22	0.22	0.22	0.21	0.21
B_{2-p_z}	0.28	0.29	0.29	0.28	0.27	0.25
B_{3-p_z}	0.11	0.12	0.12	0.12	0.12	0.12
B_{tot-p_z}	0.60	0.63	0.63	0.62	0.60	0.58
H-s	0.06	0.06	0.06	0.06	0.06	0.06
Total	0.84	0.89	0.89	0.89	0.87	0.91

$\epsilon_x = 3\%$	$\epsilon_y = 0\%$	$\epsilon_y = +1\%$	$\epsilon_y = +2\%$	$\epsilon_y = +3\%$	$\epsilon_y = +4\%$	$\epsilon_y = +5\%$
$B_{1-\sigma}$	0.16	0.16	0.16	0.16	0.16	0.18
$B_{2-\sigma}$	0.05	0.05	0.05	0.05	0.05	0.09
$B_{3-\sigma}$	0.01	0.00	0.00	0.00	0.00	0.00
$B_{tot-\sigma}$	0.22	0.21	0.21	0.21	0.21	0.27
B_{1-p_z}	0.21	0.21	0.21	0.22	0.22	0.22
B_{2-p_z}	0.28	0.28	0.28	0.28	0.28	0.26
B_{3-p_z}	0.12	0.12	0.12	0.12	0.12	0.12
B_{tot-p_z}	0.61	0.61	0.61	0.62	0.62	0.60
H-s	0.06	0.06	0.06	0.06	0.06	0.06
Total	0.89	0.88	0.88	0.89	0.89	0.93

$\epsilon_x = 4\%$	$\epsilon_y = 0\%$	$\epsilon_y = +1\%$	$\epsilon_y = +2\%$	$\epsilon_y = +3\%$	$\epsilon_y = +4\%$	$\epsilon_y = +5\%$
$B_{1-\sigma}$	0.17	0.17	0.17	0.16	0.16	0.18
$B_{2-\sigma}$	0.05	0.05	0.05	0.05	0.05	0.09
$B_{3-\sigma}$	0.01	0.00	0.00	0.00	0.00	0.00
$B_{tot-\sigma}$	0.23	0.22	0.22	0.21	0.21	0.27
B_{1-p_z}	0.21	0.21	0.21	0.21	0.22	0.21
B_{2-p_z}	0.26	0.27	0.27	0.26	0.27	0.25
B_{3-p_z}	0.12	0.13	0.13	0.13	0.13	0.12
B_{tot-p_z}	0.59	0.61	0.61	0.60	0.62	0.58
H-s	0.07	0.07	0.07	0.06	0.06	0.06
Total	0.89	0.90	0.90	0.87	0.89	0.91

$\epsilon_x = 5\%$	$\epsilon_y = 0\%$	$\epsilon_y = +1\%$	$\epsilon_y = +2\%$	$\epsilon_y = +3\%$	$\epsilon_y = +4\%$	$\epsilon_y = +5\%$
$B_{1-\sigma}$	0.18	0.18	0.18	0.17	0.17	0.18
$B_{2-\sigma}$	0.05	0.05	0.05	0.05	0.06	0.09
$B_{3-\sigma}$	0.01	0.00	0.00	0.00	0.00	0.00
$B_{tot-\sigma}$	0.24	0.23	0.23	0.22	0.23	0.27
B_{1-p_z}	0.21	0.21	0.20	0.20	0.20	0.19
B_{2-p_z}	0.26	0.26	0.26	0.25	0.25	0.22
B_{3-p_z}	0.13	0.13	0.13	0.13	0.13	0.12
B_{tot-p_z}	0.60	0.60	0.59	0.58	0.58	0.53
H-s	0.07	0.07	0.07	0.07	0.06	0.06
Total	0.91	0.90	0.89	0.87	0.87	0.86

This variations in λ_{iso} with applied strain are directly attributed to the changes in *interatomic charge densities*. Under compressive strain, the reduction in atomic separations results in increased interatomic charge densities, while the total charge within the system remains constant. Conversely, tensile strain expands atomic distances, leading to a corresponding decrease in interatomic charge densities. These interatomic charge densities (clouds) serve as an effective spring constants for lattice vibrations, where increased electronic density under compression corresponds to stiffer springs, and decreased density under tension corresponds to weaker springs. As phonon frequencies (ω) are qualitatively tied to spring constants via the relation $\omega = \sqrt{k/m}$, this explains why compressive strain leads to an increase in phonon frequencies, while tensile strain causes a decrease, which can even result in phonon softening. Through the equation $\lambda = 2 \int_0^\infty \alpha^2 F(\omega) \omega^{-1} d\omega$, it becomes evident why the *e-ph* coupling increases under tensile strain. A more comprehensive explanation of this mechanism is provided in the work of our colleagues, cited as Refs. [288, 305]. However, in our system, the situation is more complex due to the significant anisotropy, which is reflected in notably distinct behaviors when tensile strain is applied along the x or y direction. Namely, when strain is applied along the y -direction, aligned with the B_1 –(B_2 –H– B_2) bond, all B–B and B–H bonds undergo an elongation. However, when the same kind of deformation is introduced along the x -axis, although the majority of B–B and B–H bonds lengthen, the B_2 – B_2 bond exhibits a unique compression rather than elongation, in order to compensate for changes in the charge distribution, as shown in Table 4.4. This is

Table 4.4: B_2 - B_2 bond length in units of Å for different combination of applied tensile strain. In the case of uniaxial tensile strain in y direction, for $\epsilon_y = +5\%$ the B_1 - B_2 bond length is much higher compared with other cases.

STRAIN	$\epsilon_y = 0\%$	$\epsilon_y = +1\%$	$\epsilon_y = +2\%$	$\epsilon_y = +3\%$	$\epsilon_y = +4\%$	$\epsilon_y = +5\%$
$\epsilon_x = 0\%$	1.645	1.662	1.678	1.697	1.715	1.716
$\epsilon_x = +1\%$	1.644	1.661	1.678	1.695	1.714	unstable
$\epsilon_x = +2\%$	1.641	1.658	1.676	1.693	1.712	unstable
$\epsilon_x = +3\%$	1.640	1.656	1.672	1.690	unstable	unstable
$\epsilon_x = +4\%$	1.640	1.655	1.671	1.688	1.704	unstable
$\epsilon_x = +5\%$	1.639	1.655	1.671	1.687	1.702	unstable

directly reflected to distinct interatomic charge density distributions, which in turn influence the contributions of B_1 and B_2 projected DOS at the E_F , with variations observed along the x and y directions. Therefore, the variations in phonon frequencies follow the discussed trend, as indicated by our calculations which are depicted in Figure 4.8, ultimately leading to the most significant enhancement of *e-ph* coupling under a uniaxial tensile strain of $+5\%$ applied along

the y direction.

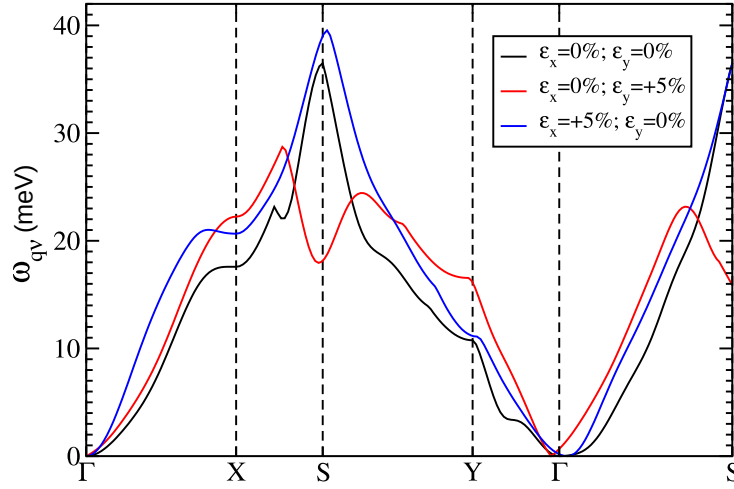


Figure 4.8: Phonon frequencies $\omega_{q\nu}$, expressed in units of meV, are presented along the selected path in the Brillouin zone for $H_{bridge-\beta_{12}}$ borophane in case (a) without applied strain, and under influence of uniaxial tensile strain of +5% applied in the (b) y or (c) x -direction.

Therefore, a detailed strain analysis identified the $H_{bridge-\beta_{12}}$ configuration as the most promising candidate for superconductivity when subjected to a +5% uniaxial tensile strain along the y -axis, beyond which no additional improvement in superconducting properties was observed. Under these optimal conditions, λ_{iso} reaches a value of 0.67, yielding a isotropic T_c^{iso} of 17.2 K. The maximum value of $\lambda_{q\nu}$ is observed at the S point, predominantly associated with low-frequency phonon modes, as depicted in Figure 4.9(a). The associated phonon mode primarily involves out-of-plane motion of B_3 atoms coupled with in-plane displacements of B_2 and H atoms, as shown in Figure 4.9(b). Furthermore, the isotropic Eliashberg spectral function, as depicted in Figure 4.9(b), reveals the presence of two additional prominent peaks: (i) the first peak appears at ~ 90 meV, originating from the in-plane motion of H atoms with a minor out-of-phase contribution from B_3 , while the most pronounced A phonon mode at ~ 110 meV arises from the in-plane motion of B atoms accompanied by slight out-of-plane displacement of H atoms. Also, Figure 4.9(d) reveals the pronounced anisotropy of the Fermi surface, motivating us to preform a detailed investigation of material's superconducting properties through fully anisotropic ME calculations. Within the ellipsoidal sheet centered around the S point, $\Delta(\mathbf{k})$ arises from the hybridized of B- p_z and H- s states. Along the $\Gamma-X$ path, the lower gap values are associated with hybridized B- p_z and H- s states, whereas the largest values emerge from the pure B- p_z states. Despite minor modifications in the Fermi surface composition, the overall characteristics and their correlation with the $\Delta(\mathbf{k})$ values are in excellent agreement with those observed in the unstrained configuration. Demonstrating a pronounced anisotropic single-gap

behavior, the $\Delta(\mathbf{k})$ values attain a maximum value of 4.95 meV at 0 K, which corresponds to an enhanced T_c^{aniso} of 28.6 K, as depicted in Figure 4.9(e).

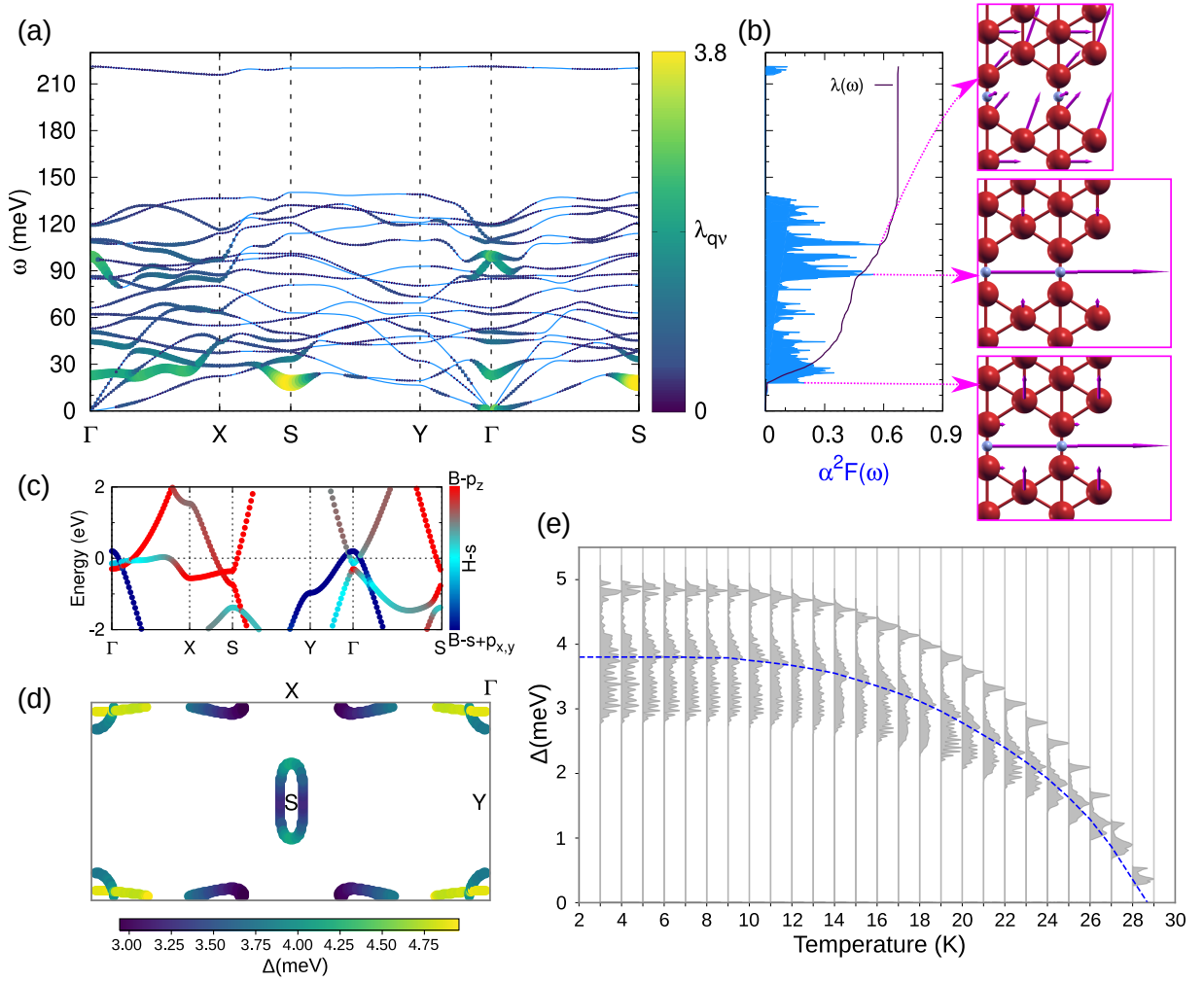


Figure 4.9: For the best candidate – $H_{\text{bridge}}\beta_{12}$ borophene under uniaxial tensile strain $\epsilon_y = +5\%$ – inset (a) shows the phonon dispersion, highlighting the momentum-resolved e -ph coupling $\lambda_{q\nu}$ through a color-coded representation; (b) illustrates the isotropic Eliashberg spectral function along with the phonon modes associated with its prominent peaks; (c) presents the orbital-resolved electronic band structure, while (d) depicts the superconducting gap distribution across the Fermi surface, calculated at 3 K; (e) illustrates the temperature dependence of Δ , with weighted averages (dashed blue line), giving $T_c^{\text{aniso}} = 28.6$ K.

4.1.3.2 Tuning superconducting properties through uniform and nonuniform (FET) electron or hole doping

In addition to strain engineering, controlled charge doping represents a well established approach for tuning the electronic properties of 2D materials. Moreover, this phenomenon can arise naturally as a secondary effect when specific substrates are employed, which is often the case for borophene structures. We performed simulations of both spatially uniform doping and

nonuniform field-effect transistor (FET)-type doping, employing a single-sided gate geometry (details are provided in **APPENDIX A4**). Initially, it was observed that the bare β_{12} borophene structure remains dynamically unstable under influence of both electron and hole doping. However, in the case of $H_{bridge}\text{-}\beta_{12}$ borophene, the dynamical stability is achieved for wide range of electron and hole doping levels, with T_c^{iso} reaching 25.1 K for hole doping level of $-0.06 e/B$, as depicted in Figure 4.10(a). Given the significant influence of the electronic DOS at the E_F on λ_{iso} , and its

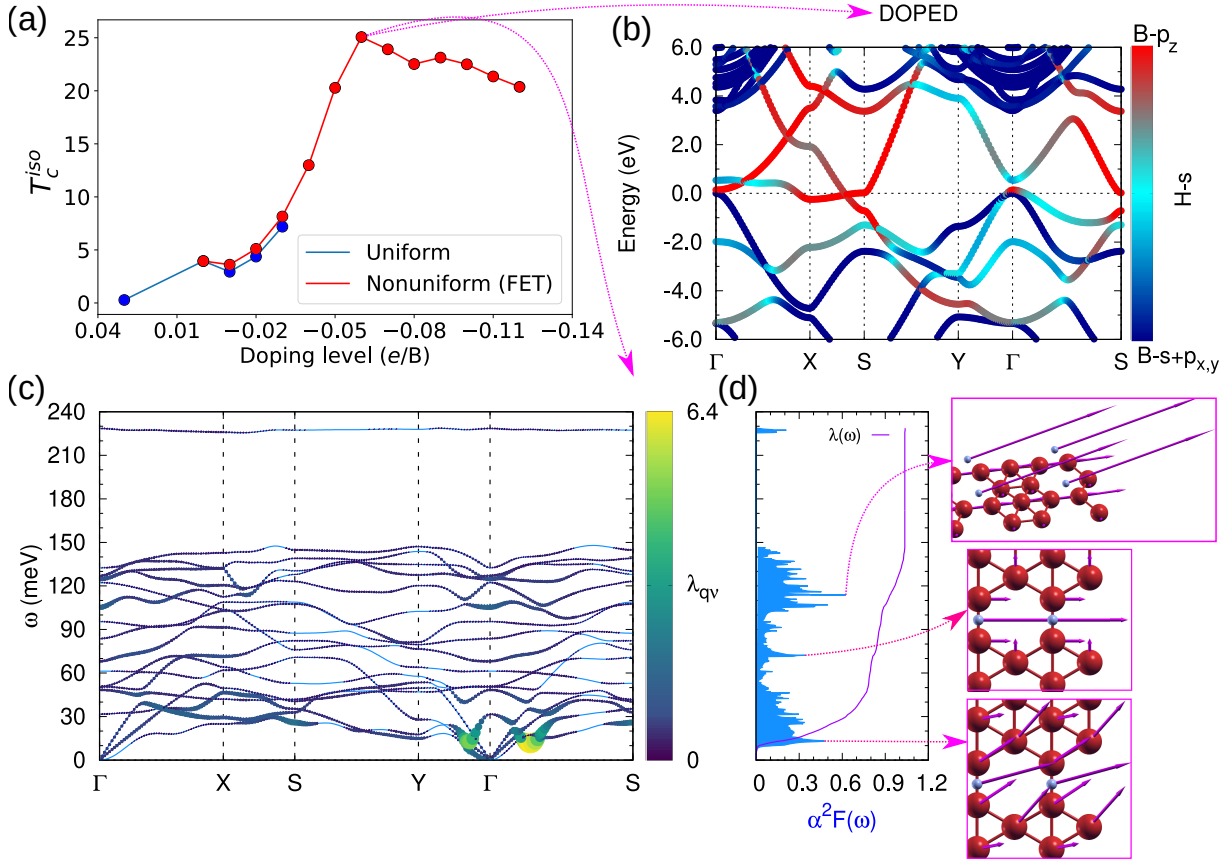


Figure 4.10: Superconducting properties of $H_{bridge}\text{-}\beta_{12}$ borophene under the effects of both uniform and nonuniform (FET) electron and hole doping. (a) Variation of T_c^{iso} as a function of doping level. (b) Electronic band structure highlighting band character (color-coded) for a doping level of $-0.06 e/B$ (hole doping). (c) Phonon dispersion with momentum-resolved e-ph coupling $\lambda_{q\nu}$, represented by color intensity. (d) Isotropic Eliashberg spectral function and phonon modes corresponding to the dominant peaks in the function.

sensitivity to carrier doping, we explored its impact on superconducting properties. Our analysis revealed that the DOS at E_F reduces with electron “injection” and rises with hole doping (see Tables 4.5 and 4.6). Interestingly, hole doping enhances the contributions from B- σ and B- p_z states, leading to a significant increase of λ_{iso} , which reaches a peak value of 1.04 at a doping level of $-0.06 e/B$. The highest $\lambda_{q\nu}$ value originates from the softened A phonon mode along $\Gamma - S$ at approximately 10 meV, driven by in-plane motion of H atoms coupled with rotational

movement of B atoms, as shown in Figure 4.10(c-d). The other significant peaks at higher

Table 4.5: The values of projected DOS at E_F in units of states/eV of $H_{\text{bridge}}\text{-}\beta_{12}$ borophene by applying uniform hole doping.

	+0.03 e/B	0.00 e/B	-0.01 e/B	-0.02 e/B	-0.03 e/B
$B_1\text{-}\sigma$	0.05	0.12	0.13	0.14	0.15
$B_2\text{-}\sigma$	0.01	0.05	0.05	0.06	0.08
$B_3\text{-}\sigma$	0.00	0.01	0.01	0.01	0.01
$B_{\text{tot}}\text{-}\sigma$	0.06	0.18	0.19	0.21	0.24
$B_1\text{-}p_z$	0.10	0.19	0.21	0.24	0.25
$B_2\text{-}p_z$	0.09	0.28	0.31	0.33	0.32
$B_3\text{-}p_z$	0.07	0.11	0.10	0.08	0.07
$B_{\text{tot}}\text{-}p_z$	0.26	0.58	0.62	0.65	0.64
H-s	0.02	0.05	0.05	0.05	0.05
Total	0.34	0.81	0.86	0.91	0.93

frequencies in the Eliashberg spectral function arise from two distinct phonon modes: (i) the A_g mode at approximately 70 meV, associated with in-plane λ_{iso} motion of B_2 and H atoms, with slight out-of-phase motion of B_3 atoms, and (ii) the phonon mode near 110 meV, attributed to in-plane and in-phase movement of B_2 atoms accompanied by slight in-plane and out-of-phase movement of B_3 atoms and out-of-plane displacement of H atoms, as illustrated in Figure 4.10(d).

Table 4.6: The values of projected DOS at E_F in units of states/eV of $H_{\text{bridge}}\text{-}\beta_{12}$ borophene by applying nonuniform hole doping (FET).

	-0.01 e/B	-0.02 e/B	-0.03 e/B	-0.04 e/B	-0.05 e/B	-0.06 e/B	-0.07 e/B	-0.08 e/B	-0.09 e/B	-0.10 e/B	-0.11 e/B	-0.12 e/B
$B_1\text{-}\sigma$	0.13	0.15	0.15	0.16	0.17	0.16	0.16	0.18	0.16	0.16	0.15	0.14
$B_2\text{-}\sigma$	0.05	0.06	0.07	0.07	0.09	0.08	0.07	0.08	0.06	0.06	0.05	0.05
$B_3\text{-}\sigma$	0.01	0.01	0.01	0.01	0.01	0.01	0.01	0.01	0.01	0.01	0.01	0.01
$B_{\text{tot}}\text{-}\sigma$	0.19	0.22	0.23	0.24	0.27	0.25	0.24	0.27	0.23	0.23	0.21	0.20
$B_1\text{-}p_z$	0.21	0.24	0.25	0.25	0.24	0.23	0.24	0.24	0.25	0.25	0.24	0.23
$B_2\text{-}p_z$	0.31	0.33	0.32	0.34	0.44	0.54	0.64	0.70	0.68	0.62	0.49	0.28
$B_3\text{-}p_z$	0.10	0.09	0.07	0.05	0.05	0.05	0.05	0.07	0.07	0.07	0.08	0.08
$B_{\text{tot}}\text{-}p_z$	0.62	0.66	0.64	0.64	0.73	0.82	0.93	1.01	1.00	0.94	0.81	0.59
H-s	0.05	0.05	0.05	0.05	0.05	0.05	0.05	0.05	0.05	0.05	0.05	0.04
Total	0.86	0.93	0.92	0.93	1.05	1.12	1.22	1.33	1.28	1.22	1.07	0.83

Overall, the results suggest that hole doping serves as a powerful approach for enhancing λ_{iso} , comparable to the effects of tensile strain. However, when strain and doping are applied together, their combined influence leads to a reduction in λ_{iso} values, primarily due to the lowered contribution of B- σ states at the E_F . For example, in the case of combined effects of +5% uniaxial tensile strain along y direction, and hole doping of -0.03 e/B, the B- σ states contribute with 0.23 states/eV at E_F .

4.1.4 Conclusions

Our study shows that hydrogen adsorption at the bridge site of β_{12} borophene is essential for both achieving dynamical stability and preserving its superconducting properties, with T_c^{aniso} reaching 6.3 K. Additionally, this hydrogenated borophene system exhibits significant T_c enhancement under influence of tensile strain or hole doping, distinguishing it from the bare borophene phase and highlighting its superior superconducting potential compared to other hydrogenated configurations. As a specific example, we demonstrated that by applying a +5% uniaxial tensile strain along the hydrogenated bridges ($\text{B}_2\text{-H-B}_2$) enhances the T_c^{aniso} to 28.6 K, exceeding the liquid hydrogen temperature of 20.3 K, thus enhancing its potential for practical applications. This increase correlates with the growing contribution of the B- σ and B- p_z states at the E_F , alongside a less significant contribution from the hybridized B- p_z /H- s states. This underscores the pivotal role of both B- σ and B- p_z states in driving superconductivity, in contrast to the bare phase where B- σ states are more “dominant”. We further showed that moderate hole doping can also yield elevated T_c values but when combined with strain it leads to opposite effect. Given its enhanced superconducting properties, alongside with its favorable electronic, mechanical, and environmental stability compared with the bare phase, our results position hydrogenated β_{12} borophene as a compelling candidate for advancing boron-based 2D superconducting technologies.

- **Publication:** Božidar N. Šoškić, Jonas Bekaert, Cem Sevik, and Milorad V. Milošević, Enhanced superconductivity of hydrogenated β_{12} borophene. *Nano Letters*, 24(40):12650–12657, 2024.
- <https://doi.org/10.1021/acs.nanolett.4c03845>

4.2 Superconducting properties of bare and intercalated bilayer β_{12} , χ_3 , δ_4 and kagome borophene phases

In the previous section, we demonstrated that hydrogenation of borophene not only reduces its susceptibility to oxidation but also enhances both its stability and intrinsic superconducting properties. However, an alternate route has been identified with the synthesis of bilayer configurations – such as the zig-zag β_{12} phase on Cu(111) or the α phase on Ag(111) substrate – which demonstrate intrinsic stability without the need for passivation strategies. Namely, in these bilayers strong covalent interlayer bonds suppress coupling with substrate, yielding a quasi-freestanding form (and even enabling its complete isolation via liquid-phase exfoliation) that resists oxidation and endures high temperatures. Moreover, first-principles studies reveal that intercalation of certain bilayer phases with alkali, alkaline-earth, or transition metals can induce phonon-mediated superconductivity with T_c values approaching 36 K. This work explores such intercalation strategies to optimize both stability and superconducting performance in the β_{12} , χ_3 , δ_4 , and kagome phases.

4.2.1 Insights into crystal structures and their stability

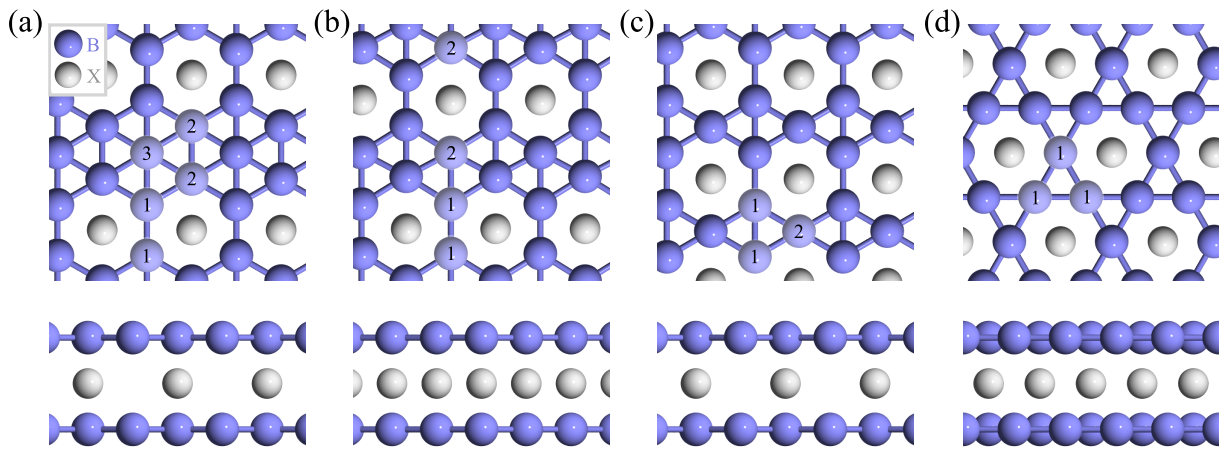


Figure 4.11: Top and side views of intercalated (a) β_{12} , (b) χ_3 , (c) δ_4 , and (d) kagome bilayer borophene phases. Blue spheres represent boron atoms while gray spheres represent intercalated atoms.

We commence by examining the structural properties of the four intercalated bilayer borophene phases – β_{12} , χ_3 , δ_4 , and kagome – depicted in Figure 4.11. To classify these different borophene phases, the coordination number (CN) of boron (B) atoms plays a crucial role, as well as the number of atoms within the corresponding unit cell (see Table 4.7). As exemplified in Figure 4.11(c–d), the δ_4 and kagome phases though sharing identical CN values they exhibit distinct lattice symmetries – the former contains two symmetrically arranged atom types (denoted as 1 and 2), while the latter consists of a single type.

Table 4.7: For the various bilayer borophene configurations explored in this work, we detail the space group, η value, unit cell B atom count (N_B), number of atoms with corresponding CN values, lattice constants, and the average interlayer distance $\langle d \rangle$.

Phase	Space group	η	N_B	N_{at} with CN = 4, 5, 6	a (Å)	b (Å)	$\langle d \rangle$ (Å)
β_{12}	$Pmm2$ (no. 25)	1/6	10	4:4:2	2.943	5.073	2.761
χ_3	$Cmmm$ (no. 65)	1/5	8	4:4:0	4.451	-	3.166
δ_4	$Pmmm$ (no. 47)	1/4	6	6:0:0	2.889	3.332	4.957
Kagome	$P6/mmm$ (no. 191)	1/4	6	6:0:0	3.316	-	4.830

As confirmed in our previous works, the CN values significantly influence the local electronic properties of B atoms, thereby directly affecting their reactivity. This is further manifested in the bilayer borophene phases and their resulting physical properties upon intercalation with specific elements from the group of alkali (Li, Na, K), alkaline earth (Be, Mg, Ca), and transition metals (Sc, Ti, V). The initial step involved the examination of various adsorption configurations for intercalants through the calculation of binding energies,

$$E_b(X) = \frac{N_X E_X + E_{BB} - E_{BXB}}{N_X}, \quad (4.1)$$

with N_X representing the number of X atoms in the unit cell ($N_X = 1$ in all considered cases), while E_X , E_{BB} , and E_{BXB} denote the total energies of the isolated intercalant, bare bilayer borophene, and intercalated bilayer borophene, respectively. Our results indicate a strong preference for metal atoms to bind in the middle of interlayer hexagonal hollow (HH) sites in AA-stacked bilayer borophene, as shown in Fig 4.11, with a detailed analysis of binding sites and their corresponding energies provided in Figure 4.12.

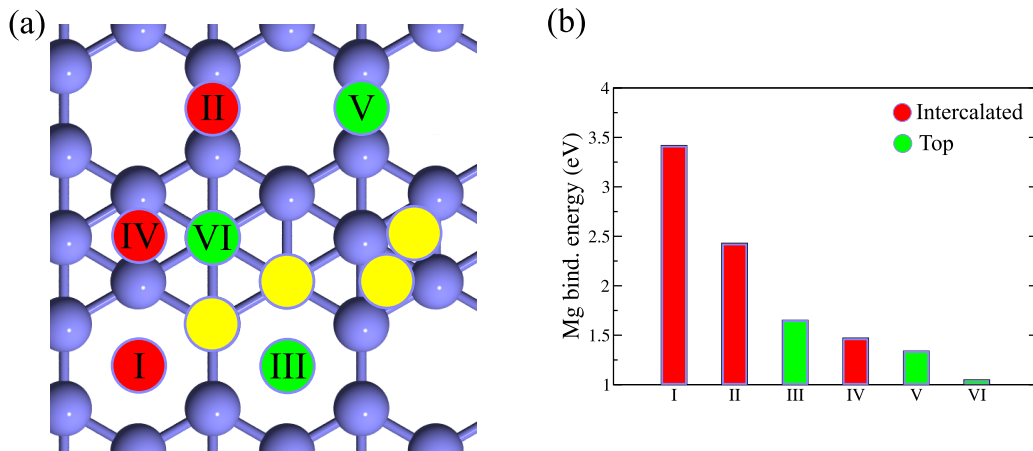


Figure 4.12: (a) Possible Mg adsorption configurations and (b) associated binding energies for the bilayer β_{12} borophene. Adsorption positions for intercalated and top-layer Mg atoms are marked by red and green circles, respectively, while unstable sites are indicated in yellow.

Clear patterns emerge for various metal intercalants, with notable differences in binding behavior. Specifically, K atoms consistently display the weakest binding energies across all investigated bilayer borophene phases, as visible in Figure 4.13(a). This trend correlates with its

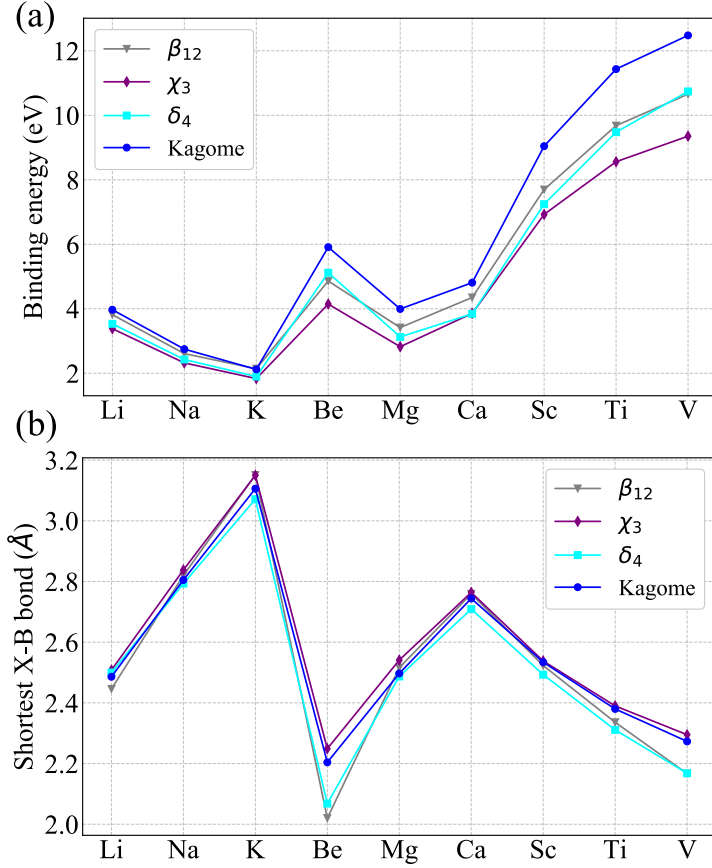


Figure 4.13: (a) Binding energies of intercalants for different bilayer borophene phases, along with (b) the shortest X–B bond distances observed in each case.

low electronegativity, as confirmed by Bader charge analysis provided in Table 4.8. A distinct trend in binding energies is observed across the different borophene phases, with the kagome exhibiting the strongest binding of intercalants, followed by β_{12} , δ_4 , and χ_3 . A few exceptions to this pattern are noted, characterized by small energy differences between neighboring phases.

Table 4.8: Bader charge analysis reveals the extent of electron (e) transfer from intercalated atoms to the borophene layers.

Structure	Li	Na	K	Be	Mg	Ca	Sc	Ti	V
β_{12}	-0.86	-0.80	-0.77	-1.59	-1.59	-1.32	-1.49	-1.41	-1.16
χ_3	-0.87	-0.81	-0.75	-1.56	-1.60	-1.29	-1.51	-1.44	-1.21
δ_4	-0.87	-0.80	-0.72	-1.57	-1.57	-1.22	-1.40	-1.37	-1.20
kagome	-0.86	-0.80	-0.71	-1.56	-1.61	-1.21	-1.47	-1.42	-1.24

Additionally, the interactions between the intercalants and boron atoms with different CN

values result in changes to their X–B bond lengths, as depicted in Figure 4.13(b). In the β_{12} phase, the shortest X–B bond was found with the B_1 atoms, possessing the shortest bond length for Be (2.02 Å) and the largest for K (3.15 Å). For the χ_3 phase, the B_2 atoms exhibit the shortest X–B bond. Lastly, the δ_4 phase is distinguished by the formation of the shortest bonds with either B_1 or B_2 atoms, depending on the “nature” of intercalant (B_1 for alkali metals, B_2 for alkaline-earth and transition metals). As shown in the figure, binding energies are inversely related to X–B bond lengths. Generally, stronger intercalant binding is linked to shorter bond formation with adjacent B atoms, with Ca being the only exception to this trend.

We next evaluate the dynamical stability by examining the DFPT-computed phonon spectra – full phonon dispersion data are provided in Figures 4.14–4.17. Previous studies have demonstrated that the β_{12} monolayer – characterized by negligible electron deficiency – achieves dynamical stability under modest biaxial tensile strain. In a comparable fashion, our findings indicate that the bilayer configuration attains dynamical stability when intercalated with “foreign” atoms, as shown in Figure 4.14. Also, upon applying tensile strain, the χ_3 monolayer phase is known to achieve dynamical stability. Our results further show that the AA-stacked bilayer form of χ_3 remains dynamically stable in its bare form and when intercalated with Li, Na, or Mg (see Figure 4.15). Examining the remaining phases, we observe a pronounced rise in electron deficiency, which leads to dynamical instability in both the δ_4 and kagome monolayers. The stabilization of their bilayer structures is realized through the incorporation of intercalants that facilitate substantial electron transfer, particularly select alkaline-earth and transition metals, as shown in Figures 4.16–4.17. The intercalation process induces significant modifications in the in-plane lattice parameters and average distance between the layers, as shown in Table 4.9.

Table 4.9: Lattice parameters and the average distances between two borophene layers.

X	β_{12}			χ_3		δ_4			Kagome	
	$\ \mathbf{a}\ $ (Å)	$\ \mathbf{b}\ $ (Å)	$\langle d \rangle$ (Å)	$\ \mathbf{a}\ $ (Å)	$\langle d \rangle$ (Å)	$\ \mathbf{a}\ $ (Å)	$\ \mathbf{b}\ $ (Å)	$\langle d \rangle$ (Å)	$\ \mathbf{a}\ $ (Å)	$\langle d \rangle$ (Å)
None	2.94	5.07	2.76	4.45	3.17	2.89	3.33	4.96	3.32	4.83
Li	2.93	5.08	3.62	4.46	3.75	2.88	3.41	3.70	3.36	3.66
Na	2.94	5.09	4.56	4.46	4.59	2.90	3.42	4.45	3.38	4.48
K	2.95	5.09	5.36	4.46	5.33	2.92	3.44	5.12	3.40	5.20
Be	2.92	5.01	2.88	4.44	3.03	2.87	3.36	2.85	3.36	2.86
Mg	2.94	5.09	3.81	4.47	3.82	2.91	3.45	3.69	3.41	3.65
Ca	2.97	5.09	4.40	4.47	4.39	2.94	3.47	4.22	3.43	4.29
Sc	2.95	5.10	3.84	4.47	3.83	2.96	3.45	3.70	3.41	3.75
Ti	2.94	5.10	3.42	4.49	3.41	2.95	3.46	3.26	3.40	3.33
V	2.91	5.15	3.02	4.49	3.10	2.90	3.53	2.86	3.42	2.99

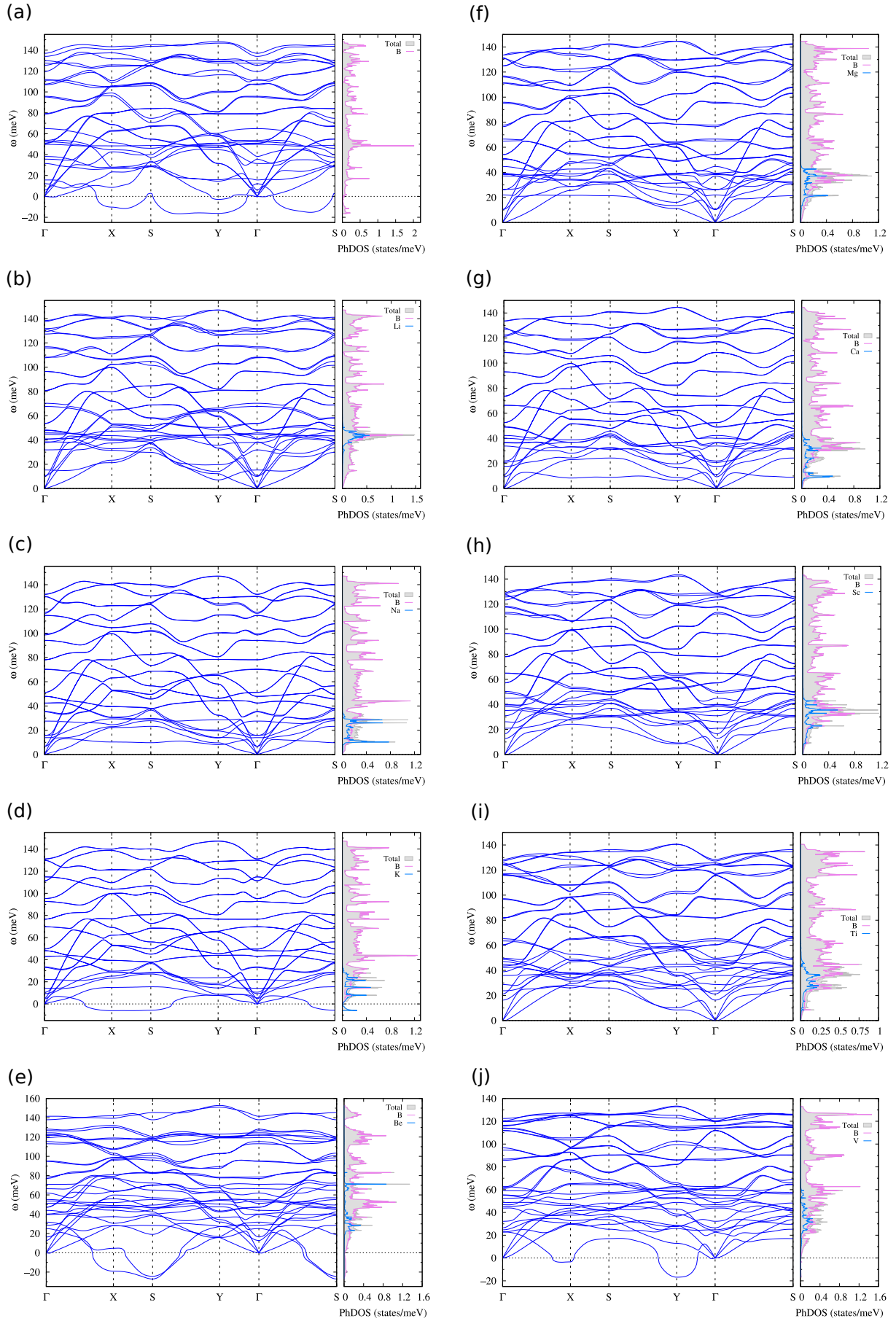


Figure 4.14: Phonon dispersion and atom-resolved phonon DOS for (a) bare bilayer β_{12} borophene and intercalated with (b) Li, (c) Na, (d) K, (e) Be, (f) Mg, (g) Ca, (h) Sc, (i) Ti, and (j) V.

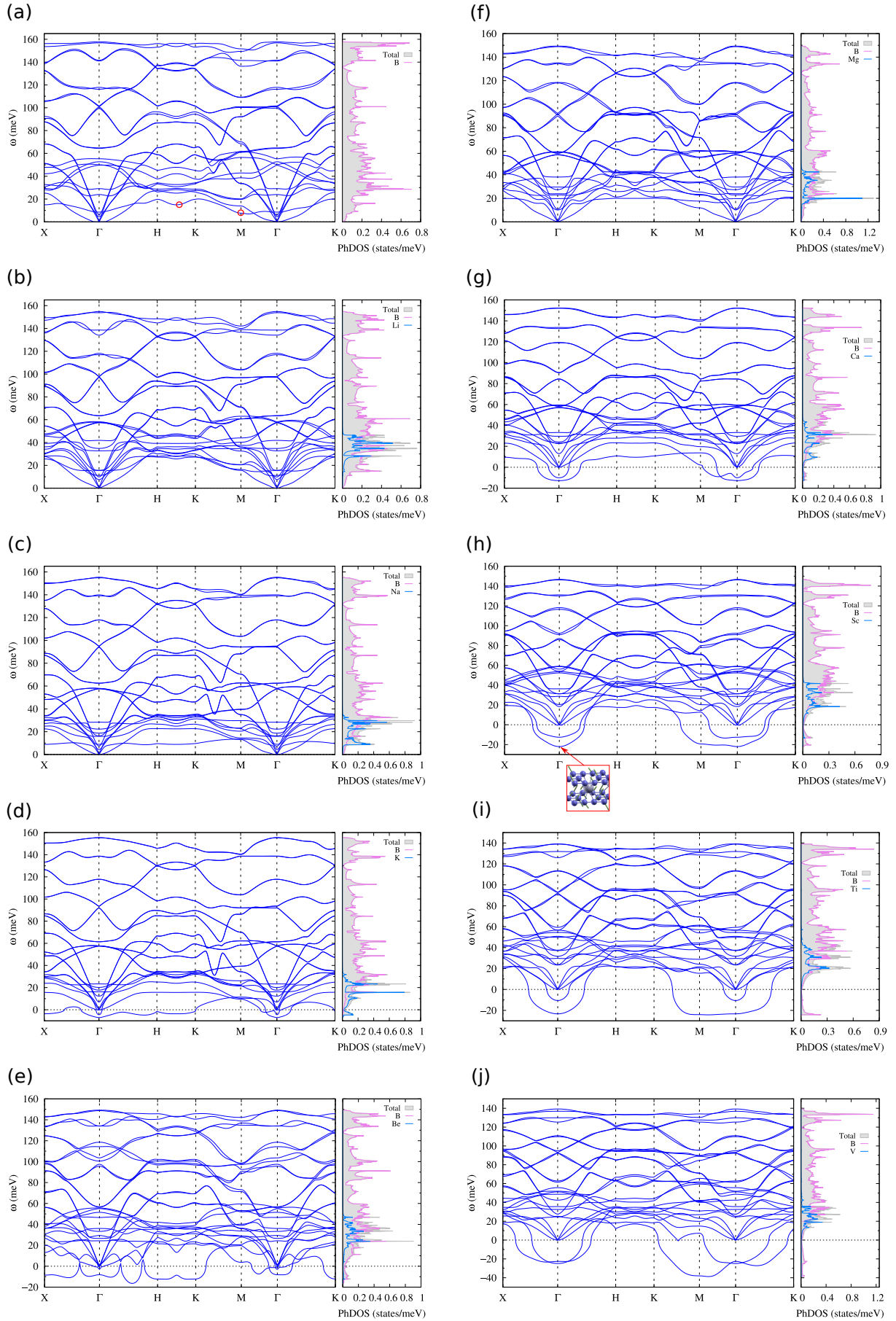


Figure 4.15: Phonon dispersion and atom-resolved phonon DOS for (a) bare bilayer χ_3 borophene and intercalated with (b) Li, (c) Na, (d) K, (e) Be, (f) Mg, (g) Ca, (h) Sc, (i) Ti, and (j) V.

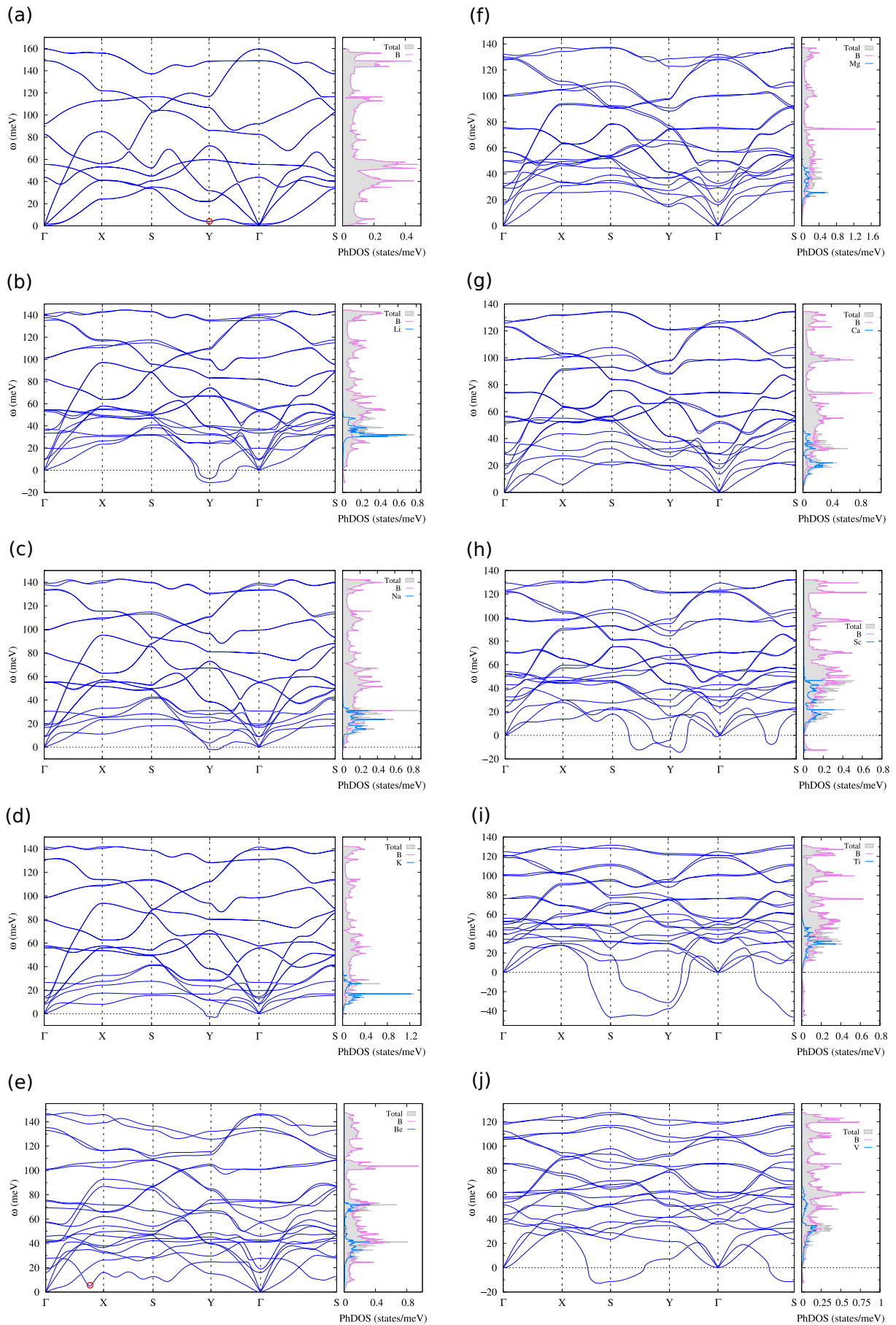


Figure 4.16: Phonon dispersion and atom-resolved phonon DOS for (a) bare bilayer δ_4 borophene and intercalated with (b) Li, (c) Na, (d) K, (e) Be, (f) Mg, (g) Ca, (h) Sc, (i) Ti, and (j) V.

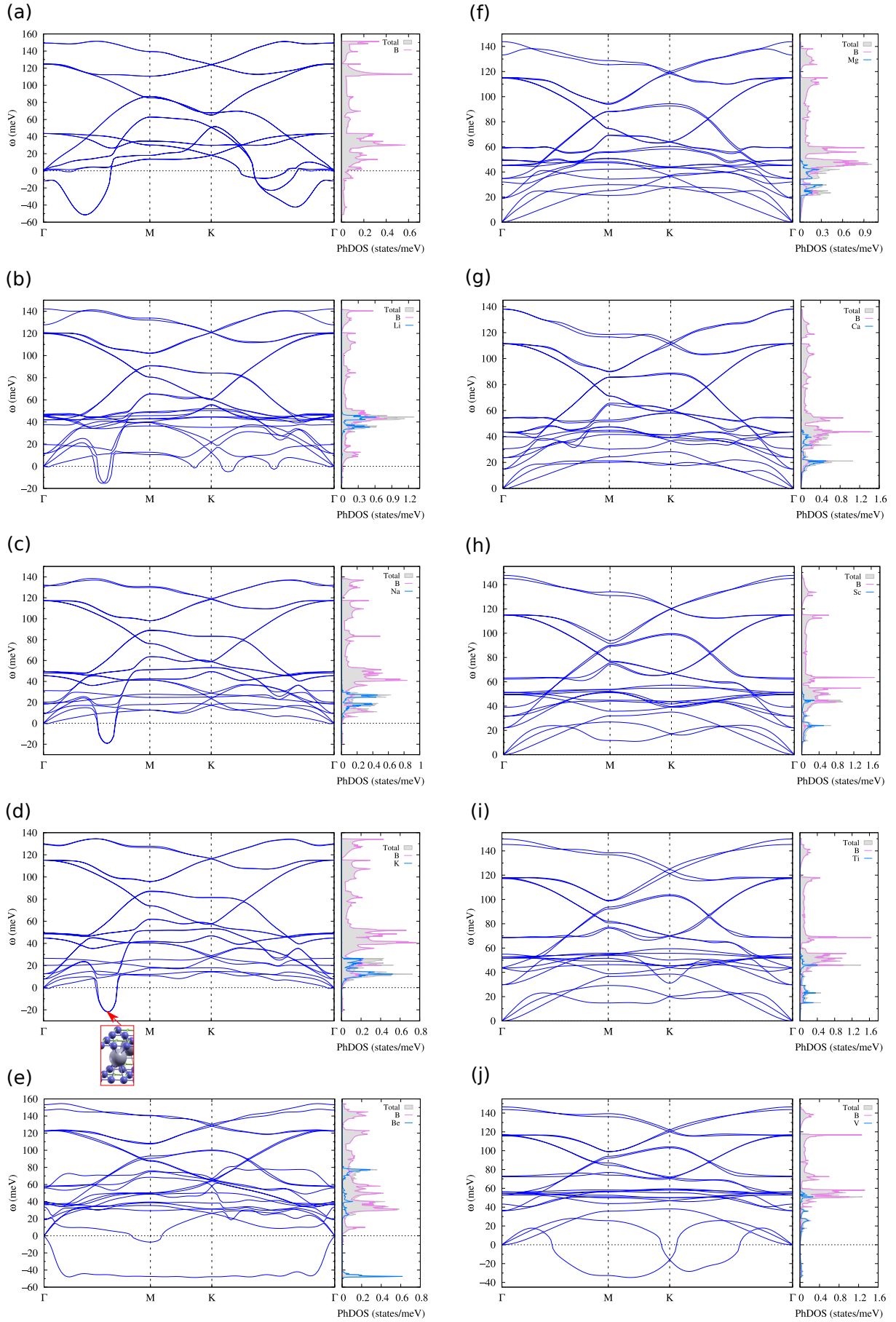


Figure 4.17: Phonon dispersion and atom-resolved phonon DOS for (a) bare bilayer kagome borophene and intercalated with (b) Li, (c) Na, (d) K, (e) Be, (f) Mg, (g) Ca, (h) Sc, (i) Ti, and (j) V.

Notably, all intercalated structures analyzed in this study exhibit nonmagnetic behavior, as confirmed by SDFT calculations. Building on this, Figure 4.18 provides a comprehensive summary of the dynamical stability of these systems, alongside the corresponding superconducting T_c^{iso} values for the identified stable configurations.

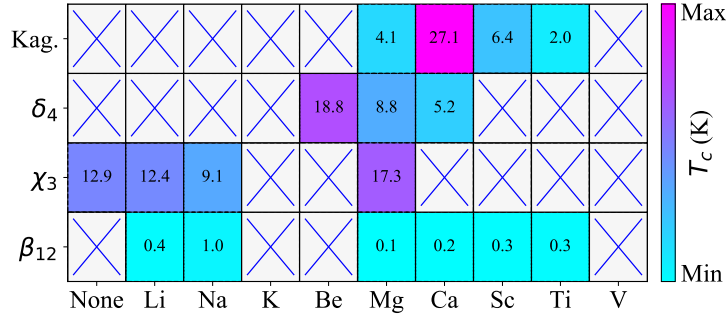


Figure 4.18: A summary of the bare and intercalated bilayer borophene configurations exhibiting dynamic stability is provided, along with their computed superconducting critical temperatures (T_c). Structures found to be dynamically unstable are marked with blue crosses.

All computational details can be found in **APPENDIX A5**.

4.2.2 Electronic, vibrational, and superconducting properties within the isotropic ME framework

This section focuses on the analysis of the electronic, vibrational, and superconducting characteristics of four borophene phases under study, aiming to identify distinct physical trends. We begin with an analysis of the bilayer β_{12} borophene.

4.2.2.1 β_{12} phase of bilayer borophene ($\eta = 1/6$)

To gain deeper insight into their superconducting properties, we now focus on the electronic properties of the bilayer β_{12} borophene phases under investigation. The metallic character of the β_{12} bilayer is clearly demonstrated by the orbital-resolved band structures shown in Figure 4.19, with the dominant contribution arising from the B- p_z orbitals. Minor contributions to this metallicity are observed from the alkali and alkaline-earth intercalants s orbitals, while transition metal intercalants play a more significant role through their d orbital contributions.

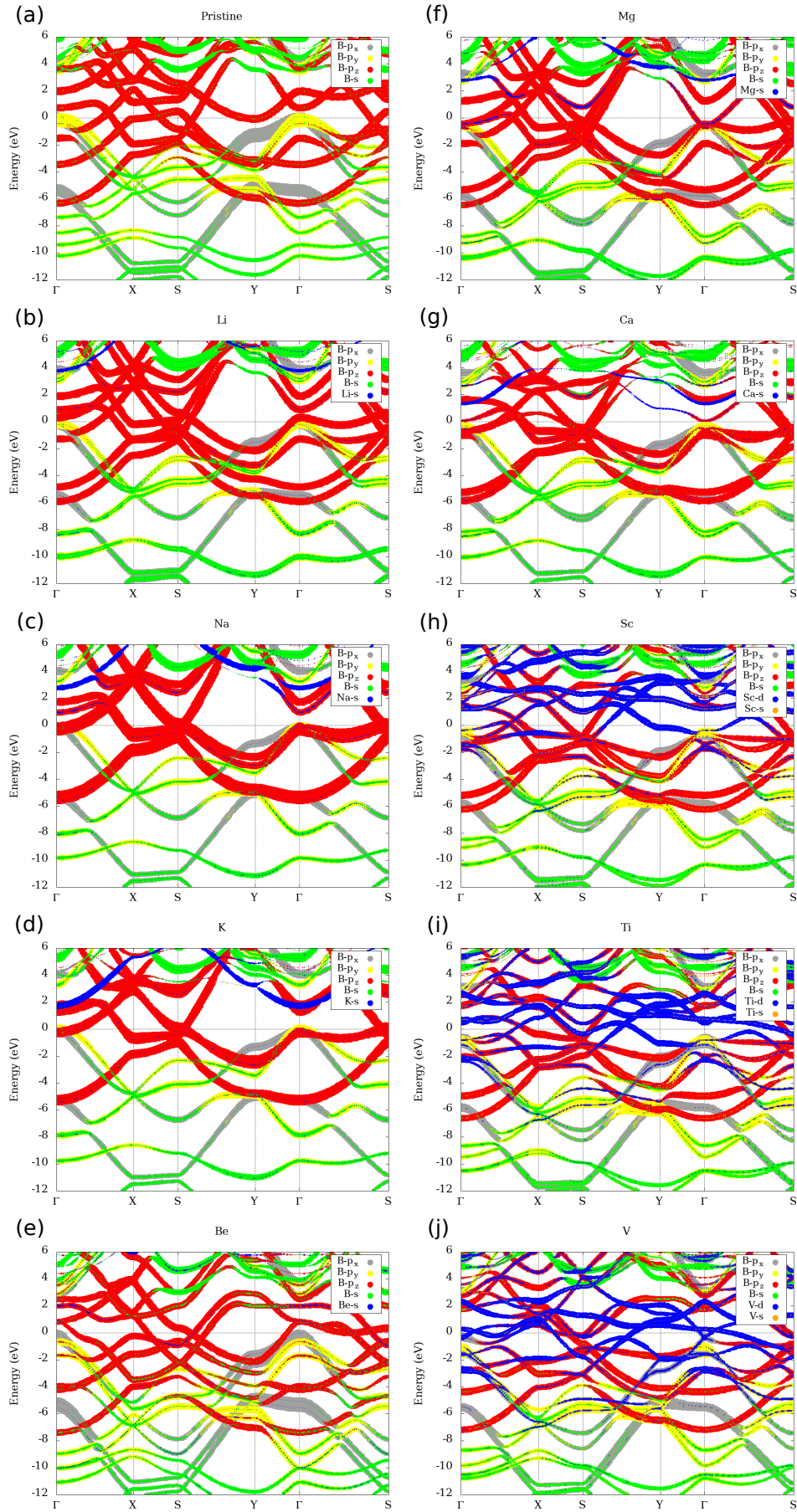


Figure 4.19: The orbital-decomposed band structures for (a) pristine (bare) bilayer β_{12} borophene and when intercalated with (b) Li, (c) Na, (d) K, (e) Be, (f) Mg, (g) Ca, (h) Sc, (i) Ti, and (j) V.

Furthermore, the β_{12} phase exhibits the smallest η value and the minimal electron deficiency in its monolayer configuration, distinguishing it from the other phases under comparison. Figure 4.20 reveals that throughout intercalation process, σ states reach near-total occupation, with a energy gap of roughly 3 eV setting them apart from σ^* states, while the remaining electrons populate the B- p_z orbitals to some extent. As predicted, this process leads to a strong rise in the p_z -resolved DOS near E_F , chiefly due to B₁ and B₂ atoms. In this context, with Na, the highest contribution to total DOS at E_F is observed, reaching 2.33 states/eV, while an opposite trend is seen with Mg, yielding the lowest value of 1.08 states/eV. For all intercalated structures, the primary contribution to the total DOS at the E_F stems from p_z states. However, for Sc and Ti intercalation, d orbitals play a more significant role, contributing with 0.64 and 0.68 states/eV at E_F , respectively. Among all dynamically stable structures, Na stands out with the largest contribution from partially filled σ states at E_F (0.33 states/eV), while Sc and Ti follow Na with values of 0.19 and 0.16 states/eV, respectively.

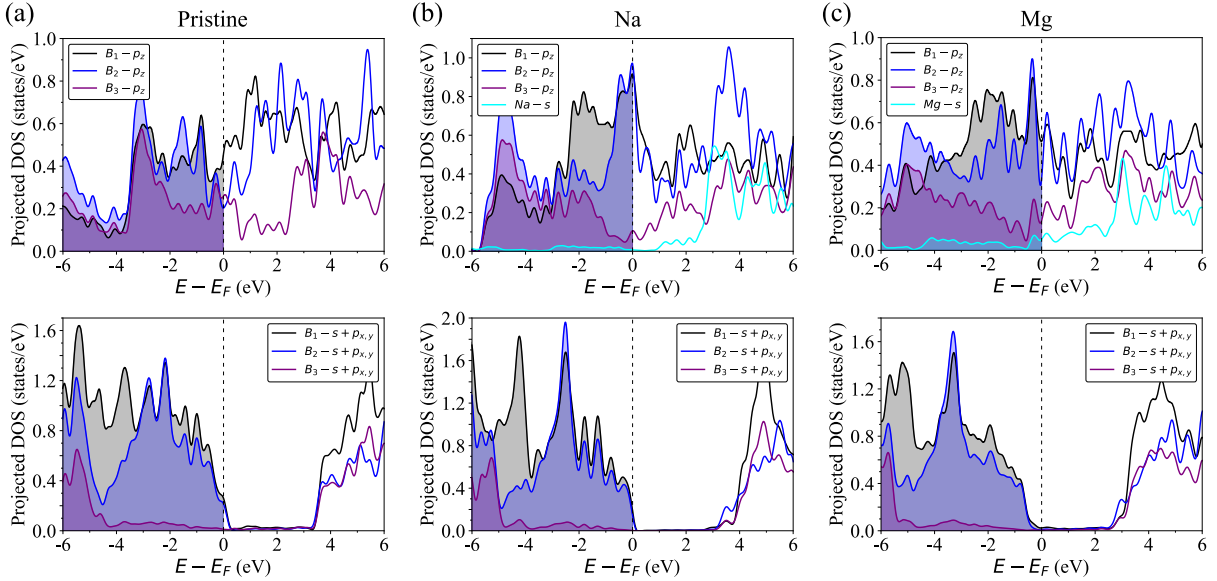


Figure 4.20: The projected DOS onto the p_z and σ orbitals for various boron sites in (a) pristine (bare), (b) Na- and (c) Mg-intercalated bilayer β_{12} borophene. Additionally, for all considered intercalated systems, the contributions from intercalants s orbitals are explicitly shown.

As illustrated in Figure 4.14, our phonon calculations showed that the β_{12} phase lacks dynamical stability in its bare form and remains unstable even after intercalation with K, Be, and V. For the remaining intercalants, the computed phonon spectra confirm their dynamical stability, characterized by several flat phonon branches that result in distinct peaks within the phonon DOS. Phonon modes below ~ 50 meV arise predominantly from the coupled vibrations of boron and intercalant atoms, whereas modes dominated solely by boron appear at higher energies

beyond this threshold. Our analysis of momentum-resolved electron-phonon (e - ph) interactions demonstrates that the most significant coupling occurs in softened phonon modes around 9 meV, particularly in the vicinity of the Y point. Given that their superconducting response falls within the margin of numerical uncertainty, our discussion will be centered on the most promising candidate – Na-intercalated bilayer β_{12} borophene – based on isotropic ME theory, as depicted in Figure 4.21.

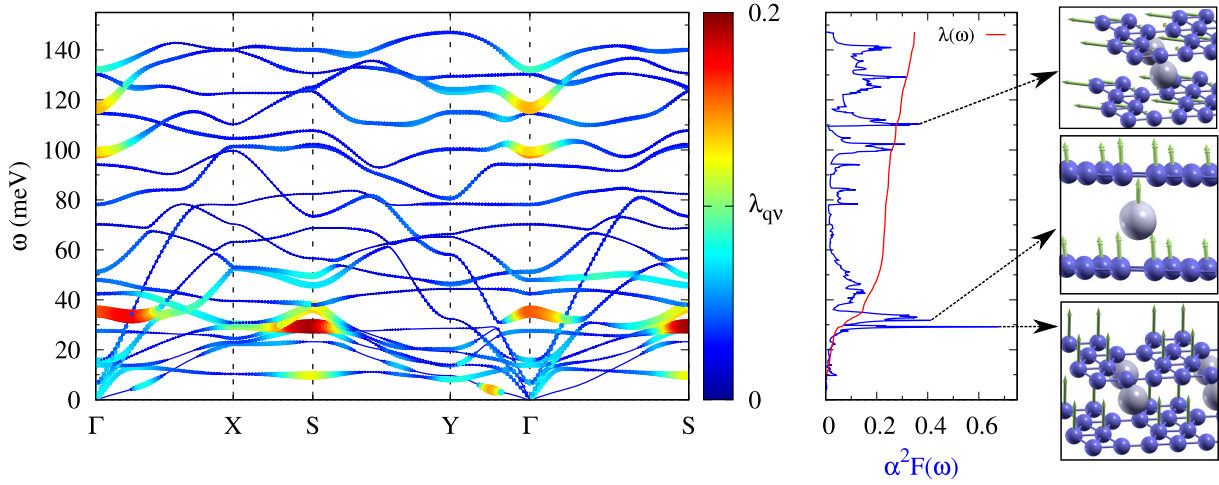


Figure 4.21: The phonon dispersion and the Eliashberg spectral function $\alpha^2 F(\omega)$, which exhibits peaks corresponding to phonon modes that strongly couple to electrons, are shown for Na-intercalated β_{12} bilayer configuration. The phonon branches (ν) and q -resolved e - ph coupling ($\lambda_{q\nu}$) are represented using color scales and point sizes proportional to λ .

In this system, the total e - ph coupling (EPC) strength reaches the value of 0.35, leading to an T_c^{iso} value of approximately 1 K. The dominant contributions to the Eliashberg spectral function arise from the ZA phonon mode associated with boron vibrations and the A_u optical mode, associated with the C_s point group, involves perpendicular displacements of both Na and B atoms, occurring around 30 meV. The enhanced EPC for Na intercalation can be attributed to its higher electronic total DOS at the E_F compared with other intercalants. However, despite this enhancement, the relatively low T_c^{iso} of this system suggests that it is not a particularly promising candidate for further theoretical or experimental investigation.

4.2.2.2 χ_3 phase of bilayer borophene ($\eta = 1/5$)

In contrast to the β_{12} phase, where electronic states near the Fermi level are primarily stemming from out-of-plane orbitals (p_z), the χ_3 phase exhibits a more mixed character. As illustrated in Figure 4.22, both σ and out-of-plane orbitals contribute significantly to the electronic states near E_F , highlighting a distinct electronic structure compared to the β_{12} configuration. To examine

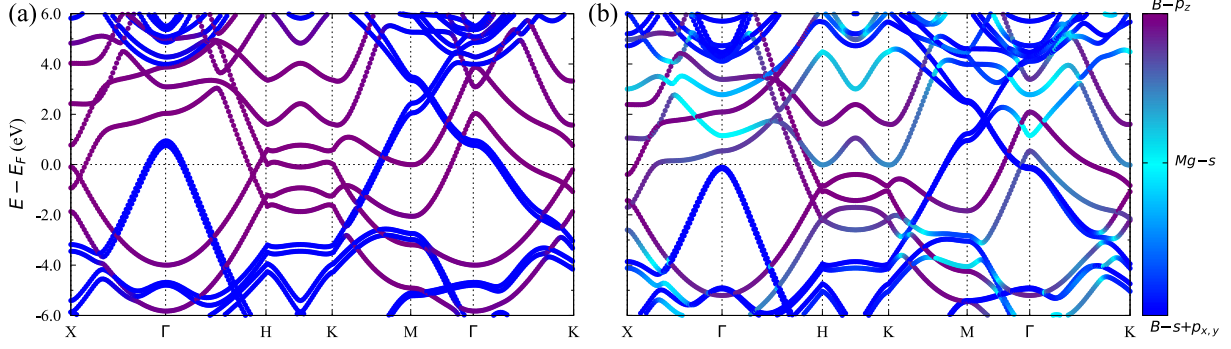


Figure 4.22: Electronic band structures resolved by orbital contributions for (a) bare and (b) Mg-intercalated bilayer χ_3 borophene. The color-coded dots indicate the dominant orbital contributions: blue for B- σ states, purple for B- p_z states, and cyan for Mg- s states.

this effect more quantitatively, we focus on Mg intercalation, given its relatively high total DOS of 1.71 states/eV at E_F and its notable superconducting T_c^{iso} value of 17 K. The contributions to the DOS at E_F (in states/eV) are 1.00 from the B- p_z , 0.65 from the σ , and 0.06 from the Mg- s orbitals (see Figure 4.22(b)). Furthermore, the combination of σ and B- p_z states leads to a rich Fermi surface with a complex network of intersecting Fermi contours, displaying a wide range of Fermi velocities, as shown in Figure 4.23(a).

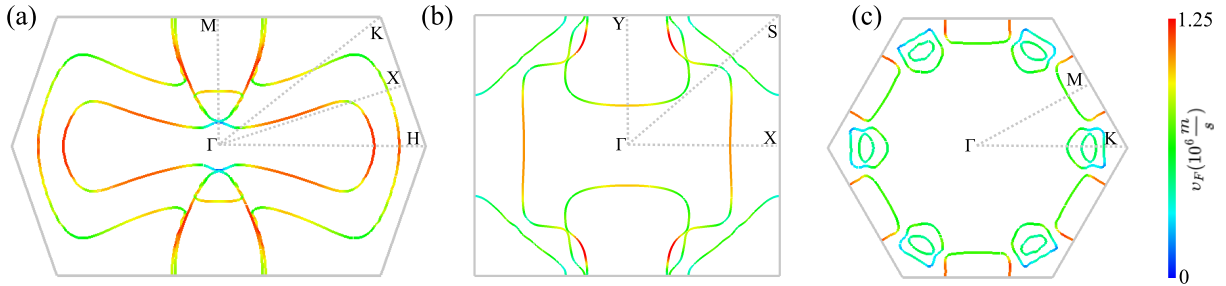


Figure 4.23: Fermi surfaces, shaded according to Fermi velocities, are shown for (a) Mg- χ_3 , (b) Be- δ_4 , and (c) Ca-kagome intercalated bilayer configurations.

Our analysis of the vibrational properties (see Figure 4.15(b)) indicates that the χ_3 phase is uniquely the only bare bilayer borophene structure that maintains dynamical stability in its AA-stacked configuration. Figure 4.24 further illustrates that the primary sources of total e - ph coupling in bare and Mg- χ_3 bilayers are predominantly located in the low-energy region, under approximately 50 meV. For bare bilayer χ_3 borophene, the Eliashberg spectral function exhibits multiple pronounced peaks within this low-frequency region, as seen in Figure 4.24(a). The first two peaks arise from an optical A_1 phonon mode belonging to the C_{2V} point group representation, with the EPC reaching a maximum value of approximately 2.8 at the Γ point. This mode, appearing around 9 meV, corresponds to a *layer-breathing* motion of two B sheets. Additionally, the most prominent peak in the Eliashberg function, observed near 30 meV, is

associated with the optical B_2 phonon mode. At the Γ point, this mode is characterized through the perpendicular and phase-opposed motion of B atoms, exhibiting both infrared and Raman activity (I+R).

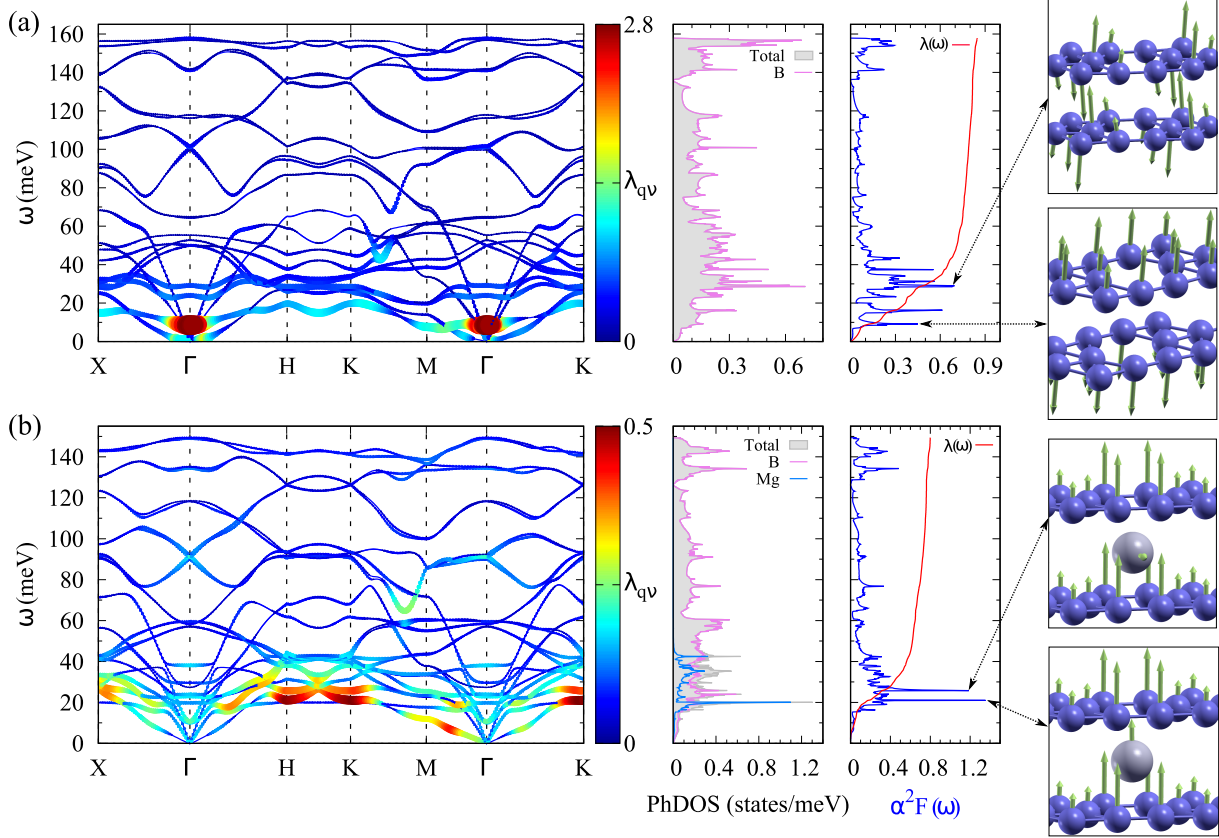


Figure 4.24: The phonon dispersion, atom-resolved PhDOS and the $\alpha^2 F(\omega)$ function, which exhibits peaks corresponding to phonon modes that strongly couple to electrons, are shown for (a) bare, and (b) Mg-intercalated χ_3 bilayer configurations. The phonon branches (ν) and q -resolved e -ph coupling (λ_{qv}) are represented using color scales and point sizes proportional to λ .

In the case of Mg intercalated bilayer χ_3 borophene, a pronounced e -ph interaction emerges along H - K BZ path. Therefore, $\alpha^2 F(\omega)$ function displays two prominent peaks: (i) lower-frequency peak which originates from an A_u acoustic mode, primarily driven by out-of-plane oscillations of all atoms (see Figure 4.24(b)), and (ii) higher-frequency peak which corresponds to an A_g optical mode. The complex topology of the Fermi surface, depicted in Figure 4.23(a), in combination with a total e -ph coupling strength of 0.8, results in a T_c^{iso} value of 17.3 K. This establishes Mg as the most promising intercalant for realizing superconductivity in bilayer χ_3 borophene.

The χ_3 bilayer structures retain their dynamical stability when intercalated with Li and Na, demonstrating robust phonon spectra without any imaginary frequencies. When Li is introduced as an intercalant, the EPC value connected to the A_1 phonon mode at the Γ point decreases to

approximately 0.6, as shown in Figure 4.25(a). Two primary peaks emerge in the Eliashberg spectral function, located at 29 and 33 meV, associated with the out-of-plane motion of B and in-plane displacement of Li atoms, respectively. Similarly, Na intercalation leads to two dominant peaks, with the most pronounced one at 33 meV, corresponding to A_g mode at X point. This mode also involves the out-of-plane motion of boron and in-plane displacement of Na, as illustrated in Figure 4.25(b). Compared to the bare bilayer form, Na intercalation enhances high-energy optical mode contributions to the e - ph coupling, increases both total DOS and ω_{log} , yet reduces EPC strength, lowering T_c^{iso} from 12.9 K to 9.1 K.

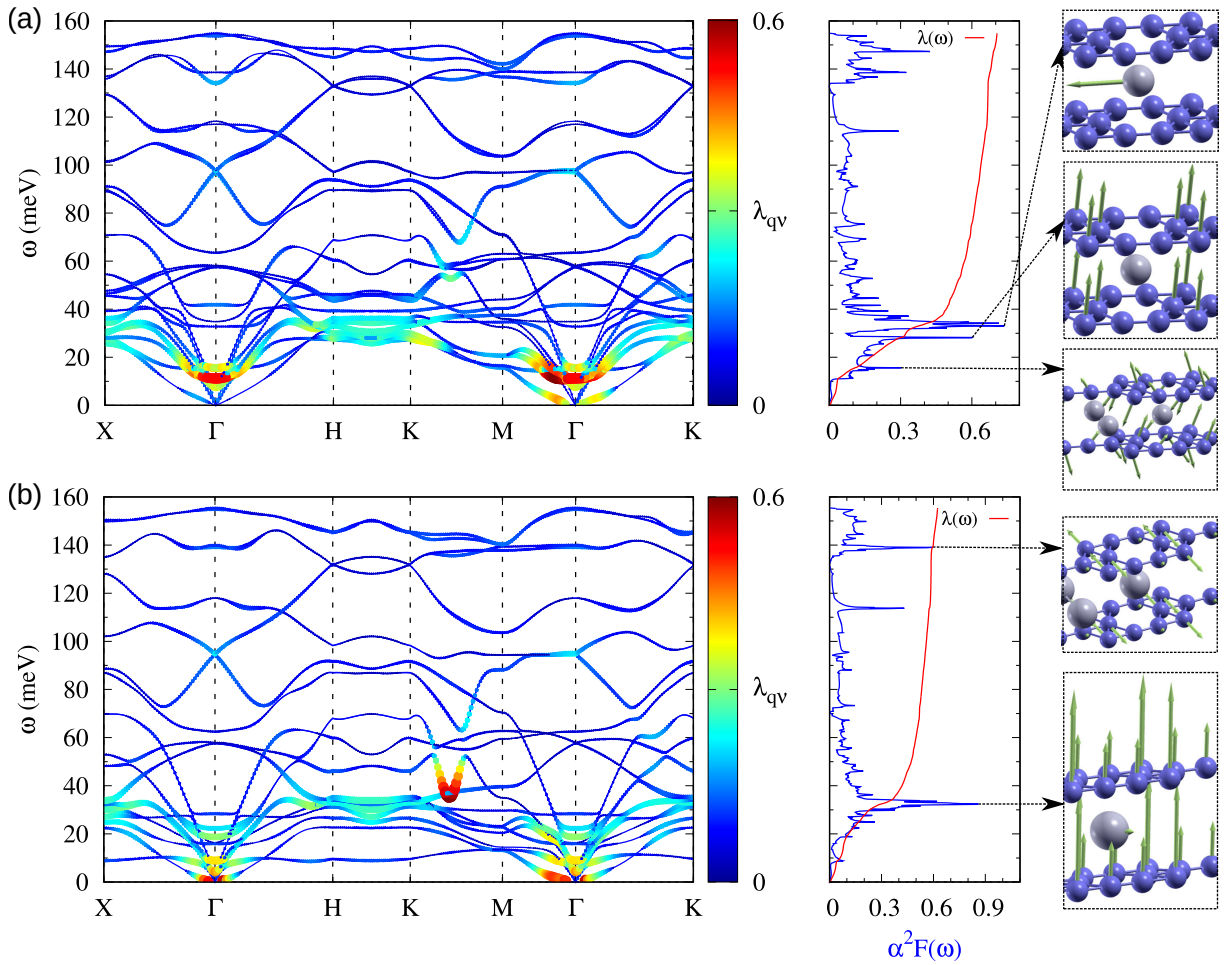


Figure 4.25: The phonon dispersion and the $\alpha^2F(\omega)$ function, which exhibits peaks corresponding to phonon modes that strongly couple to electrons, are shown for (a) Li- and (b) Na-intercalated χ_3 bilayer configurations. The phonon branches (ν) and q -resolved e - ph coupling (λ_{qv}) are represented using color scales and point sizes proportional to λ .

4.2.2.3 δ_4 and kagome phases of bilayer borophene ($\eta = 1/4$)

Finally, we examine the structures with $\eta = 1/4$. Unlike the β_{12} and χ_3 phases, where σ states are more occupied, the δ_4 and kagome configurations exhibit a significant depletion of these

states. Consequently, their contribution to the electronic DOS at the E_F becomes substantially more pronounced, as depicted in Figure 4.26.

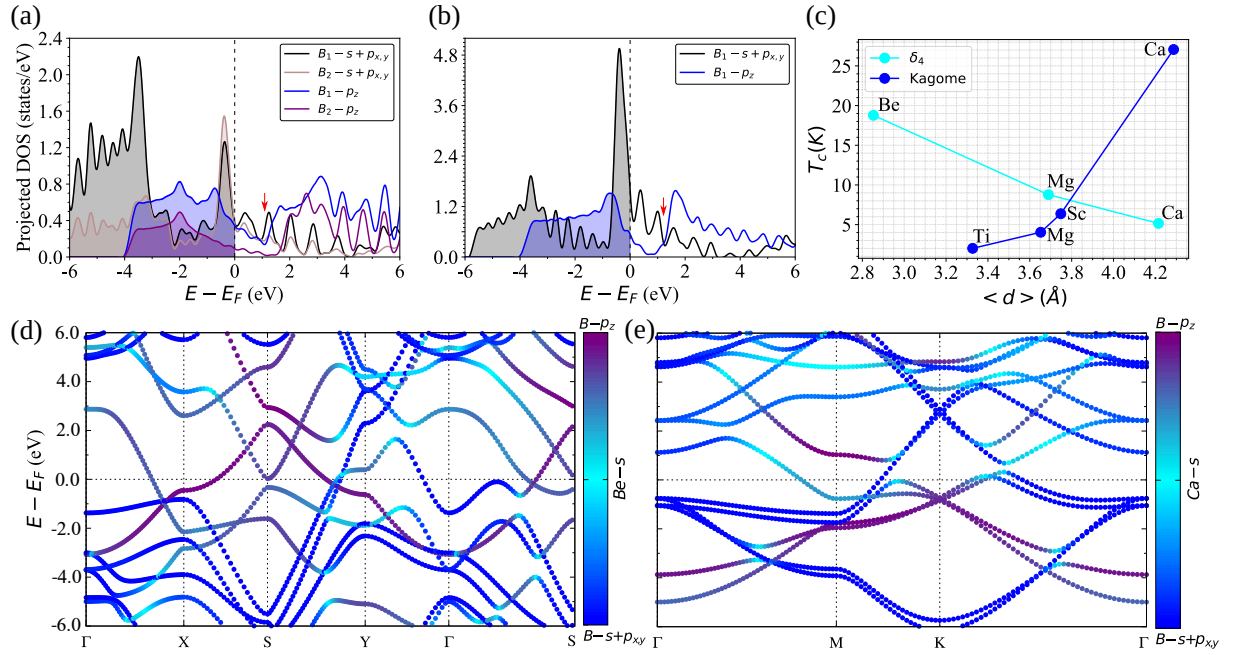


Figure 4.26: The projected DOS for the B- σ and p_z orbitals in the bare (a) δ_4 , and (b) kagome bilayers are shown. (c) Correlation between T_c^{iso} and the average interlayer distance in these phases is illustrated, where red arrows highlight the necessary Fermi level adjustment to achieve structural stabilization. Additionally, the orbital-resolved electronic band structures for (d) Be in δ_4 and (e) Ca in kagome bilayer configurations are displayed. The contributions from B- σ , B- p_z , and X- s orbitals are represented by blue, purple, and cyan markers, respectively.

Owing to the inherent electron deficiency, the partial occupation of out-of-plane (p_z) orbitals contributes to the dynamical instability of these compounds in their bare form. Additionally, the incomplete filling of these p_z states weakens the interlayer coupling, leading to increased interlayer separations (see Table 4.9). As illustrated in Figure 4.26(a–b), this partial occupation of p_z orbitals produces a noticeable gap between π and π^* states above the Fermi level. Furthermore, intercalated kagome configurations exhibits van Hove singularities at the M point¹ as well as higher-order singularities at the K point, both near or crossing the Fermi level, and arising from the hybridization of B- p_z orbitals with the intercalant's s -state, as shown in Figure 4.27.

¹Saddle points in the electronic band structure.

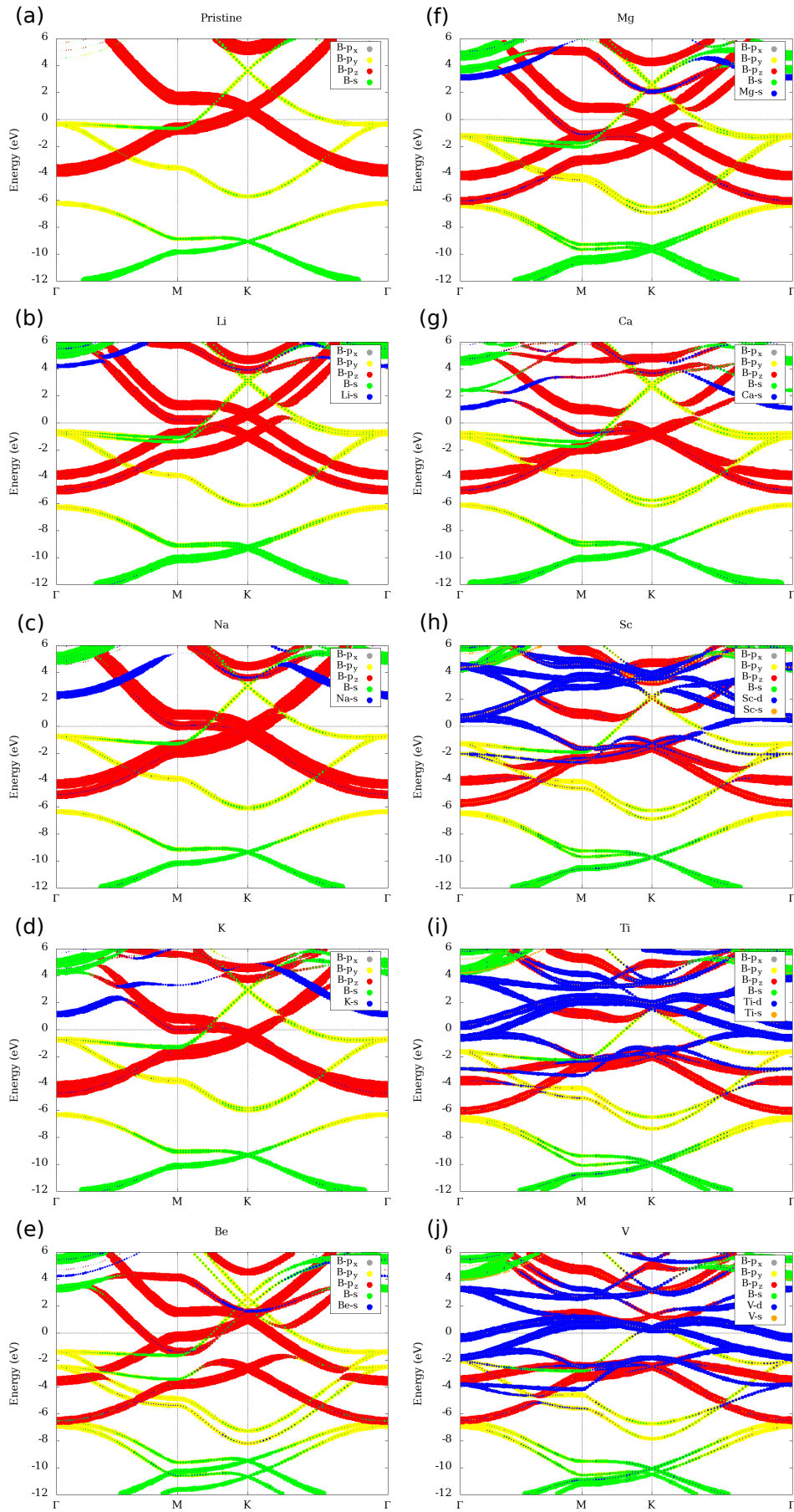


Figure 4.27: The orbital-decomposed band structures for (a) pristine (bare) bilayer kagome borophene and when intercalated with (b) Li, (c) Na, (d) K, (e) Be, (f) Mg, (g) Ca, (h) Sc, (i) Ti, and (j) V.

To ensure the stability of the δ_4 and kagome phases, intercalants must provide adequate electron transfer to the borophene layers. A shift of approximately 1.2 eV in the Fermi level is required to attain an appropriate equilibrium between σ and π^* states, which is essential for ensuring dynamical stability in the considered systems. That being said, alkali metal intercalants fall short in this regard, contributing at most $\sim 0.87 e$ per intercalant. In contrast, stability is achieved with alkaline-earth and transition metal intercalants, as they donate a significantly higher electron charge, exceeding $\sim 1.20 e$ per intercalant.

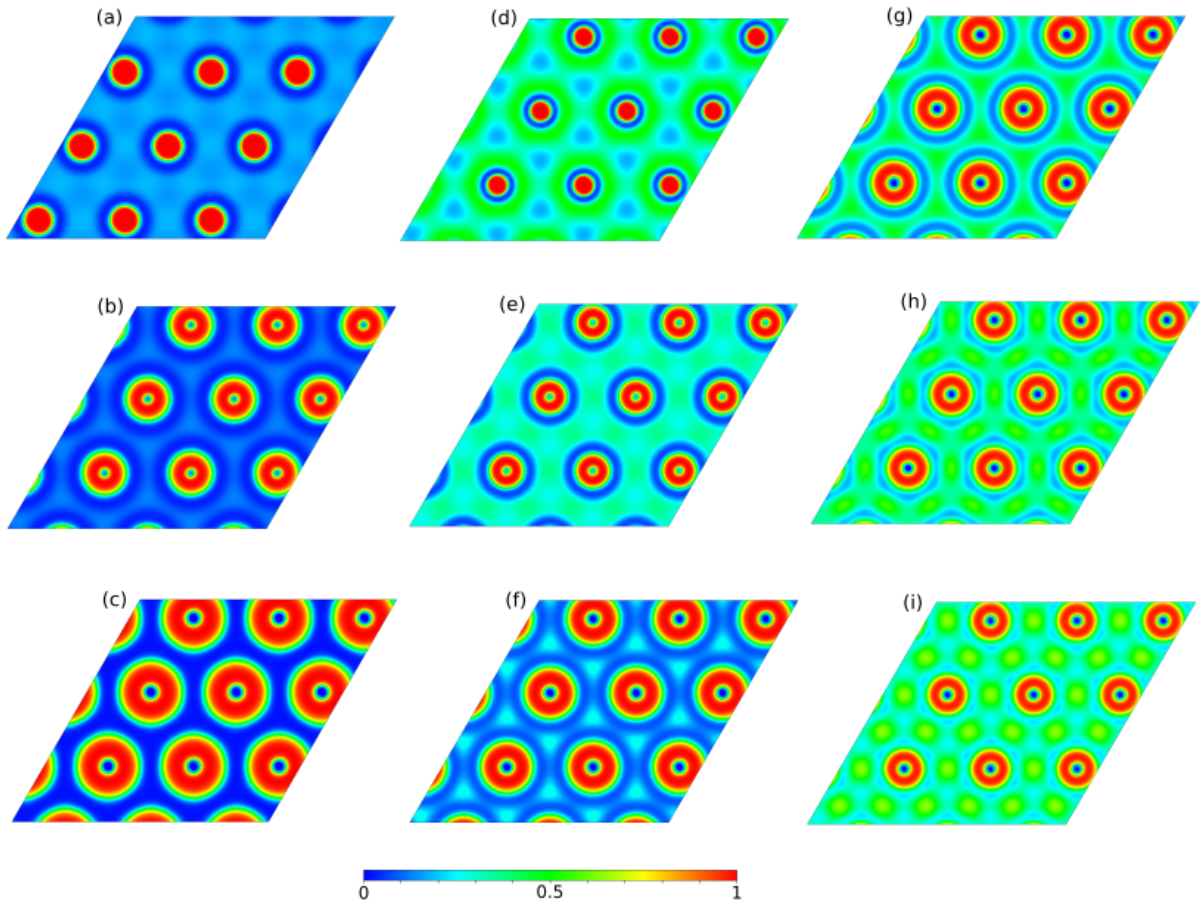


Figure 4.28: Two-dimensional (2D) maps of electron localization function (ELF) of kagome bilayer borophene intercalated with (a) Li, (b) Na, (c) K, (d) Be, (e) Mg, (f) Ca, (g) Sc, (h) Ti, (i) V, along a plane that intersects the intercalated atoms.

Although the δ_4 and kagome structures contain the same number of boron atoms per unit cell, their differing crystal symmetries lead to distinct local structural and electronic properties, especially upon intercalation. In the δ_4 phase, considerable buckling B layers occurs due to stronger bonding between alkaline-earth and transition metal intercalants with B_2 atoms compared with B_1 atoms. In contrast, the kagome phase, composed of a single atomic type, remains flat, as no such differential bonding takes place. Consequently, charge transfer in the

δ_4 phase is nonuniform, leading to variations in bond strength, whereas in the kagome phase, charge transfer is evenly distributed, as visible from *electron localization function* (ELF) plots in Figure 4.28. These structural differences result in opposite trends in T_c^{iso} as a function of the average interlayer distance, as depicted in Figure 4.26(c). A notable distinction between the two phases lies in their correlation between T_c^{iso} and the DOS contribution at the Fermi level, which is evident for kagome but absent for δ_4 phase. This trend is exemplified for kagome phase when using Ca as intercalant, exhibiting the highest DOS contribution among the $\eta = 1/4$ phases, primarily stemming from B- p_z and B- σ orbitals, and consequently reaching the highest T_c^{iso} value of 27 K.

Next, we focus on the superconducting properties of the Be-intercalated δ_4 phase. This configuration exhibits a remarkable Fermi surface, depicted in Figure 4.23(b), characterized by multiple elongated parallel segments that demonstrate pronounced nesting effects, especially along the Γ - X path. To gain deeper insight into the role of nesting, we computed the nesting function,

$$F_{\text{Nesting}} = \sum_{kij} \delta(E_{\mathbf{k},i} - E_F) \delta(E_{\mathbf{k},i} - E_{\mathbf{k}+\mathbf{q},j}), \quad (4.2)$$

where i and j denote band indices. The function exhibits pronounced maxima at specific $|\mathbf{q}|$ values when a substantial number of momentum vectors \mathbf{q} satisfy the constraints imposed by the δ -functions. This occurs in the presence of nearly parallel Fermi surface segments, a characteristic feature of what is termed *nesting*. The obtained result, presented in Figure 4.29, clearly demonstrates the presence of nesting along multiple high-symmetry directions. Notably,

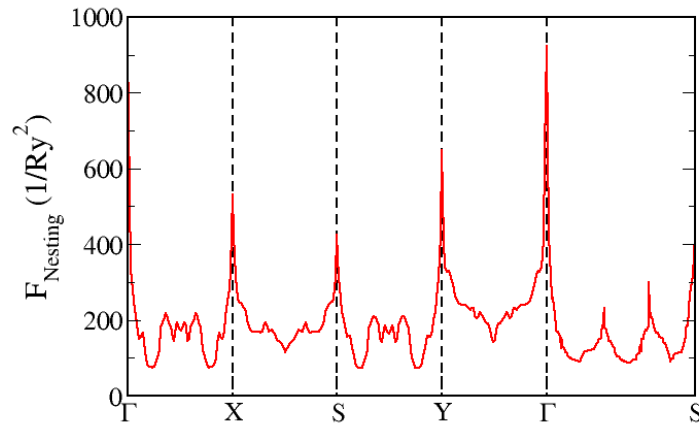


Figure 4.29: Nesting function of Be-intercalated bilayer δ_4 borophene, as obtained from EPW calculations.

the pronounced features in the nesting function along Γ - X align with the softening observed in the phonon dispersion, as depicted in Figure 4.30(a), indicating a direct correlation between

nesting features and lattice dynamics. Nevertheless, there is no CDW associated with the nesting, as we found that all the phonon modes are completely stable. In **APPENDIX A5** one can see that the phonon dispersion of Be-intercalated bilayer δ_4 borophene does not change with lower smearing widths of 0.01, 0.005 and 0.0025 Ry. Also, there is a dip in the phonon dispersion along Γ - X path but it does not evolve to an instability at low smearing values (0.0025 Ry). This indicates that there is no lattice instability like a CDW due to e - ph interaction, hence we do not expect competition with the superconducting state. Quite the contrary, the presence of a stable phonon softening contributes positively to the e - ph coupling, and strengthens the superconducting state.

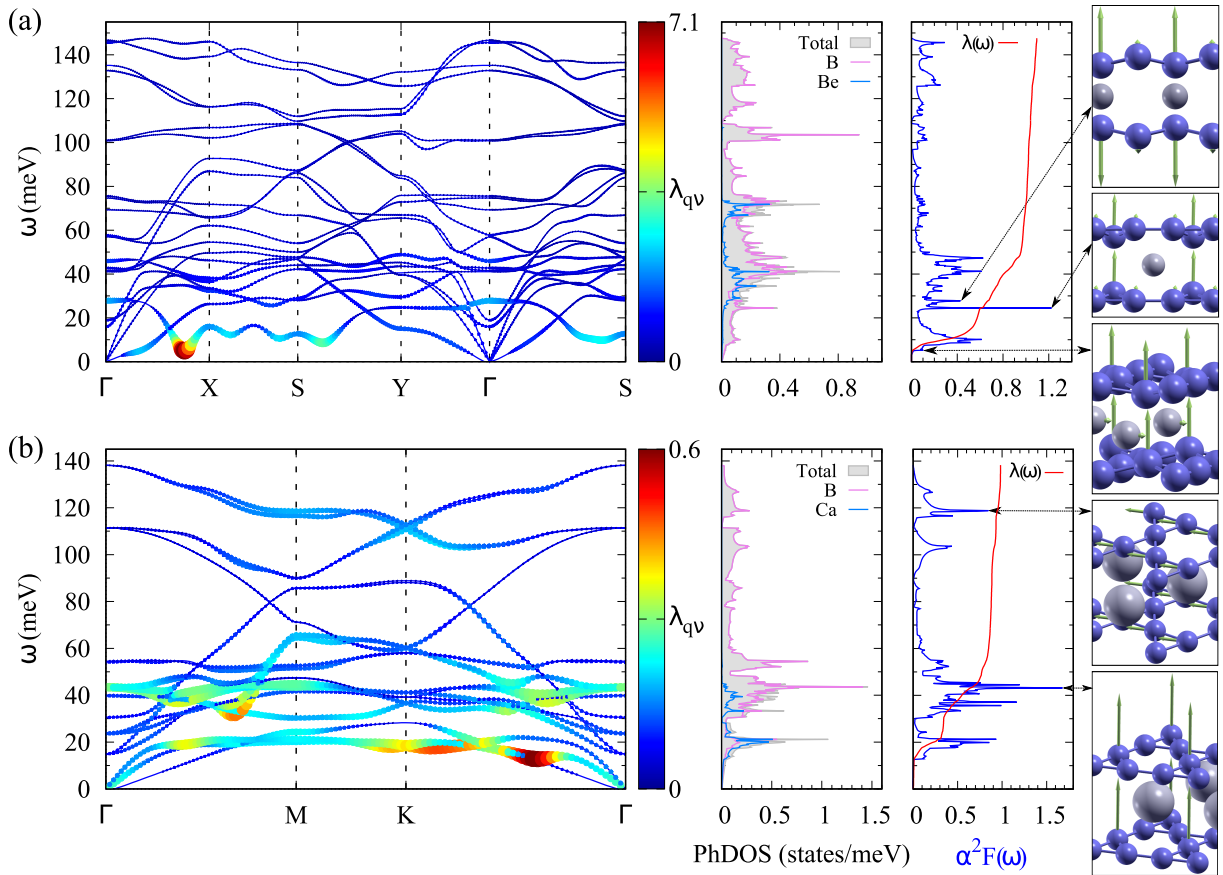


Figure 4.30: The phonon dispersion, atom-resolved PhDOS and the $\alpha^2 F(\omega)$ function, which exhibits peaks corresponding to phonon modes that strongly couple to electrons, are shown for (a) Be- δ_4 , and (b) Ca-kagome intercalated bilayer configurations. The phonon branches (ν) and q -resolved e - ph coupling (λ_{qv}) are represented using color scales and point sizes proportional to λ .

At first glance, this unexpectedly pronounced softening is observed for a specific phonon branch belonging to the A_1 representation of the C_{2V} point group. This branch exhibits multiple dips, which play a crucial role in shaping the Eliashberg spectral function, as depicted in Figure 4.30(a). Notably, the initial peak around ~ 5 meV, characterized by a remarkably strong

EPC value of 7.1, as well as the dominant peak near ~ 24 meV, both originate from the same phonon mode. It arises from the in-phase and out-of-plane movement of B_2 atoms, accompanied by small in-plane displacements of the Be atom. The underlying mechanism driving this behavior is the strong interlayer coupling within the borophene structure, facilitated by Be, which establishes a robust interaction with the B_2 atoms. As a direct consequence, the *layer-breathing* mode at Γ undergoes a frequency shift to approximately 28 meV, a notable increase compared with the bare phase χ_3 phase (see Figure 4.24(a)). Moreover, due to the distinct symmetry properties, this mode belongs to the A_g representation of the D_{2h} point group and is optically active in Raman spectroscopy.

A similar trend is observed in Mg- and Ca-intercalated δ_4 bilayers, where the most significant EPC contributions originate from softened phonon modes. However, in the case of Ca, the low-frequency peaks exhibit a reduced impact on the Eliashberg spectral function, resulting in a reduced T_c^{iso} of 5.2, compared to the 8.8 K seen for Mg intercalation.

When examining the superconducting properties of the Ca-intercalated kagome phase, a key feature to highlight is its minimally intersecting Fermi contours (see Figure 4.23(c)), which correlate with its remarkably high superconducting transition temperature T_c^{iso} of 27.1 K – the highest among all considered cases. As shown in Figure 4.30(b), the first peak in the $\alpha^2F(\omega)$ function corresponds to the highest EPC value of 0.6. It is described by the A_g (C_s) mode, characterized by rotational motion of the B atoms, while Ca atoms undergo in-plane oscillations. The most pronounced peak is linked to the nearly flat region in the phonon spectrum near the M point (~ 43 meV), predominantly characterized by the borons out-of-plane vibrational dynamics. At ~ 119 meV, an additional prominent peak emerges, associated with an optical phonon mode driven by the in-plane motion of B atoms. The overall *e-ph* coupling strength for Ca reaches a substantial value ($\lambda = 0.98$), positioning it as the most promising intercalant for enhancing superconductivity in the *kagome-structured* bilayer borophene. Intercalation of kagome bilayers with transition metals leads to a total EPC strength of 0.61 for Sc, markedly surpassing the 0.43 observed for Ti, which directly correlates with their respective T_c^{iso} values of 6.4 K and 2.0 K. In conclusion, consistent with trends observed for the β_{12} and χ_3 phases, the highest T_c^{iso} values in these configurations are achieved through intercalation of alkaline-earth elements – specifically, Be in δ_4 and Ca in the kagome phase.

4.2.3 Anisotropic ME theory applied to promising candidates

Given the pronounced anisotropy of the Fermi surfaces shown in Figure 4.23, we have conducted fully anisotropic ME calculations to achieve a comprehensive characterization of the superconducting behavior of the most promising candidates. A detailed summary of these findings is presented in Figure 4.31.

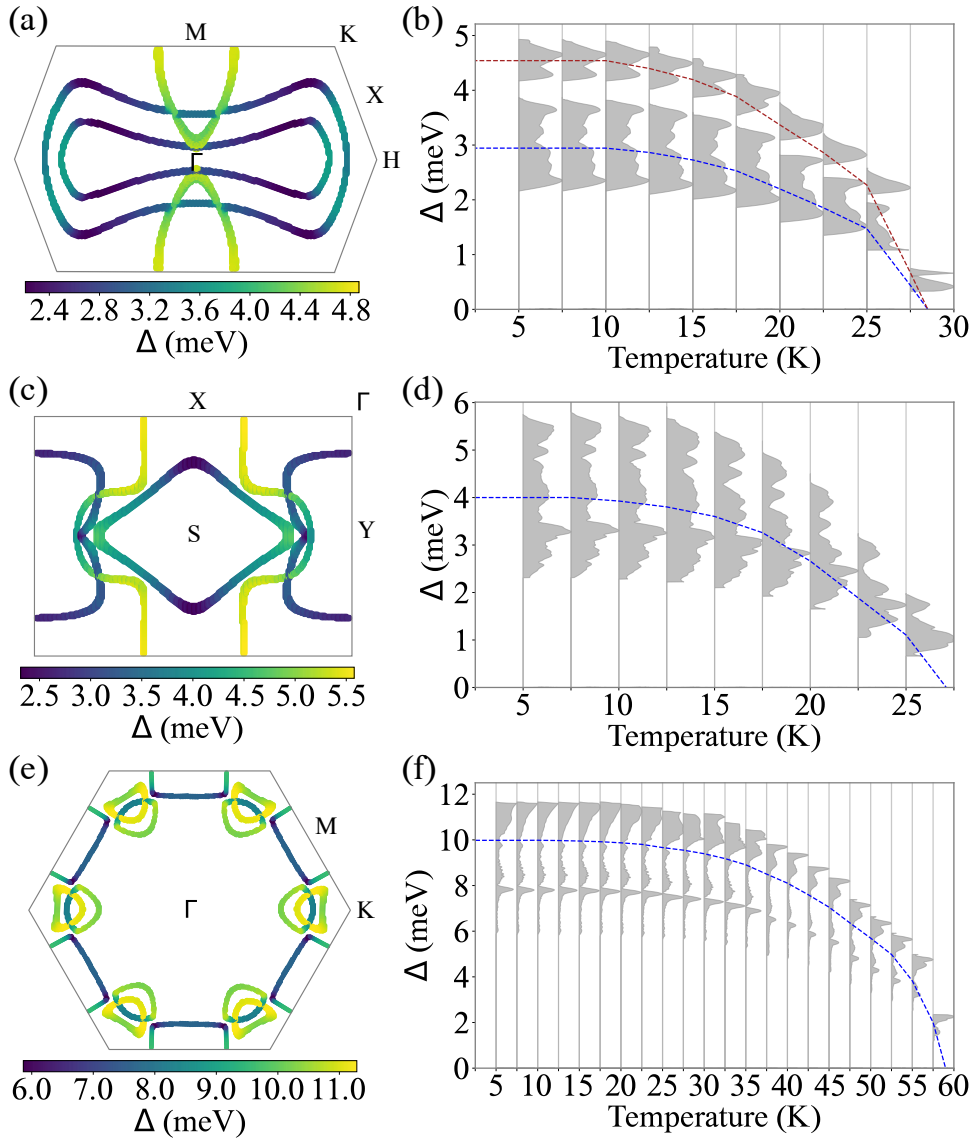


Figure 4.31: Superconducting gap distribution across the Fermi surface at 5 K, along with its temperature dependence, with weighted averages (dashed blue line), for (a,b) Mg in χ_3 , (c,d) Be in δ_4 , and (e,f) Ca in kagome bilayer borophene, respectively.

The Fermi surface of the Mg-intercalated bilayer χ_3 borophene, depicted in Figure 4.31(a), is composed of multiple intersecting contours. Among them, the ellipsoidal B- σ Fermi sheets along the Γ -M direction exhibit the most pronounced superconducting gap values within the anisotropic gap spectrum, $\Delta(\mathbf{k})$. At low temperatures, the gap associated with B- σ states reaches

4.9 meV, whereas the gap originating from B- p_z and Mg- s states displays significant anisotropy, varying between 2.2 and 3.9 meV. This distinct disparity gives rise to a characteristic of two-gap superconducting state. By solving the anisotropic ME equations across different temperatures, we determine an anisotropic superconducting transition temperature (T_c^{aniso}) of 28.5 K for this system (see Figure 4.31(b)).

In the case of Be-intercalated bilayer δ_4 borophene, the hybridization of distinct electronic states gives rise to overlapping superconducting gaps across the Fermi surface, exhibiting an anisotropic single-gap character, as illustrated in Figure 4.31(c). At low temperatures, the superconducting gap $\Delta(\mathbf{k})$ reaches a maximum value of 5.6 meV, predominantly along the Γ - X direction, where strong nesting effects are present. This enhancement is driven by the significant mixing of B- p_z and Be- s states. In contrast, the Fermi contour near the S point, which is largely composed of B- p_z states, contributes only marginally to $\Delta(\mathbf{k})$, while the segment along Γ - Y , dominated by B- σ states, exhibits a similarly weak influence. As determined from the anisotropic ME formalism, the corresponding T_c^{aniso} is 27 K, as depicted in Figure 4.31(d).

Ultimately, the most promising candidate for high-temperature superconductivity among the examined structures is the Ca-intercalated bilayer kagome borophene. This material exhibits a single, highly anisotropic superconducting gap, reaching the maximum of 11.4 meV at low temperatures, as shown in Figure 4.31(e). The dominant gap contribution originates from B- σ states along Γ - K , whereas a smaller one along Γ - M arises from hybridized B- p_z and Ca- s states. Figure 4.31(f) shows that the calculated T_c^{aniso} reaches 58 K, making Ca-intercalated bilayer kagome borophene the strongest superconducting candidate among the examined compounds.

4.2.4 Conclusions

In conclusion, we have conducted a comprehensive first-principles investigation into boron-based 2D superconductors, focusing on metal-intercalated bilayer borophene structures. Our study systematically explores four distinct bilayer phases – β_{12} , χ_3 , δ_4 , and kagome – while considering nine different intercalant elements to assess their impact on superconducting properties. To systematically compare the superconducting properties across these materials, we utilized the isotropic Eliashberg framework in conjunction with first-principles calculations of their electronic and vibrational properties. Through this approach, we identified a total of seventeen potential superconductors, exhibiting a broad spectrum of electronic and vibrational properties, with T_c^{iso} reaching up to 27.1 K.

Among all the examined structures, the intercalated β_{12} phase is unique in having nearly fully occupied σ states, separated by an energy gap from the σ^* states. As a result, their contribution at the Fermi level is minimal, leaving the metallic behavior predominantly governed by p_z orbitals. This significantly suppresses the $e-ph$ coupling strength, ultimately constraining the T_c^{iso} to a low range of 0.1–1 K.

In contrast, the χ_3 phase exhibits a metallic behavior driven by both in-plane σ states and out-of-plane p_z orbitals, a consequence of the inherently greater electron deficiency in χ_3 monolayers. This leads to a more substantial contribution of σ states at the Fermi level, enhancing $e-ph$ coupling and resulting in significantly higher T_c^{iso} , which span from 9.1 to 17.3 K – markedly exceeding those found in the β_{12} phase.

For phases with $\eta = 1/4$, specifically δ_4 and kagome, the electron deficiency increases further, leading to a well-defined gap between bonding and anti-bonding out-of-plane states. Only intercalants from the alkaline-earth and transition metal groups supply adequate charge transfer to the borophene layers, ensuring their structural stability. Moreover, the enhanced presence of σ states at the Fermi level strengthens the $e-ph$ interaction, culminating in T_c^{iso} as high as 27.1 K, as observed in the Ca-intercalated kagome bilayer.

Our findings indicate that the simultaneous stabilization of out-of-plane electronic states and a substantial contribution of σ states at the Fermi level – crucial for strong coupling with in-plane vibrational modes – leads to enhanced T_c^{iso} . Additionally, we observed a general trend where an increased contribution of B- σ orbitals to the DOS at E_F tends to limit $e-ph$ coupling from phonon modes above approximately 50 meV, as reflected in the Eliashberg spectral function. A notable exception arises in the case of transition-metal intercalants, where d orbitals play a dominant role in modifying the coupling strength. Moreover, a direct correlation emerges between higher η values and elevated T_c^{iso} , reinforcing the importance of charge transfer and electronic structure in optimizing superconducting properties.

Building on the identified trends in superconducting behavior across various intercalated borophene bilayers, we have conducted a more *in-depth* analysis of the underlying electronic mechanisms by incorporating anisotropic and multiband effects through fully anisotropic ME calculations for most promising compounds. This approach underscores the critical role of Fermi surface anisotropy, which not only drives the two-gap nature of Mg-intercalated bilayer χ_3 borophene but also enhances superconducting transition temperatures, reaching up to 58 K in the case of Ca-intercalated kagome bilayer borophene. A promising avenue for future

exploration involves accounting for anharmonic effects, which are anticipated to be particularly significant for systems incorporating lighter elements. Additionally, unlike their monolayer counterparts, these functionalized bilayer borophenes exhibit greater chemical stability and resistance to environmental degradation, including oxidation. Given the emergence of robust superconductivity and high T_c values, especially in alkaline-earth-metal-intercalated phases, our findings position bilayer borophenes as compelling candidates for advancing boron-based 2D superconducting materials and technologies.

- **Publication:** Božidar N. Šoškić, Jonas Bekaert, Cem Sevik, Željko Šljivančanin, and Milorad V. Milošević. First-principles exploration of superconductivity in intercalated bilayer borophene phases. *Physical Review Materials*, 8:064803, 2024.

- <https://link.aps.org/doi/10.1103/PhysRevMaterials.8.064803>

CONCLUSIONS

In this thesis, we have employed an extensive first-principles investigation into the magnetic and superconducting properties of boron-based 2D materials, with a particular focus on bare(hydrogenated) monolayer and bare(metal-intercalated) bilayer configurations. Our work provides crucial insights into the mechanisms governing magnetism and superconductivity in these systems, offering new perspectives for their potential applications in spintronics and *next-generation* superconducting devices.

A key finding of our first study is the identification of borophene as a *promising platform for stabilizing 2D magnetic nanostructures*. We demonstrated that Fe atoms preferentially bind to the hollow sites (HH) of β_{12} borophene on Ag(111) substrate, forming well-ordered chain-like nanostructures. Our SDFT calculations and Monte Carlo (MC) simulations revealed that these Fe-based 2D systems exhibit less pronounced antiferromagnetic coupling between chains, with stronger ferromagnetic interactions within each chain. However, the calculated Curie temperatures (T_c) remain below room temperature, suggesting that further optimization, such as substituting Fe with Co, may enhance the magnetic stability.

We further explored the microscopic origin of magnetism in dynamically stable Mn-intercalated bilayer β_{12} borophene, where Mn still retains some magnetic moment ($1 \mu_B$). Using advanced theoretical frameworks such as the four-state (4SM) and the TB2J method, we characterized the exchange interactions governing the system's magnetic behavior. Our results reveal a dominant superexchange interaction mediated by boron p_z orbitals, highlighting the fundamental role of electronic properties in determining magnetic order in borophene-based materials.

This thesis makes also significant contributions to the understanding of the *superconducting nature* of borophenes, extending beyond study of magnetic properties, by using DFPT and anisotropic Migdal-Eliashberg framework. We demonstrate that bare β_{12} borophene is

dynamically unstable and does not exhibit intrinsic superconductivity – challenging all prior reports – while also providing a *rationale* for the absence of experimental evidence confirming superconductivity in these systems. The primary cause of this behavior is the reduced B- σ state contribution to the DOS at E_F under biaxial tensile strain. However, hydrogenated borophene (borophane) emerges as a promising alternative, exhibiting enhanced stability and superconducting properties. Notably, through strain engineering (along the hydrogenated bridges) or hole doping, *borophane* achieves a critical temperature (T_c) of up to 30 K, primarily due to the combined increased contributions of B- σ and B- p_z states to the DOS at E_F .

Additionally, our another study systematically investigated intercalated bilayer borophenes, identifying seventeen potential superconductors across four distinct borophene phases (β_{12} , χ_3 , δ_4 , and kagome) with intercalants from the group of alkali, alkaline-earth, and transition metals. Some of these systems exhibit intriguing physical properties, including notable nesting effects, multi-gap behavior, and van Hove singularities, among others. The Ca-intercalated kagome bilayer emerged as a particularly promising candidate, exhibiting a T_c of up to 58 K, driven by strong *e-ph* coupling and favorable anisotropic electronic structure. The interplay of charge transfer and the balance of in- and out-of-plane boron electronic states was found to be crucial in optimizing superconducting properties, reinforcing the potential of boron-based 2D materials for fabrication of superconducting nano-devices.

In conclusion, the functionalized borophene structures investigated in this work represent the only known phases to date that exhibit resistance to oxidation while preserving their intrinsic physical properties. This exceptional stability not only enhances their practical viability but also positions borophene as a promising platform for the stabilization of 2D magnetic materials, with potential implications for spintronic applications. Furthermore, hydrogenated borophene (borophane) emerges as a strong contender for superconductivity, offering a possible resolution to the long-standing debate on whether borophene can intrinsically exhibit this phenomenon. These findings pave the way for the controlled design of tunable 2D superconductors and open new directions for future explorations in low-dimensional quantum materials.

A1: Wannier transformations and WANNIER90 code

Wannier90 is an open-source software package that generates maximally localized Wannier functions (MLWFs) from Bloch states derived from first-principles calculations. It primarily utilizes the method developed by Marzari and Vanderbilt [306]. For systems with entangled energy bands, it applies the approach introduced by Souza, Marzari, and Vanderbilt [307]. A brief overview of these methods and key definitions are provided here, with full details available in the original references, as well as in Ref. [308].

The electronic structure of periodic crystalline solids is commonly described using extended Bloch states, $\psi_{n\mathbf{k}}$. However, an alternative representation can be obtained by transforming these extended Bloch orbitals into spatially localized functions known as Wannier functions (WF). These WFs, denoted as $w_n(\mathbf{r} - \mathbf{R})$, are defined through a unitary transformation of the Bloch orbitals and are labeled according to both the band index n and the lattice vector \mathbf{R} , which corresponds to the unit cell they belong to. Therefore, the WFs given in terms of the Bloch functions are defined as:

$$w_n(\mathbf{r} - \mathbf{R}) = |\mathbf{R}_n\rangle = \frac{V}{(2\pi)^3} \int_{BZ} d\mathbf{k} e^{-i\mathbf{k}\mathbf{R}} |\psi_{n\mathbf{k}}\rangle, \quad (5.1)$$

forming an orthonormal set, where $|\psi_{n\mathbf{k}}\rangle = \sum_{\mathbf{R}} e^{i\mathbf{k}\mathbf{R}} w_n(\mathbf{r} - \mathbf{R})$, and V is the real-space primitive cell. One can then easily obtain the matrix elements of the position operator between WFs:

$$\langle \mathbf{R}_n | \mathbf{r} | \mathbf{0}_m \rangle = i \frac{V}{(2\pi)^3} \int_{BZ} d\mathbf{k} e^{-i\mathbf{k}\mathbf{R}} \langle u_{n\mathbf{k}} | \nabla_{\mathbf{k}} | u_{m\mathbf{k}} \rangle. \quad (5.2)$$

In same way, after some algebra, one can obtain:

$$\langle \mathbf{R}_n | \mathbf{r}^2 | \mathbf{0}_m \rangle = -\frac{V}{(2\pi)^3} \int_{BZ} d\mathbf{k} e^{-i\mathbf{k}\mathbf{R}} \langle u_{n\mathbf{k}} | \nabla_{\mathbf{k}}^2 | u_{m\mathbf{k}} \rangle. \quad (5.3)$$

Now, using the notation $\bar{\mathbf{r}}_n = \langle \mathbf{0}_n | \mathbf{r} | \mathbf{0}_n \rangle$, and $\bar{r}_n^2 = \langle \mathbf{0}_n | \mathbf{r}^2 | \mathbf{0}_n \rangle$ the diagonal elements are defined as:

$$\left\{ \begin{array}{l} \bar{\mathbf{r}}_n = i \frac{V}{(2\pi)^3} \int_{BZ} d\mathbf{k} \langle u_{n\mathbf{k}} | \nabla_{\mathbf{k}} | u_{n\mathbf{k}} \rangle, \\ \bar{r}_n^2 = \frac{V}{(2\pi)^3} \int_{BZ} d\mathbf{k} |\nabla_{\mathbf{k}} | u_{n\mathbf{k}} \rangle|^2. \end{array} \right. \quad (5.4)$$

$$\left\{ \begin{array}{l} \bar{\mathbf{r}}_n = i \frac{V}{(2\pi)^3} \int_{BZ} d\mathbf{k} \langle u_{n\mathbf{k}} | \nabla_{\mathbf{k}} | u_{n\mathbf{k}} \rangle, \\ \bar{r}_n^2 = \frac{V}{(2\pi)^3} \int_{BZ} d\mathbf{k} |\nabla_{\mathbf{k}} | u_{n\mathbf{k}} \rangle|^2. \end{array} \right. \quad (5.5)$$

However, WFs are inherently non-unique. For a single isolated band, this non-uniqueness arises from the arbitrary choice of phase for Bloch orbitals across different wave vectors \mathbf{k} . Consequently, an alternative set of WFs can be generated by modifying the phase of the Bloch states while preserving their validity $|u_{n\mathbf{k}}\rangle \rightarrow e^{i\phi_n} |u_{n\mathbf{k}}\rangle$. This transformation is valid only for $\bar{\mathbf{r}}_n$ but not for the spread of WF $\langle r^2 \rangle_n - \bar{r}_n^2$. In the context of composite energy bands, the freedom in choosing WFs corresponds to the ability to apply a unitary transformation among the Bloch states at each wave vector \mathbf{k} . Specifically, the Bloch states can be transformed as $|u_{n\mathbf{k}}\rangle \rightarrow \sum_m U_{mn}^{\mathbf{k}} |u_{m\mathbf{k}}\rangle$, where $U_{mn}^{\mathbf{k}}$ is a unitary matrix that mixes the Bloch functions corresponding to different bands at the same \mathbf{k} -point. This freedom is often referred to as ‘‘gauge freedom’’, and the corresponding transformations are known as ‘‘gauge transformation’’. Now the main objective is to select from the set of potential WFs, the one that is most localized based on a given criterion. In order to do so, one needs to quantify the overall delocalization of the WFs, which is defined through spread functional as:

$$\Omega = \sum_n [\langle r^2 \rangle_n - \bar{r}_n^2]. \quad (5.6)$$

The main goal is to minimize the equation (5.6) with respect to this unitary transformations $U_{mn}^{\mathbf{k}}$. Therefore it is convenient to decompose Ω in:

$$\Omega = \underbrace{\sum_n \left[\langle r^2 \rangle_n - \sum_{\mathbf{R}_m} |\langle \mathbf{R}_m | \mathbf{r} | \mathbf{0}_n \rangle|^2 \right]}_{\Omega_I} + \underbrace{\sum_n \sum_{\mathbf{R}_m \neq \mathbf{0}_n} |\langle \mathbf{R}_m | \mathbf{r} | \mathbf{0}_n \rangle|^2}_{\tilde{\Omega}}, \quad (5.7)$$

where $\tilde{\Omega}$ is positive definite, while Ω_I is positive definite and gauge invariant. Additionally, the

$\tilde{\Omega}$ can be further decomposed in off-diagonal and diagonal terms:

$$\tilde{\Omega} = \overbrace{\sum_{m \neq n} \sum_{\mathbf{R}} |\langle \mathbf{R}_m | \mathbf{r} | \mathbf{0}_n \rangle|^2}^{\tilde{\Omega}_{OD}} + \overbrace{\sum_n \sum_{\mathbf{R} \neq \mathbf{0}} |\langle \mathbf{R}_n | \mathbf{r} | \mathbf{0}_n \rangle|^2}^{\tilde{\Omega}_D}. \quad (5.8)$$

Wannier90 relies on two key inputs from an initial electronic structure calculation: (i) the overlap matrices $M_{mn}^{\mathbf{k},\mathbf{b}} = \langle u_{m\mathbf{k}} | u_{n,\mathbf{k}+\mathbf{b}} \rangle$ between the cell-periodic components of the Bloch states $|u_{n\mathbf{k}}\rangle$, where \mathbf{b} are vectors linking each \mathbf{k} -point to its nearest neighbors, and (ii) an initial *projection* guess provided by projecting the Bloch states $|\psi_{n\mathbf{k}}\rangle$ onto a set of trial localized orbitals $|g_n\rangle$, defined as $A_{mn}^{\mathbf{k}} = \langle \psi_{m\mathbf{k}} | g_n \rangle$. After some algebra, one obtains:

$$\left\{ \begin{array}{l} \Omega_I = \frac{1}{N} \sum_{\mathbf{k},\mathbf{b}} \omega_b \left(N_{bands} - \sum_{mn} |M_{mn}^{\mathbf{k},\mathbf{b}}|^2 \right) \end{array} \right. \quad (5.9)$$

$$\left\{ \begin{array}{l} \tilde{\Omega}_{OD} = \frac{1}{N} \sum_{\mathbf{k},\mathbf{b}} \omega_b \sum_{m \neq n} |M_{mn}^{\mathbf{k},\mathbf{b}}|^2, \end{array} \right. \quad (5.10)$$

$$\left\{ \begin{array}{l} \tilde{\Omega}_D = \frac{1}{N} \sum_{\mathbf{k},\mathbf{b}} \omega_b \sum_n \left(-\text{Im} \ln M_{nn}^{\mathbf{k},\mathbf{b}} - \mathbf{b} \cdot \bar{\mathbf{r}}_n \right)^2, \end{array} \right. \quad (5.11)$$

where N represents the number of cells in the system, and ω_b the corresponding weights. Using equation (5.9–5.11), we determine the variation in the localization functional Ω under an infinitesimal unitary transformation of the Bloch states ($U_{mn} = \delta_{mn} + dW_{mn}$) as a function of $M_{mn}^{\mathbf{k},\mathbf{b}}$. Once these gradients are obtained, an optimization procedure is implemented to iteratively update $U_{mn}^{\mathbf{k}}$, guiding the WFs towards maximal localization (MLWF). The minimization begins with a reference set of Bloch orbitals $|u_{n\mathbf{k}}\rangle$ derived from the initial first-principles calculation, after which the necessary quantities are computed (once and for all):

$$\left\{ \begin{array}{l} M_{mn}^{(0)\mathbf{k},\mathbf{b}} = \langle u_{m\mathbf{k}}^{(0)} | u_{n,\mathbf{k}+\mathbf{b}}^{(0)} \rangle, \end{array} \right. \quad (5.12)$$

$$\left\{ \begin{array}{l} |u_{n\mathbf{k}}\rangle = \sum_m U_{mn}^{(\mathbf{k})} |u_{m\mathbf{k}}^{(0)}\rangle. \end{array} \right. \quad (5.13)$$

By initializing all U_{mn} to δ_{mn} , the *steepest-descent procedure* is performed by calculating ΔW for a small step in the direction opposite to the gradient. The unitary matrices are updated as:

$$U^{(\mathbf{k})} \rightarrow U^{(\mathbf{k})} \exp [\Delta W^{(\mathbf{k})}], \quad (5.14)$$

after which a new set of M matrices is computed:

$$M_{mn}^{\mathbf{k},\mathbf{b}} = U^{(\mathbf{k})\dagger} M_{mn}^{(0)\mathbf{k},\mathbf{b}} U^{(\mathbf{k})}. \quad (5.15)$$

To avoid the presence of artificial “unphysical” local minima in the localization functional, an initial set of reference Bloch orbitals $|u_{n\mathbf{k}}^{(0)}\rangle$ is prepared by projecting them from a rough guess of trial orbitals $g_n(\mathbf{r})$ (initial guess for the WFs), which are then projected onto the Bloch manifold at wavevector \mathbf{k} :

$$|\phi_{n\mathbf{k}}\rangle = \sum_m |\psi_{m\mathbf{k}}\rangle \overbrace{\langle \psi_{m\mathbf{k}} | g_n \rangle}^{A_{mn}^{\mathbf{k}}}. \quad (5.16)$$

To construct MLWFs for an isolated set of bands, such as valence states in insulators, the standard procedure suffices. However, for entangled bands, a *disentanglement* approach is required. This involves defining an *outer energy window* containing $N_{win}^{(\mathbf{k})}$ Bloch states at each \mathbf{k} -point and performing a unitary transformation among them:

$$|u_{n\mathbf{k}}^{opt}\rangle = \sum_{m \in N_{win}^{(\mathbf{k})}} U_{mn}^{dis(\mathbf{k})} |u_{m\mathbf{k}}\rangle, \quad (5.17)$$

where $U_{mn}^{dis(\mathbf{k})}$ is a rectangular $N_{win}^{(\mathbf{k})} \times N$ matrix determined by minimizing the gauge-invariant spread Ω_I . The procedure then further minimizes $\tilde{\Omega}$ to obtain MLWFs. Since this process mixes states in optimal subspace, the resulting bands may not directly correspond to the original ones. To retain exact properties in a specific energy range (e.g., near the Fermi level), a second “frozen” energy window is introduced, ensuring that states within it remain unchanged.

A2: Technical details for section 3.1

First-principles calculations were performed utilizing the QUANTUM ESPRESSO software package [233], which operates on the basis of plane-wave expansions and pseudopotentials. The electronic wave functions and charge density were expanded with energy cutoffs set to 45 Ry and 300 Ry, respectively. The exchange-correlation interactions were treated within the generalized gradient approximation (GGA) using the Perdew-Burke-Ernzerhof (PBE) functional [229]. To determine electronic occupancies, the Methfessel-Paxton (MP) smearing method [231] was applied, with the width of 0.03 eV. A three-layer slab structure was adopted, incorporating a vacuum spacing of at least 20 Å to eliminate interactions between periodic images. Structural

relaxations were carried out using the Broyden-Fletcher-Goldfarb-Shanno (BFGS) algorithm, ensuring that atomic forces were minimized below $0.02 \text{ eV}/\text{\AA}$. Also, Ag atoms in the bottom layer were fixed, while all other B and Ag atoms were permitted to fully relax. The BZ of the (1×1) unit cell was sampled using a dense grid of 256 k -points [230]. For modeling Fe monomers, dimers, trimers, and extended chains, calculations were performed within a 4×2 surface cell, adjusting the k -point mesh to maintain consistency with the (1×1) unit cell simulations. The MAE of Fe-based nanostructures, required for extracting SIA constants, was determined using the WIEN2K software package [235]. The MAE was computed using the force theorem approach, which extracts the difference in band energies for two distinct magnetization orientations: (i) *easy axis* (normal to the Ag crystal), and (ii) *hard axis* (in the plane of Fe chains). In modeling the freestanding B-2D layer and its Ag(111)-supported counterpart, the (1×1) surface unit cell was periodically replicated across the 2D plane, as illustrated in Figure 3.1(a). The Monte Carlo (MC) computations were executed on a 100×100 square lattice, incorporating periodic boundary conditions. The Metropolis algorithm was used for spin updates, with the system initially equilibrated over 100 000 MC steps per site, followed by an additional 100 000 steps per site for computing temperature-dependent magnetization. To enhance statistical accuracy, this process was repeated 20 times, and therefore average values were presented.

A3: Technical details for section 3.2

The VASP *ab initio* simulation package was utilized [234], applying the Perdew-Burke-Ernzerhof (PBE) generalized gradient approximation (GGA) [229] within a plane-wave basis set. Furthermore, all calculations incorporated spin-orbit coupling (SOC). A $24 \times 42 \times 1$ Monkhorst-Pack k -grid was used for all intercalated β_{12} phases. The plane-wave basis set had a kinetic energy cut-off of 750 eV, and the energy convergence criterion was 10^{-8} eV in the ground-state calculations. Methfessel-Paxton second-order smearing of 0.01 eV was used and the pressures on the unit cell were decreased to a value lower than 0.5 KBar in all three directions. Our calculations were performed with a vacuum space of 25 \AA . Phonon calculation were performed using the frozen method as implemented in Phonopy [309]. Also, in order to include on interatomic force constants (IFC) constraints for translational and rotational invariance, ALM force constant calculator was used [310].

A4: Technical details and additional results for section 4.1

In this study, DFT calculations were performed on various borophane polymorphs using the Quantum ESPRESSO software package [233], with the PBE functional revised for solids. Applying the resources offered by the PseudoDojo project [311], this study includes norm-conserving pseudopotentials, where the wave functions and electron density were expanded using a plane-wave basis, with cutoff energies of 120 Ry and 480 Ry, respectively. To obviate the pernicious influence of periodic image interaction, a spatial expanse of 20 Å was incorporated into the system as a vacuum region. After performing convergence analysis of the phonon calculations, a Monkhorst-Pack wave-vector grid of $30 \times 21 \times 1$ was selected for integration over the k BZ during the self-consistent charge density calculation, and the electronic states were occupied by using a Methfessel-Paxton smearing value of 0.0025 Ry. Each structure was fully optimized until the Hellmann-Feynman forces acting on the atoms were reduced to below 10^{-5} Ry/Bohr. In a comprehensive analysis, the dynamical properties of the system – at the harmonic level – were explored via DFPT, wherein phonon-vector analysis was undertaken using a $10 \times 7 \times 1$ q -grid. To glean an initial understanding of the superconducting characteristics of the system, we first turned to the isotropic Eliashberg theory, which posits that the phonon line-width can be effectively approximated as

$$\gamma_{ql} = \frac{2\pi\omega_{ql}}{N_{\mathbf{k}}} \sum_{\mathbf{k}\nu\nu'} |g_{\mathbf{k}+\mathbf{q}\nu',\mathbf{k}\nu}^{ql}|^2 \delta(\epsilon_{\mathbf{k}+\mathbf{q}\nu'} - \epsilon_F) \delta(\epsilon_{\mathbf{k}\nu} - \epsilon_F), \quad (5.18)$$

where $\epsilon_{\mathbf{k}\nu}$ is the energy of electron with wave number \mathbf{k} in the band ν , ω_{ql} is the frequency of the phonon with wave number \mathbf{q} in the mode l , ϵ_F is the Fermi energy, $g_{\mathbf{k}+\mathbf{q}\nu',\mathbf{k}\nu}^{ql}$ are the e - ph matrix elements obtained from our *ab initio* calculations, and $N_{\mathbf{k}}$ is the number of \mathbf{k} points in the sum. This equation enabled us to perform additional computations of the Eliashberg e - ph spectral function

$$\alpha^2 F(\omega) = \frac{1}{2\pi N(\epsilon_F) N_{\mathbf{q}}} \sum_{\mathbf{q}l} \frac{\gamma_{\mathbf{q}l}}{\omega_{\mathbf{q}l}} \delta(\omega - \omega_{\mathbf{q}l}), \quad (5.19)$$

where $N(\epsilon_F)$ is DOS contribution at E_F , and $N_{\mathbf{q}}$ is the number of \mathbf{q} -points in the sum. Further, the e - ph coupling (EPC) constant can be calculated using the following formula:

$$\lambda = 2 \int_0^{\infty} \frac{\alpha^2 F(\omega)}{\omega} d\omega. \quad (5.20)$$

The superconducting T_c can be then obtained by solving the Allen-Dynes equation.

To go beyond the isotropic approximation, for some particular cases, we have used the Wannier interpolation methodology for the e - ph coupling constant. For the initial guess of the MLWFs we have used: sp^2 -like, and p_z -like orbitals for B atoms, and s -like orbital for H atom. By employing the proposed methodology within EPW code, the computation of e - ph matrix elements was first executed on coarse \mathbf{k} -, and \mathbf{q} -grid. These were subsequently interpolated onto a finer (denser) $210 \times 147 \times 1$ \mathbf{k} -, and $70 \times 49 \times 1$ \mathbf{q} -grid to accurately infer the appropriate and converged values of e - ph coupling constant λ . To estimate the superconducting gap, we solved the anisotropic Migdal-Eliashberg equations, using the Morel-Anderson pseudopotential value of $\mu^* = 0.1$ and the fermion Matsubara frequencies $\omega_j = (2j + 1)\pi T$ cutoff of 0.6 eV. The reported superconducting critical temperatures were ascertained by pinpointing the temperature at which the superconducting gap values reduce to zero.

Additionally, we investigated the influence of strain as well as uniform charge doping on the superconducting properties. To include the influence of field geometry, the previous doping calculations were revised using the non-uniform doping of the systems - the field-effect transistor (FET) configuration [312]. A vacuum of $L = 35 \text{ \AA}$ was used in the FET setup, as well as the potential energy barrier with a height of $V_0 = 2.5 \text{ Ry}$ and a width of $0.06 \times L$ to emulate the effect of the electrostatic barrier do to the atoms of the gate dielectric.

In our case, FET approach is feasible because applying uniform spatial doping results in only minor changes to the lattice constants. Namely, in a FET setup within QE, the structural relaxation cannot be performed directly. The applied electric field within FET setup induces forces not accounted for in standard relaxation algorithms. Additionally, the changes in lattice constants result in different charge doping per area, therefore inducing new dipole effects and complicating the accurate energy calculations.

We also noted that using the basic acoustic sum rule implemented in QE, the structures remain dynamically stable only up to a uniform/non-uniform hole doping level of 0.03 e/B . Applying the general invariance and equilibrium conditions of the lattice potential, which recover the quadratic dispersion of flexural phonons in low-dimensional materials [278], the non-uniformly doped structures show dynamical stability up to 0.12 e/B hole doping level. As this dedicated acoustic sum rule is not implemented in the EPW package, we were restricted to obtaining the T_c on the isotropic level in the subsequent analysis, using the MAD formula.

To compute phonon dispersion with momentum-resolved e - ph coupling (EPC) visualized

via color mapping, we developed a code that processes outputs from Quantum ESPRESSO for further analysis. Additionally, the figures below present our obtained results, along with the PhDOS, the Eliashberg spectral function, and phonon modes corresponding to its characteristic peaks for the bare and hydrogenated phases, as well as under the effects of strain and doping:

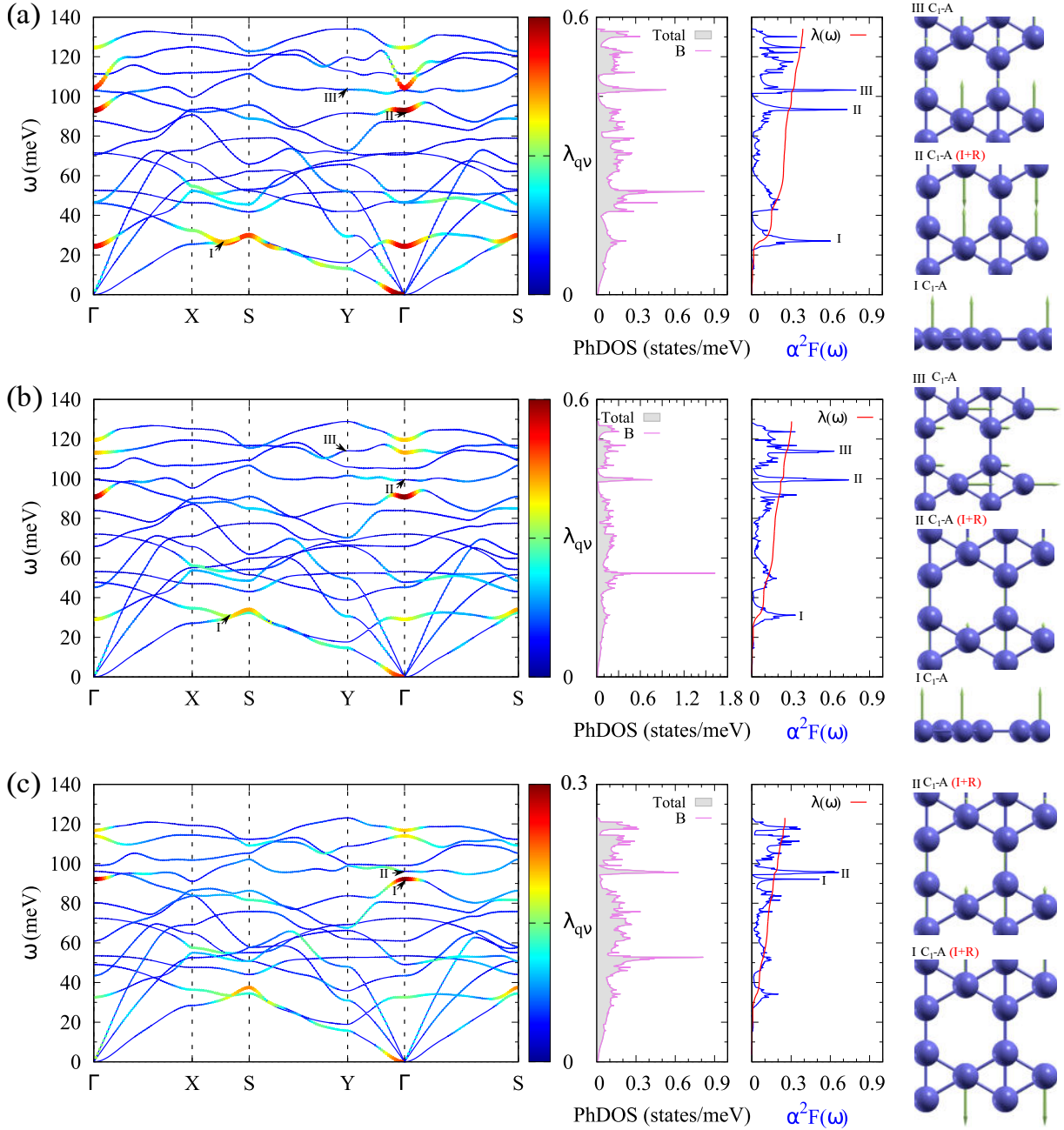


Figure 5.1: The phonon dispersions with q -resolved e - ph coupling ($\lambda_{q\nu}$) using color scales and point sizes proportional to λ , atom-resolved PhDOS and the $\alpha^2 F(\omega)$ function, which exhibits peaks corresponding to phonon modes, are shown for freestanding bare β_{12} borophene by applying biaxial tensile strain of (a) 3%, (b) 4%, and (c) 5%.

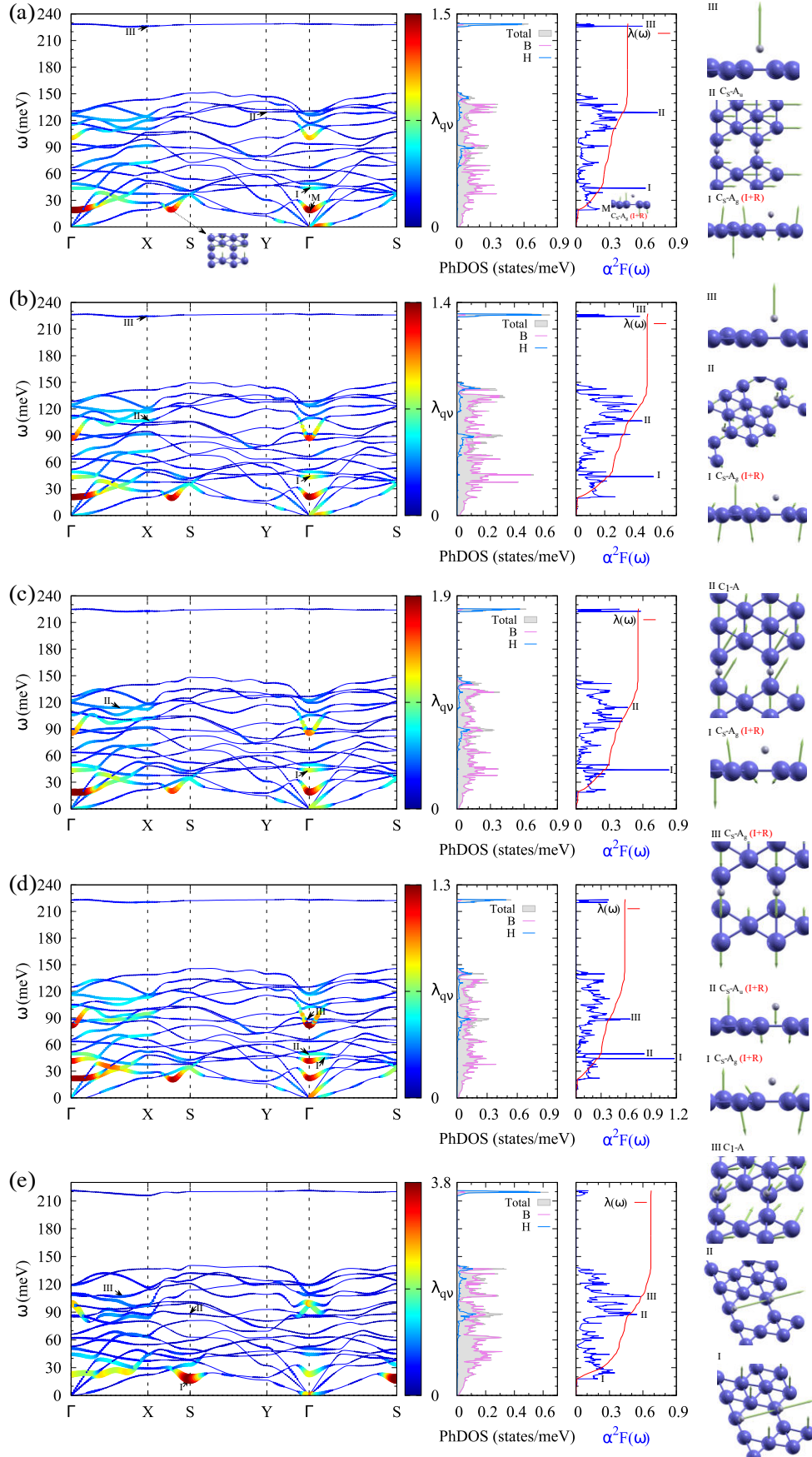


Figure 5.2: The phonon dispersions with q -resolved e -ph coupling ($\lambda_{q\nu}$) using color scales and point sizes proportional to λ , atom-resolved PhDOS and the $\alpha^2 F(\omega)$ function, which exhibits peaks corresponding to phonon modes, are shown for hydrogenated β_{12} borophene by applying tensile strain of $\epsilon_x = 0\%$ and (a) $\epsilon_y = +1\%$, (b) $\epsilon_y = +2\%$, (c) $\epsilon_y = +3\%$, (d) $\epsilon_y = +4\%$, (e) $\epsilon_y = +5\%$.

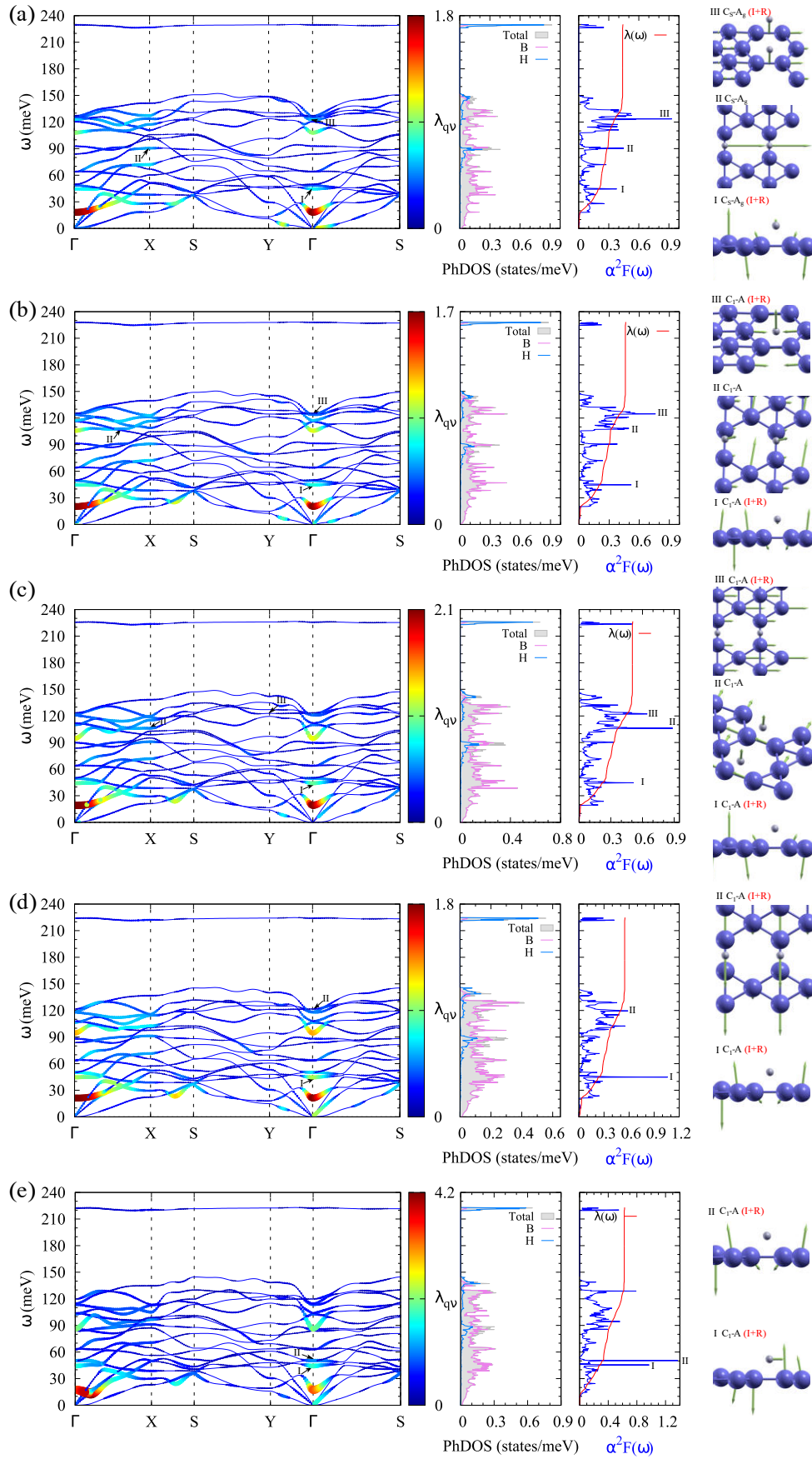


Figure 5.3: The phonon dispersions with q -resolved e - ph coupling (λ_{qv}) using color scales and point sizes proportional to λ , atom-resolved PhDOS and the $\alpha^2 F(\omega)$ function, which exhibits peaks corresponding to phonon modes, are shown for hydrogenated β_{12} borophene by applying tensile strain of $\epsilon_x = +1\%$ and (a) $\epsilon_y = 0\%$, (b) $\epsilon_y = +1\%$, (c) $\epsilon_y = +2\%$, (d) $\epsilon_y = +3\%$, (e) $\epsilon_y = +4\%$.

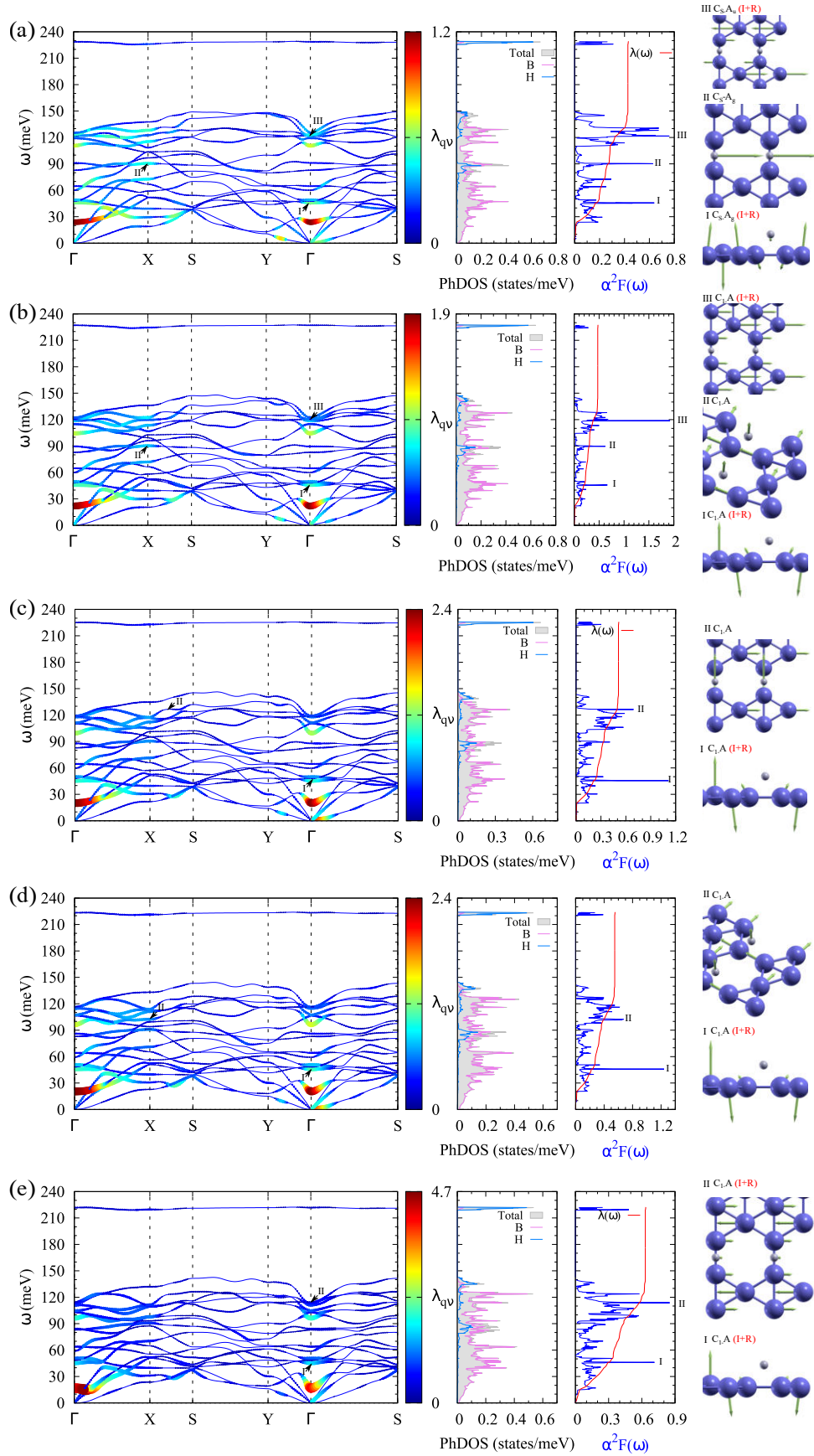


Figure 5.4: The phonon dispersions with q -resolved e -ph coupling (λ_{qv}) using color scales and point sizes proportional to λ , atom-resolved PhDOS and the $\alpha^2 F(\omega)$ function, which exhibits peaks corresponding to phonon modes, are shown for hydrogenated β_{12} borophene by applying tensile strain of $\epsilon_x = +2\%$ and (a) $\epsilon_y = 0\%$, (b) $\epsilon_y = +1\%$, (c) $\epsilon_y = +2\%$, (d) $\epsilon_y = +3\%$, (e) $\epsilon_y = +4\%$.

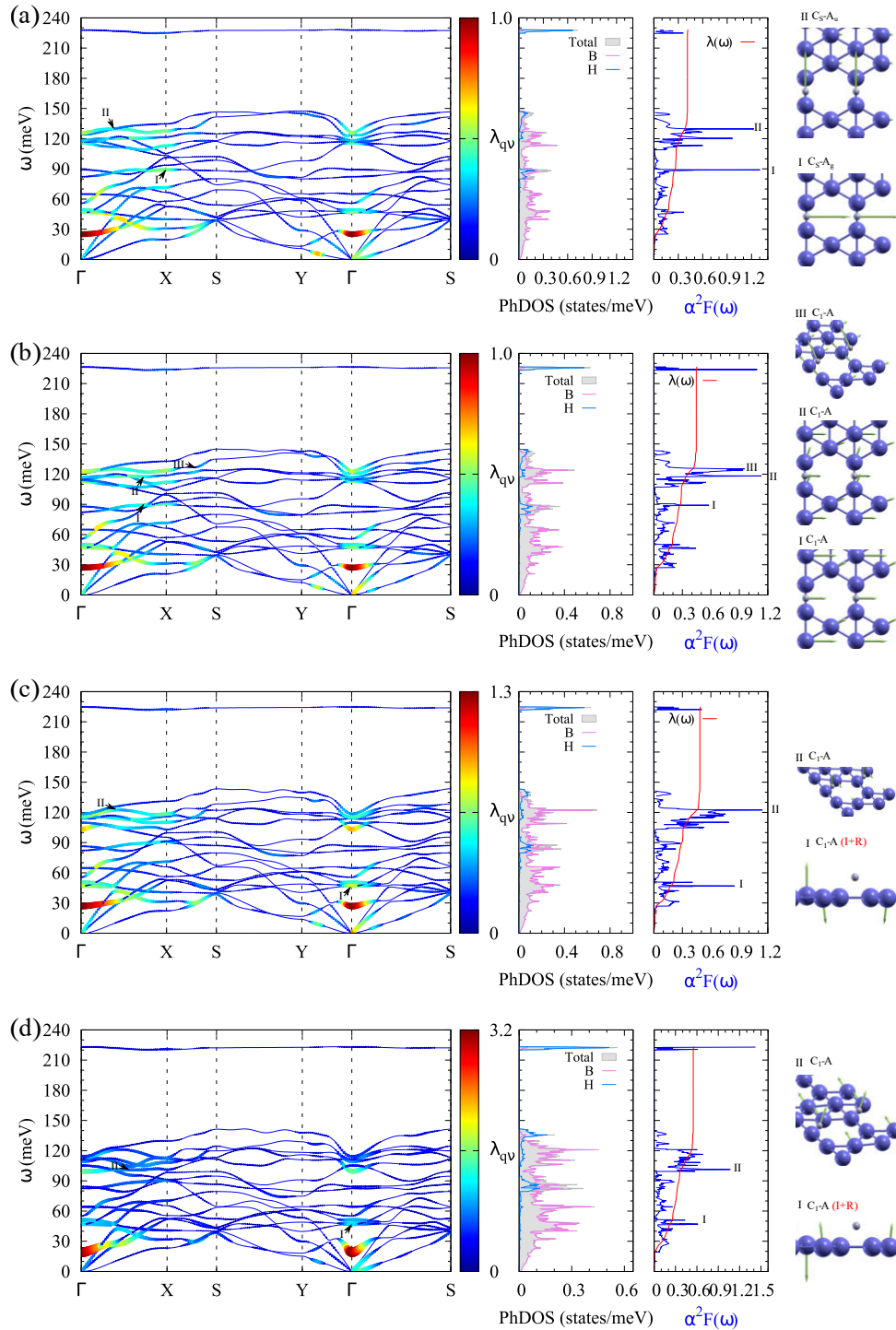


Figure 5.5: The phonon dispersions with q -resolved e - ph coupling (λ_{qv}) using color scales and point sizes proportional to λ , atom-resolved PhDOS and the $\alpha^2 F(\omega)$ function, which exhibits peaks corresponding to phonon modes, are shown for hydrogenated β_{12} borophene by applying tensile strain of $\epsilon_x = +3\%$ and (a) $\epsilon_y = 0\%$, (b) $\epsilon_y = +1\%$, (c) $\epsilon_y = +2\%$, (d) $\epsilon_y = +3\%$.

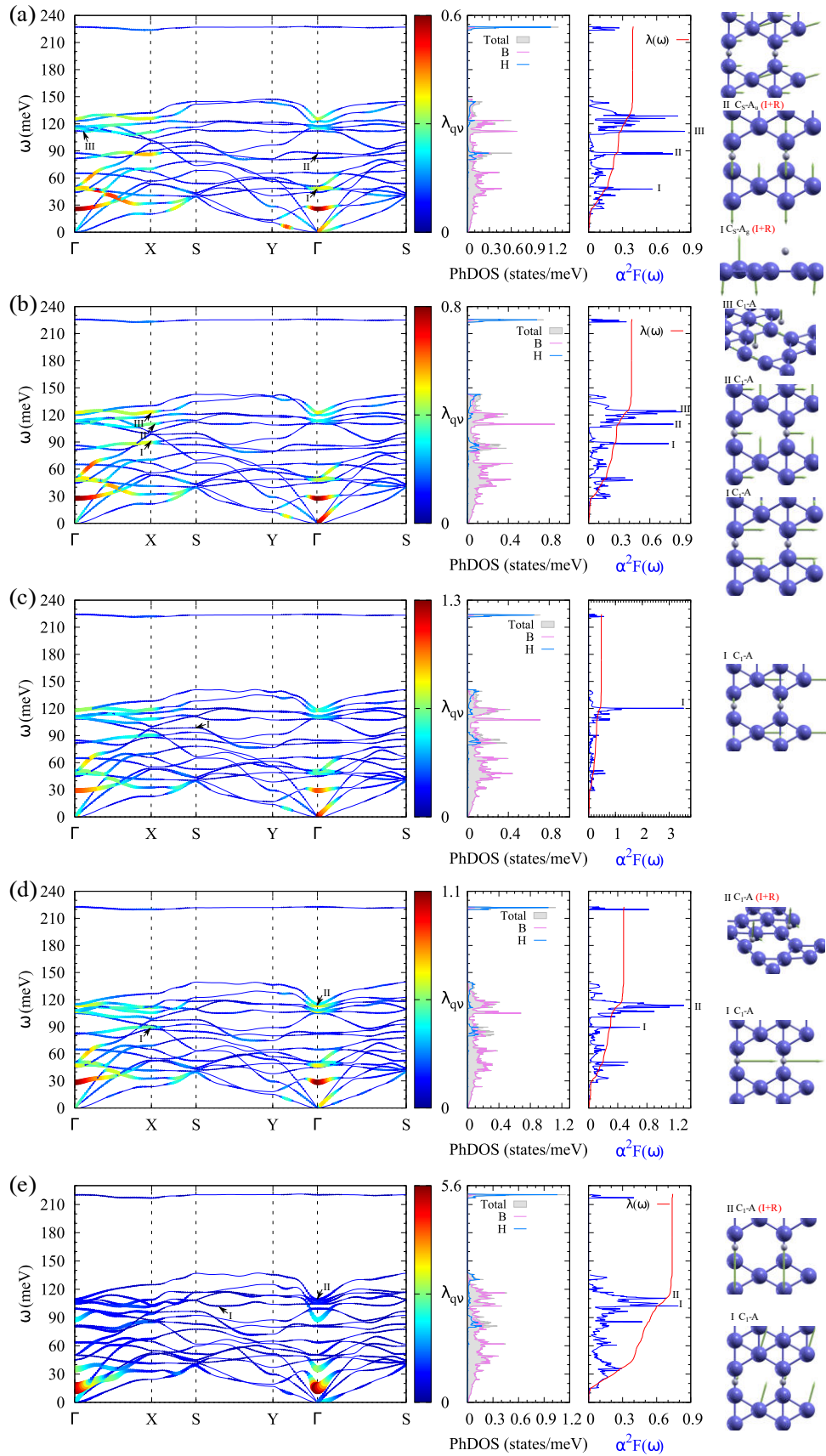


Figure 5.6: The phonon dispersions with q -resolved e - ph coupling (λ_{qv}) using color scales and point sizes proportional to λ , atom-resolved PhDOS and the $\alpha^2 F(\omega)$ function, which exhibits peaks corresponding to phonon modes, are shown for hydrogenated β_{12} borophene by applying tensile strain of $\epsilon_x = +4\%$ and (a) $\epsilon_y = 0\%$, (b) $\epsilon_y = +1\%$, (c) $\epsilon_y = +2\%$, (d) $\epsilon_y = +3\%$, (e) $\epsilon_y = +4\%$.

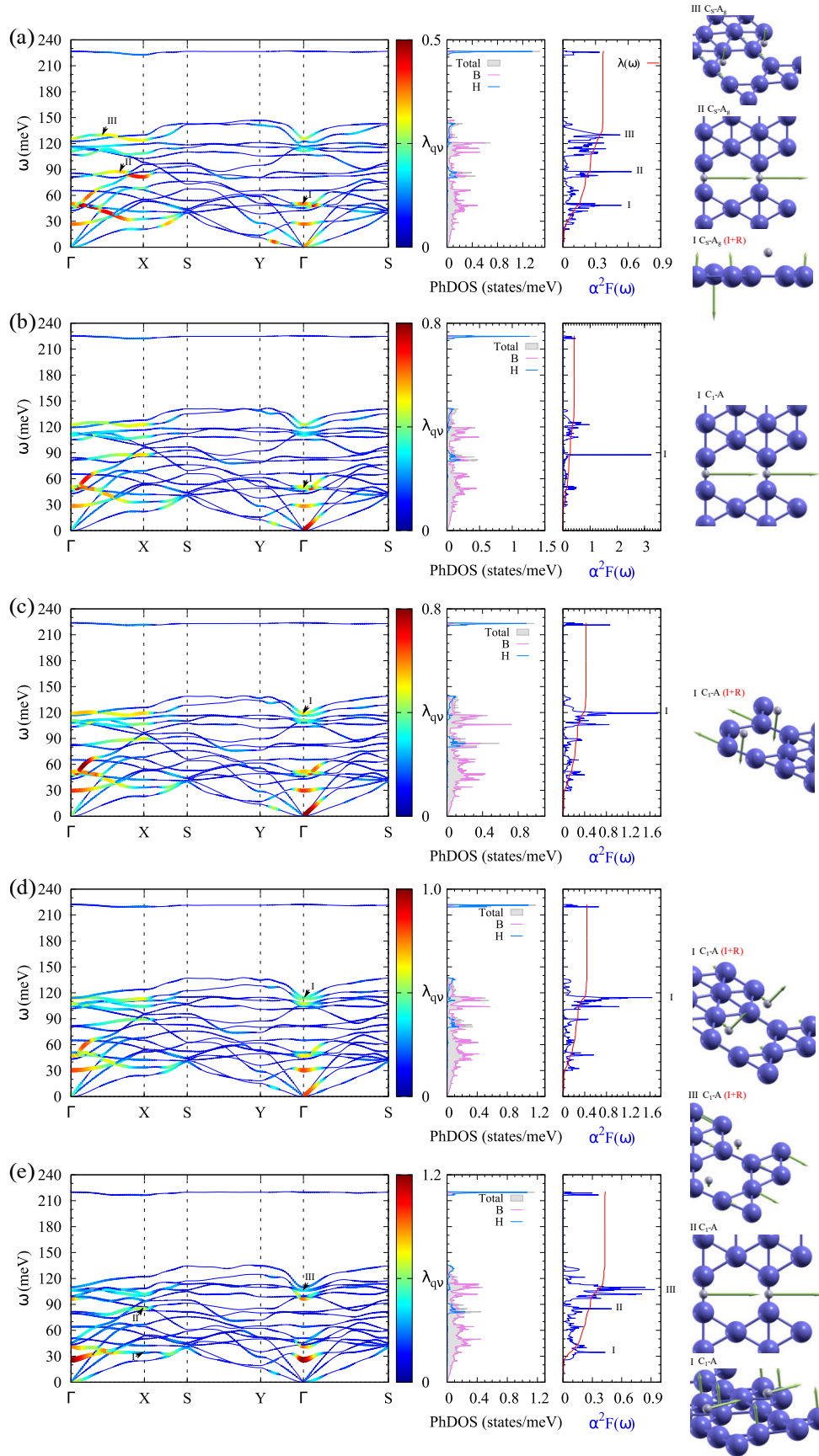


Figure 5.7: The phonon dispersions with q -resolved e - ph coupling (λ_{qv}) using color scales and point sizes proportional to λ , atom-resolved PhDOS and the $\alpha^2 F(\omega)$ function, which exhibits peaks corresponding to phonon modes, are shown for hydrogenated β_{12} borophene by applying tensile strain of $\epsilon_x = +5\%$ and (a) $\epsilon_y = 0\%$, (b) $\epsilon_y = +1\%$, (c) $\epsilon_y = +2\%$, (d) $\epsilon_y = +3\%$, (e) $\epsilon_y = +4\%$.

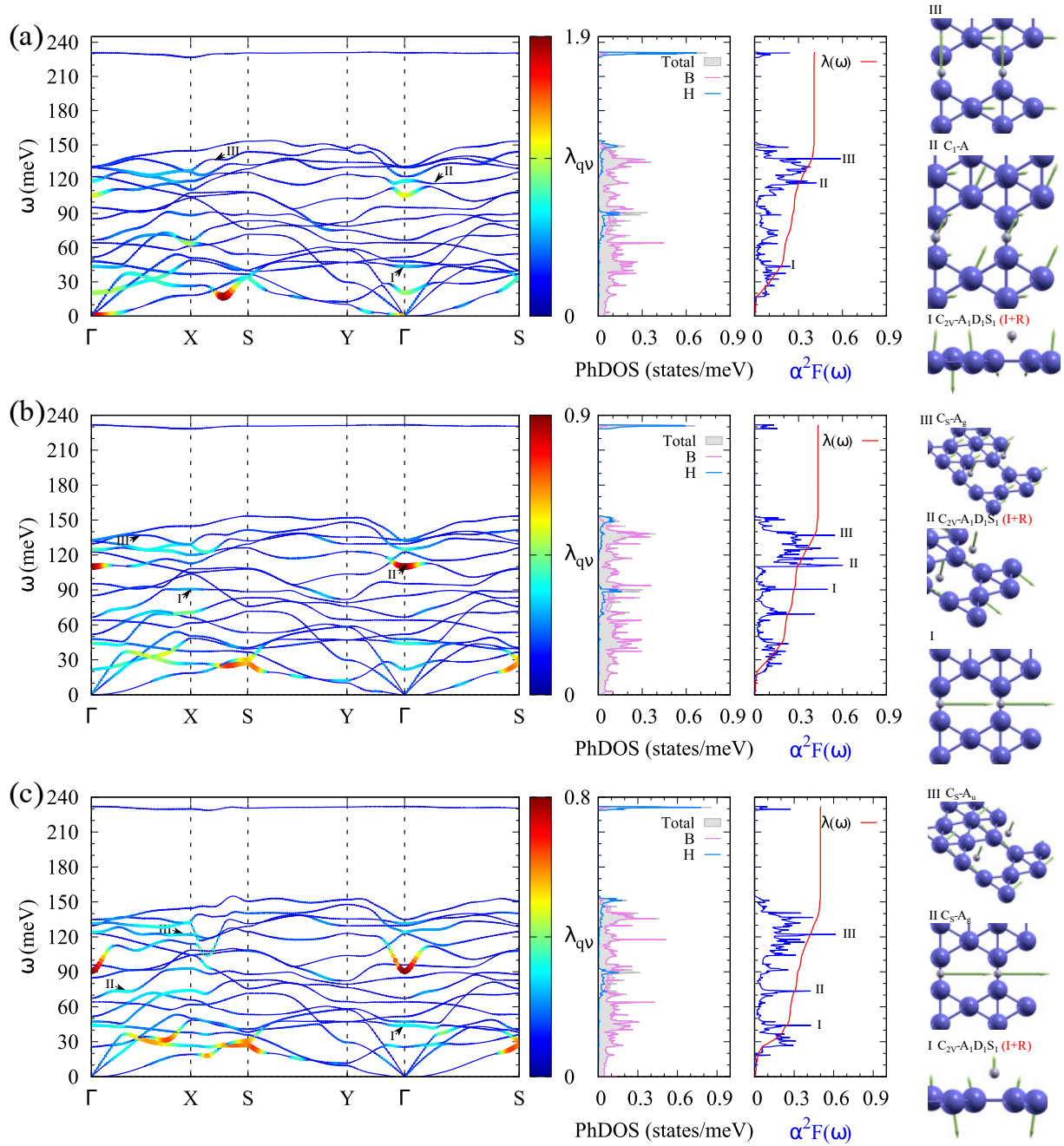


Figure 5.8: The phonon dispersions with q -resolved e -ph coupling (λ_{qv}) using color scales and point sizes proportional to λ , atom-resolved PhDOS and the $\alpha^2 F(\omega)$ function, which exhibits peaks corresponding to phonon modes, are shown for hydrogenated β_{12} borophene by applying uniform hole doping of (a) $-0.01 e/B$, (b) $-0.02 e/B$, (c) $-0.03 e/B$.

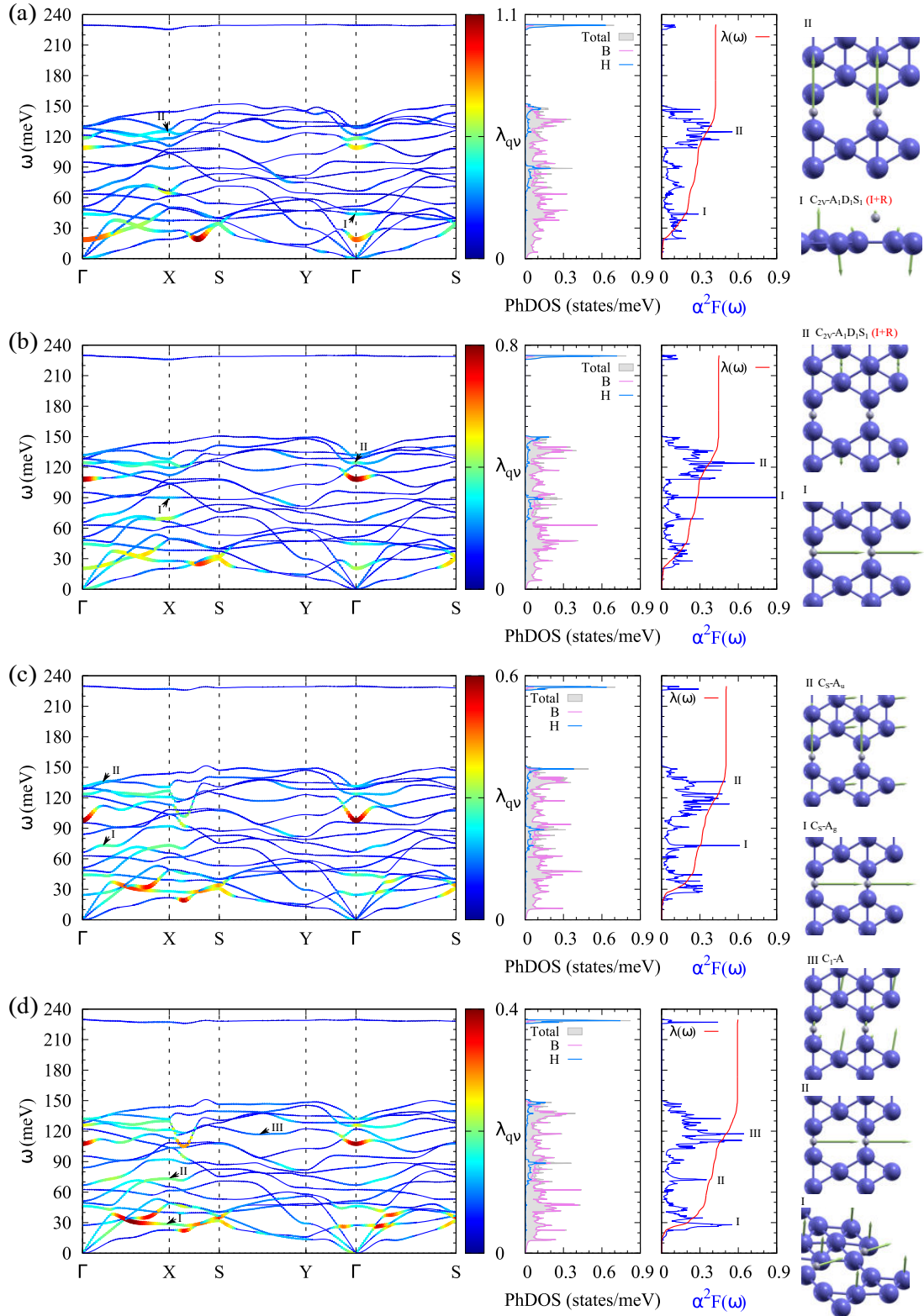


Figure 5.9: The phonon dispersions with q -resolved e - ph coupling (λ_{qv}) using color scales and point sizes proportional to λ , atom-resolved PhDOS and the $\alpha^2 F(\omega)$ function, which exhibits peaks corresponding to phonon modes, are shown for hydrogenated β_{12} borophene by applying nonuniform (FET) hole doping of (a) $-0.01 e/B$, (b) $-0.02 e/B$, (c) $-0.03 e/B$, and (d) $-0.04 e/B$.

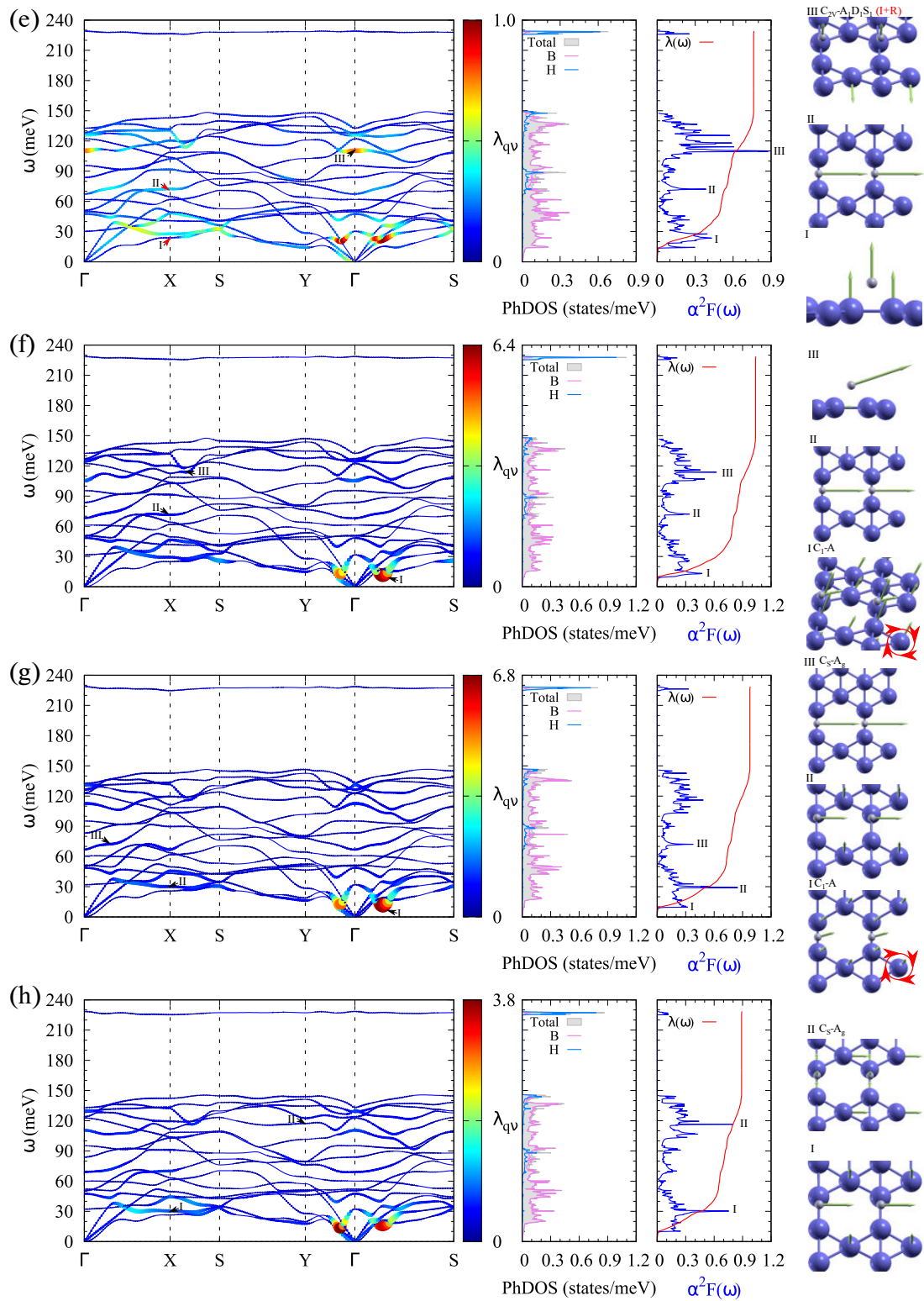


Figure 5.10: The phonon dispersions with q -resolved e - ph coupling (λ_{qv}) using color scales and point sizes proportional to λ , atom-resolved PhDOS and the $\alpha^2 F(\omega)$ function, which exhibits peaks corresponding to phonon modes, are shown for hydrogenated β_{12} borophene by applying nonuniform (FET) hole doping of (a) $-0.05 e/B$, (b) $-0.06 e/B$, (c) $-0.07 e/B$, and (d) $-0.08 e/B$.

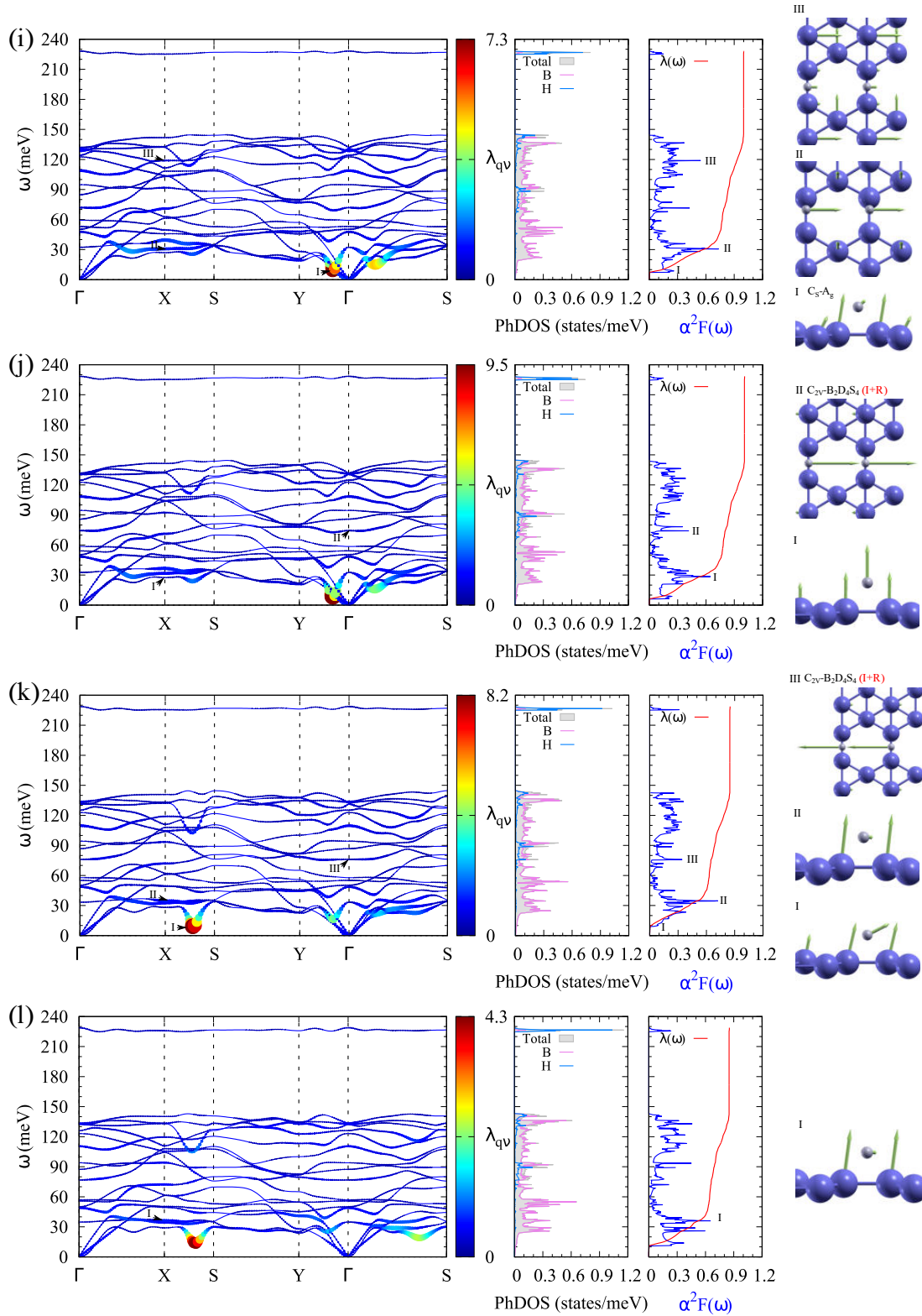


Figure 5.11: The phonon dispersions with q -resolved e -ph coupling (λ_{qv}) using color scales and point sizes proportional to λ , atom-resolved PhDOS and the $\alpha^2 F(\omega)$ function, which exhibits peaks corresponding to phonon modes, are shown for hydrogenated β_{12} borophene by applying nonuniform (FET) hole doping of (a) $-0.09 e/B$, (b) $-0.10 e/B$, (c) $-0.11 e/B$, and (d) $-0.12 e/B$.

A5: Technical details and additional results for section 4.2

The structural and electronic properties were examined through DFT calculations using the Quantum ESPRESSO package [233]. Calculations employed the Perdew-Burke-Ernzerhof (PBE) functional alongside norm-conserving pseudopotentials from the PseudoDojo repository [311]. A plane-wave basis with cutoff energies of 120 Ry for wave functions and 480 Ry for charge density was used. To minimize interactions between periodic images, a vacuum layer of 20 Å was introduced. For the β_{12} phase, electronic states were sampled using a $24 \times 18 \times 1$ Monkhorst-Pack k -point mesh, while a denser $24 \times 24 \times 1$ grid was adopted for the χ_3 , δ_4 , and kagome phases. Structural relaxations were performed until atomic forces were below 10^{-5} Ry/bohr. A Methfessel-Paxton smearing of 0.02 Ry was applied for electronic occupations; however, for cases where this led to soft phonon branches, additional phonon dispersion calculations were carried out at lower smearing values (0.01, 0.005, and 0.0025 Ry) to verify dynamical stability, as shown in Figure 5.12. Notably, the pristine δ_4 phase exhibited instability at reduced smearing values.

The phonon properties were analyzed within density functional perturbation theory (DFPT) using q -point grids of $8 \times 6 \times 1$, $8 \times 8 \times 1$, $8 \times 8 \times 1$, and $12 \times 12 \times 1$ for β_{12} , χ_3 , δ_4 , and kagome bilayer borophene, respectively. Superconducting properties were examined using isotropic Eliashberg theory, an extension of Bardeen-Cooper-Schrieffer (BCS) theory. The isotropic Eliashberg spectral function was computed as

$$\alpha^2 F(\omega) = \frac{1}{N(0)} \sum_{\mathbf{k}, \mathbf{q}} \sum_{\nu} |g_{\mathbf{k}, \mathbf{k}+\mathbf{q}, \nu}|^2 \delta(\epsilon_{\mathbf{k}+\mathbf{q}}) \delta(\epsilon_{\mathbf{k}}) \delta(\omega - \omega_{\mathbf{q}, \nu}), \quad (5.21)$$

where $N(0)$ is the density of states at the Fermi level, $\epsilon_{\mathbf{k}}$ represents electronic energies, and $g_{\mathbf{k}, \mathbf{k}+\mathbf{q}, \nu}$ denotes e - ph matrix elements. The e - ph coupling (EPC) strength was evaluated via

$$\lambda = 2 \int_0^{\infty} \frac{\alpha^2 F(\omega)}{\omega} d\omega. \quad (5.22)$$

The superconducting critical temperature (T_c) was estimated using the McMillan-Allen-Dynes equation, assuming a Morel-Anderson Coulomb pseudopotential (μ^*) of 0.1.

For materials exhibiting significant superconducting potential, a fully anisotropic solution of the Migdal-Eliashberg equations was obtained using the EPW code. MLWFs were initialized with s -, p_x -, p_y -, and p_z -like orbitals for boron and s -like orbitals for intercalated atoms. The

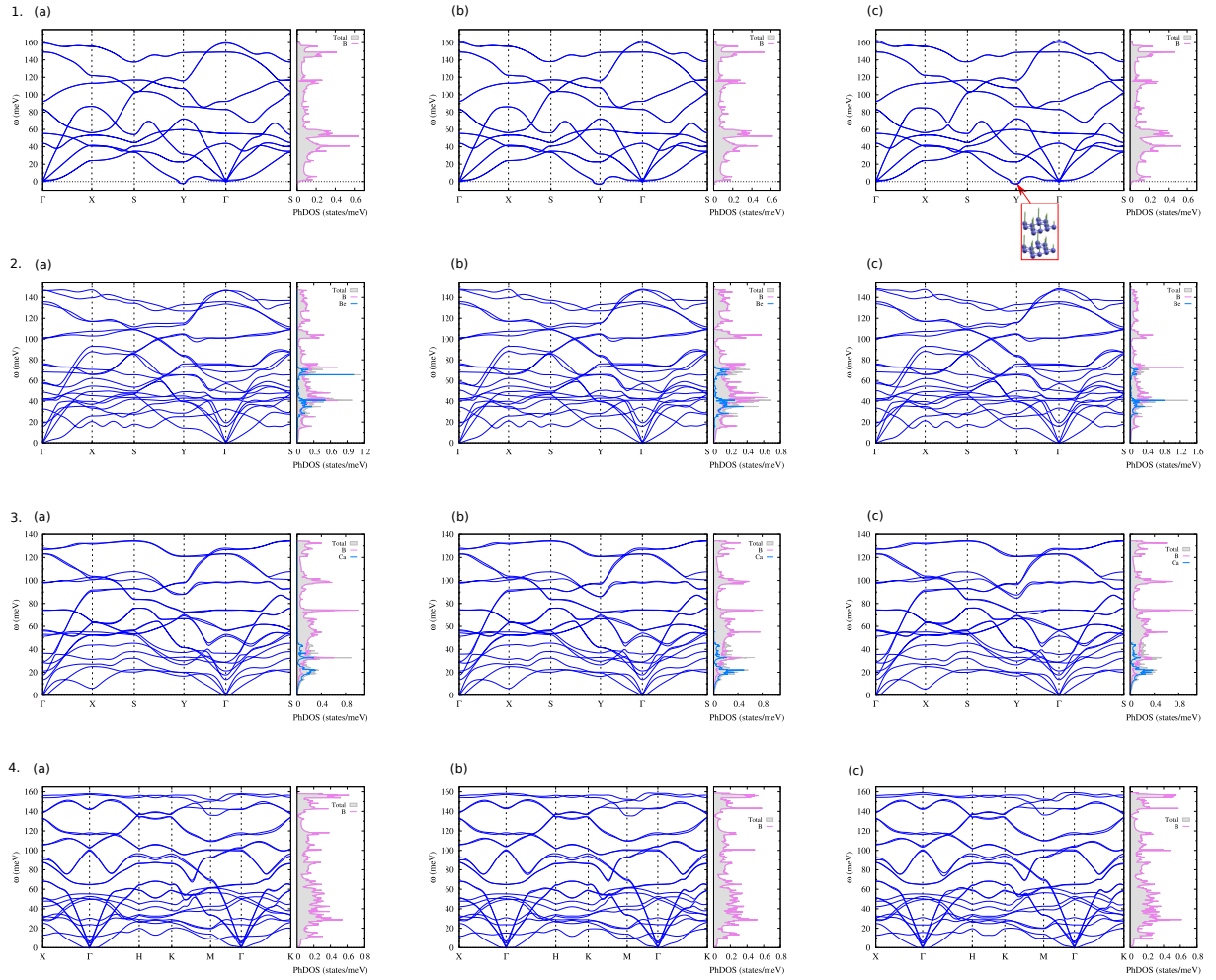


Figure 5.12: Phonon dispersion and atom-resolved phonon DOS are presented for the following systems: (1) the bare bilayer δ_4 borophene, (2) δ_4 intercalated with Be, (3) δ_4 intercalated with Ca, and (4) the bare bilayer χ_3 borophene. The calculations were performed using smearing values of (a) 0.01 Ry, (b) 0.005 Ry, and (c) 0.0025 Ry.

e - ph matrix elements were computed on the same coarse k - and q -grids as in the isotropic calculations and then interpolated onto finer grids: $192 \times 192 \times 1$, $216 \times 216 \times 1$, and $216 \times 216 \times 1$ for k -points, and $64 \times 64 \times 1$, $72 \times 72 \times 1$, and $108 \times 108 \times 1$ for q -points, corresponding to Mg in χ_3 , Be in δ_4 , and Ca in kagome bilayer borophene, respectively. The fermionic Matsubara frequency cutoff was set to 0.6 eV, with μ^* fixed at 0.1, consistent with the isotropic calculations.

BIBLIOGRAPHY

- [1] K. S. Novoselov, A. K. Geim, S. V. Morozov, D. Jiang, Y. Zhang, S. V. Dubonos, I. V. Grigorieva, and A. A. Firsov. Electric Field Effect in Atomically Thin Carbon Films. *Science*, 306(5696):666–669, 2004.
- [2] N. R. Glavin and S.-W. Nam. 2D layered materials and heterostructures: Past, present, and a bright future. *Matter*, 6(1):4–6, 2023.
- [3] B. C. Brodie. XIII. On the atomic weight of graphite. *Philosophical Transactions of the Royal Society of London*, 149:249–259, 1859.
- [4] D. R. Dreyer, S. Park, C. W. Bielawski, and R. S. Ruoff. The chemistry of graphene oxide. *Chem. Soc. Rev.*, 39:228–240, 2010.
- [5] H. P. Boehm, A. Clauss, G. O. Fischer, and U. Hofmann. Das Adsorptionsverhalten sehr dünner Kohlenstoff-Folien. *Zeitschrift für anorganische und allgemeine Chemie*, 316(3–4):119–127, 1962.
- [6] H. P. Boehm, R. Setton, and E. Stumpp. Nomenclature and terminology of graphite intercalation compounds. *Carbon*, 24(2):241–245, 1986.
- [7] J. T. Grant and T. W. Haas. A study of Ru(0001) and Rh(111) surfaces using LEED and Auger electron spectroscopy. *Surface Science*, 21(1):76–85, 1970.
- [8] J. M. Blakely and J. S. Kim H. C. Potter. Segregation of Carbon to the (100) Surface of Nickel. *Journal of Applied Physics*, 41(6):2693–2697, 1970.

- [9] A. J. Van Bommel, J. E. Crombeen, and A. Van Tooren. LEED and Auger electron observations of the SiC(0001) surface. *Surface Science*, 48(2):463–472, 1975.
- [10] A. Nagashima, K. Nuka, K. Satoh, H. Itoh, T. Ichinokawa, C. Oshima, and S. Otani. Electronic structure of monolayer graphite on some transition metal carbide surfaces. *Surface Science*, 287–288:609–613, 1993.
- [11] H. W. Kroto, J. R. Heath, S. C. O’Brien, R. F. Curl, and R. E. Smalley. C60: Buckminsterfullerene. *Nature*, 318(6042):162–163, 1985.
- [12] S. Iijima. Helical microtubules of graphitic carbon. *Nature*, 354:56–58, 1991.
- [13] A. Zham, J. Jang, and B. Z. Jang. Electrochemical method of producing nano-scaled graphene platelets. 2013.
- [14] C. Zhi, Y. Bando, C. Tang, H. Kuwahara, and D. Golberg. Large-Scale Fabrication of Boron Nitride Nanosheets and Their Utilization in Polymeric Composites with Improved Thermal and Mechanical Properties. *Advanced Materials*, 21(28):2889–2893, 2009.
- [15] M. Chhowalla, Z. Liu, and H. Zhang. Two-dimensional transition metal dichalcogenide (TMD) nanosheets. *Chem. Soc. Rev.*, 44:2584–2586, 2015.
- [16] Wonbong Choi, Nitin Choudhary, Gang Hee Han, Juhong Park, Deji Akinwande, and Young Hee Lee. Recent development of two-dimensional transition metal dichalcogenides and their applications. *Materials Today*, 20(3):116–130, 2017.
- [17] B. Anasori, M. R. Lukatskaya, and Y. Gogotsi. 2D metal carbides and nitrides (MXenes) for energy storage. *Nature Reviews Materials*, 2(2):16098, 2017.
- [18] M. Osada and T. Sasaki. Exfoliated oxide nanosheets: new solution to nanoelectronics. *J. Mater. Chem.*, 19:2503–2511, 2009.
- [19] P. Vogt, P. D. Padova, C. Quaresima, J. Avila, E. Frantzeskakis, M. C. Asensio, A. Resta, B. Ealet, and G. L. Lay. Silicene: Compelling Experimental Evidence for Graphenelike Two-Dimensional Silicon. *Phys. Rev. Lett.*, 108:155501, 2012.
- [20] M. E. Dávila, L. Xian, S. Cahangirov, A. Rubio, and G. L. Lay. Germanene: a novel two-dimensional germanium allotrope akin to graphene and silicene. *New Journal of Physics*, 16(9):095002, 2014.

- [21] L. Li, Y. Yu, G. J. Ye, Q. Ge, X. Ou, H. Wu, X. H. Chen D. Feng, and Y. Zhang. Black phosphorus field-effect transistors. *Nature Nanotechnology*, 9(5):372–377, 2014.
- [22] F.-F. Zhu, W.-J. Chen, Y. Xu, C.-L. Gao, D.-D. Guan, C.-H. Liu, D. Qian, S.-C. Zhang, and J.-F. Jia. Epitaxial growth of two-dimensional stanene. *Nature Materials*, 14(10):1020–1025, 2015.
- [23] A. J. Mannix, X.-F. Zhou, B. Kiraly, J. D. Wood, D. Alducin, B. D. Myers, X. Liu, B. L. Fisher, U. Santiago, J. R. Guest, M. J. Yacaman, A. Ponce, A. R. Oganov, M. C. Hersam, and N. P. Guisinger. Synthesis of borophenes: Anisotropic, two-dimensional boron polymorphs. *Science*, 350(6267):1513–1516, 2015.
- [24] P. Ares, F. Aguilar-Galindo, D. Rodríguez-San-Miguel, D. A. Aldave, S. Díaz-Tendero, M. Alcamí, F. Martín, J. Gómez-Herrero, and F. Zamora. Mechanical Isolation of Highly Stable Antimonene under Ambient Conditions. *Advanced Materials*, 28(30):6332–6336, 2016.
- [25] F. Reis, G. Li, L. Dudy, M. Bauernfeind, S. Glass, W. Hanke, R. Thomale, J. Schäfer, and R. Claessen. Bismuthene on a SiC substrate: A candidate for a high-temperature quantum spin Hall material. *Science*, 357(6348):287–290, 2017.
- [26] V. Kochat, A. Samanta, Y. Zhang, S. Bhowmick, P. Manimunda, S. Asif, A. S. Stender, R. Vajtai, A. K. Singh, C. S. Tiwary, and P. M. Ajayan. Atomically thin gallium layers from solid-melt exfoliation. *Science Advances*, 4(3):e1701373, 2018.
- [27] J. Yuhara, B. He, N. Matsunami, M. Nakatake, and G. L. Lay. Graphene’s Latest Cousin: Plumbene Epitaxial Growth on a “Nano WaterCube”. *Advanced Materials*, 31(27):1901017, 2019.
- [28] M. Qian, Z. Xu, Z. Wang, B. Wei, H. Wang, S. Hu, L.-M. Liu, and L. Guo. Realizing Few-Layer Iodinene for High-Rate Sodium-Ion Batteries. *Advanced Materials*, 32(43):2004835, 2020.
- [29] J. Shah, W. Wang, H. M. Sohail, and R. I. G. Uhrberg. Experimental evidence of monolayer arsenene: an exotic 2D semiconducting material. *2D Materials*, 7(2):025013, 2020.

- [30] P. V. Sarma, R. Nadarajan, R. Kumar, R. M. Patinharayil, N. Biju, S. Narayanan, G. Gao, C. S. Tiwary, M. Thalakulam, R. N. Kini, A. K. Singh, P. M. Ajayan, and M. M. Shaijumon. Growth of highly crystalline ultrathin two-dimensional selenene. *2D Materials*, 9(4):045004, 2022.
- [31] X. Huang, R. Xiong, C. Hao, W. Li, B. Sa, J. Wiebe, and R. Wiesendanger. Experimental Realization of Monolayer α -Tellurene. *Advanced Materials*, 36(6):2309023, 2024.
- [32] S. Chahal, A. Bandyopadhyay, C.-S. Yang, and P. Kumar. Beryllene, the lightest xene. *npj 2D Materials and Applications*, 7(1):55, 2023.
- [33] S. Li, C. Wang, Y. Yin, E. Lewis, and P. Wang. Novel layered 2d materials for ultrafast photonics. *Nanophotonics*, 9(7):1743–1786, 2020.
- [34] M. Yi and Z. Shen. A review on mechanical exfoliation for the scalable production of graphene. *J. Mater. Chem. A*, 3:11700–11715, 2015.
- [35] A. E. Mag-isa, J.-H. Kim, H.-J. Lee, and C.-S. Oh. A systematic exfoliation technique for isolating large and pristine samples of 2D materials. *2D Materials*, 2(3):034017, 2015.
- [36] S. B. Desai, S. R. Madhvapathy, M. Amani, D. Kiriya, M. Hettick, M. Tosun, Y. Zhou, M. Dubey, J. W. Ager III, D. Chrzan, and A. Javey. Gold-Mediated Exfoliation of Ultralarge Optoelectronically-Perfect Monolayers. *Advanced Materials*, 28(21):4053–4058, 2016.
- [37] Y. Huang, Y.-H. Pan, R. Yang, L.-H. Bao, L. Meng, H.-L. Luo, Y.-Q. Cai, G.-D. Liu, W.-J. Zhao, Z. Zhou, L.-M. Wu, Z.-L. Zhu, M. Huang, L.-W. Liu, L. Liu, P. Cheng, L.-H. Wu, S.-B. Tian, C.-Z. Gu, Y.-G. Shi, Y.-F. Guo, Z. G. Cheng, J.-P. Hu, L. Zhao, G.-H. Yang, E. Sutter, P. Sutter, Y.-L. Wang, W. Ji, X.-J. Zhou, and H.-J. Gao. Universal mechanical exfoliation of large-area 2D crystals. *Nature Communications*, 11(1):2453, 2020.
- [38] F. Liu, W. Wu, Y. Bai, S. H. Chae, Q. Li, J. Wang, J. Hone, and X.-Y. Zhu. Disassembling 2D van der Waals crystals into macroscopic monolayers and reassembling into artificial lattices. *Science*, 367(6480):903–906, 2020.
- [39] Y. Hernandez, V. Nicolosi, M. Lotya, F. M. Blighe, Z. Sun, S. De, I. T. McGovern, B. Holland, M. Byrne, Y. K. Gun'Ko, J. J. Boland, P. Niraj, G. Duesberg, S. Krishnamurthy,

- R. Goodhue, J. Hutchison, V. Scardaci, A. C. Ferrari, and J. N. Coleman. High-yield production of graphene by liquid-phase exfoliation of graphite. *Nature Nanotechnology*, 3(9):563–568, 2008.
- [40] V. Nicolosi, M. Chhowalla, M. G. Kanatzidis, M. S. Strano, and J. N. Coleman. Liquid Exfoliation of Layered Materials. *Science*, 340(6139):1226419, 2013.
- [41] M. Zhao, C. Casiraghi, and K. Parvez. Electrochemical exfoliation of 2D materials beyond graphene. *Chem. Soc. Rev.*, 53:3036–3064, 2024.
- [42] D. C. Marcano, D. V. Kosynkin, J. M. Berlin, A. Sinitskii, Z. Sun, A. Slesarev, L. B. Alemany, W. Lu, and J. M. Tour. Improved Synthesis of Graphene Oxide. *ACS Nano*, 4(8):4806–4814, 2010.
- [43] L. Gao, C. Ma, S. Wei, A. V. Kuklin, H. Zhang, and H. Ågren. Applications of Few-Layer Nb₂C MXene: Narrow-Band Photodetectors and Femtosecond Mode-Locked Fiber Lasers. *ACS Nano*, 15(1):954–965, 2021.
- [44] Z. Cai, B. Liu, X. Zou, and H.-M. Cheng. Chemical Vapor Deposition Growth and Applications of Two-Dimensional Materials and Their Heterostructures. *Chemical Reviews*, 118(13):6091–6133, 2018.
- [45] J. Cai, X. Han, X. Wang, and X. Meng. Atomic Layer Deposition of Two-Dimensional Layered Materials: Processes, Growth Mechanisms, and Characteristics. *Matter*, 2(3):587–630, 2020.
- [46] C. Tan and H. Zhang. Wet-chemical synthesis and applications of non-layer structured two-dimensional nanomaterials. *Nature Communications*, 6(1):7873, 2015.
- [47] Y. X. Gan, A. H. Jayatissa, Z. Yu, X. Chen, and M. Li. Hydrothermal Synthesis of Nanomaterials. *Journal of Nanomaterials*, 2020(1):8917013, 2020.
- [48] P. Ugo and L. M. Moretto. 16.2 - TEMPLATE DEPOSITION OF METALS. In C. G. Zoski, editor, *Handbook of Electrochemistry*, pages 678–709. Elsevier, Amsterdam, 2007.
- [49] M. Parashar, V. K. Shukla, and R. Singh. Metal oxides nanoparticles via sol–gel method: a review on synthesis, characterization and applications. *Journal of Materials Science: Materials in Electronics*, 31(5):3729–3749, 2020.

- [50] D. M. Mattox. *Handbook of physical vapor deposition (PVD) processing*. Norwich, 2nd ed. edition, 2010.
- [51] R. J. Martín-Palma and A. Lakhtakia. Chapter 15 - Vapor-Deposition Techniques. In A. Lakhtakia and R. J. Martín-Palma, editors, *Engineered Biomimicry*, pages 383–398. Elsevier, Boston, 2013.
- [52] Y. Shi, W. Zhou, A.-Y. Lu, W. Fang, Y.-H. Lee, A. L. Hsu, S. M. Kim, K. K. Kim, H. Y. Yang, L.-J. Li, J.-C. Idrobo, and J. Kong. van der Waals Epitaxy of MoS₂ Layers Using Graphene As Growth Templates. *Nano Letters*, 12(6):2784–2791, 2012.
- [53] Q. Li, Q. Zhou, L. Shi, Q. Chen, and J. Wang. Recent advances in oxidation and degradation mechanisms of ultrathin 2D materials under ambient conditions and their passivation strategies. *J. Mater. Chem. A*, 7:4291–4312, 2019.
- [54] Yuqing Wang, Sebastian Amland Skaanvik, Xuya Xiong, Shuangyin Wang, and Mingdong Dong. Scanning probe microscopy for electrocatalysis. *Matter*, 4(11):3483–3514, 2021.
- [55] G. Binnig, H. Rohrer, Ch. Gerber, and E. Weibel. Surface Studies by Scanning Tunneling Microscopy. *Phys. Rev. Lett.*, 49:57–61, 1982.
- [56] B. Voigtländer. *Scanning probe microscopy: Atomic force microscopy and scanning tunneling microscopy*. Springer, 2015.
- [57] X. Wang, J. Song, J. Liu, and Z. L. Wang. Direct-Current Nanogenerator Driven by Ultrasonic Waves. *Science*, 316(5821):102–105, 2007.
- [58] B. J. Inkson. 2 - Scanning electron microscopy (SEM) and transmission electron microscopy (TEM) for materials characterization. In G. Hübschen, I. Altpeter, R. Tschuncky, and H.-G. Herrmann, editors, *Materials Characterization Using Nondestructive Evaluation (NDE) Methods*, pages 17–43. Woodhead Publishing, 2016.
- [59] A. Gupta, T. Sakthivel, and S. Seal. Recent development in 2D materials beyond graphene. *Progress in Materials Science*, 73:44–126, 2015.
- [60] O. L. Krivanek, M. F. Chisholm, V. Nicolosi, T. J. Pennycook, G. J. Corbin, N. Dellby, M. F. Murfitt, C. S. Own, Z. S. Szilagy, M. P. Oxley, S. T. Pantelides, and S. J. Pennycook.

Atom-by-atom structural and chemical analysis by annular dark-field electron microscopy. *Nature*, 464(7288):571–574, 2010.

- [61] I. Cheliotis and I. Zergioti. A review on transfer methods of two-dimensional materials. *2D Materials*, 11(2):022004, 2024.
- [62] X. Li, Y. Zhu, W. Cai, M. Borysiak, B. Han, D. Chen, R. D. Piner, L. Colombo, and R. S. Ruoff. Transfer of Large-Area Graphene Films for High-Performance Transparent Conductive Electrodes. *Nano Letters*, 9(12):4359–4363, 2009.
- [63] L. Gao, W. Ren, H. Xu, L. Jin, Z. Wang, T. Ma, L.-P. Ma, Z. Zhang, Q. Fu, L.-M. Peng, X. Bao, and H.-M. Cheng. Repeated growth and bubbling transfer of graphene with millimetre-size single-crystal grains using platinum. *Nature Communications*, 3(1):699, 2012.
- [64] C. T. Cherian, F. Giustiniano, I. Martin-Fernandez, H. Andersen, J. Balakrishnan, and Barbaros B. Özyilmaz. ‘Bubble-Free’ Electrochemical Delamination of CVD Graphene Films. *Small*, 11(2):189–194, 2015.
- [65] M.-A. Yoon, C. Kim, J.-H. Kim, H.-J. Lee, and K.-S. Kim. Surface Properties of CVD-Grown Graphene Transferred by Wet and Dry Transfer Processes. *Sensors*, 22(10), 2022.
- [66] T. Yoon, W. C. Shin, T. Y. Kim, J. H. Mun, T.-S. Kim, and B. J. Cho. Direct Measurement of Adhesion Energy of Monolayer Graphene As-Grown on Copper and Its Application to Renewable Transfer Process. *Nano Letters*, 12(3):1448–1452, 2012.
- [67] Filippo F. Pizzocchero, L. Gammelgaard, B. S. Jessen, J. M. Caridad, L. Wang, J. Hone, P. Bøggild, and T. J. Booth. The hot pick-up technique for batch assembly of van der waals heterostructures. *Nature Communications*, 7(1):11894, 2016.
- [68] W. Liu, Q. Zou, C. Zheng, and C. Jin. Metal-Assisted Transfer Strategy for Construction of 2D and 3D Nanostructures on an Elastic Substrate. *ACS Nano*, 13(1):440–448, 2019.
- [69] M. Zhang, X.-X. Wang, W.-Q. Cao, J. Yuan, and M.-S. Cao. Electromagnetic Functions of Patterned 2D Materials for Micro–Nano Devices Covering GHz, THz, and Optical Frequency. *Advanced Optical Materials*, 7(19):1900689, 2019.

- [70] D. Teresa and J. María, editors. *Nanofabrication*. 2053–2563. IOP Publishing, 2020.
- [71] S. He, R. Tian, W. Wu, W.-D. Li, and D. Wang. Helium-ion-beam nanofabrication: extreme processes and applications. *International Journal of Extreme Manufacturing*, 3(1):012001, 2020.
- [72] A. I. Dago, S. Sangiao, R. Fernández-Pacheco, J. M. De Teresa, and R. Garcia. Chemical and structural analysis of sub-20 nm graphene patterns generated by scanning probe lithography. *Carbon*, 129:281–285, 2018.
- [73] C. Zhang, L. McKeon, M. P. Kremer, S.-H. Park, O. Ronan, A. Seral-Ascaso, S. Barwich, C. Coileáin, N. McEvoy, H. C. Nerl, B. Anasori, J. N. Coleman, Y. Gogotsi, and V. Nicolosi. Additive-free MXene inks and direct printing of micro-supercapacitors. *Nature Communications*, 10(1):1795, 2019.
- [74] L. Jia, J. Wu, Y. Zhang, Y. Qu, B. Jia, Z. Chen, and D. J. Moss. Fabrication Technologies for the On-Chip Integration of 2D Materials. *Small Methods*, 6(3):2101435, 2022.
- [75] S. Y. Chou, P. R. Krauss, and P. J. Renstrom. Imprint of sub-25 nm vias and trenches in polymers. *Applied Physics Letters*, 67(21):3114–3116, 1995.
- [76] T. H. Vo, U. G. E. Perera, M. Shekhirev, M. Mehdi Pour, D. A. Kunkel, H. Lu, A. Gruverman, E. Sutter, M. Cotlet, D. Nykypanchuk, P. Zahl, A. Enders, A. Sinitskii, and P. Sutter. Nitrogen-Doping Induced Self-Assembly of Graphene Nanoribbon-Based Two-Dimensional and Three-Dimensional Metamaterials. *Nano Letters*, 15(9):5770–5777, 2015.
- [77] S. Pineda, Z. J. Han, and K. Ostrikov. Plasma-Enabled Carbon Nanostructures for Early Diagnosis of Neurodegenerative Diseases. *Materials*, 7(7):4896–4929, 2014.
- [78] F. Liu, J. Shi, J. Xu, N. Han, Y. Cheng, and W. Huang. Site-selective growth of two-dimensional materials: strategies and applications. *Nanoscale*, 14:9946–9962, 2022.
- [79] Q. Yu, Y. Luo, A. Mahmood, B. Liu, and H.-M. Cheng. Engineering Two-Dimensional Materials and Their Heterostructures as High-Performance Electrocatalysts. *Electrochemical Energy Reviews*, 2(3):373–394, 2019.

- [80] J. T. Ye, Y. J. Zhang, R. Akashi, M. S. Bahramy, R. Arita, and Y. Iwasa. Superconducting Dome in a Gate-Tuned Band Insulator. *Science*, 338(6111):1193–1196, 2012.
- [81] C. Zhou and Y. Chai. Ferroelectric-Gated Two-Dimensional-Material-Based Electron Devices. *Advanced Electronic Materials*, 3(4):1600400, 2017.
- [82] J.-H. Chen, C. Jang, S. Adam, M. S. Fuhrer, E. D. Williams, and M. Ishigami. Charged-impurity scattering in graphene. *Nature Physics*, 4(5):377–381, 2008.
- [83] J. Narayan and K. Bezborah. Recent advances in the functionalization, substitutional doping and applications of graphene/graphene composite nanomaterials. *RSC Adv.*, 14:13413–13444, 2024.
- [84] C. Tang, H.-F. Wang, X. Chen, B.-Q. Li, T.-Z. Hou, B. Zhang, Q. Zhang, M.-M. Titirici, and F. Wei. Topological Defects in Metal-Free Nanocarbon for Oxygen Electrocatalysis. *Advanced Materials*, 28(32):6845–6851, 2016.
- [85] S. E. Thompson, M. Armstrong, C. Auth, M. Alavi, M. Buehler, R. Chau, S. Cea, T. Ghani, G. Glass, T. Hoffman, C.-H. Jan, C. Kenyon, J. Klaus, K. Kuhn, Z. Ma, B. McIntyre, K. Mistry, A. Murthy, B. Obradovic, R. Nagisetty, P. Nguyen, S. Sivakumar, R. Shaheed, L. Shifren, B. Tufts, S. Tyagi, M. Bohr, and Y. El-Mansy. A 90-nm logic technology featuring strained-silicon. *IEEE Transactions on Electron Devices*, 51(11):1790–1797, 2004.
- [86] G. Cocco, E. Cadelano, and L. Colombo. Gap opening in graphene by shear strain. *Phys. Rev. B*, 81:241412, 2010.
- [87] Y. Wu, K. Xu, C. Ma, Y. Chen, Z. Lu, H. Zhang, Z. Fang, and R. Zhang. Ultrahigh carrier mobilities and high thermoelectric performance at room temperature optimized by strain-engineering to two-dimensional aw-antimonene. *Nano Energy*, 2019.
- [88] F. Li, T. Shen, C. Wang, Y. Zhang, J. Qi, and H. Zhang. Recent Advances in Strain-Induced Piezoelectric and Piezoresistive Effect-Engineered 2D Semiconductors for Adaptive Electronics and Optoelectronics. *Nano-Micro Letters*, 12(1):106, 2020.
- [89] Y. Ma, Y. Dai, M. Guo, C. Niu, Y. Zhu, and B. Huang. Evidence of the Existence of Magnetism in Pristine VX₂ Monolayers (X = S, Se) and Their Strain-Induced Tunable Magnetic Properties. *ACS Nano*, 6(2):1695–1701, 2012.

- [90] Peng Luo, Fuwei Zhuge, Qingfu Zhang, Yuqian Chen, Liang Lv, Yu Huang, Huiqiao Li, and Tianyou Zhai. Doping engineering and functionalization of two-dimensional metal chalcogenides. *Nanoscale Horiz.*, 4:26–51, 2019.
- [91] K. S. Novoselov, A. Mishchenko, A. Carvalho, and A. H. Castro Neto. 2D materials and van der Waals heterostructures. *Science*, 353(6298):aac9439, 2016.
- [92] Y. Cao, V. Fatemi, S. Fang, K. Watanabe, T. Taniguchi, E. Kaxiras, and P. Jarillo-Herrero. Unconventional superconductivity in magic-angle graphene superlattices. *Nature*, 556(7699):43–50, 2018.
- [93] Q. Tong, F. Liu, J. Xiao, and W. Yao. Skyrmions in the Moiré of van der Waals 2D Magnets. *Nano Letters*, 18(11):7194–7199, 2018.
- [94] T. Song, Q.-C. Sun, E. Anderson, C. Wang, J. Qian, T. Taniguchi, K. Watanabe, M. A. McGuire, R. Stöhr, D. Xiao, T. Cao, J. Wrachtrup, and X. Xu. Direct visualization of magnetic domains and moiré magnetism in twisted 2D magnets. *Science*, 374(6571):1140–1144, 2021.
- [95] W. G. Woods. An introduction to boron: history, sources, uses, and chemistry. *Environmental Health Perspectives*, 102(suppl 7):5–11, 1994.
- [96] A. R. Oganov and V. L. Solozhenko. Boron: a hunt for superhard polymorphs. *Journal of Superhard Materials*, 31(5):285–291, 2009.
- [97] J. G. Gay-Lussac and L. J. Thénard. Sur la décomposition et la recomposition de l’acide boracique. *Ann. Chim. Phys*, 68:169–174, 1808.
- [98] H. Davy. Electro-Chemical Researches, on the Decomposition of the Earths; With Observations on the Metals Obtained from the Alkaline Earths, and on the Amalgam Procured from Ammonia. *Philosophical Transactions of the Royal Society of London Series I*, 98:333–370, 1808.
- [99] J. Wisniak. Henri Étienne Sainte-Claire Deville: A physician turned metallurgist. *Journal of Materials Engineering and Performance*, 13(2):117–128, 2004.
- [100] J. Wisniak. Henri Moissan. The discoverer of fluorine. *Educación Química*, 13(4):267–274, 2002.

- [101] E. Weintraub. Preparation and properties of pure boron. *Trans. Amer. Electrochem. Soc.*, 16:165–184, 1909.
- [102] D. E. Sands and J. L. Hoard. RHOMBOHEDRAL ELEMENTAL BORON. *Journal of the American Chemical Society*, 79(20):5582–5583, 1957.
- [103] R. E. Hughes, C. H. L. Kennard, D. B. Sullenger, H. A. Weakliem, D. E. Sands, and J. L. Hoard. The Structure of Rhombohedral Boron. *Journal of the American Chemical Society*, 85:361–362, 1963.
- [104] J. L. Hoard, D. B. Sullenger, C. H. L. Kennard, and R. E. Hughes. The structure analysis of β -rhombohedral boron. *Journal of Solid State Chemistry*, 1(2):268–277, 1970.
- [105] L. V. McCarty, J. S. Kasper, F. H. Horn, B. F. Decker, and A. E. Newkirk. A NEW CRYSTALLINE MODIFICATION OF BORON. *Journal of the American Chemical Society*, 80(10):2592–2592, 1958.
- [106] B. F. Decker and J. S. Kasper. The crystal structure of a simple rhombohedral form of boron. *Acta Crystallographica*, 12(7):503–506, 1959.
- [107] C. P. Talley, S. La Placa, and B. Post. A new polymorph of boron. *Acta Crystallographica*, 13(3):271–272, 1960.
- [108] M. Vlasse, R. Naslain, J. S. Kasper, and K. Ploog. Crystal structure of tetragonal boron related to α - AlB_{12} . *Journal of Solid State Chemistry*, 28(3):289–301, 1979.
- [109] R. H. Wentorf. Boron: Another Form. *Science*, 147(3653):49–50, 1965.
- [110] V. L. Solozhenko, O. O. Kurakevych, and A. R. Oganov. On the hardness of a new boron phase, orthorhombic γ - B_{28} . *Journal of Superhard Materials*, 30(6):428–429, 2008.
- [111] A. R. Oganov, J. Chen, C. Gatti, Y. Ma, Y. Ma, C. W. Glass, Z. Liu, T. Yu, O. O. Kurakevych, and V. L. Solozhenko. Ionic high-pressure form of elemental boron. *Nature*, 457(7231):863–867, 2009.
- [112] A. Masago, K. Shirai, and H. Katayama-Yoshida. Crystal stability of α - and β -boron. *Phys. Rev. B*, 73:104102, 2006.

- [113] M. J. van Setten, M. A. Uijtewaal, G. A. de Wijs, and R. A. de Groot. Thermodynamic Stability of Boron: The Role of Defects and Zero Point Motion. *Journal of the American Chemical Society*, 129(9):2458–2465, 2007.
- [114] D. N. Sanz, P. Loubeyre, and M. Mezouar. Equation of State and Pressure Induced Amorphization of β -Boron from X-Ray Measurements up to 100 GPa. *Phys. Rev. Lett.*, 89:245501, 2002.
- [115] M. I. Eremets, V. V. Struzhkin, H.-K. Mao, and R. J. Hemley. Superconductivity in Boron. *Science*, 293(5528):272–274, 2001.
- [116] Y. Ma, C. T. Prewitt, G. Zou, H. k. Mao, and R. J. Hemley. High-pressure high-temperature X-ray diffraction of β -boron to 30 GPa. *Phys. Rev. B*, 67:174116, 2003.
- [117] U. Häussermann, S. I. Simak, R. Ahuja, and B. Johansson. Metal-Nonmetal Transition in the Boron Group Elements. *Phys. Rev. Lett.*, 90:065701, 2003.
- [118] Y. Ma, J. S. Tse, D. D. Klug, and R. Ahuja. Electron-phonon coupling of α -Ga boron. *Phys. Rev. B*, 70:214107, 2004.
- [119] I. Boustani. Structure and stability of small boron clusters. A density functional theoretical study. *Chemical Physics Letters*, 240(1):135–140, 1995.
- [120] I. Boustani. New quasi-planar surfaces of bare boron. *Surface Science*, 370(2):355–363, 1997.
- [121] I. Boustani. Systematic ab initio investigation of bare boron clusters: mDetermination of the geometry and electronic structures of B_n ($n=2-14$). *Phys. Rev. B*, 55:16426–16438, 1997.
- [122] I. Boustani and A. Quandt. Nanotubules of bare boron clusters: Ab initio and density functional study. *Europhysics Letters*, 39(5):527, 1997.
- [123] D. Ciuparu, R. F. Klie, Y. Zhu, and L. Pfefferle. Synthesis of Pure Boron Single-Wall Nanotubes. *The Journal of Physical Chemistry B*, 108(13):3967–3969, 2004.
- [124] N. Gonzalez Szwacki, A. Sadrzadeh, and B. I. Yakobson. B_{80} Fullerene: An Ab Initio Prediction of Geometry, Stability, and Electronic Structure. *Phys. Rev. Lett.*, 98:166804, 2007.

- [125] H. Tang and S. Ismail-Beigi. Novel Precursors for Boron Nanotubes: The Competition of Two-Center and Three-Center Bonding in Boron Sheets. *Phys. Rev. Lett.*, 99:115501, 2007.
- [126] X. Yang, Y. Ding, and J. Ni. Ab initio prediction of stable boron sheets and boron nanotubes: Structure, stability, and electronic properties. *Phys. Rev. B*, 77:041402, 2008.
- [127] H. Tang and S. Ismail-Beigi. First-principles study of boron sheets and nanotubes. *Phys. Rev. B*, 82:115412, 2010.
- [128] Z. Zhang, E. S. Penev, and B. I. Yakobson. Two-dimensional boron: structures, properties and applications. *Chem. Soc. Rev.*, 46:6746–6763, 2017.
- [129] Evgeni E. S. Penev, S. Bhowmick, A. Sadrzadeh, and B. I. Yakobson. Polymorphism of Two-Dimensional Boron. *Nano Letters*, 12(5):2441–2445, 2012.
- [130] N. Karmodak and E. D. Jemmis. The Role of Holes in Borophenes: An Ab-Initio Study of Their Structure and Stability with and without Metal Templates. *Angewandte Chemie International Edition*, 56(34):10093–10097, 2017.
- [131] L. Z. Zhang, Q. B. Yan, S. X. Du, G. Su, and H.-J. Gao. Boron Sheet Adsorbed on Metal Surfaces: Structures and Electronic Properties. *The Journal of Physical Chemistry C*, 116(34):18202–18206, 2012.
- [132] Y. Liu, E. S. Penev, and B. I. Yakobson. Probing the Synthesis of Two-Dimensional Boron by First-Principles Computations. *Angewandte Chemie International Edition*, 52(11):3156–3159, 2013.
- [133] H. Liu, J. Gao, and J. Zhao. From Boron Cluster to Two-Dimensional Boron Sheet on Cu(111) surface: Growth Mechanism and Hole Formation. *Scientific Reports*, 3(1):3238, 2013.
- [134] Z. A. Piazza, H.-S. Hu, W.-L. Li, Y.-F. Zhao, J. Li, and L.-S. Wang. Planar hexagonal B₃₆ as a potential basis for extended single-atom layer boron sheets. *Nature Communications*, 5(1):3113, 2014.
- [135] G. Tai, T. Hu, Y. Zhou, X. Wang, J. Kong, T. Zeng, Y. You, and Q. Wang. Synthesis of Atomically Thin Boron Films on Copper Foils. *Angewandte Chemie International Edition*, 54(51):15473–15477, 2015.

- [136] Z. Zhang, Y. Yang, G. Gao, and B. I. Yakobson. Two-Dimensional Boron Monolayers Mediated by Metal Substrates. *Angewandte Chemie International Edition*, 54(44):13022–13026, 2015.
- [137] K. Wang, S. Choyal, J. E. Schultz, J. McKenzie, L. Li, X. Liu, and Nan N. Jiang. Borophene: Synthesis, Chemistry, and Electronic Properties. *ChemPlusChem*, n/a(n/a):e202400333, 2024.
- [138] B. Feng, J. Zhang, Q. Zhong, W. Li, S. Li, H. Li, P. Cheng, S. Meng, L. Chen, and K. Wu. Experimental realization of two-dimensional boron sheets. *Nature Chemistry*, 8(6):563–568, 2016.
- [139] X. Wu, J. Dai, Y. Zhao, Z. Zhuo, J. Yang, and X. C. Zeng. Two-Dimensional Boron Monolayer Sheets. *ACS Nano*, 6(8):7443–7453, 2012.
- [140] Q. Zhong, L. Kong, J. Gou, W. Li, S. Sheng, S. Yang, P. Cheng, H. Li, K. Wu, and L. Chen. Synthesis of borophene nanoribbons on Ag(110) surface. *Phys. Rev. Mater.*, 1:021001, 2017.
- [141] X. Liu, Z. Wei, I. Balla, A. J. Mannix, N. P. Guisinger, E. Luijten, and M. C. Hersam. Self-assembly of electronically abrupt borophene/organic lateral heterostructures. *Science Advances*, 3(2):e1602356, 2017.
- [142] W. Li, L. Kong, C. Chen, J. Gou, S. Sheng, W. Zhang, H. Li, L. Chen, P. Cheng, and K. Wu. Experimental realization of honeycomb borophene. *Science Bulletin*, 63(5):282–286, 2018.
- [143] X. Liu, Z. Zhang, L. Wang, B. I. Yakobson, and M. C. Hersam. Intermixing and periodic self-assembly of borophene line defects. *Nature Materials*, 17(9):783–788, 2018.
- [144] R. Wu, I. K. Drozdov, S. Eltinge, P. Zahl, S. Ismail-Beigi, I. Božović, and A. Gozar. Large-area single-crystal sheets of borophene on Cu(111) surfaces. *Nature Nanotechnology*, 14(1):44–49, 2019.
- [145] N. A. Vinogradov, A. Lyalin, T. Taketsugu, A. S. Vinogradov, and A. Preobrajenski. Single-Phase Borophene on Ir(111): Formation, Structure, and Decoupling from the Support. *ACS Nano*, 13(12):14511–14518, 2019.

- [146] B. Kiraly, X. Liu, L. Wang, Z. Zhang, A. J. Mannix, B. L. Fisher, B. I. Yakobson, M. C. Hersam, and N. P. Guisinger. Borophene Synthesis on Au(111). *ACS Nano*, 13(4):3816–3822, 2019.
- [147] X. Liu and M. C. Hersam. Borophene-graphene heterostructures. *Science Advances*, 5(10):eaax6444, 2019.
- [148] Y. Wang, L. Kong, C. Chen, P. Cheng, B. Feng, K. Wu, and L. Chen. Realization of Regular-Mixed Quasi-1D Borophene Chains with Long-Range Order. *Advanced Materials*, 32(48):2005128, 2020.
- [149] Z. Wu, G. Tai, W. Shao, R. Wang, and C. Hou. Experimental realization of quasicubic boron sheets. *Nanoscale*, 12:3787–3794, 2020.
- [150] A. B. Preobrajenski, A. Lyalin, T. Taketsugu, N. A. Vinogradov, and A. S. Vinogradov. Honeycomb Boron on Al(111): From the Concept of Borophene to the Two-Dimensional Boride. *ACS Nano*, 15(9):15153–15165, 2021.
- [151] L. Li, J. F. Schultz, S. Mahapatra, X. Liu, C. Shaw, X. Zhang, M. C. Hersam, and N. Jiang. Angstrom-Scale Spectroscopic Visualization of Interfacial Interactions in an Organic/Borophene Vertical Heterostructure. *Journal of the American Chemical Society*, 143(38):15624–15634, 2021.
- [152] M. G. Cuxart, K. Seufert, V. Chesnyak, W. A. Waqas, A. Robert, M.-L. Bocquet, G. S. Duesberg, H. Sachdev, and W. Auwärter. Borophenes made easy. *Science Advances*, 7(45):eabk1490, 2021.
- [153] K. M. Omambac, M. Petrović, P. Bampoulis, C. Brand, M. A. Kriegel, P. Dreher, D. Janoschka, U. Hagemann, N. Hartmann, P. Valerius, T. Michely, F. J. Meyer zu Heringdorf, and M. Horn von Hoegen. Segregation-Enhanced Epitaxy of Borophene on Ir(111) by Thermal Decomposition of Borazine. *ACS Nano*, 15(4):7421–7429, 2021.
- [154] Q. Li, V. S. C. Kolluru, M. S. Rahn, E. Schwenker, S. Li, R. G. Hennig, P. Darancet, M. K. Y. Chan, and M. C. Hersam. Synthesis of borophane polymorphs through hydrogenation of borophene. *Science*, 371(6534):1143–1148, 2021.
- [155] X. Liu, Q. Li, Q. Ruan, M. S. Rahn, B. I. Yakobson, and M. C. Hersam. Borophene synthesis beyond the single-atomic-layer limit. *Nature Materials*, 21(1):35–40, 2022.

- [156] P. Sutter, , and E. Sutter. Large-Scale Layer-by-Layer Synthesis of Borophene on Ru(0001). *Chemistry of Materials*, 33(22):8838–8843, 2021.
- [157] C. Chen, H. Lv, P. Zhang, Z. Zhuo, Y. Wang, C. Ma, W. Li, X. Wang, B. Feng, P. Cheng, X. Wu, K. Wu, and L. Chen. Synthesis of bilayer borophene. *Nature Chemistry*, 14(1):25–31, 2022.
- [158] R. Wu, S. Eltinge, I. K. Drozdov, A. Gozar, P. Zahl, J. T. Sadowski, S. Ismail-Beigi, and I. Božović. Micrometre-scale single-crystalline borophene on a square-lattice Cu(100) surface. *Nature Chemistry*, 14(4):377–383, 2022.
- [159] X. Liu, M. S. Rahn, Q. Ruan, B. I. Yakobson, and M. C. Hersam. Probing borophene oxidation at the atomic scale. *Nanotechnology*, 33(23):235702, 2022.
- [160] L. Li, J. F. Schultz, S. Mahapatra, Z. Lu, X. Zhang, and N. Jiang. Chemically identifying single adatoms with single-bond sensitivity during oxidation reactions of borophene. *Nature Communications*, 13(1):1796, 2022.
- [161] H. Li, J. Yang, Y. Ma, G. Liu, X. Xu, Z. Huo, J. Chen, J. Li, W. Zhang, K. Wang, L. Chen, and X. Xiao. Monolayer Borophene Formation on Cu(111) Surface Triggered by Step Edge. *Small*, 20(7):2303502, 2023.
- [162] H. Lv, C. Chen, W. Li, Z. Zhuo, P. Cheng, Y.-Q. Zhang, B. Feng, K. Wu, X. Wu, and L. Chen. Selective binding and periodic arrangement of magic boron clusters on monolayer borophene. *Proceedings of the National Academy of Sciences*, 120(11):e2215131120, 2023.
- [163] M. Jugovac, I. Cojocariu, C. A. Brondin, A. Crotti, M. Petrović, S. Bonetti, A. Locatelli, and T. O. Menteş. Coupling Borophene to Graphene in Air-Stable Heterostructures. *Advanced Electronic Materials*, 9(8):2300136, 2023.
- [164] K. M. Omambac, M. A. Kriegel, M. Petrović, B. Finke, C. Brand, F. J. Meyer zu Heringdorf, and M. Horn von Hoegen. Interplay of Kinetic Limitations and Disintegration: Selective Growth of Hexagonal Boron Nitride and Borophene Monolayers on Metal Substrates. *ACS Nano*, 17(18):17946–17955, 2023.
- [165] Q. Li, L. Wang, H. Li, M. K. Y. Chan, and M. C. Hersam. Synthesis of Quantum-Confined Borophene Nanoribbons. *ACS Nano*, 18(1):483–491, 2024.

- [166] X.-J. Weng, Y. Zhu, Y. Xu, J. Bai, Z. Zhang, B. Xu, X.-F. Zhou, and Y. Tian. Synthesis of Metalloborophene Nanoribbons on Cu(110). *Advanced Functional Materials*, 34(21):2314576, 2024.
- [167] H. Wang, P. Ding, G.-J. Xia, X. Zhao, W. E, M. Yu, Z. Ma, Y.G. Wang, L.-S. Wang, J. Li, and X. Yang. Formation of Supernarrow Borophene Nanoribbons. *Angewandte Chemie International Edition*, 63(28):e202406535, 2024.
- [168] B. Radatović, V. Jadriško, S. Kamal, M. Kralj, D. Novko, N. Vujičić, and M. Petrović. Macroscopic Single-Phase Monolayer Borophene on Arbitrary Substrates. *ACS Applied Materials & Interfaces*, 14(18):21727–21737, 2022.
- [169] Z. Wu, G. Tai, R. Liu, C. Hou, W. Shao, X. Liang, and Z. Wu. Van der Waals Epitaxial Growth of Borophene on a Mica Substrate toward a High-Performance Photodetector. *ACS Applied Materials & Interfaces*, 13(27):31808–31815, 2021.
- [170] Z. Wu, G. Tai, R. Liu, W. Shao, C. Hou, and X. Liang. Synthesis of borophene on quartz towards hydroelectric generators. *J. Mater. Chem. A*, 10:8218–8226, 2022.
- [171] H. Li, L. Jing, W. Liu, J. Lin, R. Y. Tay, S. H. Tsang, and E. H. T. Teo. Scalable Production of Few-Layer Boron Sheets by Liquid-Phase Exfoliation and Their Superior Supercapacitive Performance. *ACS Nano*, 12(2):1262–1272, 2018.
- [172] X. Ji, N. Kong, J. Wang, W. Li, Y. Xiao, S. T. Gan, Y. Zhang, Y. Li, X. Song, Q. Xiong, S. Shi, Z. Li, W. Tao, H. Zhang, L. Mei, and J. Shi. A Novel Top-Down Synthesis of Ultrathin 2D Boron Nanosheets for Multimodal Imaging-Guided Cancer Therapy. *Advanced Materials*, 30(36):1803031, 2018.
- [173] P. Ranjan, T. K. Sahu, R. Bhushan, S. S. R. K. C. Yamijala, D. J. Late, P. Kumar, and A. Vinu. Freestanding Borophene and Its Hybrids. *Advanced Materials*, 31(27):1900353, 2019.
- [174] F. Zhang, L. She, C. Jia, X. He, Q. Li, J. Sun, Z. Lei, and Z.-H. Liu. Few-layer and large flake size borophene: preparation with solvothermal-assisted liquid phase exfoliation. *RSC Adv.*, 10:27532–27537, 2020.

- [175] S. Chahal, P. Ranjan, M. Motlag, S. S. R. K. C. Yamijala, D. J. Late, E. H. S. Sadki, G. J. Cheng, and P. Kumar. Borophene via Micromechanical Exfoliation. *Advanced Materials*, 33(34):2102039, 2021.
- [176] H. Lin, H. Shi, Z. Wang, Y. Mu, S. Li, J. Zhao, J. Guo, B. Yang, Z.-S. Wu, and F. Liu. Scalable Production of Freestanding Few-Layer β_{12} -Borophene Single Crystalline Sheets as Efficient Electrocatalysts for Lithium–Sulfur Batteries. *ACS Nano*, 15(11):17327–17336, 2021.
- [177] K. Sielicki, K. Maślana, X. Chen, and E. Mijowska. Bottom up approach of metal assisted electrochemical exfoliation of boron towards borophene. *Scientific Reports*, 12(1):15683, 2022.
- [178] M. A. Chowdhury, M. M. K. Uddin, Md. B. A. Shuvho, M. Rana, and N. Hossain. A novel temperature dependent method for borophene synthesis. *Applied Surface Science Advances*, 11:100308, 2022.
- [179] K. Ledwaba, S. Karimzadeh, and T.-C. Jen. Emerging borophene two-dimensional nanomaterials for hydrogen storage. *Materials Today Sustainability*, 22:100412, 2023.
- [180] M. Ou, X. Wang, L. Yu, C. Liu, W. Tao, X. Ji, and L. Mei. The Emergence and Evolution of Borophene. *Advanced Science*, 8(12):2001801, 2021.
- [181] G. J. Adekoya, O. C. Adekoya, M. Muloiwa, E. R. Sadiku, W. K. Kupolati, and Y. Hamam. Advances In Borophene: Synthesis, Tunable Properties, and Energy Storage Applications. *Small*, n/a(n/a):2403656, 2024.
- [182] M. A. Mohebpour, S. M. Mozvashi, S. I. Vishkayi, and M. B. Tagani. Transition from metal to semiconductor by semi-hydrogenation of borophene. *Phys. Rev. Mater.*, 6:014012, 2022.
- [183] B. Feng, J. Zhang, R.-Y. Liu, T. Iimori, C. Lian, H. Li, L. Chen, K. Wu, S. Meng, F. Komori, and I. Matsuda. Direct evidence of metallic bands in a monolayer boron sheet. *Phys. Rev. B*, 94:041408, 2016.
- [184] B. Feng, O. Sugino, R.-Y. Liu, J. Zhang, R. Yukawa, M. Kawamura, T. Iimori, H. Kim, Y. Hasegawa, H. Li, L. Chen, K. Wu, H. Kumigashira, F. Komori, T.-C. Chiang, S. Meng, and I. Matsuda. Dirac Fermions in Borophene. *Phys. Rev. Lett.*, 118:096401, 2017.

- [185] B. Feng, J. Zhang, S. Ito, M. Arita, C. Cheng, L. Chen, K. Wu, F. Komori, O. Sugino, K. Miyamoto, T. Okuda, S. Meng, and I. Matsuda. Discovery of 2D Anisotropic Dirac Cones. *Advanced Materials*, 30(2):1704025, 2018.
- [186] L.-C. Xu, A. Du, and L. Kou. Hydrogenated borophene as a stable two-dimensional dirac material with an ultrahigh fermi velocity. *Phys. Chem. Chem. Phys.*, 18:27284–27289, 2016.
- [187] H. Xiao, W. Cao, T. Ouyang, S. Guo, C. He, and J. Zhong. Lattice thermal conductivity of borophene from first principle calculation. *Scientific Reports*, 7(1):45986, 2017.
- [188] H. Zhou, Y. Cai, G. Zhang, and Y.-W. Zhang. Superior lattice thermal conductance of single-layer borophene. *npj 2D Materials and Applications*, 1(1):14, 2017.
- [189] J. He, D. Li, Y. Ying, C. Feng, J. He, C. Zhong, H. Zhou, P. Zhou, and G. Zhang. Orbitally driven giant thermal conductance associated with abnormal strain dependence in hydrogenated graphene-like borophene. *npj Computational Materials*, 5(1):47, 2019.
- [190] R. Jian, S. Wu, B. Zhao, and G. Xiong. Tunable multi-peak perfect absorbers based on borophene for high-performance near-infrared refractive index sensing. *Optical Materials*, 131:112751, 2022.
- [191] V. Nagarajan and R. Chandiramouli. Borophene nanosheet molecular device for detection of ethanol – A first-principles study. *Computational and Theoretical Chemistry*, 1105:52–60, 2017.
- [192] J. Shen, Z. Yang, Y. Wang, L.-C. Xu, R. Liu, and X. Liu. The gas sensing performance of borophene/MoS₂ heterostructure. *Applied Surface Science*, 504:144412, 2020.
- [193] Q. Lin, L. Miao, Z. Qian, Y. Sun, and R. Wang. First-Principles Calculations on Magnetism Induced by Vacancies in β_{12} -Borophene Nanosheets: Implications for Property Modulation. *ACS Applied Nano Materials*, 5(1):113–119, 2022.
- [194] Q.-L. Lin, H. Liang, C.-Q. Zhou, Z.-F. Qian, Y.-L. Sun, X.-Y. Wang, and R.-H. Wang. Defect-induced magnetism in χ_3 borophene. *Rare Metals*, 41(10):3486–3494, 2022.
- [195] J. Jiang, X. Wang, and Y. Song. Tunable magnetic and electronic properties in 3d transition-metal adsorbed β_{12} and χ_3 borophene. *Computational Materials Science*, 153:10–15, 2018.

- [196] J. Ye, Z. Feng, H. Li, and X. Dai. DFT+U study on the magnetic properties of 3d transition metal doped β_{12} borophene. *Physica E: Low-dimensional Systems and Nanostructures*, 147:115576, 2023.
- [197] X. Zhang, Y. Sun, L. Ma, X. Zhao, and X. Yao. Modulating the electronic and magnetic properties of bilayer borophene via transition metal atoms intercalation: from metal to half metal and semiconductor. *Nanotechnology*, 29(30):305706, 2018.
- [198] J. Bardeen, L. N. Cooper, and J. R. Schrieffer. Theory of Superconductivity. *Phys. Rev.*, 108:1175–1204, 1957.
- [199] G. Profeta, M. Calandra, and F. Mauri. Phonon-mediated superconductivity in graphene by lithium deposition. *Nature Physics*, 8(2):131–134, 2012.
- [200] W. Wan, Y. Ge, F. Yang, and Y. Yao. Phonon-mediated superconductivity in silicene predicted by first-principles density functional calculations. *Europhysics Letters*, 104(3):36001, 2013.
- [201] D. F. Shao, W. J. Lu, H. Y. Lv, and Y. P. Sun. Electron-doped phosphorene: A potential monolayer superconductor. *Europhysics Letters*, 108(6):67004, 2014.
- [202] J. Nagamatsu, N. Nakagawa, T. Muranaka, Y. Zenitani, and J. Akimitsu. Superconductivity at 39 K in magnesium diboride. *Nature*, 410(6824):63–64, 2001.
- [203] E. S. Penev, A. Kutana, and B. I. Yakobson. Can Two-Dimensional Boron Superconduct? *Nano Letters*, 16(4):2522–2526, 2016.
- [204] Y. Zhao, S. Zeng, and J. Ni. Superconductivity in two-dimensional boron allotropes. *Phys. Rev. B*, 93:014502, 2016.
- [205] R. C. Xiao, D. F. Shao, W. J. Lu, H. Y. Lv, J. Y. Li, and Y. P. Sun. Enhanced superconductivity by strain and carrier-doping in borophene: A first principles prediction. *Applied Physics Letters*, 109(12):122604, 2016.
- [206] M. Gao, Q.-Z. Li, X.-W. Yan, and J. Wang. Prediction of phonon-mediated superconductivity in borophene. *Phys. Rev. B*, 95:024505, 2017.

- [207] C. Cheng, J.-T. Sun, H. Liu, H.-X. Fu, J. Zhang, X.-R. Chen, and S. Meng. Suppressed superconductivity in substrate-supported β_{12} borophene by tensile strain and electron doping. *2D Materials*, 4(2):025032, 2017.
- [208] Y. Zhao, S. Zeng, C. Lian, Z. Dai, S. Meng, and J. Ni. Multigap anisotropic superconductivity in borophenes. *Phys. Rev. B*, 98:134514, 2018.
- [209] S. Sheng, J.-B. Wu, X. Cong, Q. Zhong, W. Li, W. Hu, J. Gou, P. Cheng, P.-H. Tan, L. Chen, and K. Wu. Raman Spectroscopy of Two-Dimensional Borophene Sheets. *ACS Nano*, 13(4):4133–4139, 2019.
- [210] A. Meninno and I. Errea. Absence of sizable superconductivity in hydrogen boride: A first-principles study. *Phys. Rev. B*, 106:214508, 2022.
- [211] X. Li, A. Kutana, E. S. Penev, and B. I. Yakobson. Limits of Hydrogen-Boosted Superconductivity in Borophene. *The Journal of Physical Chemistry C*, 128(1):483–488, 2024.
- [212] S.-Y. Xie, X.-B. Li, W. Q. Tian, N.-K. Chen, Y. Wang, S. Zhang, and H.-B. Sun. A novel two-dimensional MgB_6 crystal: metal-layer stabilized boron kagome lattice. *Phys. Chem. Chem. Phys.*, 17:1093–1098, 2015.
- [213] J.-H. Liao, Y.-C. Zhao, Y.-J. Zhao, H. Xu, and X.-B. Yang. Phonon-mediated superconductivity in Mg intercalated bilayer borophenes. *Phys. Chem. Chem. Phys.*, 19:29237–29243, 2017.
- [214] T. Bo, P.-F. Liu, L. Yan, and B.-T. Wang. Electron-phonon coupling superconductivity in two-dimensional orthorhombic MB_6 ($M = \text{Mg}, \text{Ca}, \text{Ti}, \text{Y}$) and hexagonal MB_6 ($M = \text{Mg}, \text{Ca}, \text{Sc}, \text{Ti}$). *Phys. Rev. Mater.*, 4:114802, 2020.
- [215] C. Sevik, J. Bekaert, M. Petrov, and M. V. Milošević. High-temperature multigap superconductivity in two-dimensional metal borides. *Phys. Rev. Mater.*, 6:024803, 2022.
- [216] L. Yan, R. Ku, J. Zou, L. Zhou, J. Zhao, X. Jiang, and B.-T. Wang. Prediction of superconductivity in bilayer borophenes. *RSC Adv.*, 11:40220–40227, 2021.
- [217] Y. Mu, B.-T. Wang, S.-D. Li, and F. Ding. A family of superconducting boron crystals made of stacked bilayer borophenes. *Nanoscale*, 14:9754–9761, 2022.

- [218] R. M. Martin. *Electronic Structure: Basic Theory and Practical Methods*. Cambridge University Press, Cambridge, 2004.
- [219] E. Engel and R. M. Dreizler. *Density Functional Theory: An Advanced Course*. Theoretical and Mathematical Physics. Springer Berlin Heidelberg, 2011.
- [220] F. Finocchi. *Density Functional Theory for Beginners Basic Principles and Practical Approaches*. 2011.
- [221] F. Giustino. *Materials Modelling Using Density Functional Theory: Properties and Predictions*. Oxford University Press, 2014.
- [222] D. S. Sholl and J. A. Steckel. *Density Functional Theory: A Practical Introduction*. Wiley, 2023.
- [223] E. Cancès and G. Friesecke. *Density Functional Theory: Modeling, Mathematical Analysis, Computational Methods, and Applications*. Mathematics and Molecular Modeling. Springer International Publishing, 2023.
- [224] L. H. Thomas. Inhomogeneous electron gas. In *Proc. Cambridge Phil. Roy. Soc*, volume 23, pages 542–548, 1927.
- [225] E. Fermi. Un metodo statistico per la determinazione di alcune priorietà dell’atome. *Rend. Accad. Naz. Lincei*, 6(602–607):32, 1927.
- [226] P. Hohenberg and W. Kohn. Inhomogeneous Electron Gas. *Phys. Rev.*, 136:B864–B871, 1964.
- [227] W. Kohn and L. J. Sham. Self-Consistent Equations Including Exchange and Correlation Effects. *Phys. Rev.*, 140:A1133–A1138, 1965.
- [228] J. Harris. Adiabatic-connection approach to Kohn-Sham theory. *Phys. Rev. A*, 29:1648–1659, 1984.
- [229] J. P. Perdew, K. Burke, and M. Ernzerhof. Generalized Gradient Approximation Made Simple. *Phys. Rev. Lett.*, 77:3865–3868, 1996.
- [230] H. J. Monkhorst and J. D. Pack. Special points for Brillouin-zone integrations. *Phys. Rev. B*, 13:5188–5192, 1976.

- [231] M. Methfessel and A. T. Paxton. High-precision sampling for brillouin-zone integration in metals. *Phys. Rev. B*, 40:3616–3621, 1989.
- [232] P. E. Blöchl. Projector augmented-wave method. *Phys. Rev. B*, 50:17953–17979, 1994.
- [233] P. Giannozzi, O. Andreussi, T. Brumme, O. Bunau, M. B. Nardelli, M. Calandra, R. Car, C. Cavazzoni, D. Ceresoli, M. Cococcioni, N. Colonna, I. Carnimeo, A. Dal Corso, S. de Gironcoli, P. Delugas, R. A. DiStasio, A. Ferretti, A. Floris, G. Fratesi, G. Fugallo, R. Gebauer, U. Gerstmann, F. Giustino, T. Gorni, J. Jia, M. Kawamura, H.-Y. Ko, A. Kokalj, E. Küçükbenli, M. Lazzeri, M. Marsili, N. Marzari, F. Mauri, N. L. Nguyen, H.-V. Nguyen, A. Otero de-la Roza, L. Paulatto, S. Poncé, D. Rocca, R. Sabatini, B. Santra, M. Schlipf, A. P. Seitsonen, A. Smogunov, I. Timrov, T. Thonhauser, P. Umari, N. Vast, X. Wu, and S. Baroni. Advanced capabilities for materials modelling with Quantum ESPRESSO. *Journal of Physics: Condensed Matter*, 29(46):465901, 2017.
- [234] G. Kresse and J. Furthmüller. Efficient iterative schemes for ab initio total-energy calculations using a plane-wave basis set. *Phys. Rev. B*, 54:11169–11186, 1996.
- [235] P. Blaha, K. Schwarz, F. Tran, R. Laskowski, G. H. K. Madsen, and L. D. Marks. WIEN2k: An APW+lo program for calculating the properties of solids. *The Journal of Chemical Physics*, 152(7):074101, 2020.
- [236] U. von Barth and L. Hedin. A local exchange-correlation potential for the spin polarized case. i. *Journal of Physics C: Solid State Physics*, 5(13):1629, 1972.
- [237] R. Zeller. Spin-polarized DFT calculations and magnetism. *Computational Nanoscience*, 31:419–445, 2006.
- [238] G. Bihlmayer. Non-collinear magnetism: Exchange parameter and T_c. *Computational Nanoscience: Do it Yourself*, 31:447–467, 2006.
- [239] G. Bihlmayer. Density-functional Theory of Magnetism. *Handbook of magnetism and advanced magnetic materials*, 2007.
- [240] Wanda Andreoni and Sidney Yip. Theory and Methods for Materials Modeling: An Introduction. *Handbook of Materials Modeling: Methods: Theory and Modeling*, pages 3–12, 2020.

- [241] N. D. Mermin and H. Wagner. Absence of Ferromagnetism or Antiferromagnetism in One- or Two-Dimensional Isotropic Heisenberg Models. *Phys. Rev. Lett.*, 17:1133–1136, 1966.
- [242] H. J. F. Jansen. Magnetic anisotropy in density-functional theory. *Phys. Rev. B*, 38:8022–8029, 1988.
- [243] V. P. Antropov, M. I. Katsnelson, B. N. Harmon, M. van Schilfgaarde, and D. Kusnezov. Spin dynamics in magnets: Equation of motion and finite temperature effects. *Phys. Rev. B*, 54:1019–1035, 1996.
- [244] P. H. Dederichs, S. Blügel, R. Zeller, and H. Akai. Ground States of Constrained Systems: Application to Cerium Impurities. *Phys. Rev. Lett.*, 53:2512–2515, 1984.
- [245] P.-W. Ma and S. L. Dudarev. Constrained density functional for noncollinear magnetism. *Phys. Rev. B*, 91:054420, 2015.
- [246] Y. Ahn, X. Guo, S. Son, Z. Sun, and L. Zhao. Progress and prospects in two-dimensional magnetism of van der Waals materials. *Progress in Quantum Electronics*, 93:100498, 2024.
- [247] D. I. Khomskii. *Transition Metal Compounds*. Cambridge University Press, 2014.
- [248] M. Getzlaff. *Fundamentals of magnetism*. Springer Science & Business Media, 2007.
- [249] S. Blundell. *Magnetism in condensed matter*. OUP Oxford, 2001.
- [250] E. Koch. Exchange mechanisms. *Correlated electrons: from models to materials*, 2:1–31, 2012.
- [251] C. Timm. *Theory of Magnetism: International Max Planck Research School for Dynamical Processes in Atoms. Molecules and Solids* (Technische Univ. Dresden, Institute for Theoretical Physics, Dresden, Germany, 2015), 2011.
- [252] A. Tsirlin. *Theory of Magnetism*. Experimentalphysik VI Universität Augsburg, 2022.
- [253] X. Li, H. Yu, F. Lou, J. Feng, M.-H. Whangbo, and H. Xiang. Spin Hamiltonians in Magnets: Theories and Computations. *Molecules*, 26(4), 2021.

- [254] P. W. Anderson. Antiferromagnetism. Theory of Superexchange Interaction. *Phys. Rev.*, 79:350–356, 1950.
- [255] J. B. Goodenough. Theory of the Role of Covalence in the Perovskite-Type Manganites $[\text{La}, M(\text{II})]\text{MnO}_3$. *Phys. Rev.*, 100:564–573, 1955.
- [256] J. Kanamori. Superexchange interaction and symmetry properties of electron orbitals. *Journal of Physics and Chemistry of Solids*, 10(2):87–98, 1959.
- [257] I. Dzyaloshinsky. A thermodynamic theory of “weak” ferromagnetism of antiferromagnetics. *Journal of Physics and Chemistry of Solids*, 4(4):241–255, 1958.
- [258] T. Moriya. Anisotropic Superexchange Interaction and Weak Ferromagnetism. *Phys. Rev.*, 120:91–98, 1960.
- [259] J. L. Lado and J. Fernández-Rossier. On the origin of magnetic anisotropy in two dimensional CrI_3 . *2D Materials*, 4(3):035002, 2017.
- [260] D. Šabani, C. Bacaksiz, and M. V. Milošević. Ab initio methodology for magnetic exchange parameters: Generic four-state energy mapping onto a Heisenberg spin Hamiltonian. *Phys. Rev. B*, 102:014457, Jul 2020.
- [261] X. He, N. Helbig, M. J. Verstraete, and E. Bousquet. TB2J: A python package for computing magnetic interaction parameters. *Computer Physics Communications*, 264:107938, 2021.
- [262] A. I. Liechtenstein, M. I. Katsnelson, V. P. Antropov, and V. A. Gubanov. Local spin density functional approach to the theory of exchange interactions in ferromagnetic metals and alloys. *Journal of Magnetism and Magnetic Materials*, 67(1):65–74, 1987.
- [263] J. Wolfhard. Monte Carlo simulations of spin systems. In *Computational Physics: Selected Methods Simple Exercises Serious Applications*, pages 10–43. Springer, 1996.
- [264] G. P. Müller, M. Hoffmann, C. Dißelkamp, D. Schürhoff, S. Mavros, M. Sallermann, N. S. Kiselev, H. Jónsson, and S. Blügel. Spirit: Multifunctional framework for atomistic spin simulations. *Phys. Rev. B*, 99:224414, 2019.
- [265] P. A. Serena, N. Garcí'a, and A. Levanyuk. Monte Carlo calculations on the two-dimensional anisotropic Heisenberg model. *Phys. Rev. B*, 47:5027–5036, 1993.

- [266] S. Baroni, S. de Gironcoli, A. Dal Corso, and P. Giannozzi. Phonons and related crystal properties from density-functional perturbation theory. *Rev. Mod. Phys.*, 73:515–562, 2001.
- [267] R. Heid. 12 Density Functional Perturbation Theory and Electron Phonon Coupling. *Emergent Phenomena in Correlated Matter*, 2013.
- [268] R. Heid. Electron-phonon coupling. *Lecture Notes of the Autumn School on Correlated Electrons*; Pavarini, E., Koch, E., Scalettar, R., Martin, R., Eds, pages 399–427, 2017.
- [269] S. Yip. *Handbook of materials modeling*. Springer Science & Business Media, 2007.
- [270] M. Verstraete and Z. Zanolli. *Density Functional Perturbation Theory*. 2014.
- [271] S. Baroni, P. Giannozzi, and A. Testa. Green’s-function approach to linear response in solids. *Phys. Rev. Lett.*, 58:1861–1864, 1987.
- [272] X. Gonze. Adiabatic density-functional perturbation theory. *Phys. Rev. A*, 52:1096–1114, 1995.
- [273] S. de Gironcoli. Lattice dynamics of metals from density-functional perturbation theory. *Phys. Rev. B*, 51:6773–6776, 1995.
- [274] C. Kittel and P. McEuen. *Introduction to solid state physics*. John Wiley & Sons, 2018.
- [275] M. A. Stroschio and M. Dutta. *Phonons in Nanostructures*. Cambridge University Press, 2001.
- [276] L. A. Falkovsky. Symmetry constraints on phonon dispersion in graphene. *Physics Letters A*, 372(31):5189–5192, 2008.
- [277] L. Lindsay and T. Pandey. 6 - Modeling phonons in nanomaterials. In V. K. Tewary and Y. Zhang, editors, *Modeling, Characterization, and Production of Nanomaterials (Second Edition)*, Woodhead Publishing Series in Electronic and Optical Materials, pages 125–149. Woodhead Publishing, second edition edition, 2023.
- [278] C. Lin, S. Ponc e, and N. Marzari. General invariance and equilibrium conditions for lattice dynamics in 1D, 2D, and 3D materials. *npj Computational Materials*, 8(1):236, 2022.

- [279] M. Born and K. Huang. *Dynamical theory of crystal lattices*. Oxford university press, 1996.
- [280] E. Mariani and F. von Oppen. Flexural Phonons in Free-Standing Graphene. *Phys. Rev. Lett.*, 100:076801, 2008.
- [281] Feliciano Giustino. Electron-phonon interactions from first principles. *Rev. Mod. Phys.*, 89:015003, Feb 2017.
- [282] F. Bloch. Über die Quantenmechanik der Elektronen in Kristallgittern. *Zeitschrift für Physik*, 52(7):555–600, 1929.
- [283] N. F. Mott and H. Jones. *The theory of the properties of metals and alloys*. 1936.
- [284] J. Bardeen. Conductivity of Monovalent Metals. *Phys. Rev.*, 52:688–697, 1937.
- [285] J. Bardeen and D. Pines. Electron-Phonon Interaction in Metals. *Phys. Rev.*, 99:1140–1150, 1955.
- [286] D. Möckli and M. Azambuja. Magnetic superconductivity. *Revista Brasileira de Ensino de Física*, 46, 2024.
- [287] J. Schmalian. *Microscopic Theory of Superconductivity*. 2015.
- [288] J. Bekaert. *Ab Initio Description of Multicomponent Superconductivity in Bulk to Atomically Thin Materials: Proefschrift*. PhD thesis, University of Antwerp, 2018.
- [289] A. B. Migdal. Interaction between electrons and lattice vibrations in a normal metal. *Soviet Physics - JETP*, 7(6):996–1001, 1958.
- [290] G. M. Eliashberg. Interactions between electrons and lattice vibrations in a superconductor. *Soviet Physics - JETP*, 11(3):696–702, 1960.
- [291] G. M. Eliashberg. Temperature Green's Function for Electrons in a Superconductor. *Soviet Physics - JETP*, 112(5):1000–1002, 1961.
- [292] T. Uchihashi. Two-dimensional superconductors with atomic-scale thickness. *Superconductor Science and Technology*, 30(1):013002, 2016.
- [293] L. N. Oliveira, E. K. U. Gross, and W. Kohn. Density-Functional Theory for Superconductors. *Phys. Rev. Lett.*, 60:2430–2433, 1988.

- [294] C. Pellegrini and A. Sanna. Ab initio methods for superconductivity. *Nature Reviews Physics*, 6(8):509–523, 2024.
- [295] G. A. C. Ummarino. 13 Eliashberg Theory. *Emergent Phenomena in Correlated Matter*, 2013.
- [296] P. B. Allen and B. Mitrović. Theory of superconducting T_c . *Solid state physics*, 37:1–92, 1983.
- [297] N. B. Kopnin. *Theory of nonequilibrium superconductivity*, volume 110. Oxford University Press, 2001.
- [298] E. R. Margine and F. Giustino. Anisotropic Migdal-Eliashberg theory using Wannier functions. *Phys. Rev. B*, 87:024505, 2013.
- [299] F. Marsiglio, M. Schossmann, and J. P. Carbotte. Iterative analytic continuation of the electron self-energy to the real axis. *Phys. Rev. B*, 37:4965–4969, 1988.
- [300] W. L. McMillan. Transition Temperature of Strong-Coupled Superconductors. *Phys. Rev.*, 167:331–344, 1968.
- [301] P. B. Allen and R. C. Dynes. Transition temperature of strong-coupled superconductors reanalyzed. *Phys. Rev. B*, 12:905–922, 1975.
- [302] J. Noffsinger, F. Giustino, B. D. Malone, C.-H. Park, S. G. Louie, and M. L. Cohen. EPW: a program for calculating the electron–phonon coupling using maximally localized wannier functions. *Computer Physics Communications*, 181(12):2140–2148, 2010.
- [303] F. Giustino, M. L. Cohen, and S. G. Louie. Electron-phonon interaction using Wannier functions. *Phys. Rev. B*, 76:165108, 2007.
- [304] D. Torelli and T. Olsen. Calculating critical temperatures for ferromagnetic order in two-dimensional materials. *2D Materials*, 6(1):015028, 2018.
- [305] J. Bekaert, A. Aperis, B. Partoens, P. M. Oppeneer, and M. V. Milošević. Evolution of multigap superconductivity in the atomically thin limit: Strain-enhanced three-gap superconductivity in monolayer MgB_2 . *Phys. Rev. B*, 96:094510, 2017.

- [306] N. Marzari and D. Vanderbilt. Maximally localized generalized wannier functions for composite energy bands. *Physical review B*, 56(20):12847, 1997.
- [307] I. Souza, N. Marzari, and D. Vanderbilt. Maximally localized Wannier functions for entangled energy bands. *Phys. Rev. B*, 65:035109, 2001.
- [308] N. Marzari, I. Souza, and D. Vanderbilt. An introduction to maximally-localized Wannier functions. *Psi-K newsletter*, 57:129, 2003.
- [309] A. Togo. First-principles Phonon Calculations with Phonopy and Phono3py. *J. Phys. Soc. Jpn.*, 92(1):012001, 2023.
- [310] T. Chida and R. Masuki. Algorithm Improvement for Finite-Temperature Structural Optimization Using Anharmonic Phonon Theory. 2024.
- [311] M. J. Van Setten, M. Giantomassi, E. Bousquet, M. J. Verstraete, D. R. Hamann, X. Gonze, and G.-M. Rignanese. The Pseudodojo: Training and grading a 85 element optimized norm-conserving pseudopotential table. *Computer Physics Communications*, 226:39–54, 2018.
- [312] T. Brumme, M. Calandra, and F. Mauri. Electrochemical doping of few-layer ZrNCl from first principles: Electronic and structural properties in field-effect configuration. *Phys. Rev. B*, 89:245406, 2014.

Curriculum Vitae

Personal informations

Name : [Božidar Šoškić](#)

Date of birth : [26/02/1995](#)

Place of birth : [Einsiedeln, Switzerland](#)

Nationality : [Montenegrin](#)

Address : [Pešca III, 84300, Berane, MNE](#)

Email address : bozidarsoskic@edu.ucg.ac.me;

bozidarsoskic95@gmail.com



Education

- **2009–2013** DIPLOMA OF GRADUATION

Secondary school “Panto Mališić” Berane, Montenegro

- **2013–2016** BSC PHYSICS (8.42)

Faculty of Natural Sciences and Mathematics, University of Montenegro

- **2016–2017** SPECIALIST DEGREE IN PHYSICS (9.07)

Thesis title: “Overview of types of magnetic ordering in crystals”

Faculty of Natural Sciences and Mathematics, University of Montenegro

- **2017–2018** MSC PHYSICS (10.00)

Thesis title: “Magnetic impurities in two-dimensional (2D) materials with structural point defects”

Faculty of Natural Sciences and Mathematics, University of Montenegro

- **2019–2025** PHD PHYSICS (10.00)

Thesis title: “Magnetism and superconductivity in two-dimensional (2D) boron crystal structures”

Faculty of Natural Sciences and Mathematics, University of Montenegro

- **2022–2025** PHD PHYSICS (10.00)

Thesis title: “Magnetism and superconductivity in two-dimensional (2D) boron crystal structures”

Department of Physics, University of Antwerp, Belgium

Language skills

Montenegrin (*native*), English (*fluent*), German (*fluent*)

Computational skills

Programming languages: C, C++, Fortran, Python, and Matlab

Software packages for *ab initio* calculations: Wannier90, TB2J, Fleur, EPW, Quantum ESPRESSO, GPAW, Abinit, Phonopy and VASP

Honours and awards

- **2013** Diploma “Luča” for obtaining the highest grades in all subjects in primary and secondary school
- **2015** The third place at the competition for best student ideas – WBC Inno, TEMPUS IV, and University of Montenegro
- **2019** Scholarship for the doctoral research of the Ministry of Science of Montenegro
- **2021** *Erasmus+ mobility* scholarship at the University of Belgrade, Serbia – *winter semester*
- **2023** Doctoral scholarship holder – University of Antwerp, Belgium

Projects

- **2019** Tier-0 computational project – PRACE DECI 15 SACandM – KTH-Beskow supercomputer, Sweden
- **2022** STSM – COST action, project No. CA16218
Title: Superconductivity in doped bilayer borophene

- **2022** BOF project at the University of Antwerp, Belgium
Title: Functional materials based on borophene
- **2023** Tier-1 computational project – the Flemish Supercomputer Center (Vlaams Supercomputer Centrum - VSC), Belgium
- **2024** National research project – Ministry of Science and Technological Development of Montenegro

Conferences and seminars

- **2021** Centre Européen de Calcul Atomique et Moléculaire, Germany
All electron DFT with Fleur – a Hands-on Tutorial
- **2021** The Abdus Salam International Centre for Theoretical Physics, Italy
MaX School on Advanced Materials and Molecular Modelling with Quantum ESPRESSO
- **2021** Centre Européen de Calcul Atomique et Moléculaire, Italy
GPAW 2021: Users and Developers Meeting
- **2023** International meeting on superconducting quantum materials and nanodevices, COST, Budva, Montenegro
- **2023** Symposium on Condensed Matter Physics, Belgrade, Serbia

List of publications

- B. N. Šoškić, S. Stavrić, and Ž. Šljivančanin, Ab-initio and Monte Carlo study of Fe-based two-dimensional magnets at borophene supported by Ag(111) surface. *Physical Review Materials*, 5:074001, 2021.

- <https://link.aps.org/doi/10.1103/PhysRevMaterials.5.074001>

- B. N. Šoškić, J. Bekaert, C. Sevik, Ž. Šljivančanin, and M. V. Milošević. First-principles exploration of superconductivity in intercalated bilayer borophene phases. *Physical Review Materials*, 8:064803, 2024.

- <https://link.aps.org/doi/10.1103/PhysRevMaterials.8.064803>

- B. N. Šoškić, J. Bekaert, C. Sevik, and M. V. Milošević, Enhanced superconductivity of hydrogenated β_{12} borophene. *Nano Letters*, 24(40):12650–12657, 2024.

- <https://doi.org/10.1021/acs.nanolett.4c03845>

Izjava o autorstvu

Potpisani-a: Božidar Šoškić

Broj indeksa/upisa: 2/18

IZJAVLJUJEM

da je doktorska disertacija pod naslovom: MAGNETIZAM I SUPERPROVODLJIVOST U DVODIMENZIONALNIM (2D) KRISTALNIM STRUKTURAMA BORA

- rezultat sopstvenog istraživačkog rada,
- da predložena disertacija ni u cjelini ni u djelovima nije bila predložena za dobijanje bilo koje diplome prema studijskim programima drugih ustanova visokog obrazovanja, da su rezultati korektno navedeni, i
- da nijesam povrijedio autorska i druga prava intelektualne svojine koja pripadaju trećim licima.

U Podgorici

Potpis doktoranda:

Božidar Šoškić

**Izjava o istovjetnosti štampane i elektronske verzije
doktorskog rada**

Ime i prezime autora: Božidar Šoškić

Broj indeksa/upisa: 2/18

Studijski program: Fizika

Naslov rada: MAGNETIZAM I SUPERPROVODLJIVOST U DVODIMENZIONALNIM
(2D) KRISTALNIM STRUKTURAMA BORA

Mentor I (UCG): Predrag Miranović

Mentor II (UCG): Željko Šljivančanin

Mentor I (UA): Milorad Milošević

Potpisani-a: Božidar Šoškić

Izjavljujem da je štampana verzija mog doktorskog rada istovjetna elektronskoj verziji koju sam predao za objavljivanje u Digitalni arhiv Univerziteta Crne Gore.

Istovremeno izjavljujem da dozvoljavam objavljivanje mojih ličnih podataka u vezi sa dobijanjem akademskog naziva doktora nauka, odnosno zvanja doktora umjetnosti, kao što su ime i prezime, godina i mjesto rođenja, naziv disertacije i datum odbrane rada.

U Podgorici

Potpis doktoranda:

Božidar Šoškić

Izjava o korišćenju

Ovlašćujem Univerzitetsku biblioteku da u Digitalni arhiv Univerziteta Crne Gore pohrani moju doktorsku disertaciju pod naslovom:

MAGNETIZAM I SUPERPROVODLJIVOST U DVODIMENZIONALNIM (2D)
KRISTALNIM STRUKTURAMA BORA

koja je moje autorsko djelo.

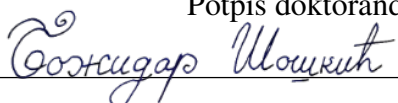
Disertaciju sa svim priložima predao sam u elektronskom formatu pogodnom za trajno arhiviranje.

Moju doktorsku disertaciju pohranjenu u Digitalni arhiv Univerziteta Crne Gore mogu da koriste svi koji poštuju odredbe sadržane u odabranom tipu licence Kreativne zajednice (Creative Commons) za koju sam odlučio.

1. Autorstvo
2. Autorstvo – nekomercijalno
3. Autorstvo – nekomercijalno – bez prerade
3. 4. Autorstvo - nekomercijalno - dijeliti pod istim uslovima
5. Autorstvo – bez prerade
6. Autorstvo – dijeliti pod istim uslovima

U Podgorici

Potpis doktoranda:



1. Autorstvo – Dozvoljavate umnožavanje, distribuciju i javno saopštavanje djela, i prerade, ako se navede ime autora na način određen od strane autora ili davaoca licence, čak i u komercijalne svrhe. Ovo je najslobodnija od svih licenci.
2. Autorstvo – nekomercijalno. Dozvoljavate umnožavanje, distribuciju i javno saopštavanje djela, i prerade, ako se navede ime autora na način određen od strane autora ili davaoca licence. Ova licenca ne dozvoljava komercijalnu upotrebu djela.
3. Autorstvo – nekomercijalno – bez prerade. Dozvoljavate umnožavanje, distribuciju i javno saopštavanje djela, bez promjena, preoblikovanja ili upotrebe djela u svom djelu, ako se navede ime autora na način određen od strane autora ili davaoca licence. Ova licenca ne dozvoljava komercijalnu upotrebu djela. U odnosu na sve ostale licence, ovom licencom se ograničava najveći obim prava korišćenja djela.
4. Autorstvo – nekomercijalno – dijeliti pod istim uslovima. Dozvoljavate umnožavanje, distribuciju i javno saopštavanje djela, i prerade, ako se navede ime autora na način određen od strane autora ili davaoca licence i ako se prerada distribuira pod istom ili sličnom licencom. Ova licenca ne dozvoljava komercijalnu upotrebu djela i prerade.
5. Autorstvo – bez prerade. Dozvoljavate umnožavanje, distribuciju i javno saopštavanje djela, bez promjena, preoblikovanja ili upotrebe djela u svom djelu, ako se navede ime autora na način određen od strane autora ili davaoca licence. Ova licenca dozvoljava komercijalnu upotrebu djela.
6. Autorstvo – dijeliti pod istim uslovima. Dozvoljavate umnožavanje, distribuciju i javno saopštavanje djela, i prerade, ako se navede ime autora na način određen od strane autora ili davaoca licence i ako se prerada distribuira pod istom ih sličnom licencom. Ova licenca dozvoljava komercijalnu upotrebu djela i prerada. Slična je softverskim licencama, odnosno licencama otvorenog koda.